Forecasts for Galaxy Cluster Observations and Cosmological Implications from the *eROSITA* All-Sky Survey

Dissertation
zur
Erlangung des Doktorgrades (Dr. rer. nat.)
der
Mathematisch-Naturwissenschaftlichen Fakultät
der
Rheinischen Friedrich-Wilhelms-Universität Bonn

vorgelegt von

Katharina Borm

aus
Geesthacht

Bonn, 2015

Dieser Forschungsbericht wurde als Dissertation von der Mathematisch-Naturwissenschaftlichen Fakultät der Universität Bonn angenommen und ist auf dem Hochschulschriftenserver der ULB Bonn `http://hss.ulb.uni-bonn.de/diss_online` elektronisch publiziert.

1. Gutachter:	Prof. Dr. Thomas H. Reiprich
2. Gutachter:	Prof. Dr. Cristiano Porciani
Tag der Promotion:	17.03.2016
Erscheinungsjahr:	2016

Abstract

One of the most commonly asked questions in astrophysics today refers to the nature of dark energy, and thus to the details of the evolution of our Universe. The characteristics of dark energy are imprinted in the large-scale structure of matter and accordingly also in the distribution of galaxy clusters as tracers of this structure. The up-coming *eROSITA* X-ray instrument, which is scheduled for launch in early 2017, will detect a sample of $\sim 100,000$ clusters of galaxies in this wavelengths range in a total of eight all-sky surveys. These observations are expected to significantly support the study of dark energy.
Already before the launch of this instrument, it is essential to provide forecasts on the expected observations and on their interpretations, as well as to test and prepare the required software and data analysis strategies. The projects within this thesis support these aims, while focusing on the observations of galaxy clusters and on the cosmological implications from the expected cluster catalogue. Based thereon, we perform predictions on how well *eROSITA* will be able to detect cluster gas temperatures and redshifts, and we quantify the impact of the tools for the analysis of the raw data on these results. In a second project, the constraints, which the expected large cluster sample will place on the cosmological parameters, including the characteristics of dark energy, are estimated.
For the first project, we simulate cluster spectra for a variety of different cluster masses and redshifts, while accounting for the expected background emission as well as for the instrumental response. An emission model is then fit to these spectra to re-obtain the cluster temperature and redshift. Convolving these results with the halo mass function and an assumed *eROSITA* selection function, yields the number of clusters with precisely estimated characteristics. For a sub-sample of cluster masses and redshifts, we test the influence of the pre-analysis procedures, which are required to extract the cluster spectra from the observed raw data. Thus, we generate event files of cluster observations and analyse them applying the available tools of the currently developed *eROSITA* data reduction software, *eSASS*. The finally extracted spectra are again analysed by the above procedures and the best-fit results are compared to the input properties. Thus, we are able to identify and quantify systematics in the simulation and data reduction strategies.
Based on the instrumental response, on X-ray cluster scaling relations, as well as on the information on cluster observations obtained above, we convert the halo mass function to a more general halo abundance function. This function considers a more direct observable, the number of observed photon counts η, instead of the cluster mass. With the help of this model, we compute a mockcatalogue of the expectedly observed *eROSITA* clusters, which is highly dependent on the applied cosmology. Implementing the mockcatalogue and the corresponding cluster abundance model into *Markov-Chain Monte Carlo* simulations, yields the credibilities, with which the different cosmological parameters, including the nature of dark energy, can be defined by the cluster sample.
Following these projects, we emphasise that *eROSITA* will observe precise temperatures with $\Delta T/T < 10\%$ for clusters up to distances of $z \lesssim 0.16$, which relates to $\sim 1,700$ new clusters with precise properties from the all-sky surveys. Also, redshifts will be accessible from the X-ray data alone up to distances of $z \lesssim 0.45$. Additionally, we quantify the bias in the best-fit temperatures as well as in the computed uncertainties to be negligible for all clusters with precise temperatures in these observations. For the remaining clusters, correction functions are defined to still allow for the computation of accurate properties. When considering the systematics, arising from the analysis of the raw data, the simulated temperature precisions decrease slightly, whereas on average the parameter space of clusters with precise temperatures remains unchanged. However, the pre-analysis tools resulted in a strong temperature

bias of $\approx 10\%$ for these clusters. The identification of this and other systematics in these software packages already initiated their advanced development and indicated the importance of similar investigations of these tools also in the future.

The cosmological forecasts, on the other hand, present the *eROSITA* instrument as powerful probe for precision cosmology and thus also for the study of dark energy. Credibilities of $\Delta\sigma_8 = 0.013(1.6\%)$, $\Delta\Omega_\mathrm{m} = 0.01(3.4\%)$, $\Delta w_0 = 0.117(11\%)$, and $\Delta w_\mathrm{a} = 0.432$ from the cluster abundances alone show comparable constraints to the *Planck* data with external priors. Combining both data sets, allows for precisions of $\Delta w_0 = 0.077(7.7\%)$ and $\Delta w_\mathrm{a} = 0.276$ with a figure of merit of $\mathrm{FoM}^{2\sigma}_{w_0,w_\mathrm{a}} = 53$ for the nature of dark energy. At the same time, the observed cluster catalogue will provide additional information to tighten the knowledge on the $M - L_\mathrm{X}$ scaling relation.

In conclusion, *eROSITA* will allow for precise studies of the galaxy cluster properties, while increasing the current sample of clusters with precise temperature estimates by a factor of $5 - 10$. The on-going development of the data analysis tools will support these expectations as well as the observations of accurate and reliable cluster characteristics and data interpretations. These cluster studies and the resulting large catalogue of objects, will provide the required information for strong and unprecedented cosmological constraints. Accordingly and based on the computed FoM, *eROSITA* is classified as the first Stage IV probe for studying the nature of dark energy.

Contents

CHAPTER 1

Prelude

"Astronomy? Impossible to understand and madness to investigate."

Sophocles, c. 420 BC

Since the dawn of time, the night sky and its phenomena have impacted the evolution of cultures as well as their strives and believes. Whereas in the early history, astronomical observations were commonly interpreted as a divine intervention, already the ancient advanced civilisations studied regularities in the motion of celestial objects and tracked the passing of time in calendars. Since these early days, a great leap in astronomical knowledge could be achieved and modern research in this field has been revolutionised to big data science governed by a complex physical framework and intensive computing. Apart from this development, the general wide-spread attraction to astronomy and the puzzles of the cosmos have remained.

The progress in astronomy and astrophysics was especially guided by the derivation of advanced theoretical models to describe e.g. General Relativity or the characteristics of spacetime, as well as by further developments in technology and of powerful telescopes. We are thus able to e.g. look deeper into space with an ever improving resolution, to identify diffuse objects as independent galaxies, comparable to our own Milkyway and at large distances of several Millions and Billions of lightyears, or to map the over-all large scale distribution of these galaxies as well as of other astrophysical objects. Another basic principle for shaping our current understanding of the Universe, is the observation of space in all wavelengths, starting from the low radio frequencies with wavelengths of the order of kilometers up to the highest gamma energies of $\sim 10^{21}$ eV. This multiwavelength approach allowed for the discovery of previously unknown classes of objects and for the study of their properties, as well as for the exploration of additional characteristics of already known objects.

All of these discoveries established the idea of the Universe as being infinite and unconfined, with an origin in an initially hot, dense state, the so-called *Big Bang*, $\sim$ 13.6 Billion years ago. From this time onwards, the Universe expanded continuously and consequently cooled down. The evolution of our Universe from this initial state to today is one of the currently most extensively studied aspects in astrophysics and is summarised in the field of *cosmology*. This topic asks the questions how the Universe evolved from the Big Bang until today, but also how it will develop in the future. Will it re-collapse into a singularity or will it expand forever? Accordingly, studying cosmology allows us to predict the initial as well as the final state of the Universe! In addition to these elementary questions, the field of cosmology combines physical processes on the largest and smallest length scales with mutliwavelength observations, complex theoretical models, and computationally expensive simulations.

To study the evolution of the Universe, it is essential to decode its geometry as well as its composition

in terms of its total energy budget, its different forms of energy and matter, and the characteristics of these components. Amongst these are radiation, consisting of photons and relativistic neutrinos, as well as ordinary baryons, massive neutrinos and particles of the physical standard model in general. However, observations indicate the additional existence of so-far not understood forms of matter and energy, which are not yet included in this standard model. These exotic forms are *dark matter* and *dark energy*.
The existence of dark matter was suggested by the Swiss astrophysicist Fritz Zwicky in 1933 (Zwicky 1933). He observed the velocity dispersions of galaxies in the Coma galaxy cluster, a gravitationally bound and virialised accumulation of these objects. Following the laws of gravity, he inferred the required mass to bind the galaxies to the cluster. As the observed mass showed a deviation from the expected, computed value with a reduction by more than an order of magnitude, Zwicky introduced an additional, dark and thus unobserved mass component, which he labeled *dark matter*. Today, we find the imprints of dark matter on all scales, where it explains e.g. rotation curves of spiral galaxies (e.g. Bertone et al. 2005), or the evolution of structures in the Universe (e.g. Bergström 2000). However, this form of matter has not been detected directly, yet, and we are able to study it only indirectly based on its effects on the surrounding luminous matter. Following this study, dark matter appears as a particle outside our current standard model of physics, which interacts especially via gravity and shows a very small cross section for other particle interactions. Apart from these hints, the characteristics of this particle species are still unidentified.
While elaborating the properties of dark matter, astrophysicists were and still are challenged by the discovery of an accelerated expansion of the Universe. At the end of the last century, two independent research groups analysed the distances to supernovae type Ia, a special type of exploding star at the end of its life time. They realised that these objects showed larger distances than expected, where these increased distances proposed an accelerated expansion of space (Perlmutter et al. 1998; Riess et al. 1998). To drive the acceleration, an additional component was introduced to our cosmological model - *dark energy*. Even though many models exist to describe this energy species, also dark energy has not been observed directly, yet, and its nature is still less accessible than the characteristics of dark matter. Within the current understanding, we treat dark energy as an attribute of space, showing a constant density in time and space.
In summary, these two dark components contribute to $\sim 95\%$ of the current total energy density of the Universe, with $\sim 70\%$ being added by dark energy only. Accordingly, only little information is available on the vast major fraction of our Universe. What is more, due to their energy dominance, dark matter and dark energy are strongly shaping the evolution of the Universe. Thus, to recover our past and to predict our future evolution, we need to study the nature of these two dark components, where especially the analysis of dark energy is one of the key research goals in cosmology. In addition to the motivations expressed above, this pursuit to explore the dark side of the Universe states a further encouragement as well as a necessity for cosmological studies.
As dark energy is not directly observable with current instruments, we investigate its nature by its imprints on the detectable Universe, which includes its geometry and the evolution of the over-all large-scale distribution of matter. The latter is especially traced by massive objects, such as e.g. galaxies and clusters of galaxies. Due to the finite speed of light, we indeed glimpse the past evolutionary stages by examining space at large distances. Especially the earliest times reveal the most essential information about the evolution of the Universe. Within this work, I am especially interested in the galaxy cluster approach, where I analyse their spatial distribution as well as their distribution with their mass to map the underlying matter structure and its development. The precision and accuracy of the reconstruction of structures depends, accordingly, on the precision and accuracy of the cluster observation data as well as on the size of the applied cluster sample, where the statistical uncertainty decreases with increasing catalogue size. One common strategy is the use of X-ray galaxy cluster catalogues, since X-ray obser-

vations have proven as an effective technique for detecting these objects as well as for recovering their characteristics. Currently, the sample of X-ray galaxy clusters with precise information consists of the order of a few hundred objects, where roughly a couple of thousand clusters are known in X-rays in total (comp. e.g. Piffaretti et al. 2011).
The study of large samples of galaxy clusters in this energy range was especially revolutionised by *ROSAT* (*Roentgensatellit*), which was launched in 1990 and performed the first X-ray all-sky survey with an imaging telescope (Trümper 1985). After the first six months of all-sky survey, *ROSAT* continued with deep exposure, pointed observations, such that during its nine years of operation time, the telescope discovered close to 2,000 clusters of galaxies (Voges et al. 1999; Rosati et al. 2002). The currently operating X-ray instruments, which are mainly the European *XMM-Newton*, the US-American *Chandra* and *NuSTAR*, and up to recently the Japanese *Suzaku*, pursue the second observational approach and follow-up already known clusters with detailed pointed observations. Accordingly, these telescopes continuously improve and extend the catalogue of galaxy clusters with precisely available characteristics. As the *ROSAT* all-sky survey covers only the brightest clusters of galaxies with fluxes of the order of $\gtrsim 10^{-13}$ erg/s/cm^2 in the energy range between $(0.5 - 2.0)$ keV (Trümper 1985) and at rather low distances with redshifts around $z \lesssim 0.5$[1], the interest is to develop a new X-ray all-sky survey. The applied instruments should show a comparable or even improved resolution and sensitivity to the currently operating instruments. However, as these current instruments perform only pointed observations, an additional all-sky survey of the same sensitivity will significantly increase the total number of observed clusters in X-rays and will thus essentially support detailed cosmological studies.
The planned *eROSITA*-telescope (*extended ROentgen Survey with an Imaging Telescope Array*) is such an instrument (Predehl et al. 2010; Merloni et al. 2012). It is scheduled for launch in early 2017 as a joint German-Russian mission and is presently assembled under the leadership of the *German Space Agency* (*DLR*) and the *Max-Planck Society* (*MPG*). The instrument is expected to detect a total of 100,000 clusters of galaxies and it will thus extend the X-ray cluster catalogue by a factor of about ~ 50 (Pillepich et al. 2012), while increasing the number of clusters with precisely known characteristics at the same time (Borm et al. 2014). Accordingly, *eROSITA* presents itself as powerful instrument to map the past evolution of structures and to thus investigate the nature of dark energy for decoding the future evolution of our Universe.
To allow for an efficient and an accurate reduction as well as interpretation of the up-coming *eROSITA* data, a diversity of preparatory tasks are required, several of which are introduced in this thesis. Following the cosmological science driver of this instrument, I simulate the abundance and distribution of clusters that *eROSITA* will observe and test how the catalogue of clusters with precise characteristics is improved quantitatively. Based on these cluster information, I predict the constraints, the instrument will place on cosmology and especially on the nature of dark energy. To investigate these research interests, this thesis is structured as follows. The subsequent two chapters emphasise on the theoretical background of cosmological studies with galaxy clusters, including the necessary software and statistical tools. Thereafter follow three chapters presenting the results for the above mentioned science goals with a summarising conclusion stated in chapter 7. The contents of chapter 4 hava already been published and accepted by the journal *Astronomy and Astrophysics* in May 2014 as Borm et al. (2014) (bibliographic code: 2014A&A...567A..65B, reprinted with permission © *ESO*), whereas the work presented in chapter 6 is in the process of being submitted.
Following these research tasks, this thesis constributes not only to the preparations of the *eROSITA* instrument, but also to the exploration of dark energy and the evolution of our Universe in general.

[1] In astrophysics, distances are commonly described in terms of redshift. A redshift of $z = 0.5$ corresponds to a time five Billion years ago or equivalently to distances of a Billion light years (ly) or a few hundred Million parsec (pc).

CHAPTER 2

Introduction

Within the last four decades, astrophysicists were able to develop a defined idea of the evolution and composition of our Universe. Based on only the physical laws and on two handfuls of so-called cosmological parameters, we are able to describe the past evolution of our Universe in detail and to predict its future development. Gradually, the values of these parameters were constrained with increasing precision, while there is still room left for improvement, e.g. in precisely quantifying the cosmological parameters, or in testing additions to the currently accepted evolution model of our Universe.
The following sections present the reader with a brief summary of our current understanding of the cosmological characteristics of our Universe and introduce the methodology of these studies based especially on the large scale distribution of matter as well as on galaxy clusters as its tracers. Additionally, the up-coming *eROSITA*-instrument is described as a promising tool for decoding the past and for forecasting the future evolution of our Universe.
The general concepts of cosmology presented in Sects. 2.1 to 2.4, are based on the literature of e.g. Kolb & Turner (1990); Peacock (1999); Dodelson (2003); Schneider (2015) if not stated otherwise.

2.1 Our Cosmological Model

Within the general understanding, the Universe formed $\sim$ 13.6 Billion years ago from an initially hot, dense state, which we refer to as the Big Bang. From this point onwards, the Universe is expanding continuously, while following the principles of being infinite and unconfined. However, we are not able to observe the entire Universe, as information can only travel with the finite speed of light. All regions, that are currently causally connected and are thus exchanging information amongst each other, are located within a sphere of the so-called *Hubble radius* (compare section 2.1.1). This radius is especially dependent on the expansion history of the Universe. Following our presently accepted cosmological model, we expect a current Hubble radius of close to 5 Gpc, where 1 pc $\approx 3.086 \cdot 10^{16}$ m. The finite speed of light also results in the phenomenon of always looking back into the past as light needs time to travel form the source to the observer. The larger the observed distances are, the larger is also the look-back time.
Another important framework is the *cosmological principle*, which is based on the elemental idea that there are no distinguished observers and that space appears uniform in all observed directions. The latter aspect is referred to as isotropy of the Universe where the combination of both of the above statements additionally results in the assumption of homogeneity. Accounting for these basic principles of our Universe, we now describe its evolution and composition within a more theoretical framework.

2.1.1 Dynamics of Spacetime

Following the concepts of general relativity, the three spatial dimensions and the time are combined into a four-dimensional, interacting continuum, referred to as *spacetime*. Accordingly, a certain position in this four-dimensional continuum is described by a time variable t and a three-dimensional spatial coordinate. The spatial vector is defined on a grid with fixed points, such that the distances between the individual grid points are stretched with the expansion of space. This relative expansion between the grid points is expressed by a dimensionless property, the so-called *scaling factor* $a(t)$, with a dependence on time and a value of unity for today $a(t_0) = 1$. Based on the expansion of the Universe with time, we accordingly constitute $a(t_1) < a(t_2)$ for $t_1 < t_2$. The location of an object in space is thus defined as $\boldsymbol{r}(t) = a(t) \cdot \boldsymbol{x}$, with the 3-dimensional coordinate $\boldsymbol{x}$ representing the position on the fixed grid. To derive the spatial evolution as well as to compute the physical distances between different objects, based on this principle, we refer to Einstein's theory of General Relativity.
One of the solutions to Einstein's field equations was derived by Friedmann, Lemaître, Robertson and Walker in the 1920s and 1930s to describe distances in the Universe. This *Friedmann-Robertson-Walker metric* (FRW-metric) reads

$$\mathrm{d}s^2 = c^2\mathrm{d}t^2 - a^2(t) \cdot [\mathrm{d}\chi^2 + f_K^2(\chi) \cdot (\mathrm{d}\theta^2 + \sin^2\theta \cdot \mathrm{d}\phi^2)] \quad . \tag{2.1}$$

The constant c represents the speed of light, whereas the parameter $\mathrm{d}s$ describes the separation between two objects in the 4-dimensional spacetime. The spatial position is written in spherical coordinates (χ,θ,ϕ), with the radial *comoving distance* χ depending on the curvature K of spacetime

$$f_K(\chi) = \begin{cases} K^{-1/2} \cdot \sin[K^{1/2} \cdot \chi] & (K > 0) \\ \chi & (K = 0) \\ (-K)^{-1/2} \sinh[(-K)^{1/2} \cdot \chi] & (K < 0) \end{cases} \quad . \tag{2.2}$$

In space, information propagates as electromagnetic waves, which follow null geodesics with the characteristics $(\theta, \phi) = \text{const.}$ and $\mathrm{d}s = 0$. Accordingly, the FRW-metric simplifies to

$$c \cdot \mathrm{d}t = -a(t) \cdot \mathrm{d}\chi \tag{2.3}$$

$$\Rightarrow \chi(t) = \int_t^{t_0} \frac{c\mathrm{d}t'}{a(t')} \quad . \tag{2.4}$$

for the comoving distance $\chi(t)$ between us and an event happening at the cosmic time t. Looking back to the beginning of the Universe at $t = 0$, the comoving distance defines the Hubble radius r_H as $\chi(0) = r_\mathrm{H}$. At the same time, the above equation is the basis to derive the expression of the *cosmological redshift* z. For this derivation, we assume a source, which emits two signals at t_e and $t_\mathrm{e} + \Delta t_\mathrm{e}$ at a constant comoving distance χ. These signals are then observed at the later times t_0 and $t_0 + \Delta t_\mathrm{obs}$ and we obtain the relation

$$\chi = \int_{t_\mathrm{e}}^{t_0} \frac{c \cdot \mathrm{d}t'}{a(t')} = \int_{t_\mathrm{e}+\Delta t_\mathrm{e}}^{t_0+\Delta t_\mathrm{obs}} \frac{c \cdot \mathrm{d}t'}{a(t')} \tag{2.5}$$

$$\Rightarrow \int_{t_\mathrm{e}}^{t_\mathrm{e}+\Delta t_\mathrm{e}} \frac{c \cdot \mathrm{d}t'}{a(t')} = \int_{t_0}^{t_0+\Delta t_\mathrm{obs}} \frac{c \cdot \mathrm{d}t'}{a(t')} \quad . \tag{2.6}$$

For small time periods Δt_0 and Δt_e and assuming $a(t)$ to only change insignificantly during these time intervals, we conclude

$$\Delta t_\mathrm{e} = a(t) \cdot \Delta t_\mathrm{obs} \quad , \tag{2.7}$$

applying $a(t_0) = 1$. The expansion of the Universe defines $a(t_e) < a(t_0) = 1$ and accordingly $\Delta t_{obs} > \Delta t_e$, following Eq. 2.7. This increase of the interval between the observed signals has an influence on the observed frequency of the signal. With $\nu_e = 1/\Delta t_e = \nu_{obs}/a(t)$ and thus $\nu_e > \nu_{obs}$, the observed frequency is decreased and the cosmological redshift z is defined as

$$(1 + z) := \frac{\nu_e}{\nu_{obs}} = \frac{\lambda_{obs}}{\lambda_e} = \frac{1}{a(t)} \quad , \tag{2.8}$$

with the wavelength $\lambda = c/\nu$. As $a(t)$ decreases continuously with increasing look-back time, also the redshift increases and $z_e > z_0$, where $z_0 = 0$ by definition. In the following, the variables t, $a(t)$ and $z(t)$ are used equivalently to represent different time epochs.
As shown by the previous considerations, distances in space are based on the evolution of the scale factor $a(t)$, which itself depends on the energy budget and the composition of the Universe. In 1922, the theoretical astrophysicist Friedmann derived a set of two independent differential equations that describe the evolution of the scale factor as a solution to Einstein's field equations (Friedmann 1922). These *Friedmann equations* read

$$\text{I)} \qquad \left(\frac{\dot{a}}{a}\right)^2 = \frac{8\pi G}{3} \cdot \rho - \frac{K c^2}{a^2} + \frac{\Lambda c^2}{3} \tag{2.9}$$

$$\text{II)} \qquad \frac{\ddot{a}}{a} = -\frac{4\pi \mathrm{G}}{3} \cdot \left(\rho + 3 \cdot \frac{p}{\mathrm{c}^2}\right) + \frac{\Lambda c^2}{3} \quad , \tag{2.10}$$

where we simplified $a(t) = a$. The variables ρ and p define the energy density as well as the pressure in the Universe, respectively, whereas Λ presents the *cosmological constant* as an additional energy source. The first Friedmann equation defines the expansion rate $\dot{a}/a$ of spacetime, which is commonly expressed by the *Hubble parameter* $H(t)$

$$H(t) = \frac{\dot{a}(t)}{a(t)} \quad . \tag{2.11}$$

Most recent measurements of today's expansion rate, the so-called *Hubble constant*, yield a value of $H_0 \approx 67.74 \pm 0.46$ km/s/Mpc (Planck Collaboration et al. 2015c), which is equivalently formulated by the dimensionless variable $h = H_0/(100$ km/s/Mpc). The second Friedmann equation states the rate of accelerated expansion of the Universe. If, as a first approach, the last term on the right hand side of equation 2.10 is neglected, an acceleration is obtained for

$$-\frac{1}{3} > \frac{p}{\rho \mathrm{c}^2} \quad . \tag{2.12}$$

In the assumption of only one dominating energy component, this component induces an accelerated expansion of spacetime, if its equation of state $w = p/(\rho \mathrm{c}^2)$ reads $w < -1/3$.

2.1.2 Composition of the Universe

As displayed in equation 2.9, the curvature K and thus the geometry of the Universe are closely linked to the total energy density. The case of a flat Universe with $K = 0$ requires a precisely calibrated density value, the so-called *critical density*

$$\rho_{\mathrm{crit}}(t) = \frac{3H(t)^2}{8\pi G} \quad . \tag{2.13}$$

In the case of $\rho > \rho_{\mathrm{crit}}$, the geometry is closed with $K > 0$, whereas for $\rho < \rho_{\mathrm{crit}}$, the curvature is negative $K < 0$ and space time is defined as open. Furthermore, the individual energy components are defined as ratios in comparison to the critical density

$$\Omega_{\mathrm{i}} = \frac{\rho_{\mathrm{i}}}{\rho_{\mathrm{crit}}} \quad , \tag{2.14}$$

with the index i noting the different energy components and $\Omega_0 = \sum_{\mathrm{i}} \Omega_{\mathrm{i},0}$ describing the total energy density today. Different experiments concordantly estimate Ω_0 to be of the order of unity with $\Omega_0 = 0.9992^{+0.0040}_{-0.0039}$ (compare e.g. Planck Collaboration et al. 2015c; Komatsu et al. 2011) and thus confirm a flat geometry of our Universe. This total energy budget is believed to be composed as follows:

Neutrinos: Current experiments estimate the effective total number of neutrino families to be consistent with $N_{\mathrm{eff}} = 3.046$ (Planck Collaboration et al. 2015c) and thus with the Standard Model of particle physics. However, since the discovery of neutrino oscillations at the beginning of this century, these particles are expected to show masses larger then zero, despite the previous assumptions of this standard model. Detailed investigations on their mass characteristics yield lower constraints on the summed mass for all neutrino species of $\sum m_\nu > 0.06$ eV (e.g. Lesgourgues & Pastor 2012). A detailed summary of neutrino physics relevant for cosmology is given by Lesgourgues et al. (2013). Depending on the neutrino masses and their corresponding current velocities, the neutrinos species contribute differently to the energy budget of the Universe as explained below.

Radiation: Radiation consists of relativistic particles, which are photons γ and neutrinos ν with masses close to zero. Induced by the evolution of spacetime, the radiation density is time dependent with $\rho_{\mathrm{r}}(a) = \rho_{\mathrm{r},0} \cdot a^{-4}$, following the cosmic expansion $\propto a^{-3}$ and an energy shift $\propto a^{-1}$ due to the cosmic redshift (compare Eq. 2.8). The radiation density ρ_{r} itself is mainly defined by the temperatures of the two species, which started to form homogeneous and isotropic radiation backgrounds very early after the Big Bang. The relations follow $\rho_\gamma \propto T_\gamma^4$ and $\rho_{\nu,\mathrm{relativistic}} \propto T_\nu^4$, respectively, with

$$\rho_{\nu,\mathrm{relativistic}} = \rho_\gamma \cdot \frac{7}{8} \cdot \left(\frac{4}{11}\right)^{4/3} \cdot N_{\mathrm{eff,relativistic}} \quad , \tag{2.15}$$

applying the comparison between the two background temperatures[2] (comp. Sect. 2.2.1), $T_\nu = (4/11)^{1/3} \cdot T_\gamma$, and the different degrees of freedom for neutrinos as fermions and photons as bosons. Here $N_{\mathrm{eff,relativistic}}$ defines the number of relativistic neutrino species.

[2] We will see in Sect. 2.2.2 that $T_\gamma = 2.73\ \mathrm{K} = T_{\mathrm{CMB}}$, with T_{CMB} as the temperature of the so-called *Cosmic Microwave Background*.

Baryonic Matter: The component Ω_b summarises all baryons, which especially show the characteristics to interact strongly electromagnetically. Accordingly, efficient photon interactions result in the transport of information of this type of matter to us as observer. Also the baryon density is influenced by the expansion of spacetime as $\rho_b(a) \propto a^{-3}$. All other matter components follow the same evolution with time.

Dark Matter: The existence of dark matter was first postulated in galaxy clusters by Fritz Zwicky in 1933 (Zwicky 1933). Today we indirectly observe dark matter on all scales through its gravitational impact on baryonic matter. Direct detections have not been accomplished, yet, and the few known characteristics are e.g. inferred from studying the primordial nucleosynthesis right after the big bang (compare 2.2.1), the history of structure formation (compare 2.3), or the interactions of galaxy clusters. Accordingly, dark matter is expected to show a non-baryonic origin and very low interaction cross-sections with estimated upper limits on the cross section for self-interactions of the order of $\sigma/m \lesssim 1$ cm^2/g in dependence on the particle mass m (e.g. Markevitch et al. 2006; Randall et al. 2008).
Depending on the particle velocities and thus on the assumed masses, three different types of dark matter are defined - "hot", "warm" and "cold". For example, neutrinos with relativistic velocities today are e.g. considered as hot dark matter, whereas neutrinos with slightly higher masses and accordingly non-relativistic velocities are referred to as warm particles. In the latter case, the neutrinos contribute to the over-all matter density of the Universe as

$$\Omega_{\nu,\mathrm{massive}} = \frac{m_\nu}{93.14 \cdot h^2 \ \mathrm{eV}} \tag{2.16}$$

(e.g. Lesgourgues et al. 2013; Böhringer & Chon 2015; Roncarelli et al. 2015) in dependence on the summed mass of all non-relativistic species. In this way of thinking, Ω_ν is independent of the number of non-relativistic species for a fixed $\sum m_\nu$, where by default $N_{\mathrm{eff,massive}}$ is commonly set to one for simplicity[3].
One commonly suggested model for cold dark matter are the so-called *WIMP*s, or *Weakly Interacting Massive Particles*. The current standard model of particle physics does not include such a massive particle with all of the above characteristics and additional theorems are required. One idea includes the concepts of supersymmetry and defines WIMPs as the lightest supersymmetric particle, the so-called *neutralino* χ, which show assumed masses of $m \approx 100\,\mathrm{GeV/c^2}$. Based on this mass estimate, a thermally averaged reaction rate for self-interaction equivalent to $\langle \sigma v \rangle \approx 3 \cdot 10^{-26}\ \mathrm{cm^3/s}$ was inferred.
In summary, we split up the dark matter budget Ω_{DM} into a cold and a warm component Ω_c and Ω_ν, respectively. The relativistic neutrinos are considered as radiation component.

Dark Energy: At the end of the last century, two research groups applied supernovae type Ia observations to measure the relation between the observed distances and redshifts (Riess et al. 1998; Perlmutter et al. 1998). Their observations were not in agreement with their fiducial cosmological model of matter and radiation as only energy components and of a steadily expanding Universe. Instead, the measurements indicated an accelerated expansion of spacetime, which is initiated by a third form of energy, a kind of vacuum energy with negative pressure. This so-called *dark energy* constitutes roughly two thirds of the entire energy budget and is thus significantly driving the evolution of the cosmos.
Often, dark energy is identified with the *cosmological constant* with $\rho_\Lambda = \mathrm{const}$ and $w = -1$ (comp. Eqs. 2.9, 2.10 & 2.12). The corresponding cosmological model is referred to as ΛCDM, with Λ for the cosmological constant and CDM for "cold dark matter". It includes all of the above mentioned energy

[3] Please refer to the file at *http://cosmologist.info/notes/CAMB.pdf* for an application example.

components and assumes a curvature of $K = 0$. However, as the characteristics of dark energy are still investigated also more generalised models are tested. These e.g. allow for a constant equation of state, w_0CDM, with $w = \text{const.}$ but $w \neq -1$, or for a variable equation of state, wCDM, with $w \neq \text{const.}$ and $w = w(a)$. Commonly, the dark energy density is labeled by the subscript "DE" as e.g. ρ_{DE}, independent of its characteristics.
A general evolution of its density is then derived as

$$\rho_{\mathrm{DE}} = \rho_{\mathrm{DE},0} \cdot \exp\left[-3 \cdot \int_1^a \frac{1 + w(a')}{a'} da'\right] \quad . \tag{2.17}$$

The most commonly applied variable equation of state (Chevallier & Polarski 2001; Linder 2003) and its corresponding evolution read

$$w(a) = w_0 + w_{\mathrm{a}} \cdot (1 - a) \tag{2.18}$$

$$\rho_{\mathrm{DE}} = \rho_{\mathrm{DE},0} \cdot \exp\left[-3 \cdot (w_{\mathrm{a}} \cdot (1 - a) + (1 + w_0 + w_{\mathrm{a}}) \cdot \ln a)\right] \quad . \tag{2.19}$$

To quantify the total energy budget in the Universe, we summarise the above considerations as (Planck Collaboration et al. 2015c)

$$\Omega_0 = \Omega_{\mathrm{r}} + \Omega_{\mathrm{b}} + \Omega_\nu + \Omega_{\mathrm{c}} + \Omega_{\mathrm{DE}} + \Omega_K \tag{2.20}$$

$$\text{with} \quad \Omega_{\mathrm{m}} = \Omega_{\mathrm{b}} + \Omega_\nu + \Omega_{\mathrm{c}} \quad , \tag{2.21}$$

and state the values of the cosmological parameters in Tab. 2.1. Please note, that some of the mentioned parameters will be explained in a later section. Following the definition of the density parameters, we rewrite the first Friedmann equation (Eq. 2.9) in a more viable formalism

$$\left(\frac{\dot{a}}{a}\right)^2 = H(t)^2 = H_0^2 \cdot (\Omega_{\mathrm{r}} \cdot a^{-4} + \Omega_{\mathrm{m}} \cdot a^{-3} + \Omega_{\mathrm{DE}} + \Omega_K \cdot a^{-2}) \tag{2.22}$$

$$\text{with} \quad E(a) = \sqrt{\Omega_{\mathrm{r}} \cdot a^{-4} + \Omega_{\mathrm{m}} \cdot a^{-3} + \Omega_\Lambda + \Omega_K \cdot a^{-2}} \quad , \tag{2.23}$$

assuming a cosmological constant as dark energy. In a more general case, the constant parameter Ω_Λ needs to be replaced by expression Eq. 2.19. From the different evolutions of the individual energy components with the scale factor, we conclude the existence of three epochs of domination. Right after the Big Bang, radiation was the dominant form of energy until $a_{\mathrm{eq}} \approx 3 \cdot 10^{-4}$, $z_{\mathrm{eq}} = 3371$ (Planck Collaboration et al. 2015c), when matter became the dominant component. At a redshift of roughly $(1 + z) = \Omega_{\mathrm{m}}^{-1/3}$ or $z \approx 0.5$, dark energy started dominating the total energy budget (e.g. Carroll et al. 1992).

2.1.3 Distance Measures

In an expanding Universe distances cannot be defined explicitly, as spacetime evolves during the travel time of light rays. We therefore consider three different approaches as distance measures: the comoving distance, the *angular diameter distance*, D_{A}, as well as the *luminosity distance*, D_{L}. Rewriting the comoving distance (Eq. 2.4) with the definition of the Hubble parameter yields

$$\chi(z_1, z_2) = \int_{a(z_1)}^{a(z_2)} \frac{\mathrm{c} \cdot \mathrm{d}a}{a^2 \cdot H(a)} = \frac{\mathrm{c}}{H_0} \int_{a(z_1)}^{a(z_2)} \frac{\mathrm{d}a}{a^2 \cdot E(a)} \tag{2.24}$$

Table 2.1: Cosmological model parameters as observed by Planck Collaboration et al. (2015c), where the last two parameter values are added to present assumptions for a complete cosmological consideration.

Parameter	Value	Description
$\Omega_\mathrm{b}h^2$	0.0223 ± 0.00014	baryon density
$\Omega_\mathrm{c}h^2$	0.1188 ± 0.0010	cold dark matter density
Ω_DE	0.6911 ± 0.0062	cosmological constant
Ω_K	$0.0008^{+0.00040}_{-0.0039}$	curvature
H_0	67.74 ± 0.46	Hubble constant
n_s	0.9667 ± 0.0040	index of the linear power spectrum
σ_8	0.8159 ± 0.0086	matter variance of scales of 8 Mpc/h
w_0	$-1.019\pm^{+0.075}_{-0.080}$	normalisation of the dark energy equation of state
w_a	consistent with 0.0	slope of the dark energy equation of state
Ω_r	$\sim 7.5 \cdot 10^{-5}$	radiation density
$\Omega_{\nu,\mathrm{massive}}h^2$	0.00064	massive neutrino density

as the comoving distance between two objects at redshifts z_1 and z_2 with $z_1 < z_2$. The angular diameter distance as well as the luminosity distance are derived in dependence on the comoving distance as

$$D_\mathrm{A}(z_1, z_2) = a(z_2) \cdot \chi(z_1, z_2) \tag{2.25}$$

$$D_\mathrm{L}(z_2) = 1/a(z_2) \cdot \chi(0, z_2) \quad , \tag{2.26}$$

assuming a flat geometry $\Omega_K = 0$ and the observer to be positioned at $z_1 = 0$ in the case of D_L. In the case of curvature these derivations modify to $D_\mathrm{A}(z_1, z_2) = a(z_2) \cdot f_K(\chi)$ and $D_\mathrm{L}(z_2) = 1/a(z_2) \cdot f_K(\chi)$, respectively, following Eq. 2.2.

2.2 Thermal History in a Nutshell

As the previous section emphasised on the general evolution of spacetime, the thermal history will now describe the evolution of the different particle species and of the energy budget with time.
About $\sim$ 13.6 Billion years ago, the Universe was formed within the Big Bang and started to evolve from an initially hot, dense state. Since then, space expanded gradually with time and causes a decrease in the temperature of the different particle species by a factor of $\propto 1/a$, or equivalently as

$$T(t) = T_0/a(t) \quad , \tag{2.27}$$

with T_0 as the current temperature. However, the following section will describe how these particle species show different temperatures according to their history of particle interactions.

2.2.1 From the Big Bang to the Epoch of Recombination

Right after the Big Bang and thus at the highest temperatures, the Universe was dominated by radiation, while only the elementary particles - quarks, leptons, bosons, dark matter particles as well as their antiparticles - existed and interacted with one another in a stable equilibrium. At times of 10^{-43} to 10^{-35} s after the Big Bang, a break in the symmetry between the strong and the electroweak interactions is believed to have happened, which resulted in an overabundance of matter compared to antimatter. This process is known as *baryogenesis*. The equilibrium in the different particle interactions holds as long as their cross sections are larger than the expansion rate of the Universe. Accordingly, as the expansion of the Universe progresses and the temperature decreases gradually, several interaction channels become inaccessible and different particle species start to *freeze-out* of this equilibrium. The first particles to follow this trend are the still hypothetical cold dark matter particles. With expected rest masses of $m \gtrsim 100$ GeV/c^2 they can no longer be produced at times of the order of $t \gtrsim 10^{-10}$ s and additionally, they only show negligible cross sections for interactions with other particles. Due to this freeze-out, the CDM-particles now free-stream across spacetime, no longer participate in interactions, and form a homogeneous and isotropic background. As these particles experience decay processes, their density gradually decreases with the currently remaining relict density depending on their time of freeze-out.
The next important step in the thermal history is the hadron epoch, starting at $t \sim 10^{-6}$ s at energies of 1 GeV, in which quarks couple to form protons and neutrons. Only at these low energies, hadrons are composed effectively since at earlier times the high radiation energy density still allows for an equilibrium between the formation of hadrons and their splitting. The newly created protons and neutrons are in equilibrium with the remaining particles and convert into one another via the β- and the inverse β-process. At $t \approx 1$ s, however, neutrinos decouple from the particle equilibrium due to their small cross sections. Followingly, the inverse β-process becomes inaccessible such that neutrons can no longer be produced and their abundance decreases continuously. Shortly after the neutrino decoupling as energies drop below 0.5 MeV ($T \approx 5 \times 10^9$ K), also the process of pair creation $\gamma\gamma \rightarrow e^+e^-$ is suppressed. The back reaction, however, continues at a high rates and thus heats the photon spectrum. As the primordial neutrinos are already decoupled at this epoch of pair-annihilation, their temperatures remain unaffected by this process.
Roughly at $t \approx 200$ s, decreased temperatures of $\sim 10^9$ K allow for the effective formation of the lightest atomic nuclei in the primordial nucleosynthesis. During this process, all neutrons are bound in the atomic nuclei to form mainly deuterium, ^{3}He and ^{4}He as well as traces of lithium. Due to the continuous decrease of the neutron abundance since the era of neutrino decoupling, the amount of atomic nuclei heavier than hydrogen strongly depends on the time interval between these two epochs. Following the model predictions, the expected mass fractions are $X \approx 75\%$ for hydrogen and $Y \approx 25\%$ for helium (for more detailed values compare e.g. Burles et al. (1999) and Burles & Tytler (1998)).
During the epoch of nucleosynthesis, the Universe was still ionised as any binding of electrons to the atomic nuclei was split due to the high photon-to-baryon ratio of $\sim 10^9$. Only at redshifts of $z \approx 1090$ (Planck Collaboration et al. 2015c), roughly 380,000 years after the Big Bang and well in the matter dominated epoch, a further decrease in the temperature and thus also in the photon energy allowed electrons to couple effectively to the nuclei to form neutral atoms. Accordingly, the photons no longer interacted with the free electrons via Compton scattering and were now able to freeze-out, which is referred to as the epoch of recombination. Since before this epoch, the photons were in thermal equilibrium with the electrons, the free-streaming photons now follow a blackbody spectrum. This radiation is known as the *cosmic microwave background* (CMB).

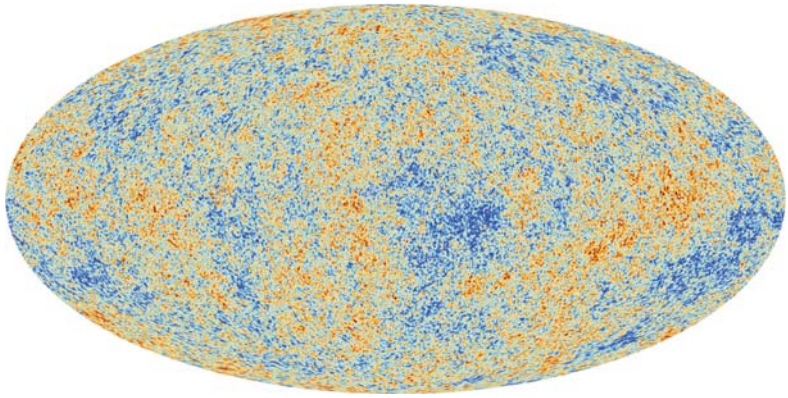

Figure 2.1: Anisotropies in the Cosmic Microwave Background as observed by the Planck satellite. The small temperature anisotropies of $\Delta T/T \approx 10^{-5}$ with the higher temperatures given in the blue colours, indicate the beginnings of structure formation at $z \approx 1090$.[4]

2.2.2 The Cosmic Microwave Background

The discovery of the CMB in the mid-1960s allowed for insight into the early moments after the Big Bang. Within numerous observational missions, the characteristics of the CMB were studied and it was found to show the best-measured blackbody spectrum in nature with a current temperature of $T \approx 2.725 \pm 0.0006$ K (comp. e.g. Fixsen 2009). Within this homogeneous and isotropic radiation, small temperature anisotropies of the order of $\Delta T/T \approx 10^{-5}$ are observed as imprints of the baryonic matter distribution at the epoch of photon decoupling (comp. Fig. 2.1). As a simplified description, the slightly cooler regions, displayed in red, present regions of matter overdensities, such that photons from these regions lose energy while climbing out of the gravitational potential. At large, the CMB contains much information on the different cosmological parameters, which include the different energy components as well as parameters defining the evolution of the matter distribution. They are imprinted in the so-called CMB power spectrum, which describes the strength of the inhomogeneities at the different scales, represented by the multipole moment l. Figure 2.2 displays the CMB power spectrum as it was measured by the Planck satellite, showing as most dominant feature the so-called acoustic peaks at scales of $l \gtrsim 100$. These peaks are due to oscillation of the strongly coupled baryon-photon fluid on scales inside the sound horizon at the epoch of decoupling. The position of the first acoustic peak at $l \approx 1^\circ$ expresses the angular scale of the sound horizon at this time and thus the geometry of the Universe. The position of the peaks is mainly dependent on the total energy density Ω_0, whereas the amplitude of the peaks is related to the matter and to the baryon density, Ω_m and Ω_b, respectively. Analogously, most of the remaining cosmological parameters leave their imprint on the CMB power spectrum, such that this spectrum allows for detailed cosmological studies. A thorough description of the dependencies of the CMB power spectrum on the different cosmological parameters is beyond the scope of this work, however, and is summarised in detail in e.g. Hu & Dodelson (2002). After the epoch of photon decoupling, the evolution of the Universe is mainly shaped by the development of the matter distribution.

[4] *Credit:* ESA (http://www.esa.int/Our_Activities/Space_Science/Planck/Planck_and_the_cosmic_microwave_background)
[5] *Credit:* ESA (http://www.esa.int/spaceinimages/Images/2013/03/Planck_Power_Spectrum)

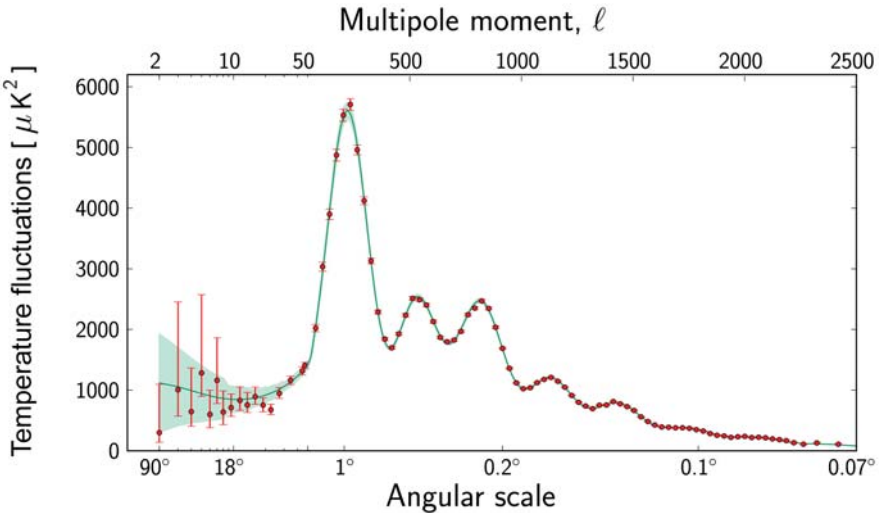

Figure 2.2: power spectrum of the *cosmic microwave background* as measured by the Planck satellite. This spectrum describes the strength of the temperature inhomogeneities on different scales, where the shape of the spectrum is strongly dependent on cosmology. The red markers indicate the Planck data, whereas the green curve represents the best-fit standard model of cosmology. [5]

2.3 Structure Formation

Following the argumentation of the cosmological principle, we expect a homogeneous and isotropic distribution of matter on large scales. The over-all distribution of matter is generally referred to as *Large Scale Structure* (LSS) and was e.g. identified by the *2dF Galaxy Redshift Survey* (Colless et al. 2001) in the allocation of galaxies. These objects form a web-like structure with large underdense *voids*, overdense *filaments* and *knots* as intersection points of these filaments (Fig.2.3). On scales larger than ~ 100 Mpc, this distribution appears to be homogeneous. The underlying matter arrangement itself is not observable with current instruments, such that galaxies as well as clusters of galaxies, which reside in the knots of the LSS, are used as tracers of the over-all matter distribution.

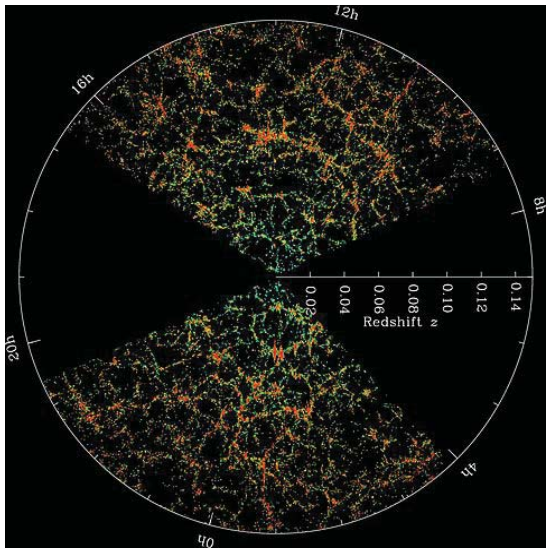

Figure 2.3: Distribution of galaxies as observed by the *Sloan Digital Sky Survey* (SDSS). The galaxy number density is imprinted in the colour scheme with the highest densities given in red. *Credit: http://www.sdss.org/science/.*

This so-called *cosmic web* of structures, was initiated by infinitely small fluctuations in the gravitational potential. The spatially deviating gravitational tug on the surrounding matter, accordingly guided the clustering of matter into increasing overdensities and into regions with continuously decreasing densities, so-called *voids*. In addition to the steady accretion of matter, the overdensities also experienced mergers with one another. They then decoupled from the over-all expansion of the Universe and eventually collapsed into virialised matter

haloes. The first imprints of the baryonic matter distribution are already visible in the temperature map of the CMB, as already discussed in the previous section. With the continuous accretion of matter along the filaments and the mergers of overdensities, the evolution of the matter distribution follows a hierarchical process (Fig. 2.4), with the most massive haloes residing in the knots of the LSS. This process is also known as the *Bottom-Up* scenario.
The process of structure formation is highly dependent on the cosmological model, including the energy budget of the Universe. Thus, tracing back the evolution of the matter structures places constraints on the cosmological parameters. For example, the observed Bottom-Up scenario is only understandable, if the majority of dark matter is in the form of a cold particle. Solely their low velocities allow structures to form on the smallest scales first. Hot or warm particles on the contrary stream out of these small scale perturbations. In the case of dark matter being composed mainly of high velocity particles, structures would thus form on large scales first and later-on break down into smaller perturbations. This scenario is also known as *Top-Down* solution. Accordingly, observations place constraints amongst others on the fraction of massive neutrinos as dark matter particles.
In the following subsections, we derive the evolution of the LSS in a more detailed approach. For this discussion of structure growth, we first emphasise on the evolution of dark matter-only perturbations and later-on introduce the influence of the other energy species.

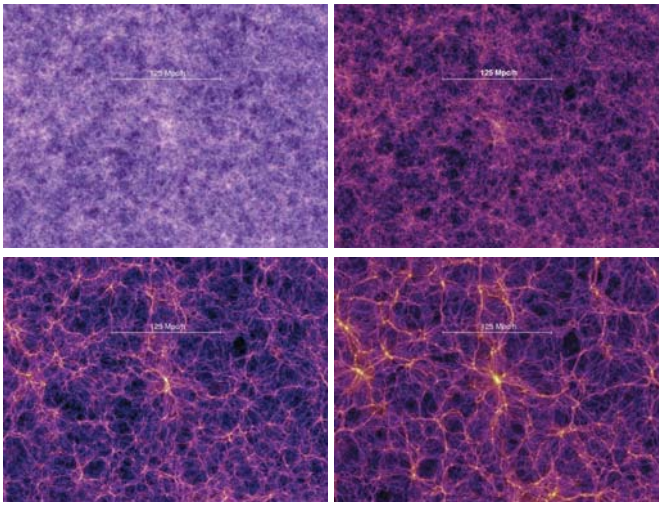

Figure 2.4: Evolution of dark matter-only structures as simulated within the *Millenium Simulation* (Springel et al. 2005). From left to right and from top to bottom, the images display the distribution of dark matter at the redshifts z = 13.8, 5.7, 1.4 ,0. with the highest overdensities expressed by the brightest colors.

2.3.1 The Transfer Function and the Matter Power Spectrum

To quantify matter perturbations, the so-called density contrast $\delta(\vec{x}, t)$ at the comoving coordinate $\vec{x}$ and at time t is expressed as

$$\delta(\vec{x}, t) = \frac{\rho(\vec{x}, t) - \bar{\rho}(t)}{\bar{\rho}(t)} \tag{2.28}$$

based on the matter density at the given coordinates $\rho(\vec{x}, t)$ and on the mean matter density $\rho(t)$ at the considered time t. For today at t_0, the mean density contrast, averaged over $\vec{x}$, is estimated as $\bar{\delta}(t_0) = 1$ with values of $\bar{\delta}(t) < 1$ for $t < t_0$, as for example $\bar{\delta}(z \sim 1090) = 10^{-5}$ at the era of matter-photon decoupling as imprinted in the CMB temperature map (Sect. 2.2.2).

Though the evolution of this matter density contrast is driven by the gravitational potential, it is influenced by the dominating energy species and depends on the considered perturbation scale as well. For a realistic description of the matter perturbations, the growth of structures thus needs to be considered in the epochs of radiation and matter domination, and we define sub- as well as superhorizon perturbations with wavelengths λ of

$$\lambda < r_H(a) \quad \text{and} \quad \lambda > r_H(a) \quad ,$$

respectively, in comparison to the Hubble radius r_H at the considered epoch. We start with describing the initial growth of perturbations at times around the recombination epoch, when a very small mean density contrast is observed, such that we can apply linear perturbation theory. To quantify this growth, a common approach is to work in the non-relativistic regime, to treat matter as a fluid and to assume the initial density perturbations to follow a so-called Gaussian random field. This Gaussian approach assumes the primordial perturbations to be generated by a stochastic process. The probability distribution of any realisation of this random field $g(\vec{x})$ is thus Gaussian shaped. Following the concepts of linear perturbation theory, the evolution of structures is expressed by the combination of the linearised Continuity Equation, the linearised Euler Equation as well as the linearised Poisson Equation. Differentiating between the two epochs of radiation and matter domination, and the two perturbation sizes, the following dependencies of the evolution of the density contrast on the scale factor are computed,

if $\lambda \gg r_H$	$\delta \propto a^2$	if $a \ll a_{\mathrm{eq}}$
	$\delta \propto a$	if $a \gg a_{\mathrm{eq}}$
if $\lambda \ll r_H$	no growth	if $a \ll a_{\mathrm{eq}}$
	$\delta \propto a$	if $a \gg a_{\mathrm{eq}}$

the evolution with the scale factor is influenced by the different expansion rates $H(a)$ during the epochs of radiation and matter domination. With time, the comoving scale λ of the perturbation remains constant, whereas the comoving horizon size r_H increases with the scale factor. Thus, for each length scale λ there is a time at which the perturbation enters the horizon. Perturbations of $\lambda > \lambda_{\mathrm{eq}} = r_H(a_{\mathrm{eq}})$ enter the horizon in the matter dominated epoch and, according to the above summary, do not change their growth rate after entering. Smaller perturbations of $\lambda < \lambda_{\mathrm{eq}}$, however, enter the horizon still during radiation domination and are suppressed in their growth by a factor of $\left(\frac{a_{\mathrm{enter}}(\lambda)}{a_{\mathrm{eq}}}\right)^2$ after entering the horizon. This suppression of small scale perturbations is described by the so-called transfer function $T(\lambda)$ with dependence on the perturbation size. In detail, the transfer function describes the ratio between two perturbation amplitudes of different lengths λ and λ^* with $\lambda^* > \lambda_{\mathrm{eq}}$ and compares their ratio at an early, initial time a_{i} to their ratio today at a_0

$$\frac{\delta_{a_0}(\lambda)}{\delta_{a_0}(\lambda^*)} = T(\lambda)\frac{\delta_{a_{\mathrm{i}}}(\lambda)}{\delta_{a_{\mathrm{i}}}(\lambda^*)}. \tag{2.29}$$

According to the considerations above, the transfer function is roughly defined as

$$T(\lambda) \approx \begin{cases} 1 & \text{for } \lambda \gg \lambda_{\mathrm{eq}} \\ (\lambda/\lambda_{\mathrm{eq}})^2 & \text{for } \lambda \ll \lambda_{\mathrm{eq}} \end{cases} \quad . \tag{2.30}$$

Often, the transfer function is also computed as $T(k)$ in terms of the wavenumber $k = 2\pi/\lambda$. For an exact description of the transfer function, the underlying set of differential equations given by the Continuity Equation, the Euler Equation as well as the Poisson Equation need to be solved. Analytical approxima-

tions to these solutions are presented e.g. by Bardeen et al. (1986) and Eisenstein & Hu (1998). The currently most effective routine to solve the differential equations of structure formation and to compute a realistic transfer function is *CAMB* (*Code for Anisotropies in the Microwave Background*) by Lewis et al. (2000). *CAMB* also includes the influence of the different energy components, which are described in Sect. 2.3.2.
To account for the growth of structures well after the epoch of radiation-matter equality when all perturbations evolve similarly, we reconsider solving the set of differential equations mentioned above for the era of matter domination and assuming negligible radiation (comp. also e.g. Linder & Jenkins 2003; Percival 2005).

$$\ddot{\delta} + \frac{2\dot{a}}{a}\dot{\delta} = \frac{3H_0^2\Omega_\mathrm{m}}{2a^3}\delta \quad . \tag{2.31}$$

The solution to this differential equation is a linear combination of one decaying $\mathcal{D}_-$ and one growing mode $\mathcal{D}_+$, of which only the latter is of interest to us. Unlike the transfer function, both modes are scale invariant. For application, the growing mode is normalised to unity today

$$D_+(a) = \mathcal{D}_+(a)/\mathcal{D}_+(1) \quad , \tag{2.32}$$

and is then named *growth factor* D_+. Combining the information on the transfer function as well as on the growth factor, the linear matter power spectrum $P(k)$, which states the significance of the different perturbation scales for the growth of structures is derived as

$$P(k,a) = A \cdot k^{n_\mathrm{s}} T^2(k) D_+^2(a) \quad , \tag{2.33}$$

including the index n_s of the power spectrum and its amplitude A. Initially, this spectrum is defined as the Fourier transform of the mean density contrast squared, evaluated for a certain scale factor a

$$P(k) = \left|\delta(k)\right|^2 = \int_{\mathbb{R}^3} \mathrm{d}\boldsymbol{x} \cdot \exp[-i\boldsymbol{x}\cdot\boldsymbol{k}] \cdot \left(\bar{\delta}(\boldsymbol{x})\right)^2 \quad . \tag{2.34}$$

This Fourier transform decomposes the spatial density contrast into its different perturbation scales $\bar{\delta}(k)$, where the displayed parameter i represents the imaginary unit. Whenever we consider the power spectrum in this work, we always refer to the linear model.
Coming back to Eq. 2.33, the index n_s is to a first approach expressed within the so-called *Harrison-Zel'dovich* theorem as $n_\mathrm{s} = 1$. This assumption defines the power spectrum to be scale-invariant, such that the density perturbations of all different scales show the same amplitude at the moment of horizon crossing. However, most recent observations of the CMB obtain values of $n_\mathrm{s} = 0.96$ (Planck Collaboration et al. 2015c). This slight deviation from scale invariance is interpreted as proof for an extension to the standard model of the Big Bang theory (compare Sec. 2.4.2). The value of the amplitude A cannot be derived theoretically, but needs to be inferred from observations, where we measure the present standard deviation of the matter distribution on scales with radius $r = 8\ h^{-1}$ Mpc, also defined as σ_8. This normalisation approach is motivated by galaxy counts which yield $\Delta N/\bar{N} \approx 1$ on these scales. In general, the mass standard deviation $\sigma(r)$ shows the theoretical form

$$\sigma^2(r,a) = \int_0^\infty \frac{\mathrm{d}^3k}{(2\pi)^3} P(k,a) \cdot |W_r(k)|^2 \quad , \tag{2.35}$$

where the power spectrum is smoothed by the *window function* $W_r(k)$ over scales with radius r, while

the integration runs over all perturbation modes k. The window function itself is defined as

$$W_r(k) = 3 \cdot \frac{\sin(kr) - kr \cdot \cos(kr)}{(kr)^3} \quad . \tag{2.36}$$

Combining expressions 2.33 and 2.35, we compute the normalisation A as

$$A = \frac{\sigma_8^2}{\left(\int_0^\infty \frac{\mathrm{d}^3k}{(2\pi)^3} k^{n_\mathrm{s}} T(k,1)^2 D_{+,0}^2 \cdot |W_{r=8h^{-1}\mathrm{Mpc}}(k)|^2\right)} \quad , \tag{2.37}$$

where the normalisation is always defined for today at $a = 1$.
Following this approach, the linear power spectrum is computed in Fig. 2.5 based on the transfer function by *CAMB* and on a *WMAP5*-cosmology Komatsu et al. (2009). The maximum in the spectrum at $k \approx 0.02$ and the following drop for smaller scales emphasise the influence of the transfer function as fluctuations on small scales with $k \gtrsim 0.02$ enter the horizon already during radiation domination and are thus suppressed. Accordingly, the position of this maximum is characteristic for the horizon size at the epoch of radiation-matter equality.
Commonly when applying e.g. *CAMB*, the power spectrum is calculated for $a = 1$. The spectrum can then be inferred for other scale factors by a multiplication with the corresponding growth factor as $P(k,a) = P(k,0) \cdot D_+^2(a)$, since within the considerations above we normalised $D_+(1) = 0$. If the powerspectrum is initially computed for a different scale factor, the growth factor need to be re-normalised correspondingly.

2.3.2 Influences on the Power Spectrum

For a proper account of the evolution of structures a dark-matter only approach does not suffice and the transfer function needs to include the influences of all energy components - photons, neutrinos, baryons, and dark energy. The impact of these components on the transfer function and thus on the power spectrum is summarised below, and in Fig. 2.5.

Radiation: In general, the abundance of radiation, including photons as well as relativistic neutrinos, defines the value of a_eq and accordingly the suppression of small scale perturbations, such that e.g. an increase in the number of relativistic neutrinos results in a decrease of the power spectrum to the right of the peak (comp. Fig. 2.5, blue dotted line). Apart from this aspect, radiation and dark matter decoupled already very early after the Big Bang so that the evolution of the dark matter overdensities was not directly influenced by radiation.

Baryons: Dark matter and baryons interact gravitationally, such that baryons fall into the overdensitites formed by dark matter and vice versa. However, before the decoupling of the CMB, the strong interactions between photons and baryons prevented the baryons from falling into the dark matter potential wells. Accordingly, the over-all matter power spectrum is suppressed on small scales for an increased fraction of baryons (comp. Fig. 2.5, dotted red line). Instead, the baryons were confined in the baryon-photon fluid and were dragged along with the photons at the speed of sound to form oscillations within the sound horizon. After the epoch of photon decoupling, baryons and dark matter eventually settle into each other's potentials, creating the so-called *Baryonic Acoustic Oscillations* (BAO) visible as wriggles in the power spectrum on scales smaller than the horizon (comp. also Fig. 2.2). With an increasing fraction of baryons Ω_b, or equivalently $\Omega_\mathrm{b}h^2$, these oscillations become more

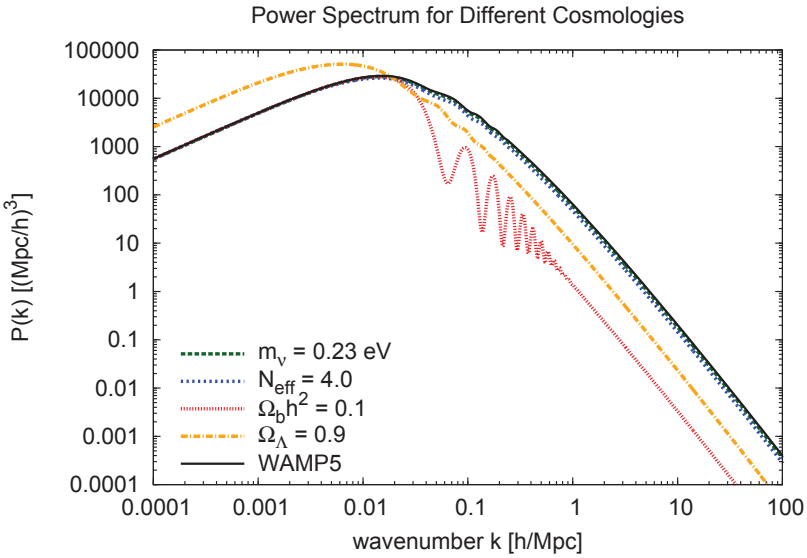

Figure 2.5: Power spectra for different cosmologies computed with *CAMB*. The default is a ΛCDM-cosmology as it is given by the results of *WMAP5* (black line). To display the effects of the individual density parameters on the power spectrum, one parameter at the time is varied, while fixing a flat geometry.

pronounced (comp. Fig. 2.5, dotted red line).
For a detailed description of the baryonic features in the transfer function and thus equivalently in the power spectrum, please refer to Eisenstein & Hu (1998).

Massive Neutrinos: Early after the Big Bang, massive neutrinos are still relativistic and thus stream out of density regions smaller than their free-streaming length. This leads to an additional suppression of perturbations on small scales, especially for $k < k_{\mathrm{eq}}$, with $k_{\mathrm{eq}} = 1/\lambda_{\mathrm{eq}}$ (comp. Fig. 2.5, green dashed line). This effect is analogous to the description of the *Top-Down* scenario for neutrino-only dark matter and accordingly results in a similar alteration of the power spectrum as the increase of the radiation abundance. At some point in time, depending on their rest mass, these particles become non-relativistic and start to actively participate in the growth of structures.
For the comparison in Fig. 2.5, we considered a mass sum of all neutrino species of $\sum m_\nu = 0.23$ as the upper limit on this parameter estimated by (Planck Collaboration et al. 2015c).

Dark Energy: Adding an additional dark energy component in a flat universe indirectly means a decrease of the matter content such that a_{eq} is increased. Accordingly, $\lambda_{\mathrm{eq:DE}} > \lambda_{\mathrm{eq:matter\_only}}$ and perturbations of larger scales enter the horizon still during radiation domination and are thus suppressed (compare Fig. 2.5, yellow dotted-dashed line).
As a second effect, a decreased matter density also leads to a reduced speed in the growth of structures. Obtaining the same density contrast today, requires a higher amplitude of the linear power spectrum than in a matter-only universe.

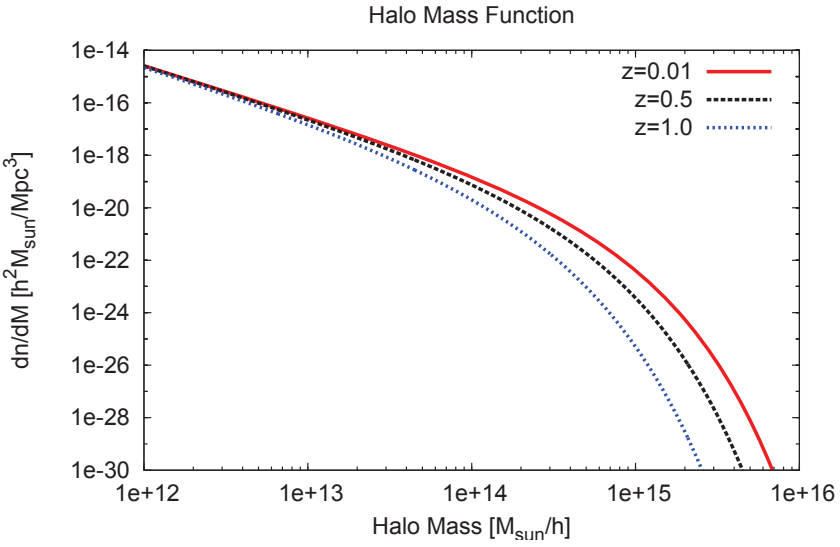

Figure 2.6: Halo mass function based on the transfer function by *CAMB* and the functional form by Tinker et al. (2008) for a *WMAP5*-cosmology.

2.3.3 From the Matter Power Spectrum to the Halo Mass Function

The power spectrum yields the foundation for other models to describe the distribution of matter perturbations across the Universe. One of them is the *halo mass function* $\mathrm{d}n/\mathrm{d}M(M,z)$, which expresses the number density of collapsed matter haloes within a certain mass interval in dependence on their mass and their redshift. In the process of matter accretion onto overdensities, these regions follow a less rapid expansion than their surroundings due to their increased gravitational potential. Accordingly, these overdensities decouple from the general Hubble flow of the Universe and increase their density contrast steadily. The overdense sphere eventually reaches a maximum expansion and then recollapses into a relaxed and virialised halo with half the radius of the maximum extension, $r_{\mathrm{vir}} = r_{\mathrm{max}}/2$ (for a summary see e.g. Schneider 2015). This scenario is also referred to as spherical halo collapse model. Following the simplified assumption of linear structure formation in an *Einstein-deSitter Universe* with $\Omega_{\mathrm{m}} = \Omega_0 = 1$ and solving the equation of motion of the sphere $\ddot{r} = -GM/r^2$ with the mass M and the radius r, yields the required density contrast for the overdensity to collapse. Accordingly, matter concentrations collapse for linear density contrasts of $\delta_{\mathrm{lin}} = 1.69$. Or in other words, for spheres to collapse at a scale factor a and to become relaxed until today, these haloes need to show present linear density contrasts of $\delta_{\mathrm{lin},0} = 1.69/a$. The mean density within the virialised region presents values of $\rho = 178 \cdot \rho_{\mathrm{crit}}(z)$, compared to the critical density at the redshift at which the halo is observed. Despite the simplified assumption for these derivations, the above values are commonly applied when considering haloes in virial equilibrium and (e.g. Percival 2005) found only a weak dependence of these results on the cosmological model.

We follow this linear approach for structure formation as we are especially interested in the larger matter haloes with scales of $r \gtrsim 10$ Mpc/h, which later-on develop into the knots of the LSS. The halo mass function is generally expressed by the functional form

$$\frac{\mathrm{d}n}{\mathrm{d}M}(M,z) = \frac{\bar{\rho}_{\mathrm{m},0}}{M} \cdot \left(\frac{\mathrm{d}\ln\sigma^{-1}}{\mathrm{d}M}\right) \cdot f(\sigma) \quad , \tag{2.38}$$

given by the mean matter density today $\bar{\rho}_{\mathrm{m},0} = \Omega_\mathrm{m} \cdot \rho_{\mathrm{crit},0}$, the mass M of the halo and the mass variance $\sigma^2 = \sigma^2(r, z)$ smoothed over the scale r of the matter concentration at redshift z. The scale and the mass of the halo are related by

$$r(M) = (3 \cdot M/(4\pi\bar{\rho}_{\mathrm{m},0}))^{1/3} \quad . \tag{2.39}$$

The first to derive these relations were Press & Schechter (1974) with the factor

$$f(\sigma) = \sqrt{\frac{2}{\pi}} \cdot \frac{\delta_\mathrm{lin}}{\sigma} \cdot \exp[-(\delta_\mathrm{lin}/\sigma)^2/2] \quad . \tag{2.40}$$

Where this formalism was obtained in a theoretical approach, the currently well-accepted models of the factor $f(\sigma)$ are defined in fits to structure formation simulations. In general, the halo mass function is believed to show a universal profile and its form is thus expected to be independent of the cosmological model, including time-variable dark energy (e.g. Jenkins et al. 2001; Evrard et al. 2002; Linder & Jenkins 2003; Kuhlen et al. 2005).The currently most commonly applied model is defined by Tinker et al. (2008) based on the formalism of Eq. 2.38 and a factor $f(\sigma)$ of

$$f(\sigma) = A_\mathrm{T}\left[\left(\frac{\sigma}{b_\mathrm{T}}\right)^{-a_\mathrm{T}} + 1\right] \cdot \exp(-c_\mathrm{T}/\sigma^2) \quad . \tag{2.41}$$

The parameters A_T, a_T, b_T and c_T are dependent on the overdensity Δ_m of the halo, defined as

$$\Delta_\mathrm{m}(z) = \frac{M_{\Delta_\mathrm{m}}}{(4/3)\pi r^3_{\Delta_\mathrm{m}} \bar{\rho}_\mathrm{m}(z)} \quad , \tag{2.42}$$

in dependence on the redshift z at which one wants to measure the halo mass function

$$A_\mathrm{T}(z) = A_{\mathrm{T},0} \cdot (1+z)^{-0.14} \tag{2.43}$$

$$a_\mathrm{T}(z) = a_{\mathrm{T},0} \cdot (1+z)^{-0.06} \tag{2.44}$$

$$b_\mathrm{T}(z) = b_{\mathrm{T},0} \cdot (1+z)^{-\alpha} \tag{2.45}$$

$$c_\mathrm{T}(z) = c_{\mathrm{T},0} \tag{2.46}$$

$$\ln(\alpha(\Delta_\mathrm{m})) = -\left[\frac{0.75}{\ln(\Delta_\mathrm{m}/75)}\right]^{1.2} \quad . \tag{2.47}$$

The parameters denoted with the index "T,0" are obtained from the fit to the structure formation simulations for different overdensities Δ_m. A commonly applied value for the halo overdensity is $\Delta_\mathrm{crit} = 500$ based on the critical density of the Universe and independent of the redshift, and thus $\Delta_\mathrm{crit} = \Delta_\mathrm{m}(z)/\Omega_\mathrm{m}(z)$. As already mentioned above, we assume this model of the halo mass function to be universal with cosmology, and extend this universality also to the redshift dependence of this function.

Combining the information of the previous sections, Fig. 2.6 presents the halo mass function based on the formalism by Tinker et al. (2008) and the transfer function from *CAMB* for a *WMAP5*-cosmology (Komatsu et al. 2009). The evolution of the number density of haloes with their mass and redshift emphasises on the concepts of structure formation: More massive haloes are less abundant at higher redshifts as a longer time period is needed to accrete the required mass. The shape of the halo mass function and thus the abundance of haloes is strongly dependent on the cosmology just as the transfer function and thus also the power spectrum are varying with cosmology (comp. Sect. 2.3.2). One of the most important parameters for structure formation is the matter density Ω_m, where structure formation

proceeds more rapidly with an increased value for Ω_m as the Universe expands more slowly. Accordingly, the abundance of massive haloes is reduced at higher redshifts in this scenario to yield the same abundance of haloes today. For the assumption of a flat Universe, an increase in dark energy Ω_Λ thus implies a slowed down growth of structures, but at the same time a larger abundance of massive haloes at larger redshifts (comp. Sect. 2.3.2). If one allows for $\Omega_0 \neq 0$, however, an increase in Ω_Λ supports the growth of density perturbations. This is explained by the dependence of $\Omega_m(z)$ on the evolution and density of dark energy, where $\Omega_m(z)$ starts to decrease only very late during the epoch of matter domination for large values of Ω_Λ and small values of w (Voit 2005), such that in this case the structure evolution is reduced only at very low redshifts.

To test this theory of structure formation and to obtain the values of the different cosmological parameters which regulate this process, this model needs to be compared to observations. In the process of this work, we base this comparison on the observation of the abundance of galaxy clusters as the largest collapsed and virialised objects in the Universe.

2.4 The Standard Model under Investigation

Before we continue with defining the characteristics of these objects and describe how galaxy clusters are adopted as cosmological tracers, we take a look at the validity of the described standard model for the evolution of the Universe.

2.4.1 Successes and Problems of the Standard Model

The greatest success of the standard model of cosmology is the discovery of the CMB, which confirms the Big Bang and the thermal evolution of the Universe. Analogously to this photon background, also the existence of a uniform, isotropic neutrino background with a current temperature of $T_{\nu,0} = 1.9$ K is expected, but could not be studied yet, due to the low neutrino cross sections. The temperature of the neutrino background is reduced by a factor of $11/4$ compared to the CMB since the neutrinos decoupled at an earlier time and thus were not heated during the epoch of e^+e^--annihilation.
A second test for our thermal evolution model is provided by the primordial abundances of the different elements, which strongly depend on the density of photons and baryons, especially on the neutron abundance, at the time of nucleosynthesis. Measurements of the different primordial abundances agree on the same baryon density of $\sim 3.6 \times 10^{31}$ g/cm^3 (comp. Burles et al. (1999)) with the tightest constraints coming from observations of the primordial deuterium abundance. However, there have been discussions on a primordial lithium problem as the expected abundance of Li^7 from Big Bang nucleosynthesis is a factor of $3-4$ above the observations of stars (Fields 2011, comp. also Burles1999). Current experiments were now able to reproduce the primordial nucleosynthesis of lithium in a laboratory and confirmed the estimated baryon abundance, leaving the discrepancy to be explained by nonstandard physical processes in the observed stars (Anders et al. 2014). At the same time, this measurement of the baryon density emphasises these particles to contribute only $\sim 5\%$ to the critical density of the Universe, such that the remaining matter density of $\sim 25\%$ needs to be provided by nonbaryonic dark matter.
However, besides these strong successes of the standard model of the Big Bang theory, some observations remain unexplained and ask for an extension to this model.

Flatness Problem: Different observations confirm our Universe to show a flat geometry with $\Omega_0 = 1.0$ (Sec. 2.1.2). Tracing back the evolution of the individual energy species according to the Friedmann Equations, a flat geometry today requires a value of $\Omega_0(z)$ very close to unity, with a decreasing deviation for increasing redshifts. For example, at the epoch of neutrino decoupling at $z \approx 10^{10}$ we ask for a deviation of $|\Omega_0(z) - 1| \lesssim 10^{-15}$. This fine-tuning of the total energy contents of the Universe lacks an explanation by the standard model.

Horizon Problem: The horizon problem is most evident in the isotropy of the CMB (comp. Fig. 2.1). Due to the finite speed of light, only regions within a well defined radius are able to communicate with one another, where this event radius is growing with time. At the epoch of photon decoupling at $z = 1090$, the angular radius of this event cone is expected to be $\theta \approx 1^\circ$ as computed from the standard model for the evolution of space. However, for the CMB to be isotropic with relative fluctuations of only $\Delta T/T \approx 10^{-5}$, all regions need to have been in causal contact at the epoch of recombination.

Initial Density Perturbations: Right after the Big Bang, radiation as well as particles were distributed homogeneously. To explain the observed structures today, initial overdensities in the distribution of matter are required, which then grow through the accretion of surrounding matter. However, the forming of these initial perturbations is not described by the standard model.

The Missing Baryons: As described above, observing the fractions of primordial elements constrains the baryon density. However, in the recent Universe with $z < 2$, which is shaped by the assembly of large structures, only $\sim 40\%$ of these baryons are found in stars, in cold or warm interstellar matter, in the hot intracluster gas of galaxy clusters, and in the intergalactic medium (e.g. Fukugita et al. 1998; Fukugita 2003). The remaining $\sim 60\%$ of the initial baryons are predict to be part of the process of structure formation. Numerical simulations of the growth of structures indicate baryons to be shock heated to temperatures of Millions of Kelvin as this matter is drawn towards the potential of forming structures by gravity. These filaments of hot baryons are considered as the *Warm Hot Intergalactic Medium* (WHIM) and are expected to show baryon number densities of $\sim 10^{-5} - 10^{-6}$ cm^{-3} with temperatures of $10^5 - 10^7$ K (e.g. Danforth & Shull 2005). They are expected to present emission lines of highly ionised elements, such as e.g. of carbon, oxygen, neon or iron, in the far-ultraviolet and soft X-ray energies (Cen & Fang 2006). Due to the small element densities, these lines are emitted with only low intensities. Additionally, observations of these lines along many independent line-of-sights are required to thoroughly test the abundance of baryons in the WHIM. However, several detections especially of O VI and of N VIII were confirmed by the *Cosmic Origins Spectrograph* (*COS*) on the *Hubble Space Telscope* (comp. e.g. Savage et al. 2011; Stocke et al. 2013; Werk et al. 2014; Tejos et al. 2015). Accordingly, only $\sim 50\%$ of the baryons remain currently missing in the present Universe. Further detections are especially expected from *COS* and additionally future instruments are designed to study the WHIM in more detail, with promising opportunities expressed e.g. for the European X-ray mission *ATHENA* (Nandra et al. 2013), which is scheduled for launch in 2028.

The Dark Universe: Observations e.g, of rotation curves in spiral galaxies, of velocity dispersions of galaxies in clusters, or of the evolution history of our Universe in general, support the believe in the existence of two dark components, dark matter as well as dark energy. Though their existence is commonly accepted today, both dark matter and dark energy have not been detected directly, yet, and there are competing models to describe the observed phenomena e.g. by a deviation from Newtonian dynamics or from Einstein's theory of General Relativity.

To address the first three problems, the concept of *inflation* was added to the standard model of cosmology. Even though the existence of dark matter and dark energy is commonly accepted, their direct observations as well as the study of their characteristics is currently the subject of intensive on-going research and is supported by a large number of current as well as future experiments. For example, one of these promising instruments to test the nature of dark energy is the future X-ray telescope *eROSITA* (*extended ROentgen Survey with an Imaging Telescope Array*) (Merloni et al. 2012). Planned future instruments with higher sensitivities will also allow for the search of the missing baryons in the WHIM. Accordingly, also the latter three problems stated above will hopefully be solved in the near future.

2.4.2 Inflation

Inflation describes a short time interval around $t \approx 10^{-34}$ s after the Big Bang, in which our Universe experienced an accelerated growth of space and expanded by more than 60 e-folds. According to the second Friedmann Equation, such an accelerated expansion requires a phase with a dominating negative pressure, analogously to the dark energy which is dominating our Universe today.
Currently, different theoretical models are investigated, which describe how inflation was initialised and driven. The most established concept describes inflation to be driven by a scalar field $\Phi(\vec{x}, t)$ and its potential $V(\Phi)$, the so-called *inflaton*. In the slow-role approximation, this scalar field slowly rolled down its potential with time to reach the global minimum. During this slow-role phase, the scalar field remained almost constant. At the end of inflation when the global minimum was reached, the energy density of the inflaton field converted into radiation, the dominant species at this point of time, and thus initiated a reheating of the Universe. However, how this short phase of negative pressure domination was initialised and which laws the transition back to radiation domination followed are still very uncertain.
The concept of inflation as an extension to the standard model solves the three first problems, described in the previous section. Due to the rapid and vast expansion of spacetime during inflation, any initial curvature is straightened as the curvature radius is stretched far beyond the current Hubble radius. Accordingly, $\Omega_0 = 1$ is obtained to a very high precision independent of the initial energy density and the *flatness problem* is answered. At the same time, any small region in space, which is in causal contact before inflation, is expanded by several ten orders of magnitude. Accordingly, the entire visible Universe today has been in causal contact before the epoch of recombination, which explains the isotropy of the CMB and thus solves the *horizon problem*. The formation of the initial density perturbations are explained on a different scope and originate from fluctuations in the inflationary scalar field, which evolved into perturbations of the gravitational potential after the epoch of inflation. These fluctuations finally drive the accretion of matter into overdensities (comp. Sect. 2.3).

Despite the fact, that the concept of inflation solves these shortcomings of the standard model, no definite proof of this epoch has yet been obtained from observations. One hint for the epoch of inflation is provided by the study of structure formation and the value of the cosmological parameter n_s (comp. Sec. 2.3.1). Following the approach of the standard model, one derives a value of $n_s = 1$ and scale-invariance of the density perturbations, where current observations, for example from the CMB power spectrum, obtain values of $n_s = 0.96$ (Planck Collaboration et al. 2015c). Only inflation is expected to allow for this slight deviation from scale-variance as the characteristic length scale of the horizon during inflation is imprinted in the perturbation spectrum.
Following the theory of structure growths described in the previous sections, we assumed primordial Gaussianity for the initial density perturbations 2.3.1. However, searching for possible primordial non-

Gaussianity is a powerful test for the confirmation of inflation and also for the validity of different inflationary models (Acquaviva et al. 2003; Maldacena 2003). Especially observations of the CMB with the *Planck* satellite allow for this study by analysing higher order correlations in its density contrasts than contained in the power spectrum. The amplitude of non-Gaussianity, f_{NL}, is then correlated to these higher order correlations (comp. e.g. Baumann 2009). Recent estimates on this parameter are in agreement with the above mentioned slow-role model of inflation, but also with only Gaussian primordial density perturbations (Planck Collaboration et al. 2014b, 2015a). Accordingly, the concept of non-Gaussianity has not be confirmed, yet.
A third proof for the inflationary period would be the existence of primordial gravitational waves. These gravitational waves are metric perturbations in the tensor field, analogously to the density fluctuations as perturbations in the scalar field. These waves eventually lead to anisotropies in the photon radiation field, which was released as CMB at the epoch of decoupling. These anisotropies are especially visible in the polarisation of the CMB, where we would expect to observe a magnetic component or so-called B-modes. The detection of these CMB B-modes and thus of primordial gravitational waves is currently widely studied among different research teams (BICEP2 Collaboration et al. 2014, 2015) with the Planck satellite as most promising instrument for this task (Planck Collaboration et al. 2015b).

2.5 Cosmological Probes

To study the variety of cosmological parameters (comp. Tab. 2.1), which define the evolution of structures in the Universe, two basic approaches can be followed: studying the geometry of the Universe by measuring distances, and analysing the history of structure growth. For both possibilities different observation methodologies and different objects are applied as cosmological probes, where the sensitivities on the parameters are deviating between the individual approaches. In the following, we present a brief summary of the main strategies, which are currently applied.

CMB Power Spectrum: As already presented in Fig. 2.2 and in Sect. 2.2.2, the power spectrum of the CMB displays the beginning of structure formation at a redshift of $z \approx 1090$. Accordingly, the dependence of the growth of structures on the different cosmological parameters is imprinted in the shape of this spectrum (comp. e.g. Hu & Dodelson 2002), with influences comparable to our considerations in Sect. 2.3.2. Based on this dependency tight parameter precisions could be constrained by current CMB observations (e.g. Hinshaw et al. 2013; Planck Collaboration et al. 2015c), including e.g. small uncertainties on n_{s} or Ω_{c}.

Supernovae Type Ia: These objects have already been applied successfully as geometrical cosmological probes during the detection of the accelerated expansion of the Universe (Perlmutter et al. 1998; Riess et al. 1998). These type of supernovae explosions always develop under the same conditions, when an accreting white dwarf becomes unstable as it reaches the *Chandrasekhar Mass*. Accordingly, their light curves are standardisable and the luminosities of these phenomena are always comparable. The observed flux thus defines the distance to the supernovae, which is then analysed in contrast to the redshift, inferred from the spectra of the phenomenon (comp. Eq. 2.26). This comparison then yields information on the cosmology.

Galaxy Clustering: Galaxies evolve in the smaller peaks of the density perturbations and thus trace the evolution of structures. The probability to find a second galaxy in a certain distance from another galaxy is stored in the redshift dependent *correlation function* of galaxies. Following the idea that structure formation initiated from a homogeneous and isotropic density field, also the correlation function is expected to be isotropic. Accordingly, studying the distribution of large samples of galaxies allows to reconstruct this correlation function and thus the underlying cosmology dependence (e.g. Laureijs 2009; Giannantonio et al. 2012).

BAO: Superimposed on the galaxy correlation function, we observe peaks at separations around >100 Mpc/h in the probability distribution, which are the acoustic peaks of the BAOs (comp. Sect. 2.3.2 Eisenstein et al. 2005; Anderson et al. 2012, 2014). Depending on the position and the amplitude of these wiggles, especially the geometry and the matter and baryon content of the Universe are tested (comp. also Hu & Dodelson 2002).

Redshift Space Distortion (RSD): When examining galaxy clustering experiments in more detail, the observed galaxy redshifts are a superposition of the galaxy velocities due to the cosmic expansion and their peculiar velocities. Accordingly, the position of objects can only be defined in a so-called redshift space, which includes these peculiar velocities. The observed correlation function of galaxies is thus distorted from the theoretical isotropical model and the amplitude of this distortion yields information on e.g. the matter budget of the Universe and on its geometry (e.g. Hamilton 1998; Hawkins et al. 2003; Beutler et al. 2014).

Galaxy Clusters: Another important probe to trace especially the evolution of structures are galaxy clusters, the most massive, virialised objects in the Universe. Since our work focuses on cosmological studies based on these objects, the following sections present details on their characteristics as well as on their applications for cosmology.

2.6 Introduction to Galaxy Clusters

As described in Sect. 2.3.3, the evolution history of the large scale structures and thus of the Universe in general, is well expressed by the distribution of dark matter haloes with the largest mass. The true observable of these haloes are the objects which reside within them: galaxies as well as clusters of galaxies towards the higher mass end. To emphasise on the importance of galaxy clusters as cosmological tracers, their characteristics as well as their observation methodologies are summarised in detail in this section.

2.6.1 Definitions

Galaxy clusters are the largest virialised objects in the Universe and are located within the knots of the LSS (comp. Sec. 2.3). They are a gravitationally bound accumulation of several hundred individual galaxies, of large amounts of gas, and of dark matter, which span scales of several megaparsecs. Characteristic for these objects are masses between $\sim 5 \cdot 10^{13} - 10^{15}$ $M_\odot$ and X-ray luminosities of several 10^{44} $L_\odot$ (e.g. Sarazin 1986). In general, one differentiates between galaxy groups, galaxy clusters and super clusters:

- **Galaxy Groups** consist of a few to ~ 50 individual galaxies with total masses of $10^{12} - 5 \cdot 10^{13}$ $M_\odot$
- **Galaxy Clusters** show between ~ 50 and up to $\sim 1,000$ member galaxies with the above mentioned masses of $\sim 5 \cdot 10^{13} - 10^{15}$ $M_\odot$
- **Galaxy Super Clusters** are the largest known objects in the Universe with $\gtrsim 1,000$ individual galaxies and masses above $\sim 10^{15}$ $M_\odot$; they started collapsing only very recently in the history of the Universe and are not virialised, yet.

Though the transition between these objects is fluent, their differences are not only expressed in their masses or number of member galaxies, but they describe systems of deviating characteristics and physical processes.
Galaxy clusters do not only reveal the formation history of structures in the Universe, but they are also laboratories for energetic hydrodynamical processes, such as for example shocks. Additionally, the enrichment history of the Universe with metals[6] as well as the physics of *Active Galactic Nuclei* (AGN) are studied in clusters. Despite this diversity of physical aspects contained in galaxy clusters, we focus on those characteristics important for cosmological studies.

2.6.2 Composition of Galaxy Clusters

Despite the commonly provided definitions above, galaxies provide only $\lesssim 5\%$ of the cluster's total mass. In general, clusters are composed as follows:

Dark Matter: The largest mass fraction of $\sim 80\%$ is made up of dark matter. It forms the halo in which the remaining cluster constituents, including the member galaxies, are gravitationally bound. Due to this large amount of dark matter, galaxy clusters show high mass-to-light ratios of $M/L \approx 350$ $M_\odot/L_\odot$ (e.g. Sarazin 1986).

[6] We adopt the common astrophysical definition of metals as elements with atomic numbers larger than that of helium.

Intra-Cluster Medium: The dark matter halo is smoothly filled by baryonic gas, called the *Intra-Cluster Medium* (ICM). In the process of structure formation, ambient baryonic matter is assembled into the potential well of the cluster and the potential energy of the in-falling matter is converted into kinetic energy. This process is also known as *violent relaxation* (compare e.g. Voit 2005). During the assembly, the matter reaches supersonic velocities and this kinetic energy is converted into heat by adiabatic compression and shocks (e.g. Borgani & Kravtsov 2011) until the gas settles into thermal equilibrium following a Maxwellian velocity distribution. Due to the cluster's deep potential well, the baryonic gas reaches temperatures of $k_B T \approx (1 - 10)$ keV, where we apply the Boltzmann constant k_B, or equivalently temperatures of $(10^7 - 10^8)$ K. According to these high temperatures, hydrogen as well as helium atoms are completely collisionally ionised and heavy elements, such as e.g. iron, are in hydrogen- or helium-like states. The ICM acts as an optically thin plasma with densities of $(10^{-3} - 10^{-1})$ particles/cm^3 and metallicities of on average $A = 0.3$ $A_\odot$ (Arnaud et al. 1992). As a whole, the ICM comprises 15% of the total cluster mass. Another commonly adopted characteristic is the gas mass fraction $f_g \equiv M_{gas}/M_{total}$, which defines the ratio between the gas mass and the total mass of a cluster. It can also be defined as $f_g = \Upsilon(z) \cdot (\Omega_b/\Omega_m)$, with $\Upsilon(z)$ accounting for star formation processes and other baryonic effects (e.g. Allen et al. 2011). Especially towards the cluster outskirts, f_g approaches the cosmological ratio of $\Omega_b/\Omega_m \approx 15\%$.

Galaxies: As mentioned above, galaxies provide $\sim 5\%$ of the total cluster mass. Due to the strong gravitational potential in the cluster, the galaxies may reach velocity dispersions of $\sim 10^3$ km/s (Sarazin 1986). The fraction of elliptical galaxies in clusters is larger than in the field as a result of frequent galaxy interactions and ram pressure stripping within the ICM. Usually, a giant elliptical galaxy , the so-called *brightest cluster galaxy* (BCG), is located close to the cluster centre.

Relativistic Particles and Magnetic Fields: A negligible, but still mentionable fraction of the energy of the cluster is contained in relativistic particles and magnetic fields which are of the order of a few μG. Relativistic particles can e.g. be generated in shocks within the ICM, for example during the merger of two clusters. They gyrate around the magnetic field lines to especially emit radio synchrotron emission.

To a first approximation, galaxy clusters are assumed to be *relaxed*, spherically symmetric systems, such that they show a hydrostatic equilibrium between the gravitational potential and the pressure gradient of the ICM. According to the spherical halo collapse model (comp. Sec. 2.3.3), this virialised region encloses an average density of $\bar{\rho} = 178 \cdot \rho_{crit}(z)$. However, as clusters reside in the LSS of the Universe, no natural cluster boundary exists and this property needs to be defined by common practice. We thus express the cluster radii $r_{\Delta_{crit}}$ as the radius within which we observe an average overdensity of $\bar{\rho} = \Delta_{crit} \cdot \rho_{crit}(z)$ and correspondingly express the cluster masses $M_{\Delta_{crit}}$ within the radius $r_{\Delta_{crit}}$.

$$M_{\Delta_{crit}} = \frac{4}{3}\pi \cdot \Delta_{crit} \cdot \rho_{crit} \cdot r^3_{\Delta_{crit}} \tag{2.48}$$

Commonly applied values for Δ_{crit} include 200, representing the virial radius, 500 and 2500, where r_{2500} describes the cluster core region. r_{500} is especially important for X-ray studies as it represents the observation limit for temperature measurement for example with the telescopes *XMM-Newton* or *Chandra* (comp. also Sec. 2.7.3). At the same time, the assumption of hydrostatic equilibrium is often a valid approach in this region and is confirmed to first order approximation by simulations (e.g. Nagai et al. 2007; Borgani & Kravtsov 2011). However, the assumption of hydrostatic equilibrium needs to be

relaxed in the cluster centres, within $\sim 10\%$ of the viriral radius, in the cluster outskirts at $r \gtrsim r_{500}$, and in clusters with recent mergers, as these regions are strongly influenced by physical processes. These processes include e.g. feedback of AGN, especially in the cluster centre, or feedback of supernovae, cooling processes, or the infall of ambient matter into the cluster. A detailed examination of these aspects, however, is beyond the scope of this work.
This work focuses on cluster characteristics within a radius of $r \lesssim r_{500}$ based on the critical density of the Universe with $\Delta_{\rm crit} = 500$ independent of redshift. For simplicity, we follow the notation $\Delta_{\rm crit} = \Delta$.

2.7 Galaxy Clusters in X-Rays

Galaxy clusters are visible in all wavelengths, where the individual energy ranges display the different components of the cluster. For example, we observe synchrotron emission of relativistic electrons in the radio wavelengths. Relativistic particles are also expected to be visible in γ-rays through various processes, including e.g. inverse Compton scatterings or decays of relativistic hadrons or of hypothetical dark matter particles. However, this emission could has not be detected from galaxy clusters, yet (e.g. Maurin et al. 2012; Ackermann et al. 2014; Prokhorov & Churazov 2014). In the mm- as well as the submm-regime, we study the ICM through the *thermal Sunyaev-Zel'dovich effect* (SZ-effect), in which photons of the CMB are up-scattered to higher energies via inverse Compton processes with the hot electrons of the ICM. The effect is dependent on the integrated pressure of the ICM along the line-of-sight and yields relative changes in the CMB intensity of the order of $\sim 10^{-5} - 10^{-4}$ (e.g. Sunyaev & Zeldovich (1970, 1972) and e.g. Borgani & Kravtsov (2011); Reiprich et al. (2013) for a review). However, in the progress of this thesis, we rely on galaxy cluster information obtained in optical observations and especially from X-ray data.

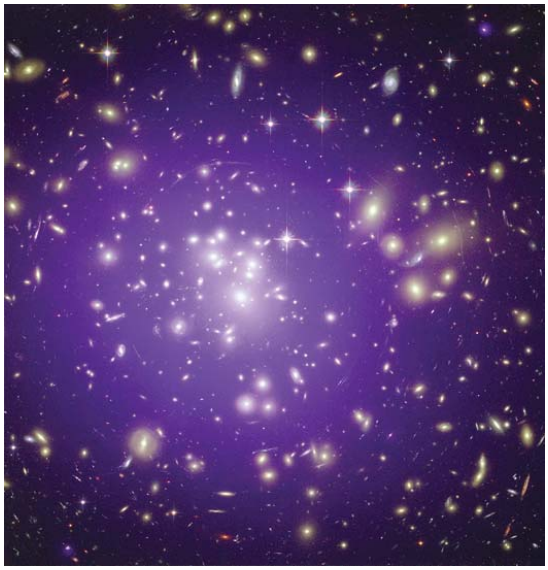

Figure 2.7: Composition of the optical (yellow colouring) and X-ray (purple colouring) emission of the cluster Abell 1689. In the optical light, the individual member galaxies are visible, whereas the diffuse X-ray emission originates from the ICM.[7]

In the optical light down to infrared energies, galaxy clusters present themselves as accumulation of individual galaxies clustering around a BCG (Fig. 2.7). Photometric and spectroscopic observations of these galaxies yield their redshifts and identify a possible projected gathering of galaxies as a bound cluster. At the same time, these observations allow for the most precise redshift measurements of galaxy clusters with $\Delta z \cdot (1 + z)$ and $\Delta z \approx 0.02$ (e.g. Merloni et al. 2012; Liu et al. 2015) or $\Delta z \ll 0.01$ (comp. Muzzin et al. 2009; Wilson et al. 2009), respectively. Due to their large potential wells, galaxy clusters deflect the light of background objects and thus act as so-called gravitational lenses. Distorted background galaxies are also visible in the optical and the degree of the distortions yields information on the mass of the galaxy cluster.
The spatially diffuse and continuous X-ray emission of clusters results from the hot ICM (comp. Sec. 2.6.2 & Fig. 2.7), where the X-ray spectra show an imprint of various cluster characteristics. Also, these

[7] *Credit:* X-ray: NASA/CXC/MIT/E.-H Peng et al; Optical: NASA/STScI; Release date: 2008

observations allow for the determination of the cluster mass, which is essential for cosmological studies with galaxy clusters. As this work focuses on the study of galaxy clusters in X-rays, this emission will be described in detail in the following section.

2.7.1 Emission Mechanisms

The X-ray spectra of galaxy clusters are a superposition of the main three emission mechanisms in the ICM - thermal bremsstrahlung of free electrons, line emission, as well as recombination emission. For electron temperatures of $k_B T_e \gtrsim 2$ keV, the main emission mechanism is thermal bremsstrahlung (compare reviews of e.g. Sarazin 1986; Reiprich et al. 2013) of energetic electrons being accelerated in the vicinity of an atomic nucleus, which is also known as free-free emission. The emissivity ϵ_ν^{ff} of this process at a given frequency ν is summarised as

$$\epsilon_\nu^{ff} \propto n_e T_e^{-1/2} \exp\left[-\frac{h\nu}{k_B T_e}\right] \quad , \tag{2.49}$$

where we adopt the electron number density n_e and generally define the emissivity ϵ_ν as emitted luminosity dL over the frequency range $d\nu$ and the volume dV

$$\epsilon_\nu \equiv \frac{dL}{d\nu dV} \quad . \tag{2.50}$$

Over all, the bremsstrahlung emission describes a smooth, continuous spectrum with an exponential cut-off towards the higher frequencies. Integrated over all energies, the total bremsstrahlung emissivity is approximated as

$$\epsilon^{ff} \propto T_e^{1/2} n_e^2 \quad . \tag{2.51}$$

At lower ICM temperatures of $k_B T_e \lesssim 2.5$ keV, line emission, also referred to as bound-bound emission, as well as free-bound emission of the highly ionised metals are the dominant processes with an approximated total emissivity of

$$\epsilon^{fb+bb} \propto T_e^{-0.6} n_e^2 \tag{2.52}$$

(comp. Sarazin 1986). Differently from the bremsstrahlung emission, the line emission decreases with increasing electron temperature, as more metals are becoming fully ionised.
In the following, we assume an equality between the electron temperatures T_e and the temperature of the remaining gas particles T_{gas} and refer to this over-all ICM temperature as T. This approach is especially reasonable within the studied radii $r \lesssim r_{500}$, where this equilibration time scale is of the order of only a few 10^8 yrs (Spitzer 1956; Reiprich et al. 2013).

2.7.2 Galaxy Cluster Spectra

Figure 2.8 presents the X-ray spectra as the superposition of bremsstrahlung, line and recombination emission for different ICM temperatures. The exponential cut-off at high frequencies and the fading emission lines with increasing temperatures, discussed in the previous section, are also visible in this figure. Especially prominent is the Fe-L line complex at $\sim$ 1 keV as well as the Fe-K line complex at $\sim$ 7 keV, which represent the electron transitions to the first excited and to the ground state in iron, respectively. Emission lines of e.g. magnesium at 1.4 keV, silicon at 1.8 keV for $k_B T < 1$ keV and at 2 keV for $k_B T > 1$ keV, and sulphur at 2.6 keV are also detectable in the spectrum (comp. e.g. Sarazin 1986). In general, the X-ray spectra are imprinted by the following characteristics:

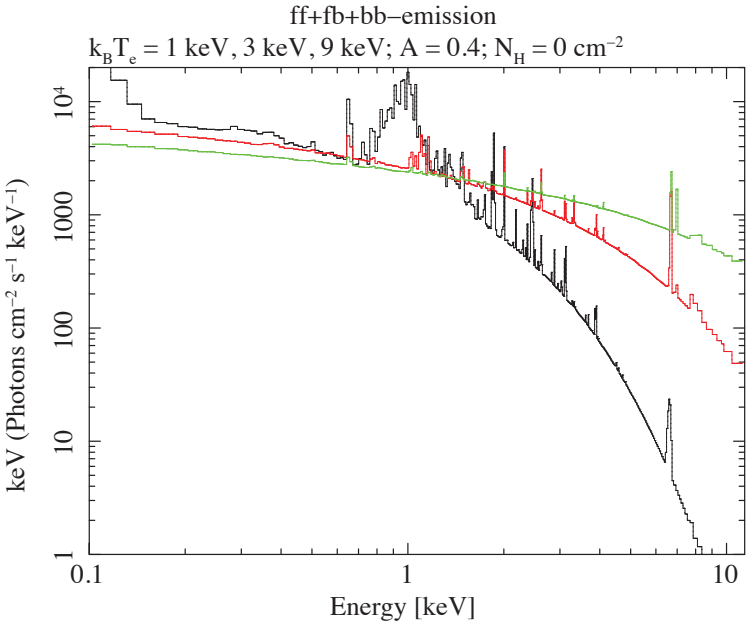

Figure 2.8: X-ray emission spectra for three individual galaxy clusters with different ICM temperatures: 1 keV (black), 3 keV (red) and 9 keV (green). All spectra are simulated for a metallicity of $A = 0.4\ A_\odot$, assuming no foreground absorption, $N_H = 0\ cm^{-2}$, and a redshift of $z = 0$. The figure describes the superposition of free-free, free-bound as well as bound-bound emission and distinctly displays the dependence on the ICM temperature. Credit: *Reiprich et al. (2013)*

Temperature: As emphasised by Fig. 2.8 as well as by Eq. 2.49 & 2.51, an increase in the ICM temperature results in an enhancement of the over-all bremsstrahlung emission. Though the emission at lower energies is reduced, the exponential cut-off is shifted to higher energies. At the same time, the emission lines are fading with increasing temperature as the fraction of fully ionised metals increases. The Fe-K lines, however, remain a prominent feature over a wide range of temperatures (Sarazin 1986).

Density: The ICM density regulates the number of particle interactions and thus the number of emitted X-ray photons (comp. e.g. Eq. 2.49). With an increased density, interactions, including bremsstrahlung emission as well as the excitation and ionisation of metals, occur more frequently such that the X-ray emissivity increases as a whole. Accordingly, the density defines the luminosity of the cluster, which is a compilation of all three emission mechanisms, as well as the normalisation of the spectrum.

Metallicity: As the metallicity defines the number of metals in the ICM, it influences the strength of the emission lines with a higher line emission rate for an increased metallicity.

Redshift: According to the cosmological redshifts z of galaxy clusters, we observe a shift in their spectral features from the emission energy E_0 to $E_{\rm obs}$ as (comp. Eq. 2.8)

$$E_{\rm obs} = \frac{E_0}{1+z} \quad . \tag{2.53}$$

Understanding these spectral dependencies allows for the determination of galaxy cluster properties from observed X-ray spectra. However, due to the degeneracy of the different properties, which lead to similar spectral changes, all of these parameters need to be fit simultaneously. At the same time, several cluster properties are related to one another, following so-called galaxy cluster scaling relations.

2.7.3 Scaling Relations

Scaling relations describe the correlation between different object characteristics as power laws. For galaxy clusters, these relations are derived following the so-called model of *self-similarity* (Kaiser 1986), which explains the cluster properties by assuming gravity as the only acting force during the cluster formation process. Since gravity has no preferred length scale, galaxy clusters of different masses are understood as scaled versions of each other. Additionally, matter overdensities are expected to collapse into bound haloes always at the same initial density contrast of $\delta_{\rm lin} = 1.69/a$ relative to the scale factor at the time of the collapse (comp. Sect. 2.3.3). Following this concept and considering Eq. 2.28 as well as $\rho_{\rm crit}(z) \propto H(z)^2$, however, we conclude the absolute density value of a collapsing halo to increase with increasing redshift.
We will consider those relations including X-ray properties, with a focus on the temperature, the luminosity, the total cluster mass as well as the redshift.

Mass-Temperature Relation: To derive the *mass-temperature relation* ($M - T_{\rm X}$ relation) from the principle of self-similarity, we recall the definition of the total cluster mass based on the critical density as presented in Eq. 2.48. Remembering Eq. 2.13 & 2.23 for the definition of the critical density and $E(z)$, respectively, the above expression rewrites as (Giodini et al. 2013))

$$M_\Delta = \frac{4\pi}{3} \cdot \Delta \cdot \rho_{\rm crit,0} E^2(z) r_\Delta^3 \quad , \tag{2.54}$$

$$\text{applying} \quad \rho_{\rm crit}(z) = \left(\frac{H(z)}{H_0}\right)^2 \cdot \rho_{\rm crit,0} \quad . \tag{2.55}$$

When adding the concept of virial equilibrium $T_{\rm X} \propto M/r$, a correlation between the cluster mass and its temperature is obtained

$$T \propto \frac{M}{r} \propto M^{2/3} E(z)^{2/3} \Delta^{1/3} \tag{2.56}$$

$$\Rightarrow \quad M \propto \frac{T_{\rm X}^{3/2}}{\Delta^{1/2} E(z)} \quad . \tag{2.57}$$

Luminosity-Temperature Relation: The luminosity L of a galaxy cluster is expressed as the product of the emissivity and the emitting volume $L \propto \epsilon \cdot r^3$. For X-rays, we follow the simplified definition of Eq. 2.51 and the luminosity thus reads (comp. Giodini et al. 2013)

$$L_{\rm X} \propto T^{1/2} n_{\rm e}^2 r^3 \quad , \tag{2.58}$$

following Eq. 2.51. Applying the proportionality between the electron number density and the gas density $n_{\rm e} \propto \rho_{\rm g}$ as well as the gas mass fraction $f_{\rm g}$, which was defined earlier, we finally obtain

$$L_{\rm X} \propto T^2 f_{\rm g}^2 \Delta^{1/2} E(z) \quad , \tag{2.59}$$

additionally considering Eq. 2.48 & 2.57.

Luminosity-Mass Relation: Replacing the temperature in the above scaling relation by Eq. 2.56 derives the $L_X - M$ relation

$$L_X \propto M^{4/3} f_g^2 \Delta^{7/6} E(z)^{7/3} \quad . \tag{2.60}$$

Outside the cluster cores, the assumption of only gravity determining the characteristics of the observed ICM is appropriate to a first order approximation and is confirmed from simulations (comp. e.g. Borgani & Kravtsov 2011, for a review). However, for a thorough investigation of the scaling relations, deviations from hydrostatic equilibrium as well as physical processes within the ICM need to be accounted for. Also, the above derivations follow the simplified assumptions of constant property values, such as a constant temperature or gas density, which is generally not the case and will be discussed in the subsequent section. Accordingly, observed scaling relations slightly deviate from the theoretical models in their normalisations as well as in their exponents (e.g. Pratt et al. 2009; Vikhlinin et al. 2009a; Mantz et al. 2010a; Reichert et al. 2011). Additionally, an intrinsic scatter σ is introduced, which accounts for unique cluster characteristics resulting in slightly different temperature or luminosity values for each individual cluster. For example, the $M - T_X$ relation shows an intrinsic scatter of the order of $\sim 15\%$ in the temperature (e.g. Vikhlinin et al. 2009a; Mantz et al. 2010a), which is a result of substructures in the cluster matter distribution (O'Hara et al. 2006). The intrinsic scatter in the L_X-M relation, on the other hand, is even broader with roughly 40% (e.g. Vikhlinin et al. 2009a) and is related to heating and cooling processes in the ICM as e.g. from AGN feedback, galactic winds or star formation (e.g. Mittal et al. 2011; Giodini et al. 2013). These considerations emphasise that even though hydrostatic equilibrium is a reasonable assumption in general, physical processes within the ICM need to be considered for an accurate interpretation of the observed data.
As expressed especially in Sec. 2.7.2, ICM temperatures, X-ray luminosities and redshifts are almost directly accessible from X-ray or optical observations, respectively. Instead, Cluster masses need to be derived indirectly from the data, based on more complex considerations. Thus, the above scaling relations allow for a comfortable estimate of the cluster masses.

2.7.4 Galaxy Cluster Profiles

Up to now, the galaxy cluster properties, such as temperature, luminosity, or also metallicity, were assumed to be constant throughout the entire ICM, whereas observations yield spatially dependent metallicity maps (Lovisari et al. 2011) and profiles in temperature and luminosity as well as in the underlying density. To derive the density profile of a galaxy cluster, the distribution of matter in the potential well is assumed to follow the model of a self-gravitating isothermal sphere and a so-called King-profile (King 1962). Following this approach and assuming the gas to trace the underlying total matter density, $\rho(r) \propto \rho_g(r)$, the gas density distribution $\rho_g(r)$ is described by a β-model (Cavaliere & Fusco-Femiano 1976)

$$\rho_g(r) = \rho_{g,0} \left(1 + \frac{r^2}{r_c^2}\right)^{-\frac{3}{2}\beta} \quad , \tag{2.61}$$

with the *core radius* r_c and the central gas density $\rho_{g,0}$. The parameters $\rho_{g,0}$, r_c and β cannot be derived from theory, but need to be obtained from observations. As the density distribution itself is not directly accessible, though, the closely related X-ray surface brightness S_X is analysed

$$S_X = \frac{1}{4\pi(1+z)^4} \int_{-\infty}^{\infty} \epsilon \, \mathrm{d}l \quad , \tag{2.62}$$

as total X-ray emissivity ϵ integrated along the line of sight dl. Considering $\epsilon \propto n_\mathrm{e}^2$ (comp. Eq. 2.51 & 2.52) for a constant temperature, and the relation $\rho_\mathrm{g} \propto n_\mathrm{e}$, the above integration is rephrased as

$$S_\mathrm{X}(R) = S_\mathrm{X,0}\left(1 + \frac{R^2}{r_\mathrm{c}^2}\right)^{-3\beta+\frac{1}{2}} \tag{2.63}$$

(Cavaliere & Fusco-Femiano 1976), with the projected radius from the cluster centre R. The searched-for parameters β and r_c, as well as the central X-ray brightness $S_\mathrm{X,0}$ are now obtained by the model fit to the observed surface brightness, where commonly retrieved values for the exponent are $\beta \approx 2/3$ (Voit 2005). Slight deviations between the theoretical model and observations result from the input assumptions of hydrostatic equilibrium and isothermality (comp. Sec. 2.7.3) and are adjusted by e.g. applying a double β-model (e.g. Reiprich 1998). Following the above concept, the surface brightness distribution mirrors the underlying density profile.
Along with the surface brightness, also the ICM temperature deviates with radius from the cluster centre. Over all, decreasing temperatures are detected with increasing radii (e.g. Zhang et al. 2004; Vikhlinin et al. 2005; Akamatsu et al. 2011) as a power law $T \propto r^{-\gamma}$, where the ICM temperatures outside the core region drop by a factor of ~ 3 towards r_{200} (e.g. Reiprich et al. 2013). In the cluster centre, however, no general trend is observable and clusters show either flat or decreasing temperature profiles with decreasing radius (e.g. Allen et al. 2001; Hudson et al. 2010), as a result of complex heating and cooling mechanisms in the cluster centre.
Due to the limited observation time and resolution of the X-ray instruments, these distributions in temperature, brightness or density are not necessarily available for all observed clusters. Especially the study of metallicity maps requires long observation times, such that the assumption of a constant ICM metallicity is commonly applied. At the same time, an isothermal ICM is a feasible approach for clusters with small angular extension or low observing time.

2.7.5 Mass Determination

Just as galaxy clusters are observable in all wavelengths, also their total mass is accessible in all energy ranges applying different theoretical approaches. However, we mainly focus on the computation of X-ray masses and briefly compare this method to mass determinations in other wavelengths.
As already expressed in Sect. 2.7.3, cluster masses can be inferred e.g. from X-ray scaling relations. To calibrate the observed scaling relations or to avoid the uncertainties in these relations when computing cluster masses, a more complex theoretical model for the mass needs to be derived. This theoretical model of X-ray masses is based on the assumption of hydrostatic equilibrium between the pressure gradient of the gas, and the gravitational potential Φ

$$\frac{1}{\rho_\mathrm{g}} \cdot \frac{\mathrm{d}P}{\mathrm{d}r} = -\frac{\mathrm{d}\Phi}{\mathrm{d}r} \quad . \tag{2.64}$$

The gravitational potential is defined via the total mass $M(< r)$ within the radius r as

$$\frac{\mathrm{d}\Phi}{\mathrm{d}r} = \frac{\mathrm{G}M(< r)}{r^2} \quad , \tag{2.65}$$

whereas the pressure P follows the equation of an ideal gas

$$P = \frac{\mathrm{k}}{\mu m_\mathrm{p}} \cdot \rho_\mathrm{g} \cdot T \quad . \tag{2.66}$$

The parameters μ and m_p express the mean molecular weight and the proton mass, respectively. Combining Eq. 2.64, 2.65 & 2.66, the definition of the *hydrostatic mass* of a galaxy cluster is derived

$$M(<r) = -\frac{\mathrm{k}Tr}{G\mu m_\mathrm{p}} \cdot \left(\frac{\mathrm{d}\ln\rho_\mathrm{g}}{\mathrm{d}\ln r} + \frac{\mathrm{d}\ln T}{\mathrm{d}\ln r} \right) \quad , \tag{2.67}$$

based on the gas density profile as well as on the temperature profile. The gas density distribution is imprinted in the X-ray surface brightness profile (comp. Sec. 2.7.4), whereas the temperature profile is obtained from the study of X-ray spectra in different annuli.
The above derivation is especially based on the assumption of hydrostatic equilibrium as well as of spherical symmetry, and accordingly excludes clusters with recent merger processes. Also for more relaxed clusters, especially the neglect of residual gas motion yields hydrostatic masses to be biased low by $\sim 10-15\%$ when compared to simulations (e.g. Nagai et al. 2007; Meneghetti et al. 2010). With the new up-coming X-ray instruments, such as e.g. *Astro-H* (Takahashi et al. 2014) or *Athena* (Nandra et al. 2013), the study of turbulent and bulk gas motion within the ICM becomes accessible and the described mass bias is expected to decrease to $\lesssim 5\%$ (Ota et al. 2015). What is more, the uncertainty in the estimated masses is mainly based on the determination of the density and temperature profiles, rather than on violated assumptions in the derivation. Still, a comparison of X-ray masses to the results of the mass determination in other wavelengths is suggested.

- **Galaxy Velocity Dispersion:** The observed velocities of the constituent galaxies in a cluster emphasise the gravitational potential required for these galaxies to remain bound within the halo. Following the virial theorem $E_\mathrm{kin} = -\frac{1}{2}E_\mathrm{pot}$, the total cluster mass is related to the galaxy velocity dispersion σ in dependence on the radius r

$$M \propto \frac{r\sigma^2}{G} \quad . \tag{2.68}$$

  The correspondingly obtained cluster masses compare well to the hydrostatic X-ray masses.

- **Gravitational Lensing:** As expressed earlier, the distortion of the images of background galaxies yields information on the mass of a foreground galaxy cluster. As a whole, lensing observations obtain the most reliable cluster mass estimates as this phenomenon is independent of the dynamical state of the cluster as well as of the type of matter. Recent comparisons indicate X-ray observations to underestimate weak lensing masses by $\sim 10\%$ on average for relaxed clusters, with an increasing deviation to $15-20\%$ for less relaxed clusters (e.g. Mahdavi et al. 2008; Planck Collaboration et al. 2012; Mahdavi et al. 2013; Applegate et al. 2015). Similar results are also reported for strong lensing observations (e.g. Hoekstra et al. 2013), with a vanishing disagreement for highly relaxed clusters (e.g. Bradač et al. 2008; Newman et al. 2011). These results accordingly reflect the observed mass bias when compared to simulations (e.g. Nagai et al. 2007) and emphasise the influence of deviations from hydrostatic equilibrium and of residual gas motion.

- **Sunyaev-Zel'dovich Effect:** Also mass measurements via the SZ-effect are based on cluster density as well as temperature profiles. However, to reconstruct the mass, X-ray information is always needed in addition to the SZ-data and accordingly, both SZ- and X-ray masses are well in agreement with each other (Planck Collaboration et al. 2012).

2.8 Galaxy Clusters as Cosmological Probes

Studying cosmology is generally based on one of the following two approaches: analysing the geometry of the Universe by measuring distances (comp. Sect. 2.1.3) or tracing the evolution of structures (comp. Sect. 2.3). The observation of galaxy clusters allows for the pursuit of both strategies. For example, measurements of the gas mass fraction $f_{\rm g}$, or of distances inferred from the combination of X-ray and SZ- information test the geometry of the Universe via the angular diameter distance (comp. e.g. Allen et al. 2011). At the same time, as most massive, virialised objects in the Universe, galaxy clusters present themselves as reliable probes for tracing the LSS (e.g. Voit 2005; Vikhlinin et al. 2009b; Allen et al. 2011) either via their spatial clustering or their abundances. The spatial clustering is e.g. described by the power spectrum of massive haloes $P_{\rm h}(k, z)$, following the relation

$$P_{\rm h}(k, z) = b^2(M, z) \cdot P(k, z) \quad , \tag{2.69}$$

based on the matter power spectrum $P(k, z)$ (comp. Sec. 2.3.1) and the bias $b(M, z)$ between the distributions of massive haloes and the underlying matter.
In this work, we focus on the abundance of galaxy clusters, while applying the halo mass function (comp. Sec. 2.3.3 & Eq. 2.38). As massive haloes are traced by the observations of galaxy clusters, the number distribution of these objects yields constraints on the cosmological parameters, especially on the parameters $\Omega_{\rm m}$ and σ_8 (for a review comp. e.g. Peacock 1999; Dodelson 2003; Voit 2005; Allen et al. 2011; Schneider 2015). At the same time, this approach is also sensitive to the dark energy equation of state described by the parameters w_0 and $w_{\rm a}$ (e.g. Vikhlinin et al. 2009b; Mantz et al. 2010b, 2015). Recently derived 68.3%-uncertainties on the above parameters from cluster studies are of the order of $\Delta\Omega_{\rm m} = 0.03$ ($\sim 11.5\%$), $\Delta\sigma_8 = 0.04$ ($\sim 5\%$) as well as $\Delta w_0 = 0.15$ ($\sim 15\%$) for constant-w_0 models (Mantz et al. 2015). The constraints on the cosmological parameters are generally described as uncertainty regions in the parameter space with different credibility levels. These levels define the probability that the enclosed region contains the parameter value, which reproduces the observed data. Fig. 2.9 presents an example of such credibility regions for the joint parameter sets $\{\Omega_{\rm m}, \sigma_8\}$ and $\{\Omega_{\rm m}, w_0\}$ obtained from the analysis of cluster counting experiments. The orientation and shape of these credibility regions expresses the level of degeneracy between the displayed parameters, with e.g. a strong degeneracy between $\Omega_{\rm m}$ and σ_8 for cluster observations. Additionally, constraints from other cosmological probes are included, such as e.g. the CMB power spectrum (comp. Fig. 2.2). Several of these other probes are briefly described in Sect. 2.5, but for detailed information of the applied data sets we ask the reader to refer to Mantz et al. (2015). In an optimal case, all constraints should overlap in one mutually shared region, despite their deviating parameter degeneracies as displayed above.

In practice when analysing cluster abundances, the number of clusters is counted in bins of finite redshift and mass intervals. These observation results are then compared to the theoretically expected numbers, which are obtained by integrating the halo mass function over the volume as well as over the defined redshift and mass bins, for a given cosmology. Especially for larger samples of clusters, measured masses are not available for all considered clusters, such that either scaling relations need to be applied to compute the masses (comp. Sec. 2.7.3) or the theoretical model needs to be re-formulated based on a more easily accessible observable, e.g. the cluster luminosity. As both approaches are based on the application of scaling relations, they are limited by the uncertainties and by the intrinsic scatter in the scaling relations. Those relations showing a low scatter, such as e.g. $M - T_{\rm X}$ or $M - Y_{\rm X}$, with $Y_{\rm X} = {\rm k_B} T_{\rm X} M_{\rm g}$, are thus best suitable for cosmological studies. Also, it is essential to simultaneously calibrate and fit the scaling relations along with cosmology (comp. the review by Allen et al. 2011).

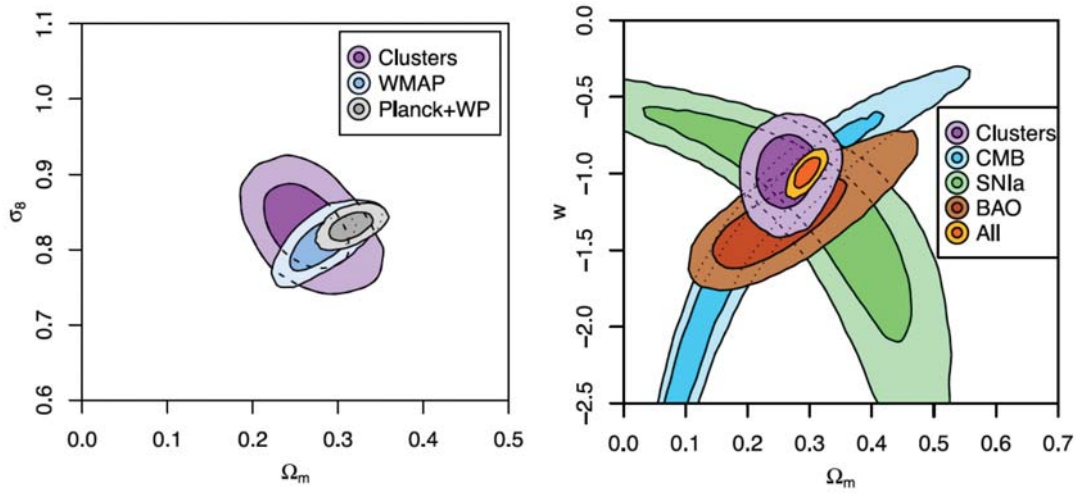

Figure 2.9: Joint 68.3% and 95.4% credibility regions for the cosmological parameters $(\Omega_\mathrm{m}, \sigma_8)$ and (Ω_m, w_0) applying different cosmological probes. *Left:* Overlap of the credibility regions for the mean matter density Ω_m and the amplitude of matter perturbations σ_8 obtained from cluster counts and observations of the CMB power-spectrum with the two instruments *WMAP*, applying the 9-year survey results, and *Planck*. *Right:* Constraints on the mean matter density Ω_m and the dark energy equation of state w_0 from various probes, including cluster abundances and the joint credibility region for all probes. *Credit:* Mantz et al. (2015)

The methodology of re-formulating the halo mass function based on X-ray observables is described in detail as well as in a practical context in Sect. 6.3.1.

2.9 The *eROSITA*-Telescope

Whereas the previous sections emphasised on the cosmological model and the concepts of studying the evolution of our Universe with the help of galaxy clusters, we now introduce a promising instrument for the required cluster observations - the *extended ROentgen Survey with an Imaging Telescope Array* (*eROSITA;* Merloni et al. 2012). The main science driver for this telescope is the analysis of the dark energy equation of state, by tracing the evolution of structures with the help of galaxy clusters. It is likely to be the first "Stage IV" dark energy probe, according to the *Dark Energy Task Force* (DETF) report of 2006 (Albrecht et al. 2006). Such a probe is expected to improve the constraints on dark energy by a factor of ~ 10 compared to the knowledge at the publication date of the report. For this aim, the telescope will need to detect at least $\sim 30,000$ clusters of galaxies up to redshifts of ~ 2.0.
The instrumental set-up as well as the different science goals for *eROSITA*, including the observation strategy to constrain the characteristics of dark energy, are summarised in the following sections.

2.9.1 Instrumental Information[8]

The *eROSITA*-telescope is a joint X-ray initiative between several institutes and universities in Germany and Russia, led by the *Max-Planck Society* (*MPG*) and the *German Space Agency* (*DLR*) on the one side, and by the Russian space agency *ROSCOSMOS* and the *Space Research Institute for the Russian Academy of Sciences* (*IKI*) on the other side. Currently, the instrument is assembled under the leadership of the *Max-Planck Institute for Extraterrestrial Physics* (*MPE*) and will then be mounted onto the Russian satellite platform *Spectrum Roentgen Gamma* (*SRG*). The launch is scheduled for early 2017 from the cosmodrome in Baikonur to an L2 orbit. The telescope will then perform eight all-sky surveys in total, each lasting half a year, with a subsequent pointed observation phase of three years.

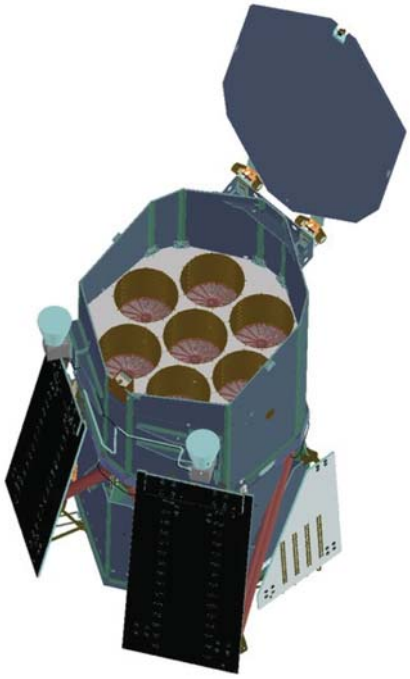

Figure 2.10: Schematic image of the *eROSITA*-instrument, looking onto the seven X-ray telescopes.[9]

The instrument consists of seven X-ray mirror telescopes, each with its own CCD (*Charged Coupled Device*) in the focal plane (Fig. 2.10). X-ray telescopes as well as CCDs need to follow certain characteristics to collect and focus the energetic photons as well as to measure their energy. X-ray photons are only reflected by a smooth metal surface and only for sufficiently small impact angles, referred to as *grazing incidence*. For example, for a photon with an energy of $E = 10$ keV, which is equivalent to a wavelength of $\lambda \approx 1$ Å, the incidence angle needs to be $< 1°$. To account for the grazing incidence and to focus all incoming light rays into one point, Wolter optics are applied (Wolter 1952a,b), where X-ray instruments, including *eROSITA*, are based on the Wolter optics Type I, which combine an outer parabolic mirror with an inner hyperbolic mirror. At the same time, these optics allow large numbers of mirror shells to be stacked to increase the effective area of the instrument. Each of the seven *eROSITA*-telescopes consists of 54 of these mirror shells with a focal length of 1.60 m. The applied X-ray CCDs show a thicker depletion layer than optical CCDs to provide for the sensitivity of high energy photons. Additionally, each X-ray photon is detected individually with its direction as well as with its energy, where *eROSITA*'s effective area covers the energy range between (0.1 – 10.0) keV with an energy resolution of ~ 5 eV (comp. Fig. 2.11). The effective area is especially large in the range between (0.5 – 2.0) keV with a sharp drop off for energies above ~ 2 keV. Following this shape, the energy range of highest sensitivity overlaps with the position of the main line emission complexes at ~ 1 keV of galaxy clusters (comp. Sec. 2.7.2) and accordingly allows for precise and accurate estimates of various cluster characteristics, including especially the ICM temperature.

Other important information on the instrument include its field-of-view (FoV) of 0.83 deg^2 and the angular resolution of ~ 15 arcsec for a pointed on-axis observation. However, the angular resolution highly depends on the observation angle and degrades with increasing off-axis angle. For the scanning observation mode of the all-sky surveys, the resolution is averaged over the entire FoV to show a value

[8] If not stated otherwise, the information on the instrumental design are published by Merloni et al. (2012).

[9] *Credit:* www.mpg.de/4710144/eROSITA_Dunkle_Energie

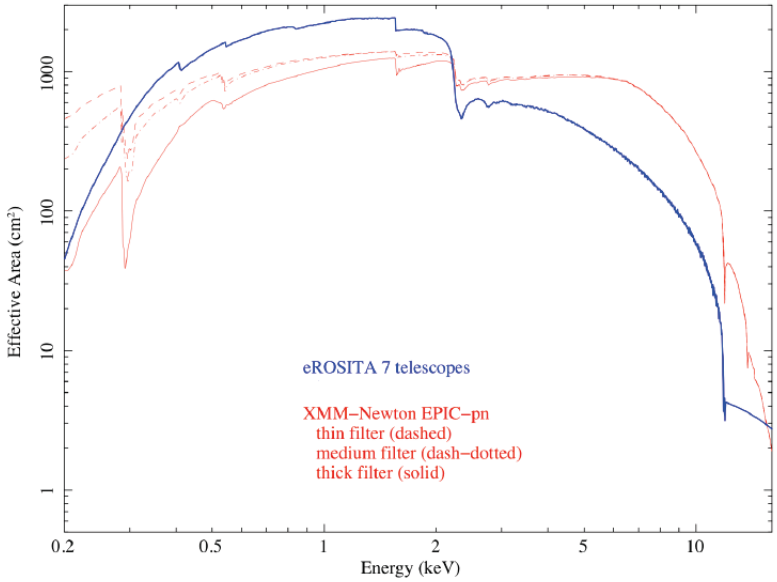

Figure 2.11: Effective area for the seven *eROSITA*-telescopes compared to the efficiency of the three *XMM-Newton EPIC-PN* filters. In the energy range between (0.5 – 2.0) keV, where most of the emission lines of galaxy clusters are located, *eROSITA* shows a higher efficiency than the current instrument. *Credit: Merloni et al. (2012).*

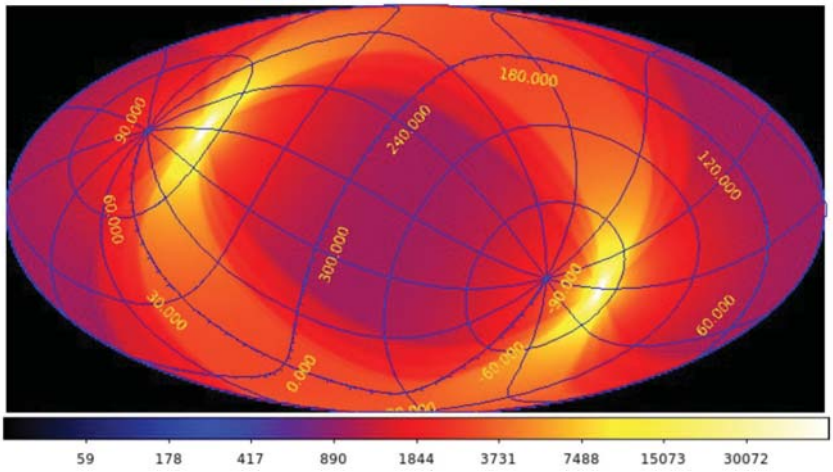

Figure 2.12: Exposure map for the four years of *eROSITA* all-sky survey given in galactic coordinates (FK5) with the colour indicating the exposure time per FoV in seconds. *Credit: J. Robrade 2014, eROSITA Collaboration private communication.*

of $\sim$ 28 arcsec. The spatial distribution of exposure times per FoV is presented in Fig. 2.12, with an average effective exposure time of 1.6 ks (Pillepich et al. 2012) after accounting for the subtraction of solar flares and slight instrumental difficulties. Due to the observation strategy, two fields with deep exposure times of $\sim$ 20 ks develop at the ecliptic poles. These fields cover only a very small sky fraction of $f_{\rm sky} = 0.0034$, but allow for more detailed studies of X-ray objects and for predictions on the efficiency of the subsequent pointed observation phase.

2.9.2 Science Goals

The interest in the *eROSITA* observations is especially promoted as it will perform the first all-sky survey after the *Röntgensatellit* (*ROSAT*) in the 1990s, while allowing for a resolution of the order of current X-ray instruments and for an improved sensitivity by one order of magnitude. The currently mainly applied instruments for galaxy cluster studies are the European *XMM-Newton*, the US-american *Chandra* and the Japanese *Suzaku* with angular resolutions of $\sim$ 15 arcsec, $\sim$ 0.5 arcsec and $\sim$ 2 arcmin, respectively. Accordingly, the resolution of *eROSITA* is comparable to that of *XMM-Newton* for the pointed observation phase, while it still remains four times as good as *Suzaku's* resolution during the survey mode. During its four years of all-sky surveys *eROSITA* will detect large samples of all types of X-ray emitting objects, including e.g. X-ray binaries, single stars, AGN and galaxy clusters. As AGN are the brightest extragalactic objects in the sky, *eROSITA* is expected to detect $(3 - 10)\cdot 10^6$ of these sources up to redshifts of $z \approx 7 - 8$. At the same time, the instrument will allow for a detailed study of the accretion processes onto the super massive black holes in the centre of the AGN. However, the main science driver of this telescope is the detection of galaxy clusters as tracers of the LSS and thus of the dark energy characteristics. To achieve this aim, the average flux limit for the observation of galaxy clusters is reduced to $3 \cdot 10^{-14}$ erg/s/cm^2 in the energy range of $(0.5 - 2.0)$ keV, which is roughly one order of magnitude below the *ROSAT* limit (Trümper 1985). Along with this sensitivity, forecasts predict *eROSITA* to detect $\sim 100,000$ clusters of galaxies with a minimum of $\eta_{\rm min} = 50$ observed photons and masses above $M = 5 \cdot 10^{13}$ M$_\odot/h$. This sample will cover redshifts of $z \lesssim 2$, while including all massive clusters with $M \gtrsim 3 \cdot 10^{14}$ M$_\odot/h$ in the observable Universe (Pillepich et al. 2012). With these characteristics, the *eROSITA* cluster catalogue will extend the present *ROSAT*-cluster sample by a factor of $\sim$ 50.

Complementary optical observations are planned to determine the cluster redshifts, such that X-ray fluxes, luminosities as well as redshifts will be available for the entire *eROSITA* cluster sample. These optical observations include e.g. the multi-band surveys *PanSTARRS* (*Panoramic Survey Telescope & Rapid Response System*, e.g. Ebeling et al. (2013)), *DES* (*Dark Energy Survey*, e.g. Crocce et al. (2015)) and *VST ATLAS* (*VLT Survey Telescope ATLAS*, Shanks et al. (2015)) for photometric redshifts, while spectroscopic observations with e.g. *4MOST* (*4m Multi-Object Spectroscopic Telescope for ESO*, e.g. de Jong et al. (2014)) and *SPIDERS* (*SPectroscopic IDentification of eROSITA Sources*, e.g. Salvato (2015)) are designed as *eROSITA* follow-up. This redshift information is especially important for cosmological studies and will improve the constraints on the cosmological parameters.

Assuming luminosities and redshifts to be accessible for all *eROSITA* galaxy clusters, first forecasts predict constraints of $\Delta\sigma_8 = 0.014$ and $\Delta\Omega_{\rm m} = 0.012$ for a ΛCDM cosmology, $\Delta w_0 = 0.053$ for a constant dark energy equation of state, and $\Delta w_{\rm a} = 0.48$ for a variable dark energy equation of state (Fig. 2.13, Pillepich et al., in prep). These simulations are based on the halo mass function as well as on the angular clustering of galaxy clusters and emphasise that *eROSITA* will allow for a significant improvement of the cosmological constraints from galaxy clusters (comp. Sec. 2.8). At the same time, it will decrease the uncertainty on the dark energy equation of state even below the current uncertainty from the *Planck* data (Planck Collaboration et al. 2015c). However, the above stated results are still

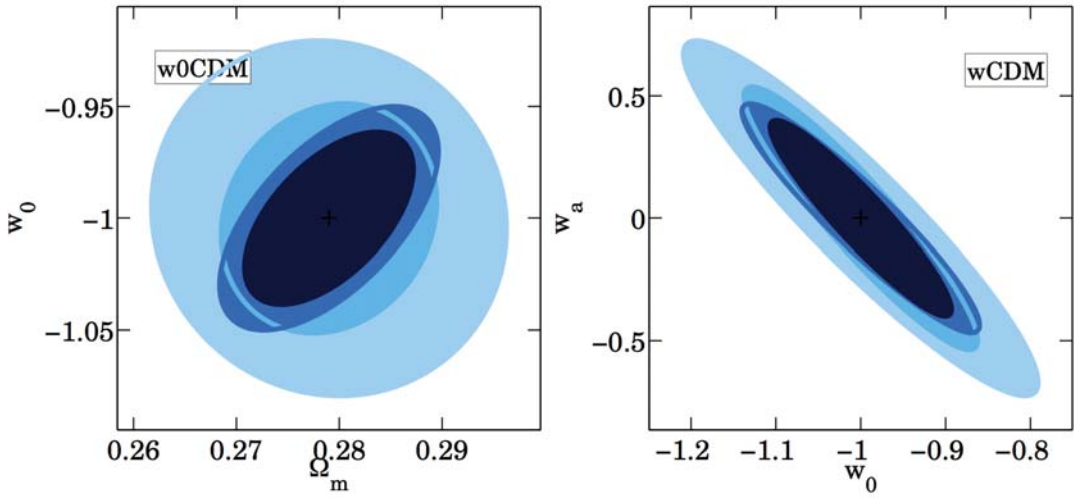

Figure 2.13: Forecasts of the cosmological constraints from the *eROSITA* galaxy cluster sample. Presented are the joint constraints for (Ω_m, w_0), assuming a w_0CDM-cosmology, and for (w_0, w_a), assuming a wCDM-cosmology. The credibility regions are centred around a *WMAP5* cosmology (Komatsu et al. 2009) and present the scenarios of *eROSITA* data with pessimistic scaling relation constraints, *eROSITA* data with optimistic constraints, *eROSITA+Planck* data with pessimistic constraints, and *eROSITA+Planck* data with optimistic constraints from bright to dark colours. *Credit: Pillepich et al., in prep.*

only a pessimistic approach and are limited by the uncertainty and scatter in the galaxy cluster scaling relations (comp. Sec. 2.8). In the up-coming years, more precise mass estimates are expected from the follow-up synergy of different X-ray instruments, including *XMM-Newton*, *Chandra*, *Suzaku*, *NuSTAR* (*The Nuclear Spectroscopic Telescope Array*) (Harrison et al. 2013) and *Astro-H* (Kitayama et al. 2014), which will decrease the scatter in the scaling relations. An additional improvement is expected from a more accurate calibrations of the X-ray cluster masses by means of weak lensing mass measurements. For a more optimistic scenario with a factor of four lower uncertainties in the scaling relations, the above constraints will improve by $\sim 30-40\%$ (Fig. 2.13). More details on these forecasts as well as an extension to the above estimates are presented in chapter 6 of this work.

2.10 Introduction to the Aims of this Work

Following the ideas of the previous section, the up-coming *eROSITA*-instrument is expected to prove as reliable and promising tool to put tight constraints on the cosmological parameters and to especially study the nature of dark energy. Within this work, we emphasise on the cosmological opportunities of this telescope, while applying galaxy clusters as cosmological probes.
As cosmology studies have indicated strong improvements in the constraints, if additional cluster information to the observed flux is available (e.g. Clerc et al. 2012), we investigate the precision and accuracy with which *eROSITA* will detect ICM temperatures. At the same time, the $M - T_X$ scaling relation shows smaller uncertainties than the relation including the luminosity. By means of a spectral analysis, we quantify the cluster masses and redshifts, which allow for the observation of low relative temperature uncertainties. Convolving this parameter space with the halo mass function, the number of *eROSITA* clusters with precise temperatures is estimated and we are able to define the corresponding sub-catalogue of clusters with additional information for our cosmological forecasts. The above analysis is then repeated for the determination of cluster redshifts to predict the results that can be obtained

from *eROSITA*-data alone. These forecasts can then be applied to optimise optical follow-up observations. In general, this spectral analysis also allows for the study of biases that may occur during the data reduction. These biases need to be quantified and convolved with the future observed data to allow for its realistic interpretation and especially for an accurate reconstruction of the halo mass function. Since the above research tasks involve the investigation of galaxy cluster spectra, which are already extracted from the *eROSITA* raw data, we additionally test for a possible bias arising from the observation itself or from the spectral extraction procedure.
Having quantified the observational strength for galaxy clusters, we continue with cosmological forecasts, while focusing on the main science driver of this telescope - the nature of dark energy. Within this work, the currently existing cosmology studies for this instrument (Pillepich et al. 2012, Pillepich et al., in prep.) are extended by applying *Markov-Chain Monte Carlo* simulations as a more detailed statistical methodology, by adding cluster temperature information, and by testing a larger variety of cosmological models. These include e.g. the analysis of the total neutrino mass and of the influence of the applied scaling relation on the cosmology results. The experiences and results obtained from these forecasts will allow for an improved approach in the reduction of the future data and for a more accurate interpretation of the cosmological results.

CHAPTER 3

Applied Software and Statistical Methodologies

Having discussed the theoretical background for studying cosmology with the help of galaxy clusters, this chapter now focuses on the methodologies and the necessary statistics for completing these projects. To forecast the precision of the observed ICM temperatures, we introduce the simulation of galaxy cluster spectra (Sect. 3.1) as well as the applied software to produce *eROSITA* event files (Sect. 3.2). For the cosmological predictions, we describe the underlying theoretical considerations (Sect. 3.3 & 3.4) and the software package *COSMOMC* (Lewis & Bridle 2002) (Sect. 3.5).

3.1 The Concepts of Simulating X-ray Spectra

The X-ray spectra simulated in the process of this work are produced by the software *xspec* (Arnaud 1996) version 12.7.0, which is a commonly applied tool in high energy astrophysics and is included within the *HEASARC* (*High Energy Astrophysics Science Archive Research Center*) package. *xspec* contains models for different X-ray emission processes and allows to perform fits of these emission models to spectral data. The models and their characteristics, which are relevant for the work of this thesis are presented below with an extended description stated in the *xspec* manual[10].

3.1.1 Applied Emission Models

The following emission models describe the spectra of galaxy clusters as well as the X-ray background observed by the *eROSITA*-instrument.

- **apec:** The apec model (Smith et al. 2001) defines the emission of a hot, collisionally-ionised, and optically thin plasma, such as e.g. the ICM of galaxy clusters. The model thus includes bremsstrahlung emission, line emission by highly ionised metals, and recombination emission as free electrons are re-captured by these heavy ions. The apec model is parametrised as:

[10] The manual of the most recent *xspec* version is located at *https://https://heasarc.gsfc.nasa.gov/xanadu/xspec/manual/XspecSpectralFitting.html*.

plasma temperature	in [keV]
metal abundance	in solar abundances $A_\odot$
redshift z	
normalisation	$\frac{10^{-14}}{4\pi[D_A\cdot(1+z)]^2}\int n_e n_H dV$, with the angular diameter distance D_A in [cm], n_e and n_H as electron and hydrogen number densities, respectively, in [cm^{-3}]; the normalisation is given in the units [photons/cm^{-5}] for a defined FoV and is directly proportional to the luminosity of the emitting object.

- **phabs:** This is a multiplicative spectral component, which describes absorption by neutral gas along the line of sight

$$phabs(E) = \exp[-N_H \cdot \sigma(E)] \tag{3.1}$$

with a dependence on the photon energy E. The parameters $\sigma(E)$ and N_H represent the photo-electric cross-section and the hydrogen column density in units of [10^{22} atoms/cm^2], respectively. The column density of hydrogen is taken as a measure of the amount of neutral gas along the line of sight, as the absorption of X-rays is dominated by heavy elements. Accordingly, N_H is the main parameter to define this spectral model.

- **powerlaw:** The powerlaw is an additive spectral component and follows the correlation

$$powerlaw(E) = K \cdot E^{-\Gamma} \quad , \tag{3.2}$$

with the variable parameters

spectral index Γ	
normalisation K	in [photons/keV/cm^2/s] at 1 keV.

Powerlaw spectra in X-rays are e.g. observed for the inverse Compton or synchrotron emission of AGN, which partially cannot be resolved by X-ray instruments and thus generate a background signal.

3.1.2 Accounting for the Instrumental Response

The observed spectra are always a convolution of the emission of the source with the observational response of the instrument, which includes its energy and spatial resolution, as well as its effective area (Fig 2.11). This resolution and sensitivity information is stored in the instrumental *response file* (*RSP*), which thus expresses the probability that a photon with a certain energy E is detected in an energy band I. Followingly, the number of observed photons $\eta(I)$ is computed as (Arnaud et al. 2011)

$$\eta(I) = \int_0^\infty f(E) \cdot RSP(I,E)\, dE \quad , \tag{3.3}$$

with the spectrum $f(E)$ of the source in units of [photons/s/keV].
The RSP itself is composed of the *response matrix file* (*RMF*), which stores the energy-dependent energy resolution of the instrument, and the *ancillary response file* (*ARF*) to define the spatial instrumental sensitivity across the field-of-view.
Fig. 3.1 displays two simulated galaxy cluster spectra, modeled as a $phabs * apec$ emission and convolved with the *eROSITA*-RSP. The solid lines present the emission model, while the data points describe one realisation of this model, including statistical scatter in the photon counts. Additionally, the energy

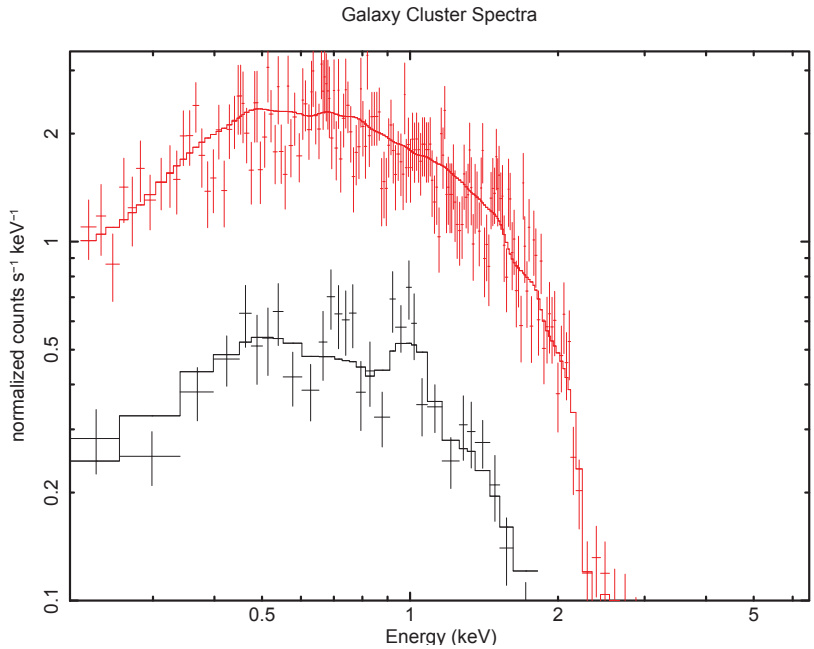

Figure 3.1: Simulation of two galaxy cluster spectra observed with *eROSITA*. The two clusters show different temperatures and redshifts of ($k_B T$ = 2.2 keV, z = 0.1) and ($k_B T$ = 9.8 keV, z = 0.3), respectively, while both clusters are absorbed by a galactic foreground of $N_H = 0.02 \cdot 10^{22}$ particles/cm^2. More details on the simulated clusters are described in Sect. 4.2.1

.

bins I are re-grouped to show at least 20 photons per energy bin for display purposes. Compared to Fig. 2.8, the black spectrum shows broadened emission lines, due to the finite instrumental energy resolution. At the same time, however, these lines are also intensified due to the increased effective area around energies of 1 keV. The drop in the intensity at the lower energy end emphasises the absorption processes by neutral gas. Concluding, the characteristics of the instrumental response are imprinted in the observed spectra and need to be accounted for in the analysis of this data.

3.2 Simulating *eROSITA* Event Files

Moving a step further towards a more realistic consideration of the *eROSITA* data, spectra are no direct observable and the observed data will initially be stored in so-called event files. These contain the information on all detected photons, including e.g. their individual energies, the coordinates of their origin and the time of their detection. During the future data analysis, the cluster spectra are extracted from these files. As no event files are available for this telescope, yet, studying the characteristics of these files and the methodology of extracting the spectra requires the simulation of these event files. This is accomplished by applying the software packages *SIXTE* by C. Schmid for the simulation(Schmid, C. 2008; Schmid 2012) as well as *eSASS*[11] (*extended Science Analysis Software System*) by H. Brunner for the spectral extraction. This approach thus allows for the simulation, the identification and the correction of many detailed instrumental effects, which are not captured within common *xspec* simulations of cluster spectra.

[11] Further information on this software package is provided on the *eROSITA*-wiki web page, but is currently only accessible for members of the consortium: https://wiki.mpe.mpg.de/eRosita/EroCat.

3.2.1 The Tool *SIXTE*

Applying the software package *SIXTE*, a catalogue of objects and their characteristics is converted into an event file. The catalogue of sources needs to be stored in the so-called *SIMPUT*-format (*SIMulation inPUT*) (Schmid et al. 2013), which is based on the commonly used *FITS*-file format. To describe a source unambiguously, the *SIMPUT*-file contains the following information: the source position, its flux in a well-defined energy range, its mission-independent spectral information as well as its surface brightness profile.
Having defined the source catalogue as expressed above, the event file is produced by simulating the spatial as well as energetic distribution of observed photons in a generic *Monte Carlo* approach, which is based on a series of random number processes (comp. Sect. 3.4). These event files are strongly dependent on the characteristics of the considered instrument. Though *SIXTE* was especially developed for *eROSITA* predictions, instrumental responses of many other X-ray telescopes are implemented in the software as e.g. those of *XMM-Newton* or of *Athena*. On the whole, *SIXTE* allows for the simulation of pointed as well as of survey observations, where in the latter scenario additional information on the exposure maps of the observations are required. A detailed description of the procedures to simulate these event files is summarised in Appendix A.2.

3.2.2 The Tool *eSASS*

The software system *eSASS* is maintained within the German *eROSITA*-consortium under the responsibility of H. Brunner and it is currently developed to provide all necessary tools for the analysis of simulated as well as of future observed event files. These tasks include e.g. the calibration of events, the creation of images of the photon events, the computation of the exposure maps (comp. Fig. 2.12), the detection of sources in the distribution of photon events, as well as the extraction of source spectra. Many of these tools are still in the process of being completed and tested, such that we focused only on the task *SRCTOOL*, in order to investigate the systematics of this tool thoroughly and independent of the other tasks.
Given the instrumental characteristics, such as e.g. the ".rmf" and ".arf" files, as well as the centre position and region of the source, *SRCTOOL* extracts the source spectrum. Analogously, also the background spectrum is obtained for a specified region. For further analysis steps, these spectra are compatible with the file format required by *xspec*. Appendix A.3 expresses a detailed summary of the application of this tool.

3.3 Statistical Tools

Estimating temperatures and their precision from the *eROSITA* cluster spectra and especially forecasting cosmological constraints are based on a complex statistical framework. The following sections now describe how to determine the searched for information by fitting models to observed data.

3.3.1 Bayes Theorem

Let's assume, we have an observed data set of N data points for the observable x, which we inspect in dependence on a set of parameters y. We thus define the pairs (x_i, y_i) with $i \in [1, N]$. The expected relation between the set of parameters and the observable is defined by a model, which itself depends on M variables θ_j with $j \in (1, M)$ and $\Theta = (\theta_1, \theta_2, ..., \theta_M)$. Accordingly, we define

$$x_i(y_i) = x_i(y_i|\Theta) \quad , \tag{3.4}$$

where the observed value x_i for the parameter set y_i is based on the model and its parameters Θ. Given this relation between the observable and the model, there are two different schools in statistics: Frequentist and Bayesian. Following the Frequentist's way of thinking, there is a true set of model parameters, which results in the observed data. The probability for one specific event (x_i,y_i) is then defined by its occurrence in a set of trials. In Bayesian statistics, on the other hand, only the data is real and the model needs to be estimated from this data. Some model parameter values are more believable than others, depending on how well they reproduce the data and on the prior knowledge on these parameters. In this case, the probability with which the data is re-produced by the parameter set Θ defines the degree of believe of these model parameters. This belief is described by the *posterior probability distribution* $P(\Theta|x)$. Throughout this work, we follow the Bayesian approach and the so-called *Bayes' theorem* (e.g. Press et al. 2007)

$$P(\Theta|x) = \frac{P(\Theta)}{P(x)} \cdot P(x|\Theta) \quad . \tag{3.5}$$

The function $P(\Theta)$ represents the *prior* knowledge on the model Θ and thus e.g. includes the information which model parameter values can be excluded or whether some sets of these values are more expected than others. If a priory all possible parameter values are equally probable, this is referred to as *flat prior*. The *evidence* $P(x)$ normalises the posterior to unity for an integration over all possible model parameter combinations $\int \mathrm{d}\Theta\ P(x|\Theta) = 1$, such that

$$P(x) = \int \mathrm{d}\Theta\ P(\Theta) \cdot P(x|\Theta) \quad . \tag{3.6}$$

The third multiplier, $P(x|\Theta)$, is named the *likelihood* function and expresses the probability to re-obtain the observations x given a defined set of model parameter values Θ. Thus, to find the model which best describes the observations, the likelihood needs to be maximised. Those model values are accordingly considered as *maximum likelihood estimates*.

3.3.2 Gaussian and Poissonian Statistics

To describe the likelihood $P(x|\Theta)$ either a Gaussian or a Poissonian probability distribution are commonly applied, depending on the characteristics of the observed data set. The Gaussian function, or *normal* distribution, defines the distribution of random variables which are drawn independently from independent sets. Its functional form follows an exponential shape, multiplied over all data points i (e.g. Press et al. 2007)

$$P(x|\Theta) = \prod_i \frac{1}{\sqrt{2\pi\sigma_i^2}} \cdot \exp\left[-\frac{(x_i - \mu_i)^2}{2\sigma_i^2}\right] \quad , \tag{3.7}$$

where σ_i^2 describes the variance in the observed data point x_i, and $\mu_i = \mu_i(y_i|\Theta)$ represents the expected value given the model parameters Θ. For a best fit between observations and model parameters, the expression in the exponent needs to be minimised

$$\chi^2 = \sum_i \left(\frac{x_i - \mu_i}{\sigma_i}\right)^2 \quad . \tag{3.8}$$

For a fit with $\nu = N - M$ degrees of freedom, a result of $\chi^2 \approx \nu$ is expected at the maximum likelihood. Additionally, the χ^2-value is applied to estimate the uncertainty regions of the parameter values, where e.g. for a 2-dimensional credibility region, $\Delta\chi^2 = 2.3$ expresses the 1σ- or 68.27%-uncertainty region

and $\Delta\chi^2 = 6.18$ the 2σ- or 95.45%-uncertainty region.
In the case of correlated data points, the Gaussian statistics are extended to

$$\chi^2 = \sum_{ij}(x_i - \mu_i)C_{ij}^{-1}(x_j - \mu_j) \quad , \tag{3.9}$$

applying the covariance matrix $C_{ij} = \langle(x_i - \mu_i) \cdot (x_j - \mu_j)\rangle$ between the individual data points.
Analogous to the considerations above, a *log-normal* distribution is defined, in which the natural logarithm of the observable follows a Gaussian function

$$P(\ln x|\Theta) = \prod_i \frac{1}{\sqrt{2\pi\sigma_i^2}} \cdot \exp\left[-\frac{(\ln x_i - \ln \mu_i)^2}{2\sigma_i^2}\right] \quad . \tag{3.10}$$

The Poisson distribution, on the other hand, is usually applied for observables resembling a discrete small number of independent events, which are counted in a specified interval such as e.g. time or volume

$$P(x|\Theta) = \prod_i \frac{\mu_i^{x_i}}{x_i!} \exp[-\mu_i] \quad , \tag{3.11}$$

with the same notation as above. For large numbers in μ_i, this distribution approaches a Gaussian shape with $\sigma_i^2 = \mu_i$. Just as before, the maximum likelihood is found by minimising the following expression

$$-\ln[P(x|\Theta)] = \sum_i \left(\sum_{n=1}^{x_i} \ln n + \mu_i - x_i \cdot \ln \mu_i\right) \quad , \tag{3.12}$$

which is often referred to as the negative *log-likelihood*. When neglecting all constants, the equation above simplifies to

$$-\ln[P(x|\Theta)] = \sum_i (\mu_i - x_i \cdot \ln \mu_i) \quad . \tag{3.13}$$

Poisson statistics are especially preferred for photon counting experiments with a low number of photons per investigated bin as is the case of X-ray observations. In this example, x_i represents the observed number of photons in a specified energy bin, where μ_i gives the number of photons expected from the emission model and the instrumental response. Especially for these low photon counts experiments, the *Cash*-statistics and the corresponding *C*-parameter are derived based on Eq. 3.13 (Cash 1979)

$$C = -2 \cdot \ln[P(x|\theta)] = 2 \cdot \left(\mu - \sum_i (x_i \cdot \ln \mu_i)\right) \quad , \tag{3.14}$$

with $\mu = \sum_i \mu_i$. Accordingly, the *C*-parameter is the equivalent to the χ^2 in Gaussian statistics. As these statistics allow to analyse small number of events per bin, the bins may be defined reasonably small for an improved resolution, whereas for the application of the χ^2-statistics several bins need to be merged to yield sufficient events. Unlike the χ^2-value, however, a *C*-value cannot be interpreted as direct indicator of the uncertainty level. Accordingly, the χ^2-statistics are generally considered in the limit of large number of photon counts or large number of events (e.g. Humphrey et al. 2009).

3.4 The Concepts of *Markov-Chain Monte Carlo* Simulations

In practice, the maximum likelihood as well as the uncertainty on the maximum likelihood estimates are often obtained in *Markov-Chain Monte Carlo* (*MCMC*) simulations. Thereby, the expression *Monte Carlo* generally refers to a computer algorithm, which is based on a series of random numbers, and which was first derived by Enrico Fermi in the 1930s and by Stanislaw Ulam in 1947. The *Markov-Chain* defines a sequence of random variables, in which the subsequent variable value only depends on the present position and not on the past values. Within these simulations the likelihood is computed for various different combinations of model parameter values Θ. In the end, the procedure converges towards those model parameters, which yield the maximum likelihood. The statistics behind these simulations as well as the algorithms, applied to obtain convergence, are explained in the following sections in detail. A description of the statistical aspects is also given by e.g. Press et al. (2007).

3.4.1 The Statistics in *MCMC*

To find the maximum of the likelihood function $P(x|\Theta)$, or of the probability for the model parameters Θ to re-produce the data sample x, we define a M-dimensional parameter space for the M model parameters. Starting at an arbitrary point $\Theta_1 = (\theta_{1,1}, \theta_{1,2}, ..., \theta_{1,M})$, the likelihood $P(x|\Theta_1)$ is computed for this first set of model parameter values. Thereafter, we step to a second point Θ_2 and compute the corresponding likelihood $P(x|\Theta_2)$, where the step to this second parameter set is defined by the *proposal distribution* $q(\Theta_2|\Theta_1)$. Usually, this proposal distribution is described as a log-normal function, which is symmetric around Θ_1, but most importantly, the distribution depends only on the current position Θ_1 and not on the previous steps. The sequence of steps between the parameter sets is referred to as *chain*. Having stepped to Θ_2, we need to decide whether to accept this new point. For this, we consider the *acceptance probability*

$$\alpha(\Theta_2|\Theta_1) = \min\left\{1, \frac{P(x|\Theta_2)}{P(x|\Theta_1)}\right\} \quad , \tag{3.15}$$

where symmetric proposal distributions of $q(\Theta_2|\Theta_1) = q(\Theta_1|\Theta_2)$ are assumed. Based on the value of the acceptance probability, different algorithms are available to decide whether to accept the new step. Due to the algorithms, the chains will eventually move to the region of highest probability and cluster in this part of the parameter space.

3.4.2 The Metropolis-Hastings Algorithm

The sampler we apply in our *MCMC*-simulations is the *Metropolis-Hastings Algorithm*. The individual steps within this sampling to decide on the acceptance of a new parameter point are summarised as

1. Compute the acceptance probability α of Θ_2 according to Eq. 3.15.
2. Generate a random number r from a uniform distribution of $(0, 1)$.
3. Compare r to α.
   - If $\alpha > r$, Θ_2 is accepted and taken as the starting point of a new step Θ_3.
   - If $\alpha < r$, Θ_2 is rejected and the sampler steps back to Θ_1 to find a new point Θ_2.

Following this acceptance strategy, parameter sets with a higher likelihood than the previous step are always accepted, whereas those with a lower likelihood still have a chance to be accepted. These

sampling steps are then repeated for each new chain step and gradually direct the chain towards the parameter space of the highest likelihood. Due to this sampling strategy, the number of accepted points increases with an increasing likelihood, such that the density of the chain steps increases towards the peak of the maximum likelihood estimates.

3.4.3 Computing Parameter Uncertainties

As the *MCMC*-chains step towards the parameter space of highest likelihood, this region is thus characterised by the highest density of chain steps and the maximum likelihood estimates are represented by the mean of all steps. The uncertainty on these estimates is then described by the distribution of the chain steps, which also represents the posterior distribution (Fig. 3.2). This uncertainty region is also referred to as *credibility interval*, following the Bayesian approach. A credibility level of e.g. 68% between the parameter limits Θ_A and Θ_B expresses, that this percentage of the chain steps is located between the two limits.
To define these intervals for certain percent levels, we need to integrate over the distribution of chain steps in the M-dimensional parameter space. The integration boundaries need to be set such, that the volume of the region, containing the defined percentage of steps, is minimised. Computing but also displaying this credibility interval becomes more complex with an increasing number of parameters M. For $M = 1$, the credibility interval is unambiguously defined by an upper and a lower boundary value of the only model parameter θ_1, whereas for $M = 2$ already a 2-dimensional contour in parameter space needs to be described (comp. Fig. 3.2). As we fail to plot M-dimensional credibility contours effectively for $M > 3$, we *marginalise* the posterior distribution over all additional parameters. The marginalisation is realised by an integration of the likelihood over those additional parameters as

$$P(\theta_1|x) = \int P(x|\Theta)\mathrm{d}\theta_2\mathrm{d}\theta_3...\mathrm{d}\theta_M \tag{3.16}$$

$$P(\theta_1,\theta_2|x) = \int P(x|\Theta)\mathrm{d}\theta_3...\mathrm{d}\theta_M \tag{3.17}$$

for a 1-dimensional and a 2-dimensional credibility region, respectively. These mariginalised uncertainty regions then need to be computed for all of the M parameters or for all pair combinations.
However, in practice, there are several additional aspects that need consideration.

3.4.4 Further Aspects of Running *MCMC*-Simulations

To thoroughly explore the region of highest likelihood, commonly several chains are run in parallel, but completely independent from one another - they do not communicate their positions and the step to the next point is not influenced by the positions of the other chains. An excerpt of a chronological stepping sequence for multiple chains is displayed in Fig. 3.3, together with several further aspects which need to be considered in *MCMC* simulations.

Burn-in: As the chains start from an arbitrary initial point Θ_1, several steps are needed to reach the parameter space of highest likelihood, where the chains then start scattering around the maximum likelihood estimates. The first steps towards this region of interest are referred to as *burn-in* and need to be rejected for the analysis of the chains. In Fig. 3.3, the first $\sim 2,500$ steps, which is $\sim 10\%$ of the total chain, describe the burn-in. Thereafter, the chains start to scatter around the maximum likelihood at $\Omega_m = 0.28$. However, the percentage of burn-in steps depends on the simulation and needs to be chosen

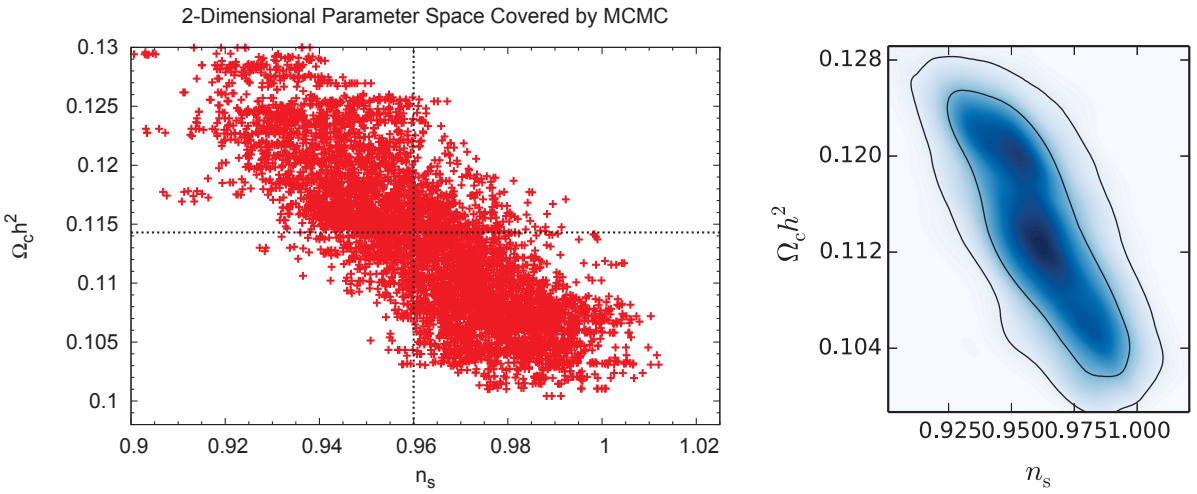

Figure 3.2: *Left:* Distribution of *MCMC*-chain steps in the parameter space $\{n_s, \Omega_c h^2\}$ for a ΛCDM-simulation and for a simultaneous fit of the variables $\{\sigma_8, \Omega_m, n_s, h, \Omega_b\}$. The dotted black lines represent the true values of the applied cosmology. More details on this simulation are presented in chapter 6.6.1. *Right*: Credibility intervals of the 68.27%- as well as of the 95.45%-level as black contours, corresponding to the distribution of steps displayed in the left panel. The blue background describes the density of chain steps with a higher density being represented by a darker shade.

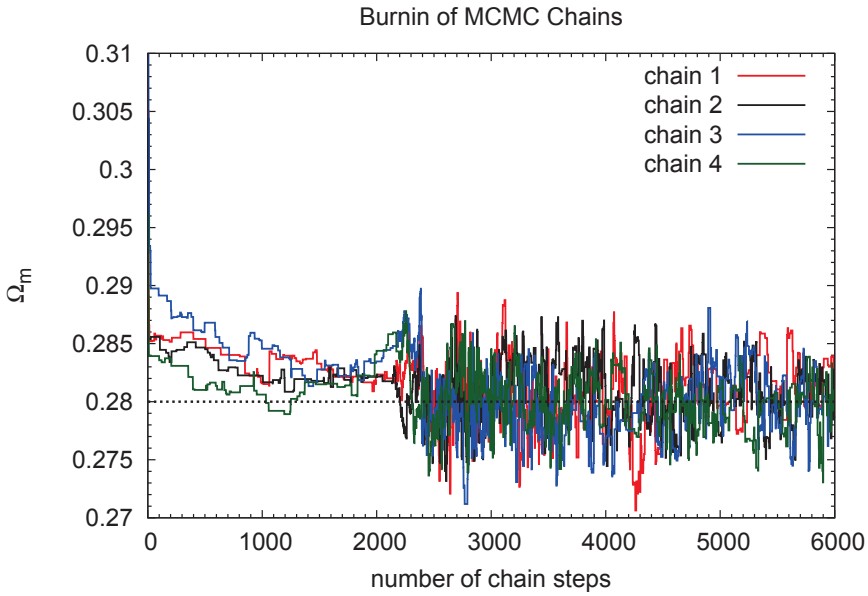

Figure 3.3: Excerpt of an example chronological sequence of *MCMC* steps in Ω_m for four parallel chains and a simulation for a ΛCDM-cosmology with $\Omega_m = 0.28$ (black dotted line). The first $\sim 2,500$ steps of the chains are considered as *burn-in* and need to be rejected for the analysis.

such, that it does not influence the computed credibility regions or the maximum likelihood estimates values.

Mixing: The length between steps in the chains is drawn from the proposal distribution $P(\Theta)$ (comp. Sect. 3.3.1), where the width of this distribution needs to be adapted to the width of the credibility region. For a too narrow proposal distribution and thus for too small steps, most of the steps are accepted, but the chains do not explore the parameter space of interest within a reasonable time. On the other hand, for a too broad proposal distribution, the chains frequently propagate out of the region of maximum likelihood, such that only few steps are accepted and the actual credibility region is explored poorly. The term *mixing* describes how well the Markov-Chains explore the posterior distribution. Accordingly, the width of the posterior distribution $P(\Theta|x)$ either needs to be investigated in a test *MCMC* run to obtain a reliable estimate or the proposal distribution needs to be up-dated during the run. The latter approach is also followed by our simulations, which partially explains the change in the step widths and the relative variations in the parameter values after the burn-in.

Convergence Criteria: As soon as the chains start to survey the posterior distribution in the parameter space, several different criteria exist to decide whether the chains converged to a maximum likelihood region. In the case of a single chain, convergence is e.g. investigated by comparing especially the chain means for different chain lengths. This is also known as the *Geweke*-criterium. For simulations with multiple chains, we test whether all chains, having started at different initial points, find the same target distribution. Within the *Gelman-Rubin*-criterium, the ratio

$$R = \frac{\text{variance of chain means}}{\text{mean of chain variances}} = \frac{\sigma(\langle\Theta\rangle)}{\langle\sigma(\Theta)\rangle} \tag{3.18}$$

is computed for the second half of the chains. Following this criterium, a value of $R = 0.2$ is commonly applied, where this value as well as the ratio in the *Geweke*-criterium, depends on the requested accuracy. When the defined convergence is met, the chain means and the credibility intervals are obtained from the posterior distribution as expressed in Sect. 3.4.3.
For our simulations, we generally run four parallel chains and define the state of convergence similar to the *Geweke*-criterium, while computing the mean and the credibility intervals for the combination of all chains, excluding the burn-in. As soon as the deviation of these to properties between different chain lengths drops below 1%, the chains are considered to be converged (Sect. 6.8.1).

3.5 An Introduction to *COSMOMC*[12]

The publicly available software package *COSMOMC* (Lewis & Bridle 2002) includes the *MCMC* approach for the analysis and forecasts of cosmological studies. Many data sets as well as their likelihoods, such as e.g. for *Planck*, for the *Hubble Key Project* or for supernovae type Ia surveys, as well as cosmological tools, such as *CAMB* (Lewis et al. 2000), are already implemented in this programme. When adding your own data set and likelihood function to this software package, you are able to apply the *MCMC* simulator and the implemented tools also on your own data as well as to compute joint credibility regions of your data set and the data stored in the package. In general, *COSMOMC* can be modified to the individual requirements of the user and includes a large variety of different application options.
The parameterisation is defined such, that the different parameters show close to Gaussian posterior

[12] Detailed information on this programme are summarised in the *COSMOMC*-readme at *http://cosmologist.info/cosmomc/readme.html*

distributions to optimise the performance of the MCMC simulations. Those parameters, important for our studies, are (comp. Tab. 2.1)

$\Omega_b h^2$	present baryon density, normalised by the Hubble paramter
$\Omega_c h^2$	present cold dark matter density, normalised by the Hubble paramter
θ	the angular size of the sound horizon at the era of recombination
w_0	normalisation of the dark energy equation of state, following Eq. 2.18
w_a	time evolution of the dark energy equation of state, following Eq. 2.18
n_s	scalar spectral index of the linear matter power spectrum (comp. e.g. Eq. 2.33)
$\log A$	$\equiv \ln[10^{10} \cdot A]$, with the amplitude A of the linear matter power spectrum (comp. e.g. Eq. 2.33).

Other commonly studied cosmological parameters, such as e.g. H_0, Ω_m or σ_8, are derived from these initial parameters within the programme.
What is more, also the evaluation of the generated chains, including the computation as well as the plotting of up to 3-dimensional credibility regions, can be executed within *COSMOMC*.

CHAPTER 4

Constraining Galaxy Cluster Temperatures and Redshifts with *eROSITA* Survey Data

This chapter presents the first project of my thesis on the observational power for cluster temperatures and redshifts with the *eROSITA* survey data. Apart from minor adaptations to the context of this thesis, the following sections have been published as Borm et al. (2014) (bibliographic code: 2014A&A...567A..65B) with the journal *Astronomy & Astrophysics*. The theoretical aspects explained in Sect. 4.1 are a summary of the discussions especially in Sect. 2.7, 2.8 & 2.9.

Abstract

The nature of dark energy is imprinted in the large-scale structure of the Universe and thus in the mass and redshift distribution of galaxy clusters. The up-coming *eROSITA*-instrument will exploit this method of probing dark energy by detecting $\sim 100,000$ clusters of galaxies in X-rays.
For a precise cosmological analysis the various galaxy cluster properties need to be measured with high precision and accuracy. To predict these characteristics of *eROSITA* galaxy clusters and to optimise optical follow-up observations, we estimate the precision and accuracy with which *eROSITA* will be able to determine galaxy cluster temperatures and redshifts from X-ray spectra. Additionally, we present the total number of clusters for which these two properties will be available directly from the *eROSITA* survey.
We simulate the spectra of galaxy clusters for a variety of different cluster masses and redshifts while taking into account the X-ray background as well as the instrumental response. An emission model is then fitted to these spectra to recover the cluster temperature and redshift. The number of clusters with precise properties is then based on the convolution of the above fit results with the halo mass function and an assumed *eROSITA* selection function.
During its four years of all-sky surveys, *eROSITA* will determine cluster temperatures with relative uncertainties of $\Delta T/T \lesssim 10\%$ at the 68%-confidence level for clusters up to redshifts of $z \sim 0.16$, which corresponds to $\sim 1,670$ new clusters with precise properties. Redshift information itself will become available with a precision of $\Delta z/(1+z) \lesssim 10\%$ for clusters up to $z \sim 0.45$. Additionally, we estimate the increase in the number of clusters with precise properties that is achieved by a deepening of the exposure.
For these clusters, the fraction of catastrophic failures in the fit is below 20% and in most cases even much lower. Furthermore, the biases in the best-fit temperatures as well as in the estimated uncertainties are quantified and shown to be in general negligible in the relevant parameter range. For the remaining

parameter sets, we provide correction functions and factors. In particular, the standard way of estimating parameter uncertainties significantly underestimates the true uncertainty, if the redshift information is not available.
In conclusion, the *eROSITA* survey will increase the current number of galaxy clusters with precise temperature measurements by a factor of $5 - 10$. Thus, the instrument presents itself as a powerful tool for determining tight constraints on the cosmological parameters. At the same time, this sample of clusters will extend our understanding of cluster physics, for instance through precise $L_X - T$ scaling relations.

4.1 Introduction

Over the past years, galaxy clusters have become reliable cosmological probes for studying dark energy and for mapping the large-scale structure (LSS) of the Universe (e.g., Borgani & Guzzo 2001; Voit 2005; Vikhlinin et al. 2009a,b; Mantz et al. 2010a; Allen et al. 2011). Further improved constraints on the nature of dark energy require the analysis of a large sample of galaxy clusters with precisely and accurately known properties. The future *eROSITA* (**e**xtended **Ro**entgen **S**urvey with an **I**maging **T**elescope **A**rray) telescope (Predehl et al. 2010; Merloni et al. 2012), which is scheduled for launch in early 2017, will provide such a data sample (Pillepich et al. 2012).
X-ray observations of galaxy clusters allow for the precise determination of various cluster properties such as the total mass as well as the gas mass of the cluster or the temperature and the metal abundance of the intra-cluster medium (ICM) (e.g. Henriksen & Mushotzky 1986; Sarazin 1986; Vikhlinin et al. 2009a). The information on these properties is imprinted in the emission spectrum of the ICM, which follows a thermal bremsstrahlung spectrum superimposed by emission lines of highly ionised metals (e.g., Sarazin 1986). Especially notable are the Fe-L and the Fe-K line complexes at energies of ~ 1 keV and ~ 7 keV, respectively. For low gas temperatures of $k_B T \lesssim 2.5$ keV, emission lines are prominent features in the spectrum in the energy range of roughly $(0.5 - 8)$ keV. With increasing temperatures the lines at the lower energies fade as the metals become completely ionised, whereas other emission lines, such as the hydrogen-like Fe-K line, increase with higher gas temperatures (e.g., Fig. 2 in Reiprich et al. 2013). Analogously to the temperature, the spectrum also reflects the density and metallicity of the ICM, as well as the cluster redshift, which allows these properties to be recovered in the analysis of X-ray data. While very precise redshifts with uncertainties of $\Delta z \ll 0.01$ can be obtained in optical spectroscopic observations, estimating redshifts from X-ray data directly allows for an optimisation of these time-consuming optical spectroscopic observations.
Cosmological studies based on galaxy clusters are especially dependent upon the information on their redshift and total mass. As the cluster mass is not a direct observable, galaxy cluster scaling relations are commonly applied to estimate this property based for example on the ICM temperature and the cluster redshift (e.g., Vikhlinin et al. 2009a; Pratt et al. 2009; Mantz et al. 2010a; Reichert et al. 2011; Giodini et al. 2013). This then allows for an analysis of the distribution of galaxy clusters with mass and redshift. This halo mass function traces the evolution of the large-scale structure (LSS) and is highly dependent on the cosmological model, implementing galaxy clusters as cosmological probes (e.g., Press & Schechter 1974; Tinker et al. 2008). Testing the cosmological model through the study of the halo mass function has become an important method in the past years (e.g., Reiprich & Böhringer 2002; Voit 2005; Vikhlinin et al. 2009a,b; Mantz et al. 2010a). This analysis methodology is not only based on X-ray obervations, but can also be applied to *Sunyaev-Zel'dovich* (SZ) observations of galaxy clusters. Current SZ cluster surveys, performed for example by the *Atacama Cosmology Telescope* (ACT), the *South Pole Telescope* (SPT) and *Planck*, are increasing the impact of these observations and already led

to an improvement in constraining the cosmological parameters (e.g. Vanderlinde et al. 2010; Planck Collaboration et al. 2013; Reichardt et al. 2013). Additionally, a combination of SZ and X-ray observations allows for the calibration of hydrostatic cluster masses, which in turn improves the cosmological constraints. The *eROSITA* instrument will soon improve the data sample of available X-ray clusters in terms of precision, accuracy, and number of clusters. This sample will thus especially allow for optimised cosmological studies by means of X-ray galaxy clusters. As a side effect, future SZ observations will profit from this cluster sample as well.
eROSITA is the German core instrument onboard the Russian Spektrum-Roentgen-Gamma (SRG) satellite, which is scheduled for launch in early 2017 (Predehl et al. 2010; Merloni et al. 2012). The main science driver of this mission is studying the nature of dark energy. The first four years of the mission are dedicated to an all-sky survey, followed by a pointed observation phase, both in the X-ray energy range between (0.1 − 10) keV. Within the all-sky survey, a conservatively estimated effective average exposure time of $t_{\mathrm{exp}} = 1.6$ ks is achieved, and we expect to detect a total of $\sim 10^5$ galaxy clusters, including basically all massive clusters in the observable Universe with $M \gtrsim 3 \times 10^{14} h^{-1}\ \mathrm{M}_\odot$ (Pillepich et al. 2012). For these calculations a minimum of 50 photon counts within the energy range of 0.5 − 2.0 keV is assumed for the detection of a cluster. With this predicted data sample, current simulations estimate an increased precision of the dark energy parameters to $\Delta w_0 \approx 0.03$ (for $w_{\mathrm{a}} = 0$) and $\Delta w_{\mathrm{a}} \approx 0.20$ (Merloni et al. 2012, Pillepich et al., in prep.), assuming an evolution of the equation of state of dark energy with redshift as $w_{\mathrm{DE}} = w_0 + w_{\mathrm{a}}/(1 + z)$.
These forecasts consider only the galaxy cluster luminosity and redshift to be known with an assumed uncertainty, whereas the precision on the cosmological parameters will be improved if additional cluster information, such as the ICM temperature, is available (compare e.g., Clerc et al. 2012). In this work we thus present how accurately and precisely *eROSITA* will be able to determine the ICM temperature in dependence on the cluster masses and redshifts. In an analogous simulation, we investigate for which clusters the survey data will allow for a redshift estimate to optimise optical follow-up observations (compare e.g., Yu et al. 2011).
The outline of this chapter is as follows: in Sect. 4.2, we define the properties of the clusters included in our simulations. We also introduce the applied model for the X-ray background and the simulation and analysis methods. The following section presents the predicted precisions and accuracies for the cluster temperatures and redshifts, while Sect. 4.4 emphasises the number of clusters for which precise properties will be available from *eROSITA* data. The final two sections, 4.5 and 4.6, contain the discussion and conclusion of this work.
If not stated otherwise, we apply a fiducial cosmology of $H_0 = 100 \cdot h$ km/s/Mpc with $h = 0.7$, $\Omega_{\mathrm{m}} = 0.3$, $\Omega_\Lambda = 0.7$, $\sigma_8 = 0.795$ and the solar metallicity tables by Anders & Grevesse (1989).

4.2 Simulation Method and Analysis

The predictions for the cluster temperatures and redshifts are based on the analysis of galaxy cluster spectra, for which we applied the software ***xspec*** (Arnaud (1996); comp. also Sect. 3.1) version 12.7.0. To simulate the spectra, the cluster temperature, its luminosity, its redshift, its metallicity, and the foreground absorption need to be known, as well as the background emission observed by *eROSITA* and the instrumental response (RSP) of the detector. The RSP applied in our simulations contains the combined resolution of all seven telescopes averaged over the entire field-of-view ("erosita_iv_7telfov_ff.rsp").

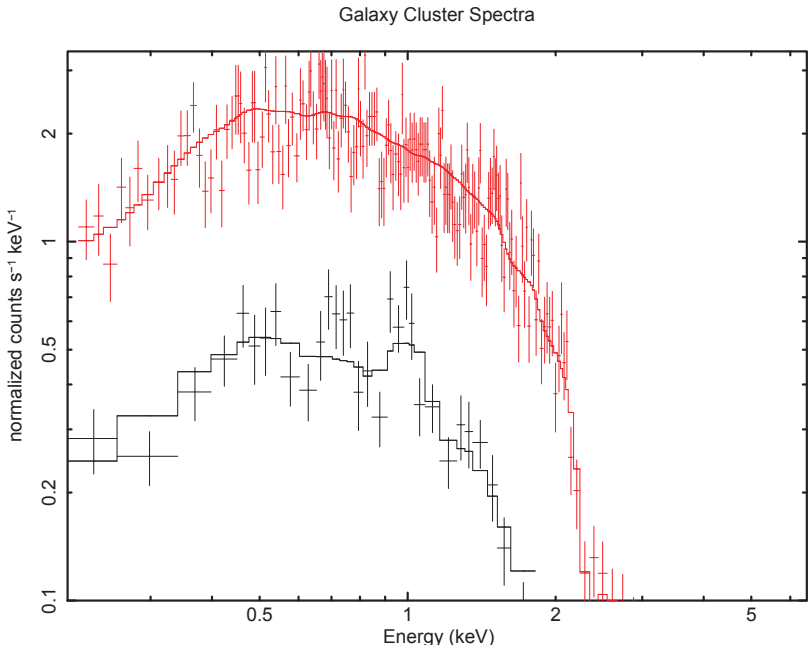

Figure 4.1: Simulated spectra of a galaxy cluster with $M_{500} = 10^{14}\,\mathrm{M}_\odot$ (black), $k_B T = 2.2$ keV, and with $M_{500} = 10^{15}\,\mathrm{M}_\odot$ (red), $k_B T = 9.8$ keV, respectively. The spectra are simulated for a redshift of $z = 0.1$ and $z = 0.3$, respectively, and for an exposure time of $t_{\mathrm{exp}} = 1.6$ ks. The model emission convolved with the instrumental response (continuous line) as well as the simulated emission (data points) are presented. For the simulated emission the energy bins are regrouped to yield at least 20 photons per group for display reasons.

4.2.1 Cluster Properties

For the clusters included in our simulations, we defined the total mass M_{500} and redshift z within the ranges of $13 \leqslant \log(M/\mathrm{M}_\odot) \leqslant 15.7$ and $-2 \leqslant \log(z) \leqslant 0.25$ in logarithmic steps of 0.15, which is equivalent to $10^{13} \leqslant M/\mathrm{M}_\odot \leqslant 5 \times 10^{15}$ and $0.01 \leqslant z \leqslant 1.78$, respectively. Based on these two input parameters, the remaining cluster properties were estimated through galaxy cluster scaling relations (comp. Sect. 2.7.3), where we applied the findings by Reichert et al. (2011).

$$T \quad [\mathrm{keV}] \quad = \quad \left(\frac{M}{10^{14}\,\mathrm{M}_\odot} \cdot 3.44 \right)^{0.62} \cdot E(z)^{0.64} \tag{4.1}$$

$$L_{\mathrm{X}} \quad [10^{44}\mathrm{erg/s}] \quad = \quad \left(\frac{M}{10^{14}\,\mathrm{M}_\odot} \cdot 0.61 \right)^{1.92} \cdot E(z)^{1.7} \quad , \tag{4.2}$$

with the bolometric luminosity L_{X} measured in the energy range between $(0.01 - 100)$ keV and the redshift evolution

$$E(z) = [\Omega_{\mathrm{m}}(1+z)^3 + \Omega_\Lambda]^{1/2} \quad . \tag{4.3}$$

This scaling relation is the most conservative approach for high-redshift clusters when compared to other works, for instance Vikhlinin et al. (2009a) and Pratt et al. (2009) (see Sect. 4.5). Note that we neglected the intrinsic scatter in the scaling relations for our simulations to only focus on the performance of the instrument. However, to compute the cosmological parameters by means of galaxy cluster data, this intrinsic scatter needs to be taken into account.
Throughout all simulations, the cluster metallicity was set to $A = 0.3\,\mathrm{A}_\odot$, which is a commonly observed

value for nearby clusters (e.g. Arnaud et al. 1992; Mushotzky & Loewenstein 1997). Even though an evolution of the metallicity with redshift was observed, it could not be definitely quantified yet (Balestra et al. 2007; Maughan et al. 2008; Baldi et al. 2012), and we thus preferred to apply the constant metallicity stated above. For a more detailed treatment of this evolution, we include a discussion of the effect of an abundance evolution with redshift in Sect. 4.5.2. At the same time, we assumed the absorbing column density to be $N_{\rm H} = 3{\times}10^{20}$ particles/cm^2 as typical value for regions at galactic latitudes of $b \gtrsim 20°$ (Kalberla et al. 2005), which are relevant for the *eROSITA* cluster survey. Figure 4.1 presents two example galaxy cluster spectra simulated as an absorbed thermal emission (Smith et al. 2001) **phabs*apec**, convolved with the *eROSITA* response. All clusters are simulated to show an isothermal emission.
Furthermore, the simulations focused on clusters with fluxes below the *eHIFLUGCS* limit of 9×10^{-12} erg/s within the energy range of $(0.1-2.4)$ keV (Schellenberger et al., in prep.). All clusters in this complete all-sky sample have high-quality *Chandra* and/or *XMM* observations and, therefore, temperatures and redshifts are known. For clusters below this flux lumit no precise and accurate properties are usually available. At the same time, only clusters with a minimum of 100 detected photons by *eROSITA* in the energy range of $(0.3-8)$ keV were considered to ensure a stable performance of the applied software. What is more, no reliable temperature and redshift measurements are expected for clusters with this low number of source events.
Even though the angular extension of the cluster does not define its over-all spectral emission, the extension is essential for the simulation of the X-ray background as the background normalisation is proportional to the observed region. The angular extension of the galaxy cluster is determined as α_{500} in dependence on the cluster mass and redshift

$$M_{500} = \frac{4\pi}{3}\rho_{\rm crit}(z) \cdot 500 \cdot R_{500}^3 \tag{4.4}$$

$$\alpha_{500} = \frac{R_{500}}{D_{\rm A}(z)} \quad , \tag{4.5}$$

applying the critical density $\rho_{\rm crit}$ and the angular diameter distance $D_{\rm A}$

$$\rho_{\rm crit} = \frac{3H(z)^2}{8\pi {\rm G}} \quad \text{with} \quad H(z)^2 = H_0 \cdot E(z)^2 \tag{4.6}$$

$$D_{\rm A}(z) = \frac{c}{H_0(1+z)} \int_0^z E(z)^{-1} \quad {\rm d}z \quad . \tag{4.7}$$

4.2.2 *eROSITA* X-ray Background

The background, observed by *eROSITA*, was simulated following the modelled emission

$$\underbrace{\textbf{phabs}}_{1} * (\underbrace{\textbf{powerlaw}}_{2} + \underbrace{\textbf{apec}}_{3} + \underbrace{\textbf{apec}}_{4}) + \underbrace{\textbf{powerlaw}}_{5} \quad .$$

The different components include 1) the absorption by the neutral gas in our Galaxy, 2) the unresolved cosmic X-ray background, that is distant AGN, 3) the plasma emission by the hot ISM and 4) the emission by supernova remnants in our Galaxy, as well as 5) the particle background. The first four components are defined by Lumb et al. (2002) and express the cosmic X-ray background, whereas the particle background is estimated by Tenzer et al. (2010). The instrumental background was included in the particle background and since the *eROSITA* detectors will be equipped with a graded-Z shield, we do not expect to observe a significant component of fluorescent emission lines. Additionally, the influence of bad and hot pixels was assumed to be negligible. The individual values for the model are presented

Table 4.1: Model values of the *eROSITA* background. The numbering of the components is equivalent to the numbering in the model definition (Sect. 4.2.2). The units of the individual model parameters are as follows: $[N_{\rm H}]= 10^{22}$ particles/cm^2 and $[{\rm k_B}T]$=keV. The normalisations are given for an *eROSITA* field-of-view of 0.83 deg^2 with the units [norm]=photons/keV/cm^2/s at 1 keV for the powerlaw and [norm]=photons/cm^5 for the apec model.

Component	Parameter	Model Value
1	$N_{\rm H}$	1.7×10^{-2}
2	photon spectral index	1.42
2	norm	0.0028
3	${\rm k_B}T$	0.204
3	norm	0.0019
4	${\rm k_B}T$	7.4×10^{-2}
4	norm	0.029
5	photon spectral index	0.0
5	norm	0.29

in Table 4.1, where all components except the particle background are convolved with the instrumental RSP. This background model is the default for the *eROSITA* instrument and is also described by Merloni et al. (2012).
Figure 4.2 provides an illustration of the background spectrum, which is dominated by the particle background for energies above $\sim$ 2 keV. When observed over the entire *eROSITA* field-of-view (FoV) of 0.83 deg^2, the total background emission shows count rates of 12 cts/s within the energy range between (0.3 − 8) keV. For a commonly observed cluster of $M_{500} = 10^{14}$ M$_\odot$ ad $z = 0.1$ as simulated in Fig. 4.1, this background results in a signal-to-noise ratio of $S/N \approx 23.5$ and in a source-to-background ratio of 1.4.

4.2.3 Simulation Outline

To simulate the characteristics of *eROSITA* galaxy clusters the following methodology was applied:

1. For a given set of cluster mass and redshift, we simulate the total X-ray spectrum, which includes both the absorbed galaxy cluster emission itself as well as the background.

2. A model is fit to the simulated emission. However, before the fitting procedure, we define the background emission, such that this emission is removed from the above spectrum during the fit and only the model of an absorbed cluster emission needs to be adjusted to the remaining spectrum. The fit then determines the best fit values of the cluster temperature and redshift.

3. To obtain a proper statistical distribution of these best-fit values, steps 1.) - 3.) are repeated 300 times for each parameter set.

For the simulations we defined two different exposure times $t_{\rm exp} = 1.6$ ks and $t_{\rm exp} = 20$ ks, which describe the effective average exposure time for *eROSITA* after its four years of all-sky surveys and the observation time of two deep-exposure fields at the ecliptic poles, respectively (Pillepich et al. 2012; Merloni et al. 2012). For the fitting we also follow two approaches, which assume the redshift either to be known, for example from optical follow-up observations, or that no redshift information is available yet. In the latter case, we introduced the redshift as variable parameter during the fit and determined

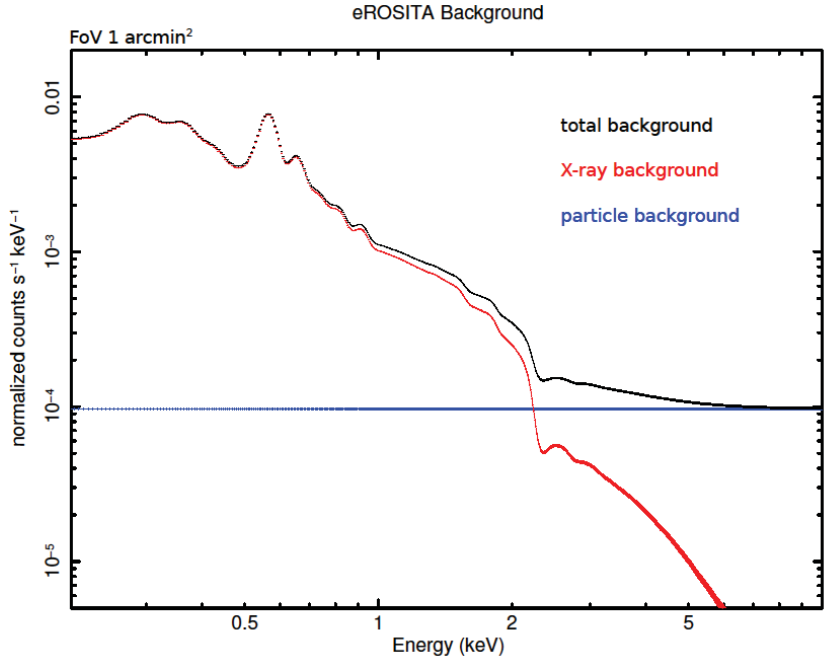

Figure 4.2: Spectrum of the *eROSITA* background for a FoV of 1 arcmin^2.

its value through the X-ray spectrum (e.g., Yu et al. 2011). These considerations yielded a total of four different simulations.
Throughout the different simulation steps, Cash statistics were applied (Cash (1979); comp. also Sect. 3.3.2) to ensure a good performance during the fit despite the small number of photons in each energy bin of the simulated spectra. To realise the total spectrum during the first step, we defined the exposure time and convolved the emission models of the cluster and background with the instrumental responses, where the background normalisation is rescaled to match the cluster extension (see Sect. 4.2.1). The spectrum was re-grouped to yield at least one photon count per energy bin, to avoid failures during the fit due to empty energy bins (compare Leccardi & Molendi 2007; Krumpe et al. 2008). In the next step, the background emission was defined by applying the `backgrnd`-command, such that this emission was removed during the final spectral fit. The procedures of normalising the background and employing the `backgrnd`-command are essential to account for the statistical scatter in the photon counts in the spectra. For this background model, we realistically assumed an exposure time of $t_{\rm exp} = 100$, while keeping the area fixed to the cluster extension. Finally, an absorbed apec emission model was fitted to the remaining spectrum within an energy range of (0.3 – 8) keV, which reflects the effective energy range of the *eROSITA* instrument (Merloni et al. 2012). During this simulation step, the cluster temperature and the normalisation of the spectrum, which is proportional to the emission measure

$$\mathrm{norm} = \frac{10^{-14}}{4\pi[D_{\rm A}(1+z)]^2} \int n_{\rm e} n_{\rm H} \mathrm{d}V \quad , \tag{4.8}$$

were recovered. In case of an unavailable cluster redshift, this property was also estimated in this step. To allow for the most accurate fit values to be obtained, we thoroughly inspected the more-dimensional space of the best-fit parameters for a global minimum in the goodness of the fit by applying the multi-dimensional `steppar`-command. The investigated parameter space is defined as ±50% around the

initial best-fit value with 50 steps each for the temperature and the redshift and 20 steps for the normalisation. In a last step, we estimated the 68%-confidence intervals of the best-fit values by means of the *xspec* `error`-command. The complete simulation procedure was then repeated 300 times for each set of parameters resulting in a well-sampled distribution of best-fit values. This distribution allowed us to define a second 68%-confidence interval around the median best-fit value. In the following, this last confidence range is applied for the analysis of the simulation and is considered as the true uncertainty on the fit values.

4.2.4 Analysis Procedure

Before analysing the simulated data, we removed all catastrophic failures in the fit results, which we devided into two types. The first type of catastrophic failures contains inconsistencies in the fit, where the 68%-confidence interval calculated by the `error`-command was not set around the best-fit value. These inconsistencies may occur during the simulations with unknown redshift. When appearing in the analysis of observed data, the spectral fit needs to be repeated, while being adapted individually to this spectrum by means of re-defined starting values for the fit, for example. This approach is not feasible for the extent of our simulations, such that we were limited to the conservative procedure of discarding these spectra.
During the analysis, we addressed each parameter set separately and defined the second type of catastrophic failures as fit values, whose true $3 \times 68\%$-confidence interval does not include the input value. This type of failures can only be quantified if the input cluster parameter values are known. In the analysis of observed data, however, they cannot be identified and thus decrease the accuracy of the analysed data sample.
If these two types of catastrophic failures made up to more than 20% of the fit data, the parameter set was rejected (see Sect. 4.5), i.e. it was assumed that the cluster property values cannot be recovered typically from the *eROSITA* data. However, to ensure a conservative analysis, the fits showing the second type of catastrophic failure were included in the analysis of all our data sets since these catastrophic failures can generally not be identified for observed data.
The analysis considered three different interpretations of the temperature and the redshift fit results, all of which are presented in dependence on the input values of the cluster mass and redshift. First we inspect the relative uncertainties, which we defined as $\Delta T/\langle T_{\rm fit}\rangle$ and $\Delta z/\langle 1+z_{\rm fit}\rangle$. The elements ΔT and Δz express the true 68%-confidence range from the distribution of the fit values. The typical fit values $\langle T_{\rm fit}\rangle$ and $\langle 1+z_{\rm fit}\rangle$ were estimated by the median of the distribution. Especially of interest are relative uncertainties of the two properties with values of $\lesssim 10\%$ since these uncertainties are similar to the intrinsic scatter in the $M-T$ scaling relation (e.g., Mantz et al. 2010a). We focused on the fit results of the temperature since for future *eROSITA* observations the total cluster mass is more precisely estimated by the $M-T$ relation, due to its smaller intrinsic scatter in comparison to the $M-L_{\rm X}$ relation (e.g., Mittal et al. 2011). However, analysing the recovery of the cluster mass from the simulated spectra is beyond the scope of this paper.
The bias on the best-fit cluster properties was computed as $\langle T_{\rm fit}\rangle/T_{\rm input}$ and $\langle 1+z_{\rm fit}\rangle/(1+z_{\rm input})$, expressing the ratio between the median of the fit values and the input value. As a last analysis, we investigated the deviation between the median uncertainty computed by the `error`-command and the uncertainty obtained from the distribution of the fit results as $\langle \Delta T_{\rm error}\rangle/\Delta T$. Analogously, the deviation in the redshift uncertainties was analysed. This so-called bias in the error estimates is an important quantity since from the reduction of observed data only the uncertainty by the `error`-command will be available, whereas the proper statistical uncertainty is given by the distribution.

4.3 Results

4.3.1 Relative Uncertainties

Figures 4.3 to 4.8 illustrate the relative temperature and relative redshift uncertainties, expected after four years of the *eROSITA* all-sky survey. The relative uncertainties were computed in dependence on the input cluster mass and redshift, such that each pixel represents a galaxy cluster with a different combination of input mass and redshift, where the values of the two properties are given by the centre of the pixel. The colour of the pixel indicates the relative uncertainty of either the temperature or the redshift of the cluster. The colour bar expresses this relative uncertainty and is given in a linear scale. According to the defined flux limit and photon count limit (Sect. 4.2.3), only the cluster parameter space within the two white dashed lines was considered. In the simulation of the *eROSITA* deep exposure fields with $t_{\rm exp}$ = 20 ks, this parameter space increases to higher redshifts as fainter clusters are detected above the photon-count threshhold (Figs. 4.4 to 4.8).
For display purposes, we include countour lines for the relative uncertainty in white and for the number of detected photons in black, where each cluster on the contour line shows at least the stated precision or number of photons. In Figs. 4.6 and 4.8, the parameter space of clusters with relative uncertainties of $\lesssim 10\%$ in temperature or redshift is indicated as the area between the solid white contour lines. The white-framed dark-blue pixels present the parameter sets which were rejected because of a large fraction of catastrophic failures (Sect. 4.2.4).

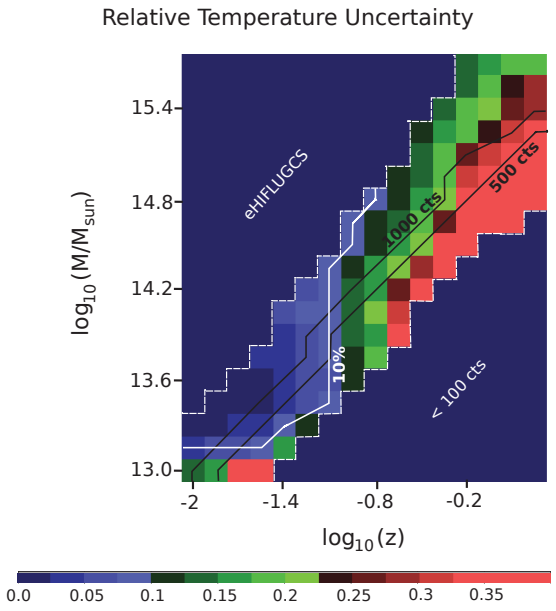

Figure 4.3: Expected relative temperature uncertainties $\Delta T/\langle T_{\rm fit}\rangle$ in dependence on the total cluster mass and the cluster redshift. This simulation assumes an exposure time of $t_{\rm exp}$ = 1.6 ks and the redshift of the clusters to be available. We present white and black contour lines to emphasise on the relative uncertainties and the number of source counts, respectively.

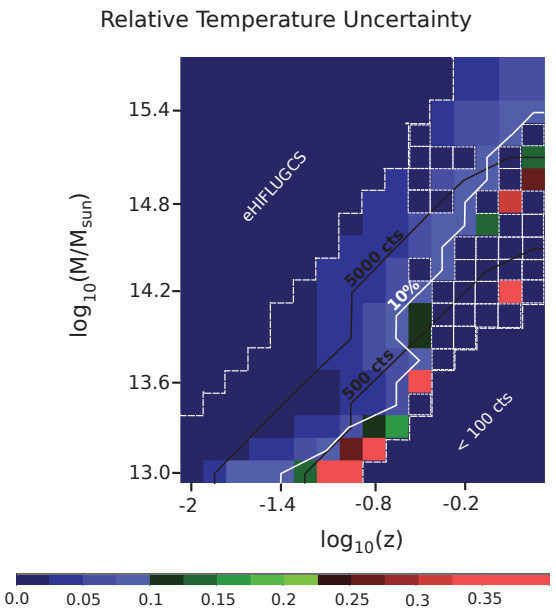

Figure 4.4: Expected relative temperature uncertainty for an exposure time of $t_{\rm exp}$ = 20 ks, if the redshift of the cluster is available.

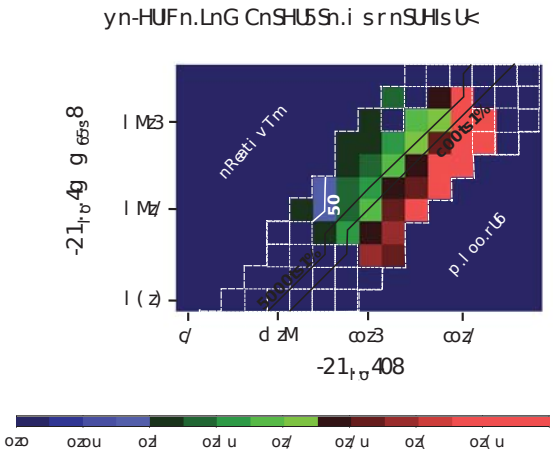

Figure 4.5: Relative temperature uncertainty as presented in Fig. 4.3, but assuming the cluster redshift to be unavailable. The dark blue pixels with dashed white contours indicate the catastrophic failures in the fit.

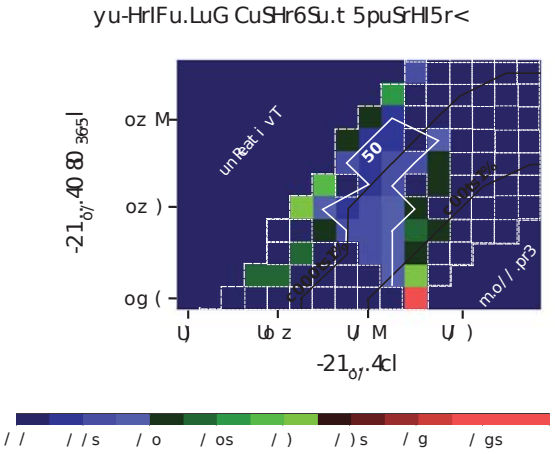

Figure 4.6: Expected relative temperature uncertainty for the simulation of t_{exp} = 20 ks and unknown cluster redshift.

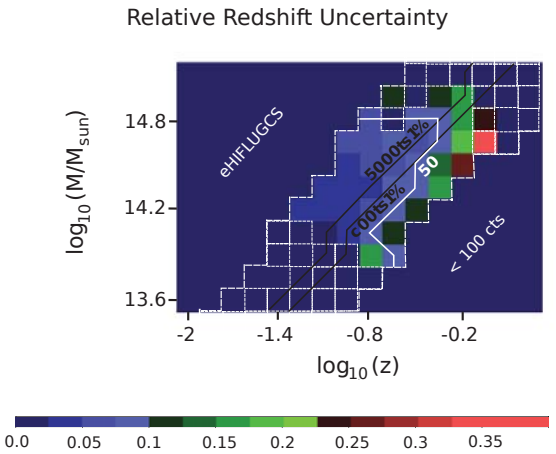

Figure 4.7: Expected relative redshift uncertainty $\Delta z/\langle 1 + z_{\mathrm{fit}}\rangle$ for an exposure time of t_{exp} = 1.6 ks.

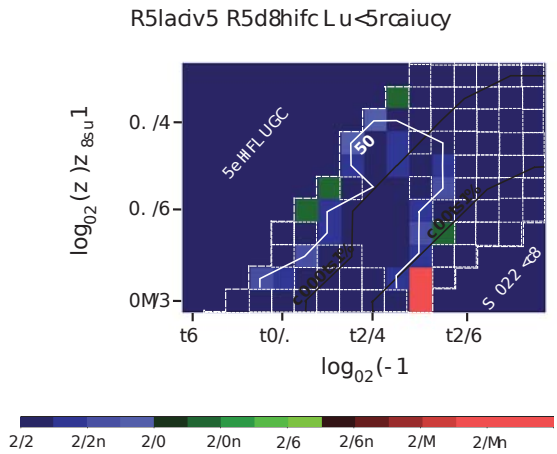

Figure 4.8: Expected relative redshift uncertainty for an exposure time of t_{exp} = 20 ks.

Compared with the simulation with t_{exp} = 1.6 ks and known redshift (Fig. 4.3), the number of rejected pixels increases when the exposure time is increased, particularly when we assumed the redshift to be not available. For the simulation results with unknown redshift the figures were clipped to the intermediate mass range of $13.6 \lesssim \log(M/\mathrm{M}_{\odot}) \lesssim 15.1$ since all parameter sets including the remaining masses were rejected (Figs. 4.5 & 4.7 and 4.6 & 4.8). With increasing exposure time, the increased number of detected photons reduces the statistical scatter in the simulated spectra, which allows for a higher precision of the fit. Accordingly, this increased precision tightens the absolute constraints on the catastrophic failures. Futhermore, introducing the redshift as an additional free parameter in the simulations complicates the fitting procedure and yields less accurate and less precise fit results (Sect. 4.3.2). The occurence of a high level of failed spectral fits when determining the X-ray redshift of a cluster has also been observed by Lloyd-Davies et al. (2011) (see also Sect. 4.5.3).

In all simulation approaches, the precision of temperature and redshift generally increased with increasing cluster mass and, in particular, with decreasing cluster redshift.

According to these findings, the galaxy clusters that are relevant for cosmological studies with relative parameter uncertainties of $\leqslant 10\%$ are observed in the local Universe. For the all-sky survey with an average effective exposure time of $t_{\rm exp} = 1.6$ ks, we expect the temperature to be detectable with this precision up to maximum redshifts of $\log(z) \approx -0.8$, $z \lesssim 0.16$ (Fig. 4.3), if the redshift of the cluster is known, and up to $\log(z) \approx -1.1$, $z \lesssim 0.08$ (Fig. 4.5), if the redshift is not available. The redshift itself will be obtained with relative uncertainties of $\leqslant 10\%$ from X-ray data for clusters as far as $\log(z) \approx -0.35$, $z \lesssim 0.45$ (Fig. 4.7). At the ecliptic poles of the mission with exposure times of $t_{\rm exp} = 20$ ks, the parameter space of clusters with precision temperatures increases in theory to redshifts of $z \lesssim 1.78$ (Fig. 4.4), assuming the redshift is known. At these redshifts precise temperatures are only obtained for the most massive galaxy clusters of which not many are expected to be observed (compare Fig. 4.15), especially in the low sky area of the deep exposures. Additionally, pollution of the spectra by the cluster AGN needs to be expected for these deep observations (see Sect. 4.5.5). In the case of unavailable redshifts, both temperature and redshift are detectable up to $\log(z) \approx -0.35$, $z \lesssim 0.45$ (Figs. 4.6 & 4.8). For these observations, catastrophic failures in the spectral fit restrict the parameter space of clusters with precise temperature and redshift estimates.
The parameter space of clusters with high-precision temperatures decreased for the simulation with unknown redshift, because the redshift was introduced as an additonal free parameter during the fit and the resulting degeneracy between the cluster redshift and the cluster temperature (compare Sect. 4.5.3). The cluster redshift is more difficult to determine from X-ray spectra than the cluster temperature (e.g., Yu et al. 2011; Lloyd-Davies et al. 2011). But because of the deviating definitions of the relative uncertainties as $\Delta T/\langle T_{\rm fit}\rangle$ and $\Delta z/\langle 1 + z_{\rm fit}\rangle$, precise redshifts are expected to be detected for more distant clusters than are precise temperatures. According to this, the number of clusters for which both precise redshifts and temperatures will be available from X-ray data is limited by the determination of the temperature.
The analysis of the relative uncertainties clearly shows that the precision of temperature and redshift does not only depend upon the number of detected photons, but also upon the cluster properties (see Sect. 4.5.1).

4.3.2 Biases in the Best-Fit Properties

The bias in the best-fit temperatures and redshifts was analysed in dependence on the cluster redshift within five mass ranges, defined by the input cluster masses. These mass intervals were centred on the values $\log(M/{\rm M}_\odot) = 13.15$, 13.75, 14.35, 15.95 and 15.55, where the parameter biases of these cluster masses are illustrated in Figs. 4.9 - 4.14 within the simulated redshift intervals. The uncertainty of the bias is given by the scatter in the best-fit values. We also present correction functions for these biases, which we obtained as a fit of the exponential function

$$f(x) = A \cdot \exp(B \cdot x) + 1 \quad , \tag{4.9}$$

with variables A and B and $x = \log(z)$, to the data points.
The best-fit values of A and B are provided Appendix C.1. The parameter sets that we rejected due to large numbers of catastrophic failures are displayed as empty symbols. They were included in the fit of the correction function to avoid an underestimation of the correction of the best-fit property values. However, cluster masses that showed only catastrophic failures for all redshifts were excluded from this fit. For the simulations with known redshift, we define correction functions individually for the five cluster masses stated above. However, we assumed the correction function to be an estimate for all masses within the defined mass range and within the simulated redshift interval (Appendix C.1). When the cluster redshift is unknown, the parameter biases are to a first approximation independent of the

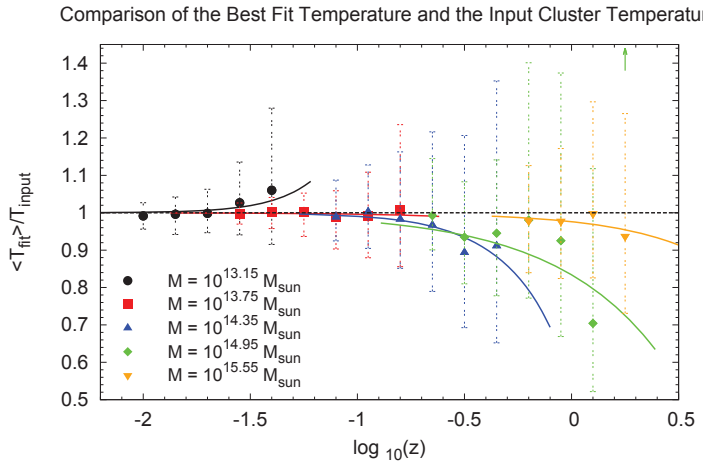

Figure 4.9: Bias on the best-fit temperature in dependence on the cluster redshift for the simulation of $t_{\mathrm{exp}} = 1.6$ ks and known redshift. For each displayed cluster mass individual bias correction functions are suggested as solid curves with the corresponding colour.

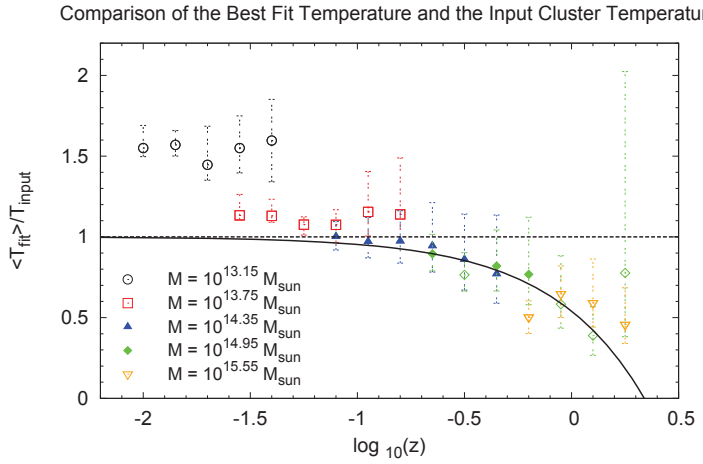

Figure 4.10: Bias on the best-fit temperature for the simulation of $t_{\mathrm{exp}} = 1.6$ and assuming the cluster redshift to be unavailable. For all simulated cluster masses the bias is described by a single function (black curve), where the empty symbols indicate the rejected data sets due to a large fraction of catastrophic failures.

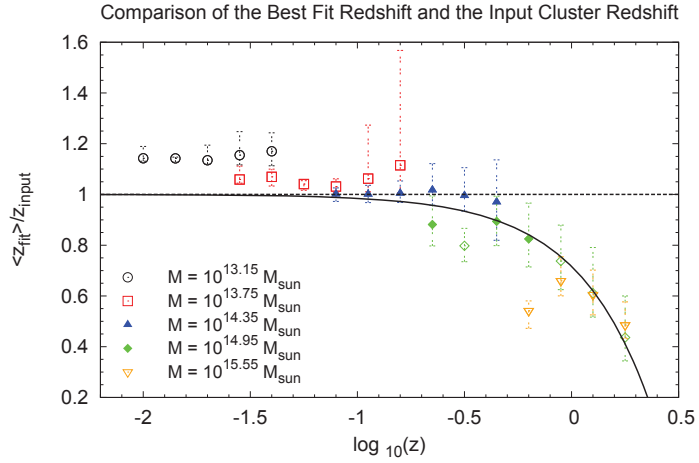

Figure 4.11: Bias on the best-fit redshift assuming an exposure time of $t_{\mathrm{exp}} = 1.6$. Also the bias on the redshift can be parameterised by a single function for all cluster masses.

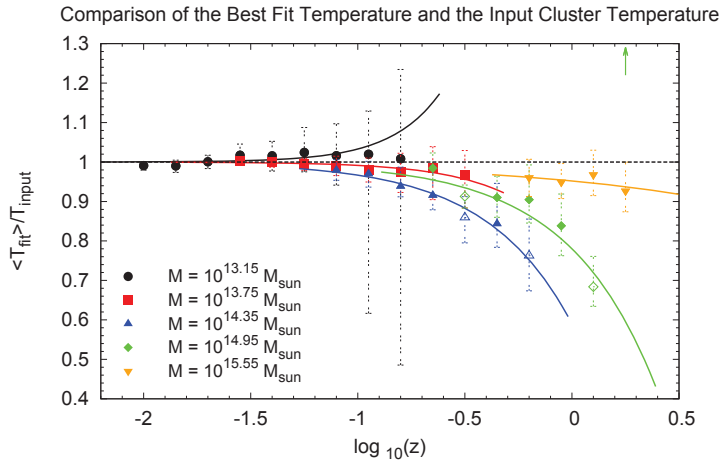

Figure 4.12: Bias on the best-fit temperature for the deep exposure fields of $t_{\mathrm{exp}} = 20$ ks and for clusters with known redshift. Again, suggested correction functions for this bias are presented.

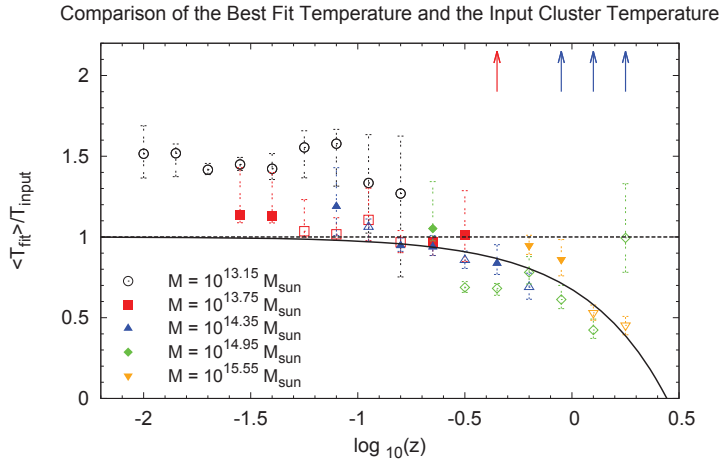

Figure 4.13: Bias on the best-fit temperature for clusters in the deep exposure fields with unknown redshift. For the entire mass range, the bias is described by a single function.

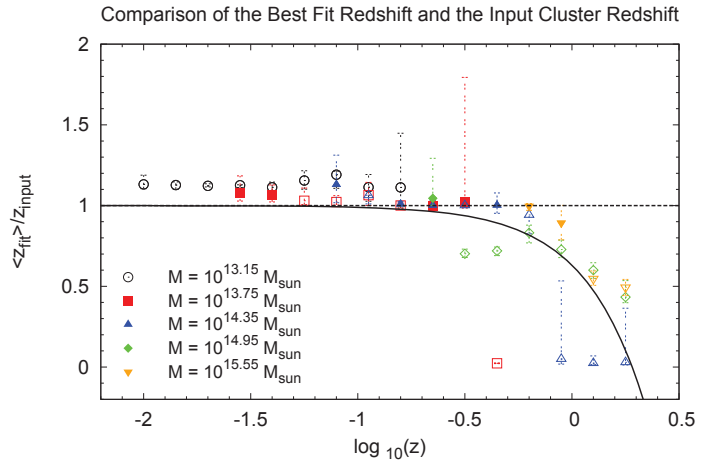

Figure 4.14: Bias on the best-fit redshift for clusters in the deep exposure fields and the estimated correction function for this bias.

cluster mass (Figs. 4.10 & 4.11 and 4.13 & 4.14). According to this, we describe these biases by a single exponential function for all cluster masses. The degeneracy in the cluster masses occurs because for the simulation with unavailable redshift a larger scatter is introduced in the median values of the parameter bias.
In general, the biases in the best-fit properties a decrease with declining cluster redshift, and for the simulated clusters with known redshifts, the bias additionally increases with decreasing cluster mass. For local redshifts of roughly $\log(z) \approx -0.7$, the parameter bias becomes negligible for all cluster masses and simulation approaches. Even for higher redshifts the best-fit value is still consistent with the input value within the error bars.
With increasing exposure time, the median bias values improve moderately, whereas the uncertainty on the best-fit value decreases significantly. According to this, the bias is only consistent with unity for smaller redshift ranges when compared to the results for $t_{\mathrm{exp}} = 1.6$ ks (compare Figs. 4.9 & 4.12). Similar to the findings for the relative uncertainties, the temperature bias rises when the redshift of the cluster is unavailable. According to the deviating definitions for the temperature and redshift (Sect. 4.2.4), the redshift appears as more accurate property.
The development of the bias in the best-fit properties in dependence on the cluster redshift, temperature, and number of photons is analogous to the evolution of the relative uncertainties. Thus, both results are explained by similar considerations (see Sect. 4.5.1). We recall that we investigated an isothermal cluster emission model in our simulations to focus only on the performance of the *eROSITA* instrument. To analyse observed data and thus mainly multi-temperature gas, additional systematics might arise in the temperature estimation, according to the shape of the effective area. A first assessment of this effect is presented by Reiprich et al. (2013) in their Figure 18.
The underestimation of the proper input property value has also been studied by Leccardi & Molendi (2007). They explained the deviation through the increasing relative background contribution with increasing redshift compared to the source counts as well as through the calibration of the instrument.
When convolving these results for the bias in the properties with the parameter space of *eROSITA* clusters with precise temperatures and redshifts, we find that the bias is negligible for all clusters with relative parameter uncertainties of $\lesssim 10\%$ during the all sky survey ($t_{\mathrm{exp}} = 1.6$ ks). This is independent of the available information on the redshift. The same result is observed for $t_{\mathrm{exp}} = 20$ ks and for clusters with unknown redshift. Only clusters with available redshifts and precise temperatures in the deep exposure fields require a correction of the best-fit temperatures for distances above $\log(z) \gtrsim -0.5$, which is equivalent to $z \gtrsim 0.32$.

4.3.3 Bias in the Error Estimates

For the bias in the error estimates no definite dependence on the input cluster mass or the redshift is observed, therefore, simple correction factors were calculated. Thus, we present estimates of these biases averaged over the complete simulated mass and redshift range (Table 4.2). In analogy to the fit of the bias on the best-fit properties, masses with only catastrophic failures for all simulated redshifts were excluded from the estimation.
When the redshift of the cluster is known, the temperature uncertainty computed by the `error`-command represents the statistical scatter in the best-fit values well, with a ratio in the uncertainties of $\langle \Delta T_{\mathrm{error}} \rangle / \Delta T = 1 \pm 0.1$. For spectral fits with unavailable redshifts, we observe a general underestimation of the proper uncertainty in the fit value by the `error`-command, where the uncertainty in the redshift experiences a stronger bias than the uncertainty in the temperature (Table 4.2).
This increase in the bias for clusters with unknown redshift is explained by the additional free parameter during the spectral fit and by the difficulty in recovering the cluster redshift from X-ray spectra (Yu et al.

Table 4.2: Bias in the error estimates for the different simulations. The bias is avaraged over the complete mass and redshift range. For the simulations with known redshift, the bias in the uncertainties is in general negligible.

simulation	bias	exposure time	
		$t_{\mathrm{exp}} = 1.6$ ks	$t_{\mathrm{exp}} = 20$ ks
known z	$\langle \Delta T_{\mathrm{error}} \rangle / \Delta T$	1	1
unknown z	$\langle \Delta T_{\mathrm{error}} \rangle / \Delta T$	~ 0.3	~ 0.5
	$\langle \Delta z_{\mathrm{error}} \rangle / \Delta z$	~ 0.25	~ 0.15

2011). In addition, a longer exposure time does not necessarily result in a reduced bias in the error estimates. Unlike the bias in the best-fit parameter values, the bias in the error estimates typically needs to be considered for the analysis of clusters with relative parameter uncertainties of $\lesssim 10\%$. In the reduction of *eROSITA* data for clusters with unavailable redshifts, the provided corrections are a necessary tool to compute reliable parameter uncertainties.

4.4 Cosmological Interpretation

To compute the number of clusters for which high-precision temperatures and redshifts will be available directly from *eROSITA* data, we applied the halo mass function by Tinker et al. (2008) (comp. Sect. 2.3.3). This mass function was convolved with the $M - L_{\mathrm{X}}$ and $M - T$ scaling relation by Reichert et al. (2011) as well as with the *eROSITA* response to obtain a distribution of the number of clusters in dependence on the number of observed photons (comp. chapter 6.3). As in Sect. 4.3, the results are dependent on the input cluster properties. Figure 4.15 presents this distribution of clusters for an exposure time of $t_{\mathrm{exp}} = 1.6$ ks. For our computation we assumed a minimum number of photons $\eta_{\mathrm{min}} = 50$ in the energy range of $(0.5 - 2.0)$ keV for a source to be detected as a galaxy cluster by *eROSITA* (following Pillepich et al. 2012). Accordingly, no constant flux cut was applied for our computations, but for each considered combination of cluster mass and redshift the number of observed counts was estimated based on the applied scaling relations. Additonally, we applied an effective lower mass cut of $M_{\mathrm{cut}} = 5 \times 10^{13} / h \, \mathrm{M}_{\odot}$, which is equivalent to $M_{\mathrm{cut}} = 7.1 \times 10^{13} \, \mathrm{M}_{\odot}$ for our choice of $h = 0.7$. With this cut we removed low-mass clusters and groups, which show a strong scatter in their scaling relations (e.g. Eckmiller et al. 2011). During the simulation, this mass cut is converted into a redshift-dependent cut of the photon counts, as explained by Pillepich et al. (2012) and in chapter 6.3.1, since for the analysis of X-ray data the cluster mass is initially unknown. According to our applied cosmology ($\Omega_{\mathrm{m}} = 0.3$, $\Omega_{\Lambda} = 0.7$), we adjusted the normalisation of the matter power spectrum to $\sigma_8 = 0.795$ by means of the relation

$$\sigma_8 \propto \Omega_{\mathrm{m}}^{-0.38} \tag{4.10}$$

(Reiprich & Böhringer 2002), which we normalised according to the WMAP5 results of $\Omega_{\mathrm{m}} = 0.279$ and $\sigma_8 = 0.817$ (Komatsu et al. 2009). This normalisation was chosen for a better comparison between our calculations and the work by Pillepich et al. (2012). We defined the observed sky fraction to be $f_{\mathrm{sky}} = 0.658$ for the all-sky survey with $t_{\mathrm{exp}} = 1.6$ ks. This sky fraction considers the entire sky, excluding a region of $\pm 20°$ around the Galactic plane as well as regions with a high X-ray flux such as the Magellanic Clouds and the Virgo Cluster.

Following these approaches, we expect to detect a total of $\sim 113,400$ clusters of galaxies with the *eROSITA* instrument during its four years of all-sky survey (Table 4.3). The peak of the cluster distribution is located at a redshift of $\log(z) \approx -0.5$, $z \approx 0.3$, and at a cluster mass of $\log(M/M_{\odot}) \approx 14$ (compare

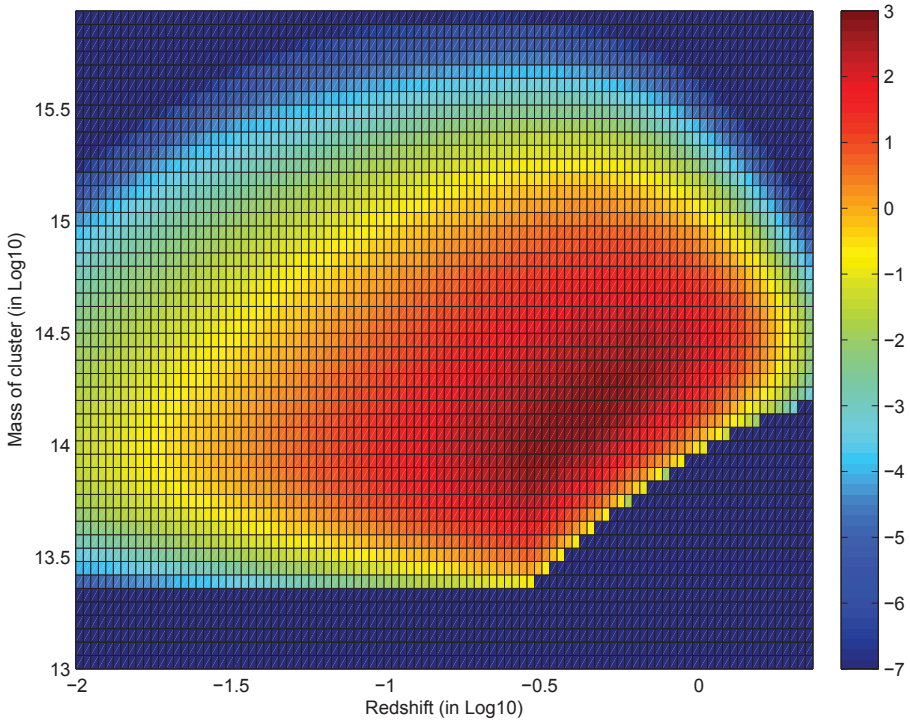

Figure 4.15: Distribution of galaxy clusters with mass and redshift as it will be detected by the *eROSITA* instrument during its four years of all sky survey based on the mass function by Tinker et al. (2008) and on the scaling relations by Reichert et al. (2011). The colour bar indicates the number of galaxy clusters in the individual bins in units of $\log_{10}$ and the cluster mass is considered in units of $\log(M/\mathrm{M}_\odot)$. We assume that a minimum number of $\eta_{\mathrm{min}} = 50$ photons is necessary to identify a cluster and effectively apply a lower mass cut to exclude low mass galaxy groups.

Pillepich et al. 2012). For the highest cluster masses, the number of observed clusters is strongly limited at the local redshifts (Fig. 4.15), due to the small observed volume. Moreover, at the highest redshifts we do not expect to detect any high-mass clusters according to our concordance cosmology, which disfavours the existence of massive clusters at high redshifts. Galaxy clusters with low masses of $\log(M/M_\odot) \lesssim 14$ only show small fluxes at high redshifts of $\log(z) \gtrsim 0.3$, which results in fewer than 50 photons for an exposure time of $t_{\mathrm{exp}} = 1.6$ ks, and thus does not allow for a detection. Figure 4.16 presents the distribution of the observed clusters in dependence on their number of photon counts for the all-sky survey. As a rough estimate, the currently known X-ray clusters are located in the two bins with the highest counts. Accordingly, this graphic emphasises the large amount of so-far unknown clusters that will be discovered by *eROSITA*.

To analyse the deep-exposure fields with $t_{\mathrm{exp}} = 20$ ks, the sky coverage is re-defined to be $f_{\mathrm{sky}} = 0.0034$ (Merloni et al. 2012), such that the total number of observed clusters for these regions decreases to $2,600$. At the same time, the clusters are observed at more distant redshifts in these deep fields.

In convolving this number distribution of *eROSITA* clusters with the results obtained in Sect. 4.3.1, we computed as a first estimate the number of clusters for which *eROSITA* will detect precise temperatures and redshifts in addition to the already studied 184 *eHIFLUGCS* clusters (Table 4.3). For this we integrate over the mass and redshift space with precise cluster properties, where we define the integration boundaries to be centred between the last pixel within this precise parameter space and its neighbouring pixel. In addition, we investigated the compatibility between the assumed limit of $\eta_{\mathrm{min}} = 50$ for the

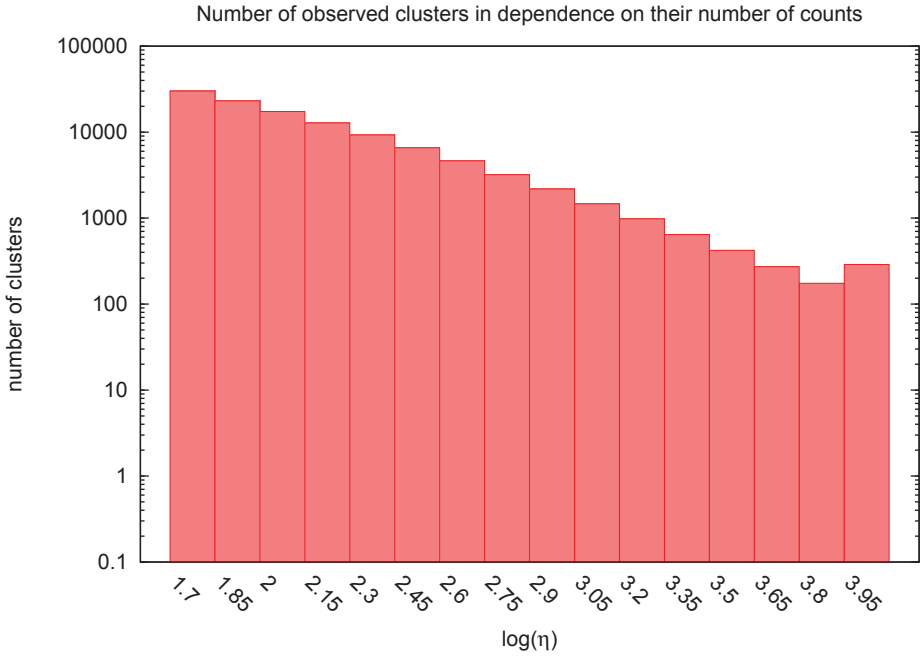

Figure 4.16: Number of observed galaxy clusters in dependence on their number of photon counts η on logarithmic scale. The clusters are binned according to their number of observed photons in bins of the size $\Delta \log(\eta) = 0.15$, starting at $\log(\eta) = 1.7$ or $\eta = 50$, respectively. The final bin includes all clusters with more than $\log(\eta) = 3.95$ or $\eta \approx 9,000$ counts.

detection of a cluster and the required limit of 100 counts for the reliable analysis of the cluster spectrum. Even though these two limits are based on different energy bands, (0.5 – 2.0) keV and (0.3 – 8.0) keV, respectively, all clusters, analysed in Sect. 4.3, are within the detection limit. According to these assumptions, *eROSITA* is expected to obtain precise temperatures for $\sim 1,670$ clusters during its all-sky survey if the redshift of the clusters is already known. This number of precision clusters emphasises the importance of this instrument, because the number of clusters with precise temperatures will be increased by a factor of ~ 9 compared to *eHIFLUGCS*. Assuming the redshifts to be unavailable for all clusters, the number of clusters with precise temperatures decreases to ~ 300, because the parameter space of precise temperatures reduces significantly (compare Fig. 4.5). For all of these 300 clusters precise X-ray redshifts will be available as well from *eROSITA* data. Additionally, the simulations predict *eROSITA* to obtain precise X-ray redshifts with relative uncertainties of $< 10\%$ for a total of $23,000$ clusters. This entire cluster sample can then be employed for cosmological studies where a first estimate can already be obtained knowing only the cluster redshift and luminosity (compare Pillepich et al. 2012). Following Table 4.3, the percentage of *eROSITA* clusters with precise properties increases significantly with increasing exposure time, which is allowing us an outlook also into the successive pointed observation phase of the mission as well. Only the redshift estimates in the deep exposure fields are significantly limited by catastrophic failures in the spectral fit.
Even though we defined a minimum number of photons of $\eta_{\min} = 50$ for a galaxy cluster to be detected by *eROSITA*, the number of clusters with precise properties is limited by the 100 photon counts that are required for a reliable analysis of the cluster spectrum (Sect. 4.2.3). However, applying $\eta_{\min} = 50$ to compute the number of clusters allows for a comparison of the number of clusters with precise property values with the total number of observed clusters. If we assume a less conservative approach with

Table 4.3: Number of clusters expected to be detected by *eROSITA* in total, with relative temperature uncertainties of $\lesssim 10\%$, when assuming the cluster redshift to be available, and with relative uncertainties of $\lesssim 10\%$ in temperature and redshift for unavailable redshift. The presented numbers for the precision clusters refer to clusters with fluxes of $F < 9 \times 10^{-12}$ erg/s/cm^2, i.e. clusters without high quality observations already studied through *eHIFLUGCS*. The values in parentheses denote the fraction of clusters with precise X-ray properties compared with the total number of clusters for each exposure time.

simulation		$t_{\rm exp} = 1.6$ ks, $f_{\rm sky} = 0.658$	$t_{\rm exp} = 20$ ks, $f_{\rm sky} = 0.0034$
total		113,400	2,600
known z	precise T	1,670 ($\sim 1.5\%$)	280 ($\sim 11\%$)
unknown z	precise T	300 ($\sim 0.3\%$)	140 ($\sim 5\%$)
	precise z	23,000 ($\sim 18\%$)	340 ($\sim 13\%$)

$\eta_{\rm min} = 100$, the total number of observed clusters in the all-sky survey decreases to 60,100, whereas the number of clusters with precise properties remains the same. With this assumption, the percentages stated in Table 4.3 increase significantly, to $\sim 2.8\%$ for clusters with known redshift in the all-sky survey, for example.

4.5 Discussion

4.5.1 Dependence of the Relative Uncertainties

The fit of the model emission to the cluster spectrum is generally guided by the observed spectral lines, the over-all shape of the spectrum, and by the position of the exponential cut-off at high energies. For clusters with temperatures of $k_B T \lesssim 2.5$ keV, the fit is dominated by the line emission, because most of the emitted photons are observed in this spectral characteristic. With increasing cluster temperature, the spectral shape and the cut-off become more important for the fit.
In Sect. 4.3.1 as well as in Figs. 4.3 through 4.8 we see a general increase of the relative uncertainties with increasing redshift and with decreasing cluster mass. This dependence is explained by the following aspects.
For a constant cluster luminosity, the photon flux strongly declines with increasing redshift as $F \propto 1/D_{\rm L}^2$ with the luminosity distance $D_{\rm L}$. This reduction is alliviated, but not fully compensated for, by the increase in luminosity with rising redshift, if we consider clusters with a constant mass (Eq. 4.2). Thus, the uncertainty of the fit parameters increases with increasing redshift. However, clusters with increasing total mass yield a strong increase in their luminosities, which improves the fit results despite the higher temperatures of these clusters. These increased temperatures result in a depletion of the emission lines and in a shift of the position of the exponential cut-off to higher energies and thus out of the *eROSITA* effective area.
The parameter space of clusters with precise properties extends to larger distances for the increased exposure time of $t_{\rm exp} = 20$ ks as more photon counts are observed from the individual clusters and the statistical scatter in the spectrum is reduced. However, as already expressed in Sect. 4.3.1, the relative uncertainties are not only depending on the number of detected source photons, but also on the cluster characteristics. These characteristics include in particular the strength of emission lines and the position of the high-energy cut-off compared with the *eROSITA* effective area.

4.5.2 Remarks on the Relative Uncertainties

According to our simulation results, we expect *eROSITA* to detect X-ray redshifts for $\sim 23,000$ clusters, which appears as an optimistic number at first glance. To test the reliability of these results, we analysed the relative redshift uncertainties for the two *eHIFLUGCS* clusters RXCJ 1504 and A2204, kindly provided by G. Schellenberger. Both clusters show high redshifts of $z = 0.215$, $\log(z) = -0.67$, and $z = 0.15$, $\log(z) = -0.82$, with masses of $M = 10^{15}\,\mathrm{M}_\odot$ and $M = 7 \times 10^{14}\,\mathrm{M}_\odot$, $\log(M/\mathrm{M}_\odot) = 14.85$, respectively. To allow for a comparison, the exposure times of the two *Chandra* observations were decreased to $t_{\mathrm{exp}} < 2$ ks and only the temperature, redshift, and normalisation of the spectrum were left free to vary during the fit. With this approach RXCJ 1504 and A2204 show a relative redshift uncertainty of $\Delta z/(1+z) \approx 0.04$ and of $\Delta z/(1+z) \approx 0.07$, respectively. Furthermore the best-fit redshifts represent the true redshifts very well, with a deviation of only a few percent in the case of RXCJ 1504 and with no deviation for A2204. This result agrees well with the precise redshift estimates for clusters with large distances obtained in our simulations (compare Fig. 4.7). Furthermore, the analysed *eHIFLUGCS* clusters are located in a parameter range in which our simulations predict a large fraction of catastrophic failures (compare Fig. 4.7). According to this, the above analysis of observed data illustrates the conservative approach of our simulations to re-obtain the cluster properties.

Since the estimation of ICM metallicities commonly presents large uncertainties when analysing observed data (Balestra et al. 2007; Werner et al. 2008; Baldi et al. 2012), we quantified the effect of an incorrectly assumed metallicity on our simulations. As the metallicity presents itself especially in the strength of the emission lines, we only expect the metallicity to influence our results for clusters with $\mathrm{k_B}T \lesssim 2.5$ keV. To test this influence, we repeated our simulation for a choice of clusters with different masses and redshifts, where the cluster temperature meets the above criterion and the redshift is assumed to be known. During the fitting procedure, the metallicity is wrongly fixed to the extreme values of either $A = 0.2\,\mathrm{A}_\odot$ or $A = 0.4\,\mathrm{A}_\odot$ instead of the true value $A = 0.3\,\mathrm{A}_\odot$ (Maughan et al. 2008). Even for these strong deviations in the metallicities, the relative temperature uncertainties only display an increase for the more distant clusters of $\log(z) \gtrsim 1.1$, $z \gtrsim 0.1$, by a few percent. However, the accuracy of the temperature fit is unaffected by the incorrectly fixed metallicity.

Since the metallicity of a cluster is not only definded by the value of A, but also by the applied abundance model, we repeated our simulation for $t_{\mathrm{exp}} = 1.6$ ks and a sample of clusters with the more recent abundance model by Asplund et al. (2009). Assuming the redshift of the tested clusters to be known, we obtained differences in the relative temperature uncertainties of $\sim 5\%$ and differences of only a few percent for the bias in the temperature estimates. These differences do not show an apparent dependence on the simulated cluster properties. In summary, we conclude that neither an incorrectly fixed metallicity nor a change in the abundance model significantly alters the simulated parameter spaces or the numbers of clusters with precise properties.

A possible evolution of the metallicity with redshift could not be definitely quantified in the literature so far, and we thus applied a constant metallicity in our simulations (compare Sect. 4.2.1). Assuming a metallicity evolution would impact our simulation results for the higher redshifts because the metallicity might decrease to half its value at redshifts of $z \approx 1$ (e.g. Maughan et al. 2008). Since redshift estimates will be possible up to $z \approx 0.3$ (compare Fig. 4.7) in the all-sky survey, we quantified the influence of such an evolution on the redshift analysis. In an extreme scenario of $A = 0.2\,\mathrm{A}_\odot$ for clusters at $z \approx 0.3$, the relative redshift uncertainties increase to $\lesssim 12\%$. This results in a shift of the contour line of $\Delta z/(1+z) < 10\%$ to lower redshifts by one pixel. However, the tested scenario requires an strong metallicity evolution with an already strong decrease in metallicity over a small redshift range, which is not anticipated in the literature (e.g. Balestra et al. 2007; Maughan et al. 2008).

Despite our realistic treatment of the background and its statistical scatter (compare Sect. 4.2.2), system-

atic errors in the anaysis of future observed data might arise from an incorrectly constrained background model. To investigate its effect on our results, we reran the simulations for a set of parameters of typically observed *eROSITA* cluster masses of $M \approx 10^{14}$ $M_\odot$ up to $M \approx 10^{14.8}$ $M_\odot$ with relative temperature uncertainties of $\sim 10\%$. In these simulations we then assumed a background model with a systematic error of $\pm 10\%$. This is a conservative approach given that for *Chandra*, for instance, uncertainties of $\sim 3\%$ are quoted (Markevitch et al. 2003), such that we expect a lower value for *eROSITA*. For clusters with precise parameter estimates and low temperatures of $kT \lesssim 3$ keV ($M \lesssim 10^{14}$ $M_\odot$), the difference in the newly simulated parameter bias and in the relative uncertainty is only a few percent when compared with the simulation without applying any background uncertainty. These differences slightly increase to $\sim 10\%$ for clusters with precise parameters, but intermediate temperatures, corresponding to $M \approx 10^{14.8}$ $M_\odot$. This is true for the all-sky survey as well as for the deep exposures. According to this, introducing a possible background error in our simulations does not influence the presented parameter space of clusters with precise properties. Moreover, the temperature bias still remains negligible for clusters within this parameter space, apart from the exclusions already stated in Sect. 4.3.2 for clusters observed in the deep exposure fields.

4.5.3 Occurrence of Catastrophic Failures

As described in Sect. 4.3.1, catastrophic failures particularly occur for spectral fits with unknown cluster redshifts, especially for the very low mass and the very high mass clusters (e.g. Fig 4.5). This finding is generally explained by the degeneracy between the redshift and the temperature for these cluster masses. This degeneracy in dependence on the cluster mass and temperature is illustrated in Fig. 4.17, where we plot the distribution of temperature and redshift best-fit values for three different parameter sets, each with roughly the same number of counts. The low- and the high-mass parameter set is rejected because of large numbers of catastrophic failures, and both sets show a strong correlation between their best-fit redshifts and temperatures. The stripe features, especially visible in the top image, are the result of the `steppar`-fit and are addressed in Sect. 4.5.4.

This degeneracy and the simulation results for the clusters with unknown redshift are explained by several spectral charactersitics that interact with one another. We find two possible examples to explain the simulation results in the strength of the emission lines, especially in the strength of the Fe-K line, and in the detectability of the exponential cut-off.

Low mass clusters only show small numbers of detected photons and thus a large statistical scatter in their spectra. Additionally, the individual emission lines are not resolved (compare Fig. 4.1) and the observed emission line complexes around energies of 1 keV are shifted to higher energies with increasing temperatures. This latter characteristic leads to a degeneracy between the imprint of the redshift and the temperature on the spectrum. Furthermore, due to the scatter in the emission lines at the energies of the exponential cut-off, the exact energy of this spectral feature is not detectable, which complicates the spectral fits. Considering these two aspects, we explain the large fraction of catastrophic failures for the fit to spectra of clusters with low masses (compare e.g., Fig. 4.5). Only for higher cluster temperatures of $k_B T \gtrsim 2.5$ keV and thus with fading emission lines, this degeneracy is partially lifted. For these clusters, the spectral fit is mainly guided by the position of the exponential cut-off, which is no longer obscured by the emission lines, and by the Fe-K line, which increases in strength with increasing cluster temperatures. However, when we consider clusters with even higher masses of $M \gtrsim 10^{15}$ $M_\odot$ as well as higher redshifts, which of the two competing effects, higher temperatures or higher redshifts, dominates the shift of the exponential cut-off?

To answer this question, we investigated the position of the exponential cut-off in dependence on the cluster mass and redshift for clusters with roughly the same number of source counts. As displayed in

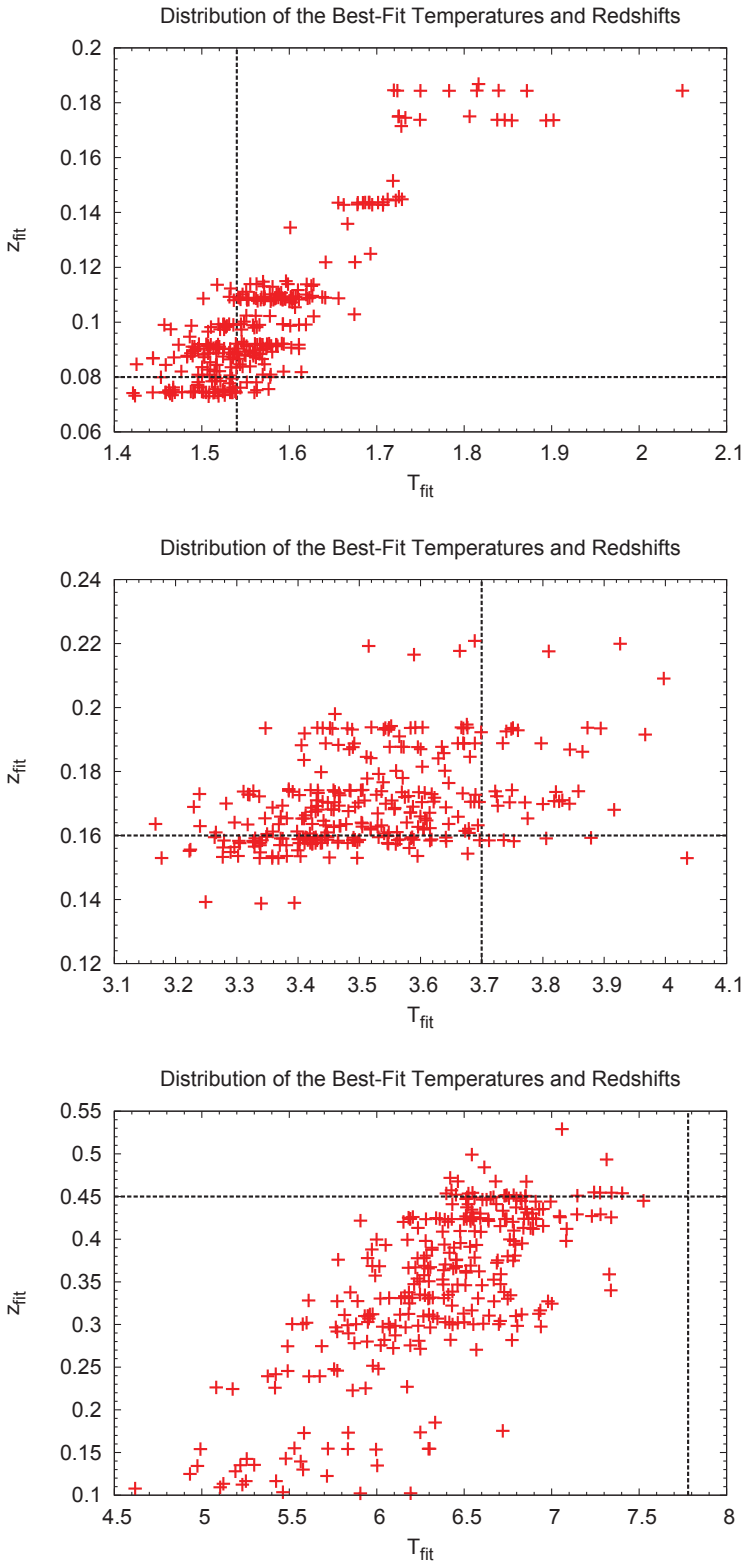

Figure 4.17: Distribution of the best-fit temperatures and redshifts for three different clusters in the deep exposure fields, each with roughly 5,000 counts, but with different cluster masses and temperatures. From top to bottom: $\log(M/\mathrm{M}_\odot) = 13.75, 14.35, 14.8$. The horizontal and vertical lines indicate the input redshifts and temperatures, respectively. The low and high mass parameter set is rejected from the analysis due to large numbers of catastrophic failures. For these cluster masses, the correlation between the fit values of the temperature and the redshift emphasises the degeneracy between these two properties.

Figs. 4.3 - 4.8, the contour lines of constant counts can be approximated as linear functions with a slope of $m = 1$. Moving up along this contour line, both cluster mass and redshift increase by a factor of $\Delta = 10^{0.15} = 1.41$ with every pixel (compare Sect. 4.2.1). According to the emissivity of the thermal bremsstrahlung

$$\epsilon_\nu^{ff} \propto T^{-1/2} \cdot \mathrm{e}^{-\frac{h\nu}{k_B T}} \quad , \tag{4.11}$$

the position E of the exponential cut-off, where $\epsilon_\nu^{\mathrm{ff}} \propto 1/\mathrm{e}$, is proportional to the cluster temperature. When also considering the cluster redshift, the position of the cut-off shows the relation

$$E \propto \frac{T}{(1+z)} \quad , \tag{4.12}$$

such that the ratio between E_1 and E_2 for two neighbouring pixels along the line of constant photon counts derives as

$$\frac{E_2}{E_1} = \frac{T_2}{T_1} \cdot \frac{(1+z_1)}{(1+z_2)} = \frac{T_2}{T_1} \cdot \frac{(1+z_1)}{(1+z_1 \cdot \Delta)} \quad , \tag{4.13}$$

with $z_2 > z_1$. According to equation 4.1, the ratio between the two temperatures is defined by the $M-T$ scaling relation

$$\frac{T_2}{T_1} = \left(\frac{M_2}{M_1}\right)^{0.62} \cdot \left(\frac{\Omega_\mathrm{m} \cdot (1+z_2)^3 + \Omega_\Lambda}{\Omega_\mathrm{m} \cdot (1+z_1)^3 + \Omega_\Lambda}\right)^{0.32} \tag{4.14}$$

$$= \Delta^{0.62} \cdot \left(\frac{\Omega_\mathrm{m} \cdot (1+z_1 \cdot \Delta)^3 + \Omega_\Lambda}{\Omega_\mathrm{m} \cdot (1+z_1)^3 + \Omega_\Lambda}\right)^{0.32} \quad . \tag{4.15}$$

Combining expressions 4.13 and 4.15, we obtain the final ratio of the position of the exponential cut-offs along the line of constant photon counts

$$\frac{E_2}{E_1} = \Delta^{0.62} \cdot \left(\frac{\Omega_\mathrm{m} \cdot (1+z_1 \cdot \Delta)^3 + \Omega_\Lambda}{\Omega_\mathrm{m} \cdot (1+z_1)^3 + \Omega_\Lambda}\right)^{0.32} \cdot \frac{(1+z_1)}{(1+z_1 \cdot \Delta)} \quad . \tag{4.16}$$

A graphical analysis of this function indicates a ratio of $\frac{E_2}{E_1} > 1$ for our choice of $\Delta = 1.41$ and for the entire simulated redshift range. This result emphasises the shift of the exponential cut-off to higher energies for clusters with increased masses and redshifts along the lines of constant photon counts. In fact, for all $\Delta > 1$ the result of $\frac{E_2}{E_1} > 1$ holds true. For clusters with masses of $\log(M/\mathrm{M}_\odot) \gtrsim 15$ for which catastrophic failures occur in the simulation with unavailable redshift the exponential cut-off is located at energies of $E \gtrsim 8$ keV and thus out of the spectral fitting range. The difficulty in the spectral fit that thus arises is additionally appended by the decreasing S/N-ratio for clusters with the same number of source photons, but with increasing redshifts. This evolution of the S/N-ratio with increasing redshift is explained by the increasing extent of the cluster, from e.g. $R_{500} \approx 5.7$ Mpc for a cluster with ~ 1000 counts at $z \approx 0.08$ to $R_{500} \approx 8.8$ Mpc at $z \approx 0.45$, and the consequently rising background emission.

4.5.4 Influence of the Analysis Strategy

To test the reliability of our predictions, we analysed the influence of the simulation setup on our results. For several parameter sets we reran the simulation with 500, 700 and 1000 repetitions and compared the outcome to the results for 300 repetitions. The changes in the biases and in the relative uncertainties for temperature and redshift are only a few percent, and these deviations become negligible for clusters with relative uncertainties of $\lesssim 0.1$. An equivalent development is observed when altering the number

of steps within the steppar-fit. Even though with varying numbers of fitting steps the results show deviations of up to 20% for parameter sets with high relative uncertainties, the results for clusters with high precise properties are similar. We therefore conclude that the parameter space of cosmologically interesting clusters with relative uncertainties of $\lesssim 0.1$ in their properties is independent of the number of repetitions and of the number of steps in the more dimensional steppar-fit. For these clusters already 300 repetitions for the realisation of each parameter set yield a proper statistical, Gaussian-like distribution of the fit results.
However, a small bias might arise in the steppar-fit with variable redshift for clusters with local redshifts of roughly $z \lesssim 0.1$. This bias is observed for clusters with unknown redshift and with low masses of $\log(M/\mathrm{M}_\odot) \lesssim 14$ and for intermediate mass clusters in the deep exposure fields (compare Figs. 4.7 and 4.8). For these clusters statistical artefacts might arise (compare Fig. 4.17 Top) since too little information is available for the fit. We ran a thorough investigation for the fitting statistics of these clusters and conclude that cluster with artefact features are generally rejected because of large numbers of catastrophic failures. Even though, these clusters show a strong deviation between their input redshift and the starting value for the fit with $z = 0.3$, the fit is not improved by an adaptation of the starting value.
Generally, the simulated precisions and accuracies are not necessarily influenced by the starting values of the spectral fit, so that we applied commonly observed values of $\mathrm{k_B}T = 2$ keV and $z = 0.3$ for the start of the fit. Only in the simulations with unknown cluster redshift, the number of rejected data sets for both intermediate- and high-mass clusters (e.g. Fig. 4.8) at their highest simulated redshifts can be improved if we choose values close to the input parameter values for the start of the fit. In this case, a strong decrease in the biases and in the relative uncertainties of up to $\lesssim 25\%$ of the former value is observed. This results in fewer catastrophic failures in the mentioned mass ranges, and for the deep exposures the parameter space of clusters with high-precision properties increases to higher redshifts. However, with this adaptation of the fitting strategy, the percentage of precision clusters changes only for the deep-exposure fields and only by $< 1\%$. According to this, our setup, which does not require any knowledge on the input properties, presents a reliable estimate of the number of detected clusters with precise characteristics.
To improve the analysis of future *eROSITA* clusters with unavailable redshift, we suggest to refit the spectrum for different starting redshifts, where the starting value of the temperature is adapted to the redshift via an $L_\mathrm{X} - T$ scaling relation (compare Lloyd-Davies et al. 2011). The fit that returns the smallest parameter uncertainties is expected to also record the highest parameter accuracy.
Finally, we also tested the influence of the definition for rejected pixels on our results, since we required a minimum of 80% of the repetitions to yield consistent and non-catastrophic data. This percentage emphasises that more than 20% of unreliable fit results is unacceptable. For an increased minimum percentage of accepted data to 90%, the simulation results for $t_\mathrm{exp} = 1.6$ ks and clusters with known redshift remain unchanged. Within the other simulations, more parameter sets with especially high redshifts are rejected, in particular, in the simulations with unknown redshift. However, this development reduces the parameter space of clusters with known redshift and relative temperature uncertainties of $\lesssim 10\%$ only insignificantly.

4.5.5 Remarks on the Cosmological Interpretation

Our simulations present an overview of the number of clusters for which *eROSITA* will be able to obtain precise data. However, the future data reduction very likely requires individual models for each observed cluster, which include individual background emissions, for instance, and might thus slightly alter the presented numbers of clusters. In the previous sections of our discussion, we already concluded

these numbers to be only insignificantly influenced by an incorrectly assumed metallicity of the cluster and by the background emission. For a possible evolution of the metallicity with redshift, however, the number of high- and intermediate-redshift clusters with precise properties might decrease depending on the scale of the evolution.
Additionally, the emission of a possible central AGN in clusters needs to be considered in the analysis of observed data, especially for deep exposures. In these observations, bright central AGN can impede the extraction of cluster spectra and even the detection of the clusters as extended source. Currently, investigations on the efficiency of different source-detection algorithms are conducted. Meanwhile, we reconsidered the simulation results for the deep-exposure fields, which indicated the temperatures to be available with high precision up to the highest redshifts for high mass clusters (Fig. 4.4). Taking into account the above mentioned AGN confusion, a detection of precise temperatures up to a redshift limit of $z \approx 1$ presents a more reliable and conservative estimate for those high-mass clusters. With this redshift limit, however, the total number of precise clusters in the deep-exposure fields remains the same since only very few clusters with the highest masses of $M \gtrsim 10^{15}$ $M_\odot$ are found at $z \gtrsim 1.0$ (compare Fig. 4.15), in particular when limited to the one hundred square degrees for the deep-exposure fields. The estimation of precise redshifts in these fields is already limited to $\log(z) \lesssim -0.35$, $z \lesssim 0.45$ because of catastrophic failures (compare Fig. 4.6) and is thus not influenced by AGN confusion.

Recent simulations have shown the possibility of cosmological estimates with only luminosity and redshift information of the galaxy clusters available (Pillepich et al. 2012). Redshift information on *eROSITA* clusters will be obtained through optical follow-up observations shortly after the launch of the mission. This work now discusses the number of clusters for which precise temperatures will be observed. In an upcoming work we will qualitatively test the improvement in the cosmological uncertainties with the help of these additional information. The cosmological analysis of cluster data is especially sensitive to the information coming from massive clusters. Our simulations now indicate that at the beginning of the *eROSITA* survey precise information on massive clusters are rather difficult to obtain (compare Sects. 4.3.1 & 4.5.3). X-ray follow-up observations with eROSITA and with other instruments, such as *XMM* or *Astro-H*, will determine the surface brightness and the temperatures of massive clusters soon after this. These information will then set tighter constraints on the cosmology, even though not for all of the massive clusters temperature estimates will be available because ofthe large numbers of observed clusters.

4.5.6 Comparison between Different Scaling Relations

We compared five commonly applied scaling relations (Maughan 2007; Pratt et al. 2009; Vikhlinin et al. 2009a; Mantz et al. 2010a; Reichert et al. 2011) with one another and analysed the effects of a change in the scaling relation on the results of our simulations. For a recent review on cluster scaling relations see Giodini et al. (2013).
The five different $M - T$ relations deviate from one another especially for the smallest cluster masses of $\log(M/M_\odot) \lesssim 14$ with an increasing inconsistency for increasing redshifts. The scaling relation reported by Mantz et al. (2010a) shows the strongest increase of the temperature with cluster mass for a fixed redshift, and the relation given by Maughan (2007) presents the shallowest slope. The relation by Reichert et al. (2011) approximates an average value for the slope. The luminosities computed by means of the different considered scaling relations for a fixed cluster mass are very similar at local redshifts (Fig. 4.18). For a cluster mass of $\log(M/M_\odot) = 14$ they start to deviate from one another for $\log z \gtrsim -0.5$, $z \gtrsim 0.3$, where this deviation starts at lower redshifts for declining cluster masses. Within this comparison, the $M - L_X$ relation reported by Reichert et al. (2011) exhibits the most moderate

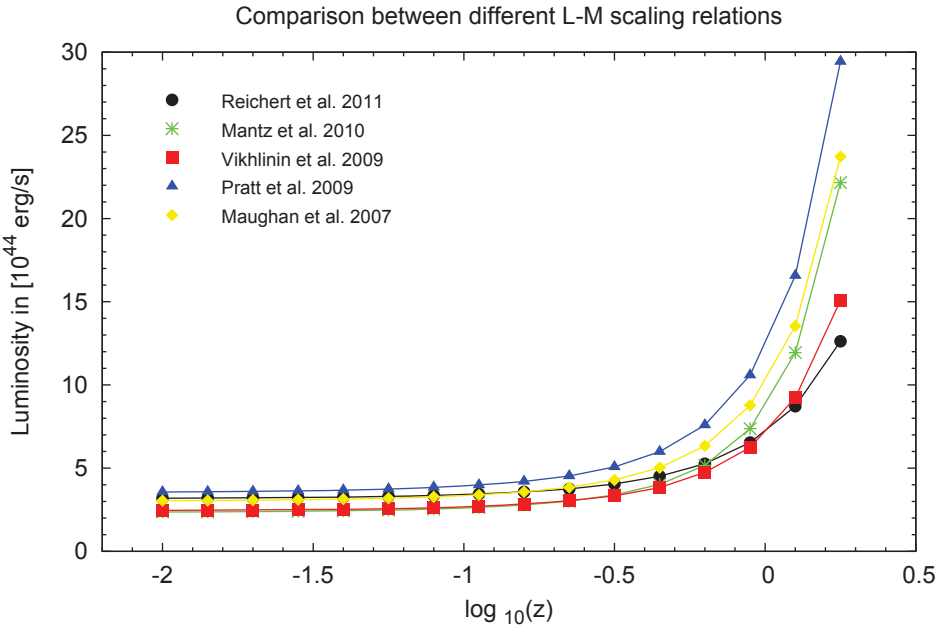

Figure 4.18: Luminosity in dependence on the cluster redshift for different scaling relations and a cluster mass of $M \approx 5 \times 10^{14}$ $M_\odot$. The luminosities are computed within the energy range of (0.1 − 2.4) keV for all relations.

evolution of the luminosity with redshift. The shallow development of the $M - L_X$ relation with redshift given by Reichert et al. (2011) favours the application of this scaling relation because distant clusters with $z \gtrsim 0.3$ show lower luminosities than the other scaling relations and thus fewer source counts. This characteristic is especially important for simulating the deep-exposure fields, in case the cluster redshift is available. In the remaining three simulations, the parameter space of precise cluster porperties is mainly located at lower redshifts for which all considered scaling relations are similar.
The galaxy cluster sample on which Reichert et al. (2011) based their findings covers the largest mass and redshift range with $M = (5 \times 10^{13} - 3 \times 10^{15})$ $M_\odot$ and $z \leqslant 1.46$, such that we only required a small extrapolation of this scaling relation to cover our simulated mass and redshift range. According to this aspect and to the evolution of the relations, the scaling relations applied by Reichert et al. (2011) describe the most conservative approach in terms of characterising high-z clusters.
The deviations in the individual scaling relations also result in differences in the distribution of clusters with mass and redshift (Appendix C.2). For example, because of the slightly lower luminosity in the scaling relation reported by Vikhlinin et al. (2009a) at the local redshifts, the total number of clusters decreases to $\sim$ 103,700 compared to $\sim$ 113,400 clusters for the relations given by Reichert et al. (2011) when applying the same cosmology for both relations. However, the number of clusters with precise properties from *eROSITA* data is similar for both scaling relations with a deviation of $< 2\%$. For example, for the scaling relation given by Vikhlinin et al. (2009a), this deviation results in 1,700 clusters with precise temperatures and already known redshifts for the all sky survey compared to the 1,670 clusters for the relation by Reichert et al. (2011).

4.5.7 Comparison with Other Works

Similar to the findings by Lloyd-Davies et al. (2011), Planck Collaboration et al. (2011) and Yu et al. (2011), among others, our simulations depicted cluster X-ray spectra as sensitive estimators of the redshift of the object. However, our simulations forecast the determination of cluster redshifts for the *eROSITA* instrument and for exposure times as short as $t_{\rm exp} = 1.6$ ks for the first time. Our findings for the *eROSITA* deep fields are similar to those reported by the Planck Collaboration et al. (2011), who derived precise redshifts up to distances of $z = 0.54$ for $t_{\rm exp} = 10$ ks with the XMM-Newton instrument, when not correcting for the underestimation of the uncertainties. In addition, like these publications, our work shows a decrease of the fit accuracy for the analysis of cluster spectra with unavailable redshift.
We emphasise that the precision and accuracy of the cluster properties strongly depend upon the values of these cluster properties themselves and not only on the number of detected photons, equivalently to the analysis by Yu et al. (2011). However, in contrast to their findings, our simulations predict X-ray redshifts to be available also for clusters with fewer than $1,000$ photon counts, if these clusters show temperatures of $k_B T \lesssim 5.5$ keV (Figs. 4.7 & 4.8). This aspect is explained by the difference in the instrumental spectral responses between *eROSITA* and *Chandra*, on whose data Yu et al. (2011) base their analysis. For two clusters with the same total number of detected photons, *eROSITA* will show more photons in the soft-energy band, which improves the fitting statistics especially for the low-temperature clusters above.
Our expected number of $\sim 113,400$ *eROSITA* clusters is increased by $\sim 15\%$ compared to the analysis by Pillepich et al. (2012), because this work applied the scaling relation by Vikhlinin et al. (2009a) and the cosmological model of the WMAP5 results (Komatsu et al. 2009, compare Sect. 4.5.6 & C.2) instead of the scaling relation by Reichert et al. (2011) used in our calculations. However, if we had based the computation on the same setup as Pillepich et al. (2012), we would have obtained a negligible deviation of only 1% from their results, which emphasises on the reliability of our code.

4.6 Summary and Conclusions

The upcoming *eROSITA* instrument presents a powerful tool for testing our current cosmological model and especially for studying the nature of dark energy by investigating the distribution of galaxy clusters with mass and redshift. Moreover, it will allow studying cluster physics, for example in terms of scaling relations, in unprecedented detail. With the simulations we presented, we predict the accuracy and the precision with which the *eROSITA* instrument will be able to determine the cluster temperature and redshift, and we introduce the number of clusters for which these properties will be available.
The highest precision and accuracy of the temperature and redshift were obtained for clusters at the most local redshifts. In general, the precision and the accuracy of the cluster properties did not only show a dependence on the number of detected photons, but also on the cluster properties themselves, especially on the redshift. For the average exposure time during the *eROSITA* all-sky survey, high-precision temperatures will be available for clusters as distant as $z \lesssim 0.16$ and the instrument will allow for precise X-ray redshifts up to $z \lesssim 0.45$, where for the very local clusters the uncertainty in the redshift is even similar to optical photometric estimates. However, for the simulation with unknown cluster redshifts, catastrophic failures occurred within the spectral fit and limited the parameter space of high-precision properties, especially for the lowest and the highest masses $\log(M/M_\odot) \lesssim 14$ and $\log(M/M_\odot) \gtrsim 15$. These failures arise from the redshift as an additional free parameter in the fit and because of the thus resulting degeneracy between redshift and temperature. As *eROSITA* cluster spectra prove as sensitive estimators of the redshift for local clusters with intermediate masses, optical follow-up observations are most effective if they first cover clusters without reliable X-ray redshifts, and we predict that these will

preferentially be found above $z \approx 0.45$. Additionally, these follow-up observations will eventually allow for more precise redshift estimates also for clusters at lower redshifts.
Within the *eROSITA* deep-exposure fields, X-ray redshift and temperature information will be more strongly limited by catastrophic failures than for the lower exposure time. Because of this, precise X-ray redshifts are only observed to the same maximum distance as for the all sky survey. In this aspect, our simulations followed the conservative approach of no constraints on the starting values of the fit. However, the number of catastrophic failures for the spectral fit of intermediate- and high-mass clusters can be reduced if additional information on the starting values, for example through coupling of the fit parameters by the $L_X - T$ relation or with the help of first redshift estimates from shallow optical surveys, are available.
If the redshift of the clusters in the deep-exposure fields is known, the percentage of clusters with precise temperatures still increases significantly to the highest redshifts. Even though these deep fields only cover a small sky fraction, the findings for these regions shed light on the expectations for the subsequent pointed-observation phase.
The entire parameter space of clusters with precise properties displays great parameter accuracies, such that for these clusters no parameter bias needs to be corrected for. Only for the long exposure times of $t_{exp} = 20$ ks the bias in the temperature needs to be considered for clusters with available redshifts at distances of $z \gtrsim 0.32$. We additionally introduced correction functions that need to be applied to spectral fits of clusters with a bias in their best-fit properties. To analyse observed *eROSITA* data, these correction functions should be applied iteratively. During this procedure the analysis of spectral cluster data yields preliminary values of the cluster temperature, redshift and luminosity from which the total mass can be estimated. Implementing the redshift and the total mass, the correction functions will return a revised cluster temperature and redshift, which sequently describe a corrected total mass. These steps should be repeated until negligible changes of the properties are obtained with each iteration, and the final values can be adopted as best estimates.
Through our simulations, we also investigated the deviation in the uncertainties between the results by the *xspec* `error`-command and a statistical distribution. These corrections of the uncertainties need to be considered for the data analysis of clusters with unknown redshift independently of the precision in the cluster properties because *xspec* underestimates the statistical uncertainty.
In convolving the galaxy cluster mass function and scaling relations with the *eROSITA* response, we obtained the distribution of clusters with mass and photon counts as it will be observed by the instrument. Applying the scaling relations reported by Reichert et al. (2011), we expect *eROSITA* to detect $\sim 113,400$ clusters of galaxies in total with a minimum photon number of $\eta_{min} = 50$. Out of this total number of clusters, *eROSITA* will provide precise temperatures with $\Delta T / \langle T_{fit} \rangle \lesssim 10\%$ for $\sim 1,670$ new clusters in the all-sky survey, which is equivalent to a percentage of $\sim 1.5\%$ of the total amount of detected clusters. This *eROSITA* sample, consisting mainly of so-far unstudied clusters, will increase the current catalogue of clusters with precise temperatures by a factor of $5 - 10$ depending on the refered-to catalogue.
Large samples of precise and accurate cluster data as will be available from the *eROSITA* instrument are essential for computing tight constraints on the cosmological parameters. Because the current simulations on the constraints that *eROSITA* will implement on the cosmology do not yet include information on the cluster temperature yet (Pillepich et al. 2012), we aim to improve these constraints through our findings (compare Clerc et al. 2012) and will predict these improvements in our future work.

CHAPTER 5

Investigating Systematic Biases in the *eROSITA* Event Files of Galaxy Cluster Observations and their Analysis

The considerations within the following chapter present an extension to the work in chapter 4, where we now emphasise on additional systematics, which might arise in the observation and analysis of *eROSITA* data. The tasks and aims of this project, as well as the approach for applying the simulation and the analysis software were designed by myself. Many of the results, however, were obtained by A. Wenzel in his bachelor thesis "Simulation and Analysis of *eROSITA* Galaxy Cluster Observations" (September 2014), with my supervision. Those results will be cited as Wenzel (2014) and are re-interpreted and re-discussed in the following chapter. Additionally, this work was based on intensive discussions with the developers of the applied software tools within the German *eROSITA* collaboration, especially with C. Schmid, T. Brand, H. Brunner, and T. Dwelly. Sect. 5.1 summarises the main theoretical aspects necessary for the study of this project, where a more detailed overview of the theoretical background is given in Sects. 2.7.2, 2.8 & 2.9.

Abstract

For the correct and robust interpretation of observational results, it is essential to understand and quantify the occurring systematics in the observation of the data as well as in its reduction. This aspect is of significant importance, especially for the study of precision cosmology, which will be performed e.g. by the up-coming *eROSITA* instrument. The main science driver of this telescope is to investigate the nature of dark energy by tracing the distribution of galaxy clusters in the Universe. After the observational power of galaxy cluster characteristics by this instrument has been analysed (Borm et al. 2014, comp. also chapter 4), we now emphasise on the possible bias in the cluster characteristics arising from systematics in the observation of the data and in the data reduction software.
For a set of galaxy clusters with different cluster masses and redshifts, *eROSITA* event files are simulated, based on the software *SIXTE* (*Simulation of X-ray Telescopes*) (Schmid, C. 2008; Schmid 2012). These event files are then reduced by means of the future *eROSITA*-tools within *eSASS* (*extended Science Analysis Software System*) to extract the cluster spectra. Thereafter, we perform a spectral analysis to re-obtain the cluster temperatures and compare the results to those presented in Borm et al. (2014) (comp. also chapter 4) to quantify the influence of these two software programmes on the measured

temperature precision and accuracy. At the same time, this approach allows for a more realistic treatment of the extracted source as well as of the background spectra.
We find that precise temperature information with relative uncertainties of $\Delta T/\langle T_{\rm fit}\rangle \lesssim 10\%$ will be available for galaxy clusters up to redshifts of $z \approx 0.06$, where the applied software influences the study of precise cluster temperatures only insignificantly. However, a bias between the input and the best-fit temperatures is estimated, which requires a correction also in the data analysis for precise clusters.
In summary, this project allows us to quantify several systematic uncertainties in the data simulation and reduction tools for *eROSITA* and to improve these tasks to decrease the bias in the galaxy cluster characteristics. Though, a progress in the temperature accuracy still needs to be achieved, the current *eROSITA* analysis tools already yield promising results and underline the instrument's potential for cosmological studies.

5.1 Introduction

Within the last decades, a great improvement in precision cosmology could be accomplished by various cosmological probes, including galaxy clusters (e.g. Borgani & Guzzo 2001; Voit 2005; Vikhlinin et al. 2009b; Mantz et al. 2010b; Allen et al. 2011). As most massive virialised objects in the Universe, galaxy clusters trace the large scale structure (*LSS*) of the distribution of matter and thus the evolution of the Universe as a whole. The future X-ray instrument *eROSITA* will exploit this approach to study cosmology by observing a large sample of $\sim 100,000$ clusters of galaxies (Pillepich et al. 2012; Merloni et al. 2012). However, progress in the cosmological constraints is not only based on more powerful instruments and on larger data samples, but also on an advanced understanding of the observed data as well as of the systematics in the analysis.
The most important cluster characteristics for cosmological estimates are the cluster mass and the cluster redshift. The latter will be available from optical spectroscopic and photometric follow-up observations for almost the entire *eROSITA* cluster catalogue (e.g. Ebeling et al. 2013; de Jong et al. 2014; Crocce et al. 2015; Salvato 2015). Cluster masses, on the other hand, are indirectly accessible through more directly observed cluster properties. In X-rays, these include e.g. the luminosity and the temperature of the *intra-cluster medium* (ICM) (e.g. Sarazin 1986; Vikhlinin et al. 2009a), which are both estimated based on the cluster spectrum (comp. Sect. 2.7.2). Applying galaxy cluster scaling relations, the measured luminosity ($M - L_{\rm X}$ relation) and ICM temperature ($M - T_{\rm X}$ relation) then yield the required cluster mass in combination with the redshift (e.g. Vikhlinin et al. 2009a; Pratt et al. 2009; Mantz et al. 2010a; Reichert et al. 2011; Giodini et al. 2013).
The main science driver of the *eROSITA*-instrument is to study cosmology and especially the equation of state of dark energy with the help of galaxy clusters (Sect. 2.9). The instrument is scheduled for launch in early 2017 as a joint German-Russian mission. During its four years of all-sky surveys, the telescope will observe $\sim 100,000$ clusters of galaxies with masses above $M \gtrsim 5 \cdot 10^{13}\ {\rm M}_\odot/h$ and with at least 50 detected photon counts in the energy range between (0.5-2.0) keV (Pillepich et al. 2012). Based on this large catalogue and assuming only the cluster luminosities and redshifts to be available, we expect constraints on the nature of dark energy of $\Delta w_0 \approx 0.03$ (for $w_{\rm a} = 0$) and $\Delta w_{\rm a} \approx 0.20$ for a dark energy evolution as $w_{\rm DE} = w_0 + w_{\rm a}/(1+z)$ (Merloni et al. 2012, Pillepich et al., in prep.). Current surveys and data samples, e.g. from joint *Planck* cosmic microwave background, weak lensing, baryonic acoustic oscillation, and Hubble parameter measurements, yield weaker constraints on the dark energy of $\Delta w_0 = ^{+0.075}_{-0.080}$ (Planck Collaboration et al. 2015c).
As the $M - T_{\rm X}$ scaling relation is showing a smaller intrinsic scatter than the $M - L_{\rm X}$ relation in X-rays, additional cluster temperature information is expected to allow for tighter cosmological constraints (e.g.

Vikhlinin et al. 2009a; Mantz et al. 2010a; Allen et al. 2011; Clerc et al. 2012; Giodini et al. 2013). In a previous project, we estimated that precise and accurate ICM temperatures with relative uncertainties of $\Delta T/\langle T_{\rm fit}\rangle \lesssim 10\%$ will be available for a total of $\sim 2,000$ *eROSITA* galaxy clusters (Borm et al. 2014, comp. also chapter 4), including the *eHIFLUGCS* catalogue (Reiprich 2012) and assuming known redshifts for the clusters. Therefore, this new instrument will increase the current cluster samples with precise temperatures by a factor of $5-10$, depending on the referred-to catalogue. However, this computation focused on the analysis of available cluster spectra, whereas additional systematics might arise from the observations of the data themselves or from the extraction of the spectra from the initial raw data. Accordingly, the best possible precision and accuracy in the cosmological parameters is amongst others also dependent on the calibration and systematics of the data analysis.
To reduce these biases in the instrumental specific *eROSITA* software for extracting and analysing the spectra or for the observation of the raw data itself, we thoroughly inspected the corresponding data reduction steps. The observed raw data is stored in event files, which list the detected photons, including their coordinates of origin and their energy information. As these files are not available yet for the *eROSITA*-instrument, they were simulated for galaxy clusters with different masses and redshifts by means of the software *SIXTE* (*Simulation of X-ray Telescopes*) (Schmid, C. 2008; Schmid 2012). This software allows the creation of event files for various X-ray telescopes based on their instrumental characteristics, as e.g. the point-spread function and the energy resolution, the pattern distribution and the distinction between pointed and survey mode observations. Based on a generic Monte Carlo simulation, the expected observed photons are then distributed spatially and energetically. Applying the future *eROSITA* analysis software *eSASS* (*extended Science Analysis Software System*), source spectra were then extracted from these event files and were analysed to re-obtain the cluster characteristics. Following this methodology, the systematics in the analysis software were investigated by comparing the values of the best-fit cluster properties to the input values as well as to the results of the spectra-only analysis by Borm et al. (2014).
The outline of this chapter is as follows: Sects. 5.2 & 5.3 describe the individual steps to generate *eROSITA* event files, to extract the included cluster spectra, and to subsequently analyse these spectra. The following two sections present the analysis results as well as an investigation of the systematic uncertainties in the applied software tasks. Thereafter Sect. 5.6 discusses the obtained results and possible origins of the observed systematics. Finally, Sect. 5.7 summarises the simulation approach, its results as well as the software systematics and suggests further investigation procedures.
Throughout this work, we applied the scaling relations by Reichert et al. (2011), and a cosmology of $\Omega_{\rm m} = 0.3$, $\Omega_\Lambda = 0.7$, and $H_0 = 100{\cdot}h$ km/s/Mpc^2 with $h = 0.7$ for consistency with the work by Reichert et al. (2011). The spectra, which are defined during the simulation procedures, are based on the solar metallicity tables by Anders & Grevesse (1989) and the described cluster masses and radial extents are given as M_{500} and r_{500}, respectively, in comparison to the critical density $\rho_{\rm crit,z} = 3H^2(z)/(8\pi G)$.

5.2 Simulation of Event Files

5.2.1 Outline of the Simulation and Analysis Strategy

The general concepts of this work include the investigation of possible systematics, which might arise from a more realistic analysis procedure in general or from the two tools to simulate *eROSITA* survey event files and to extract source spectra from these files - the tools *SIXTE* and *eSASS*. Whereas *SIXTE* is developed to support the simulation of various X-ray instruments, *eSASS* is officially established for the reduction of the future *eROSITA* data under the responsibility of H. Brunner and the German *eROSITA*-Consortium. However, we focused on the application of only the *SRCTOOL*-task within *eSASS* for

Table 5.1: Summary of the details for simulating the event files and analysing the extracted spectra. The horizontal lines distinguish between the different steps in this computation.

Set-up	Input
Observation mode	Survey
Event file emission	galaxy cluster + X-ray background + particle background
Instrumental response (event file simulation)	"erosita_iv_1telonaxis_ff.rsp" + vignetting
Event file size	3.6×3.6 deg^2
Exposure time	$t_{\rm exp} \approx 1.6$ ks
Energy range	$(0.3 - 8.0)$ keV
Instrumental response (spectral extraction)	"erosita_iv_1telonaxis_ff.rsp"+vignetting
Instrumental response (spectral analysis)	"erosita_iv_7telfov_ff.rsp"

the extraction of the source spectra. For both tools *SIXTE* and *SRCTOOL*, the versions of May 2014 were applied. The spectral analysis was managed by the *HEASARC* (*High Energy Astrophysics Science Archive Research Center*) tool *xspec* (Arnaud 1996), version 12.7.0.
The steps from the simulation of the event files to the final analysis read as follows

1. Defining the characteristics of the galaxy clusters to be simulated in the event files as well as of the X-ray background observed by *eROSITA*.
2. Creating the input files in the *SIMPUT*-format (*SIMulation inpPUT*) for the event simulation.
3. Simulating the survey event files with *SIXTE*, where the same source is modeled 108 times for good statistics.
4. Defining the extraction regions for the source spectra as well as for the background spectra.
5. Extracting the spectra by means of *SRCTOOL*.
6. Spectral analysis within *xspec* to re-obtain the ICM temperatures.
7. Analysing the best-fit temperatures and their uncertainties.

These steps will be elaborated in more detail in the subsequent sections, where the main set-up is summarised in Tab. 5.1.

5.2.2 Cluster Characteristics

For the simulation of the event files, we defined a sample of in total 19 distinct galaxy clusters with different combinations of cluster mass and redshift, where we included masses of $\log_{10}[M/M_\odot] = [10^{13.6}, 10^{13.9}, 10^{14.2}, 10^{14.5}]$ and redshifts of $\log_{10}[z] \in [-1.7, -0.5]$ with logarithmic steps of $\Delta(\log_{10} z) = 0.15$. These combinations present a subset of the (M, z)-sample studied in Borm et al. (2014) (Fig. 5.1) with a focus on investigating the parameter space of relative temperature uncertainties of $\Delta T/\langle T_{\rm fit}\rangle \lesssim 10\%$ and its boundaries. Following the approach in the above mentioned work, we also neglected clusters with less then 100 expected photons in the energy range between $(0.3 - 8.0)$ keV and assumed

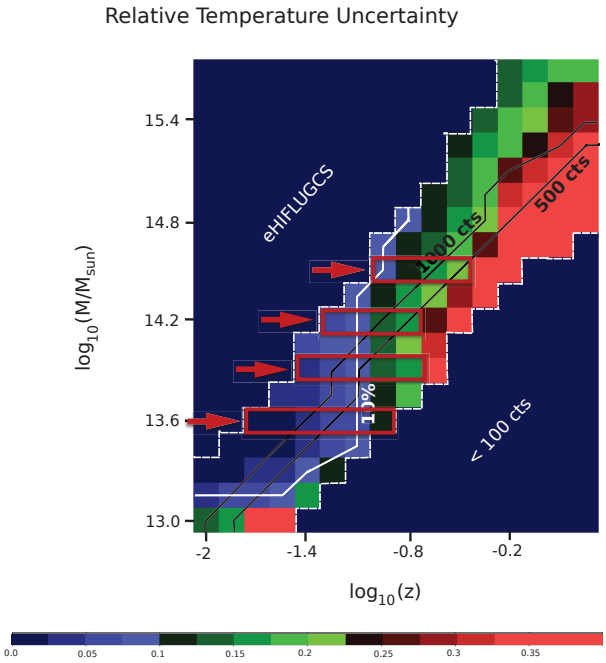

Figure 5.1: Expected relative temperature uncertainties for various clusters with different combinations of mass and redshift as simulated by Borm et al. (2014) (comp. Sect. 4.3.1 & Fig. 4.3). The colours of the pixels represent the relative temperature uncertainties, where clusters with less than 100 detected photons in the energy range between (0.3 – 8.0) keV as well as the *eHIFLUGCS* clusters were excluded in the computation. The combinations of masses and redshifts marked in red define the clusters, which were simulated in the event files.

temperatures to already be precisely available for all clusters with $F > 9 \cdot 10^{-12}$ erg/s in the energy range (0.1 – 2.4) keV. These clusters are included in *eHIFLUGCS* (Reiprich 2012), such that their ICM temperatures are precisely known from pointed observations with *Chandra*, *XMM* or *Suzaku*.
To simulate the photon events, which will be detected by *eROSITA* for the different galaxy clusters, their cluster spectra as well as their surface brightness profiles need to be defined. The cluster spectra are modeled analogously to those described in Borm et al. (2014) (Sect. 4.2.1) based on a *phabs*apec* emission, where the required ICM temperatures and X-ray luminosities were computed via the scaling relations by Reichert et al. (2011)

$$T \quad [\mathrm{keV}] \quad = \quad \left(\frac{M}{10^{14}\ \mathrm{M}_\odot} \cdot 3.44 \right)^{0.62} \cdot E(z)^{0.64} \tag{5.1}$$

$$L_\mathrm{X} \quad [10^{44}\mathrm{erg/s}] \quad = \quad \left(\frac{M}{10^{14}\ \mathrm{M}_\odot} \cdot 0.61 \right)^{1.92} \cdot E(z)^{1.7} \quad , \tag{5.2}$$

with $E(z) = (\Omega_\mathrm{m} \cdot (1+z)^3 + \Omega_\Lambda)^{1/2}$ and the bolometric luminosity L_X in the energy range (0.01-100.0) keV. Additionally, we applied a redshift independent metallicity of $A = 0.3\ \mathrm{A}_\odot$ for the cluster ICM (e.g. Arnaud et al. 1992; Mushotzky & Loewenstein 1997), in accordance to the argumentation given in Sect. 4.2.1 & 4.5.2. The absorption of the cluster emission by the galactic foreground was modeled for a neutral hydrogen column density of $N_\mathrm{H} = 3 \cdot 10^{20}$ particles/cm^2 (Kalberla et al. 2005).

The radial extent of the simulated galaxy clusters was interpreted as

$$r_{500} = \left(\frac{3}{4\pi} \cdot \frac{M_{500}}{500 \cdot \rho_{\mathrm{crit,z}}} \right)^{1/3} \quad , \tag{5.3}$$

with an equivalent angular extent of

$$\alpha = \frac{r_{500}}{D_{\mathrm{A}}} \quad , \tag{5.4}$$

considering the angular diameter distance D_{A} (comp. Eqs. 2.25 & 4.7).
The X-ray surface brightness profile $S_{\mathrm{X}}(R)$, on the other hand, is defined as a β-profile (Cavaliere & Fusco-Femiano 1976)

$$S_{\mathrm{X}}(R) = S_{\mathrm{X,0}} \cdot \left(1 + \frac{R^2}{r_{\mathrm{c}}^2} \right)^{-3\beta+\frac{1}{2}} \quad , \tag{5.5}$$

with the projected radius R from the cluster centre (comp. also Eq. 2.63). The core radius r_{c} and the β-parameter were expressed by commonly observed values of $r_{\mathrm{c}} = 0.1 \cdot \alpha_{500}$ and $\beta = \frac{2}{3}$ (Voit 2005). Images corresponding to these surface brightness profiles were computed by means of the tool *dis45x*, which is commonly applied in the analysis of *Suzaku* data.

5.2.3 The *eROSITA* Background

The background, which is expected to be observed by *eROSITA*, is expressed by the following components

$$\underbrace{\textbf{phabs}}_{1} * (\underbrace{\textbf{powerlaw}}_{2} + \underbrace{\textbf{apec}}_{3} + \underbrace{\textbf{apec}}_{4}) + \underbrace{\textbf{powerlaw}}_{5} \quad ,$$

including 1) the absorption by the neutral gas in our Galaxy, 2) the unresolved cosmic X-ray background, that is distant AGN, 3) the plasma emission by the hot ISM and 4) the emission by supernova remnants in our Galaxy, as well as 5) the particle background. A more detailed description of the *eROSITA* background is presented in Sect. 4.2.2 and especially in Tab. 4.1. The first four components constitute the X-ray background and were defined based on the work by Lumb et al. (2002). The instrumental particle background, on the other hand, which is induced by the interaction of cosmic rays with the detector material, was simulated by Tenzer et al. (2010) and starts to dominate the total background emission at energies above $\sim$ 2 keV. When simulating a realisation of the background emission, the first four components are convolved with the entire *instrumental response* (*RSP*), whereas the particle background is folded only with the *response matrix file* (*RMF*), since this emission is independent of the effective area of the mirrors (comp. Sect. 3.1.2). Following this concept, the total background emission shows count rates of 12 cts/s within the energy range between (0.3 − 8.0) keV, when observed over the entire *eROSITA* field-of-view (FoV) of 0.83 deg^2.
During the simulation of the event files, however, only the emission of the X-ray background was defined as a source with a flat surface brightness profile. The instrumental specific particle background was modeled by *SIXTE* itself.

5.2.4 Simulation Steps

The simulation of event files with *SIXTE* required a specific input format, named *SIMPUT* (*SIMulation inPUT*), for the source catalogue, which contained information on the source positions, on their instrument-independent spectra and on their flux within a specified energy range as well as on their surface brightness profile. Defining the different galaxy cluster coordinates and characteristics, as well as

the X-ray background emission, these input catalogues were generated within *SIXTE* (comp. appendix A.2). As the *eROSITA* event files were created to represent survey observations of the instrument, the coordinates of the galaxy clusters define the exposure time of the simulated event files based on the exposure maps of the survey. The objects in the catalogue were thus centred at $(0.0, 0.0)$ in equatorial coordinates, where exposure times of $t_{\mathrm{exp}} \approx 1.6$ ks during the total of four years of all-sky observations were expected (comp. Fig. 2.12). This value states the average effective observation time per field-of-view of the instrument (Pillepich et al. 2012). The spectral information as well as the surface brightness profiles were obtained as described in Sect. 5.2.2 and were attached for the *SIMPUT*-files.
To optimise the computing time for the event files, we uniformly distributed several realisations of the same galaxy cluster in one event file. Since the size of one survey observation is limited to 3.6×3.6 deg^2, the number of sources per event file depended on the angular extent of the clusters, where the spacing between the different sources was chosen to still allowed for both source and background extractions. Accordingly, distinct catalogues were defined for the galaxy clusters with different (M, z)-combinations. Having defined the source catalogues in the *SIMPUT*-format, seven event files were simulated within *SIXTE* for each catalogue with one event file for each *eROSITA*-telescope (comp. appendix A.2). During this process, the source as well as the background emission were convolved with the RSP of the instrument to yield a spatial and an energetic distribution of the observed photons. To model the RSP for a survey observation, *SIXTE* folds the instrumental resolution of a pointed observation with an assumed vignetting. Additionally, the particle background of the telescopes was summed to the photon events. This simulation of the event files was repeated for each catalogue to obtain a total of 108 realisations of the same cluster for good statistics. In general, we ensured a random variation in the distribution and in the number of observed photon counts between the seven event files of one simulation run as well as between the different runs for the same catalogue. Fig. 5.2 presents the image of an excerpt of an example event file for a cluster with $\log_{10}[M/M_{\odot}] = 14.5$ and $z = 0.11$. The position of the source is easily recognised as a rotational symmetric gathering of photon events, with the innermost green circle representing α_{500} of the cluster and the outer annuli defining the background region.

5.3 Analysis Procedure

5.3.1 Defining the Cluster and the Background Regions

To guide the extraction of source as well as of background spectra from the photon event lists, region files were defined. For the clusters, we applied circular regions, in analogy to the rotational symmetric β-profiles, and annuli around the sources for the definition of the background region. Commonly, when reducing observational data, the source position as well as the source region are selected by detection algorithms. These tools will also be included within the *eSASS* software, but were currently still under investigation by the *eROSITA* Collaboration. Accordingly, to focus on the systematics arising in the simulation of the event files and especially in the extraction of the spectra, we manually defined the region files based on the cluster characteristics.
The galaxy cluster regions were centred around the source coordinates with a radius of α_{500} (Eq. 5.4). This radius did not only represent our assumed cluster mass of M_{500}, but it also stated the limit for X-ray temperature measurements with the current instruments *XMM-Newton* and *Chandra* (Reiprich et al. 2013). Additionally, when applying a β-surface brightness profile as defined above for the galaxy clusters (Sect. 5.2.2), α_{500} contains $\gtrsim 90\%$ of the total number of expected source photons (comp. Sect. 5.6.2 & Fig. 5.6).
The background regions were selected as annuli around the individual sources and were also centred around the input cluster coordinates. The inner radius was chosen as $\alpha_1 = 1.14 \cdot \alpha_{500}$, whereas the outer

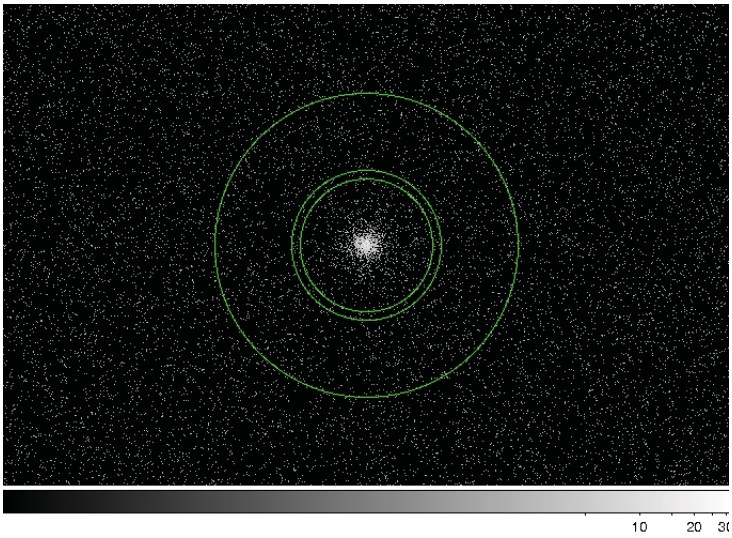

Figure 5.2: Image extracted from an event file simulated with *SIXTE* for a galaxy cluster with $\log_{10}[M/M_\odot] = 14.5$ and $z = 0.11$, while including both the X-ray as well as the particle background. The pixel colour represents the number of observed photons, where the colour brightens for an increasing amount of events. The galaxy cluster is easily detected as gathering of events with the source and the background region displayed in green as circle and as annuli, respectively. *Credit:* Wenzel (2014)

radius α_2 was computed such, that the annuli covered four times the area of the source region. This strategy ensured the background regions to contain at least 100 detected photons and a lower statistical scatter in the emission than in the source spectra. At the same time, the close location of the background regions to the sources allowed the distribution of a larger number of separate objects within the survey field of 3.6×3.6 deg^2.

5.3.2 Extracting the Spectra

To extract the spectra, we applied the task *SRCTOOL* within *eSASS* (comp. appendix A.3) and the region files defined above. The seven individual event files for the seven telescopes were analysed separately, as only the calibration file for a single telescope had been defined, yet. Analogous to the approach within *SIXTE* also during the spectral extraction the instrumental resolution for a survey observation was modeled as the resolution of a pointed observation convolved with a vignetting file. Finally, we obtained seven spectra for each defined region, where the spectra of the individual telescopes were stacked to mirror the survey data observed with the complete instrument, corresponding to the response "erosita_iv_7telfov_ff.rsp". Additionally, the statistical scatter in the observed photon numbers was thus decreased compared to the observation with only one *eROSITA* telescope (comp. Sect. 4.2).

5.3.3 Spectral Analysis

For the spectral analysis, the source spectra and the corresponding background spectra were read into the software *xspec*. The subsequent analysis steps were performed analogously to the reduction expressed in Borm et al. (2014) (comp. Sect. 4.2.3 & 4.2.4), so that we only repeat the basic concepts at this point. The background emissions were obtained in the spectral extraction within the annuli, whereas the spectra of the circular source regions contained a superposition of the cluster as well as of the background emission. To remove the latter, we applied the `backgrnd`-command, while referencing the spectra of

the annuli and accounting for the deviating area sizes of the two extraction regions. Accordingly, only a *phabs*apec* model was fit to the source spectrum, while leaving the ICM temperature as well as the spectral normalisation free to vary during the fit. The cluster redshift was assumed to be known and was set to the catalogue value, while the galactic hydrogen column density and the ICM metallicity were fixed to the values stated above (Sect. 5.2.2). The `steppar`-command was applied to improve the best-fit values, and the 1σ-uncertainty regions were computed by means of the `error`-command. Accordingly, for each (M, z)-combination, we obtained a list of 108 best-fit temperatures and normalisations, including the uncertainties on these properties.
Before the final analysis steps, all catastrophic failures were removed from the fit results, where two different types of failures were considered (comp. Sect. 4.2.4). In the following, three main results were computed:

- The relative temperature uncertainty $\Delta T/\langle T_{\mathrm{fit}}\rangle$: $\langle T_{\mathrm{fit}}\rangle$ was taken as the median of the best-fit temperatures and ΔT was defined as symmetrised 1σ-region around the median, where $2 \cdot \Delta T$ contained 68% of the fit results.

- The temperature bias $\langle T_{\mathrm{fit}}\rangle/T_{\mathrm{input}}$: ratio of the median best-fit temperature and the input temperature for the emission model.

- The bias in the temperature uncertainties $\Delta T/\langle \Delta T_{\mathrm{error}}\rangle$: ratio of the 68%-uncertainty estimated from the distribution of best-fit values ΔT and the median of the values from the `error`-command $\langle \Delta T_{\mathrm{error}}\rangle$.

5.4 Results

5.4.1 Relative Temperature Uncertainties

The analysis results for the relative temperature uncertainties are presented in Figs. 5.3 & 5.4 for the individual cluster masses in dependence on the cluster redshift and on the number of extracted cluster photon counts, respectively. For clusters within the parameter space of $\Delta T/\langle T_{\mathrm{fit}}\rangle \lesssim 10\%$, we considered cluster temperatures to be precisely measurable, such that we marked this region of interest by a black dashed line. The presented dotted lines, smoothing the distribution of data points for the different cluster masses, display the general trend of the evolution of the relative temperature uncertainty with redshift and with the number of detected photon counts, respectively. However, they do not state a fit to the data.
In general, the relative temperature uncertainty improved with decreasing cluster mass as well as with decreasing redshift, where the influence of the redshift was more prominent (comp. Fig. 5.3). Up to redshifts of $z \approx 0.06$, precise temperatures will be available for all simulated cluster masses (Wenzel 2014). Also for farther redshifts, clusters of lower masses may still be located in the parameter space of interest.
Additionally, the temperature precision improved with an increasing number of detected photon counts, where the presented photon number in Fig. 5.4 represents the number of extracted galaxy cluster events in the chosen source region. However, as the temperature precision depended more strongly on the cluster mass in this analysis, a well-defined photon number, above which precise temperatures are obtained, could not be quantified. For example, for clusters with masses of $M = 10^{13.6}\ \mathrm{M}_{\odot}$, already ~ 200 photon counts sufficed for a precise temperature estimate, whereas for clusters with $M = 10^{14.5}\ \mathrm{M}_{\odot}$, more than $\sim 5,000$ events were required to yield the same precision.
In summary, the relative temperature uncertainties mainly depended on the cluster mass, and especially

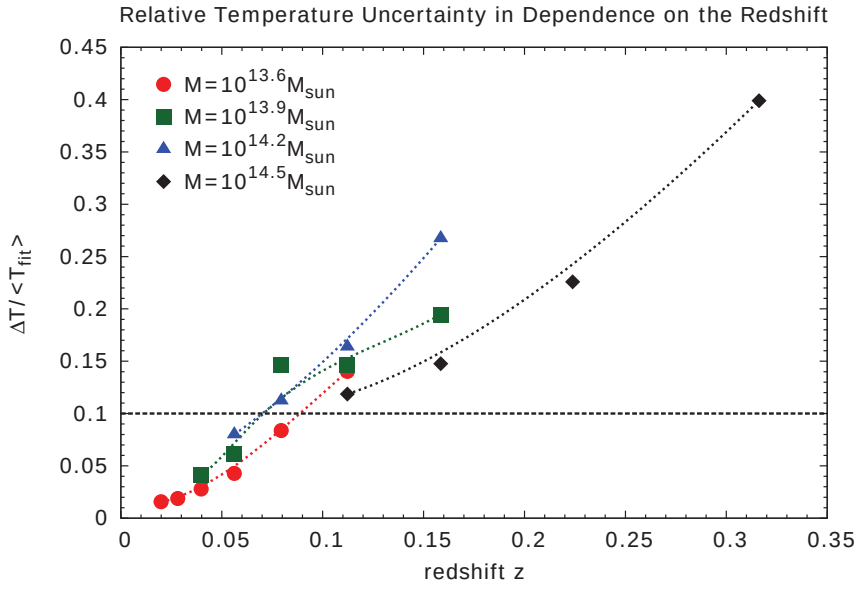

Figure 5.3: Simulated relative temperature uncertainties $\Delta T/\langle T_{\mathrm{fit}}\rangle$ in dependence on the cluster redshift for the four considered cluster masses. The region of interest, $\Delta T/\langle T_{\mathrm{fit}}\rangle \leq 0.1$, is marked by the dashed black line. The smooth connecting curves between the data points of the individual masses (dotted lines) display the general trend of the evolution with redshift. *Credit:* Data taken from Wenzel (2014)

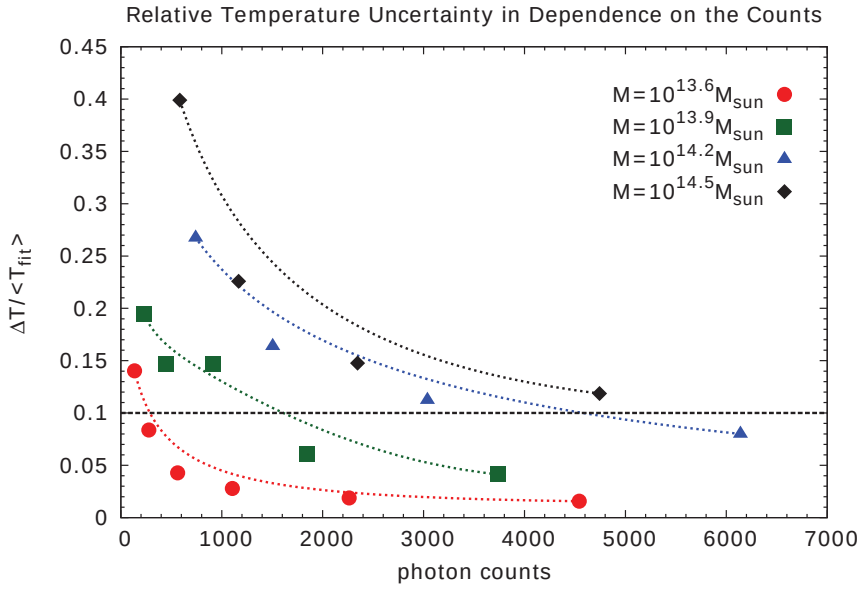

Figure 5.4: Simulated relative temperature uncertainties $\Delta T/\langle T_{\mathrm{fit}}\rangle$ in dependence on the extracted number of cluster photons for the four considered cluster masses. The description of the dotted and dashed lines are analogous to Fig. 5.3. *Credit:* Data taken from Wenzel (2014)

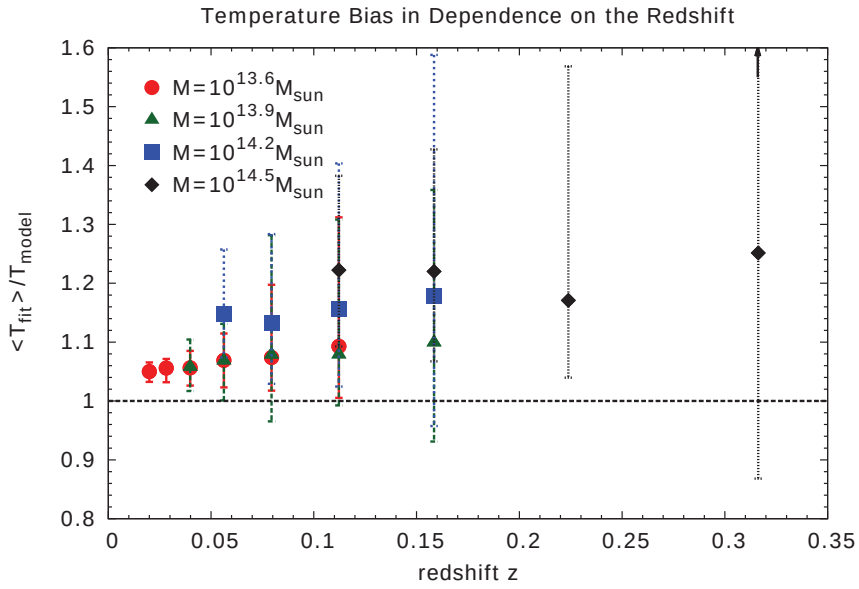

Figure 5.5: Bias between the best-fit ICM temperature and the model temperature in dependence on the redshift for the different cluster masses. The error bars represent the 68%-uncertainties. For all (M, z)-combinations, the best-fit temperature overestimates the model value. *Credit:* Data taken from Wenzel (2014)

on the cluster redshift, where the latter was the most significant characteristic to define, for which clusters precise temperatures will be available with *eROSITA*.

5.4.2 Temperature Bias

The bias in the best-fit temperatures was defined as the ratio between the median of the best-fit temperatures $\langle T_{\mathrm{fit}} \rangle$ and the initial model temperature T_{model} and was i.a. computed in dependence on the cluster redshift and on the cluster mass (Fig. 5.5). For all simulated (M, z)-combinations, the spectral fit overestimated the model temperature, where in general the bias increased with increasing cluster mass and with increasing redshift (Wenzel 2014). The same trend was also observed for the uncertainties on the bias. However, for the larger cluster masses of $M \gtrsim 10^{14.2}$ $\mathrm{M}_\odot$ the dependence on the redshift became negligible, whereas for the low cluster masses the dependence on the cluster mass seemed to disappear. The bias remained below $\sim 10\%$ for the simulated cluster masses $M = 10^{13.6}$ $\mathrm{M}_\odot$ and $M = 10^{13.9}$ $\mathrm{M}_\odot$ for all considered redshifts. The highest cluster mass, on the other hand, yielded biases of up to $\sim 25\%$. What is more, the number of photon counts showed only an insignificant effect on the temperature bias with a slight improvement in the bias for an increasing number of observed events.
Accordingly, we considered the bias to be negligible and of the order of only a couple of percent for redshifts of $z \lesssim 0.04$. In comparison to the results of the relative temperature uncertainties, we thus concluded that not for all clusters with precise temperature estimates also accurate temperature values will be obtained. For the precise clusters above $z \approx 0.04$, biases of up to $\sim 15\%$ need to be corrected for.

5.4.3 Bias in the Temperature Uncertainties

In addition to the bias in the best-fit temperatures, also the bias in the uncertainty, computed by the *xspec* `error`-command, was quantified as $\Delta T/\langle\Delta T_{\rm error}\rangle$, which is the ratio of the uncertainty defined by the distribution of best-fit values ΔT and the median uncertainty obtained from the `error`-command $\langle\Delta T_{\rm error}\rangle$. This bias is an important property for the interpretation of observed data as only the uncertainty computed within *xspec* is available, though ΔT follows more reliable statistics. Different than the previous results, the bias in the uncertainty showed no well-defined dependence on the redshift or the cluster mass, but generally decreased with an increasing number of detected photons (Wenzel 2014). In summary, this bias was of the order of $\pm 15\%$ for most of the inspected (M, z)-combinations and averaged to a ratio of ~ 1.0 for the 19 considered clusters. However, for the clusters with the lowest number of observed photons, the bias may increase up to $\sim 25\%$ with an underestimation of the true uncertainty by the `error`-command. Accordingly, the bias in the temperature uncertainties was generally negligible for clusters with precise temperature estimates, but the general underestimation of the true statistical uncertainties for clusters with few detected photon counts should be considered in the future data analysis.

5.5 Systematic Bias in the Applied Software

To investigate and interpret possible biases in the applied software, the results obtained from the above event file simulations and analysis were compared to the results by Borm et al. (2014), or equivalently to the results in chapter 4. As those findings were based on a spectral analysis only, deviations in the results were related to the current set-up of the event file simulations, of the handling of the raw data, or of the spectral extraction. To allow for this direct comparison, the analysis steps for the extracted spectra were performed completely equivalently to the procedures in the previous chapter. In general, a small deterioration in the precision as well as in the accuracy of the new results were expected, as the additional and more realistic simulation steps introduced further impacts on the data.
For the relative temperature uncertainties, we observed a comparable strong dependence on the cluster mass as well as especially on the cluster redshift for both approaches (comp. Sect. 4.3.1 & Fig. 4.3). The redshift cut at $z \approx 0.06$ in the current simulations, below which all clusters yielded precise temperatures, underestimated the findings for the spectral analysis only with $z \lesssim 0.08$. Also when considering the discrete values of the relative temperature uncertainties, the event file simulations resulted in a slightly reduced precision with a difference of approximately $\sim 3\%$ on average for clusters with $\Delta T/\langle T_{\rm fit}\rangle \lesssim 15\%$. However, this deviation increased with decreasing precision and showed differences of up to $\sim 20\%$ for the clusters with the least temperature precisions. As a whole, for the clusters of interest with precisions around $\Delta T/\langle T_{\rm fit}\rangle \lesssim 10\%$, the simulation procedure including the event file treatment behaved as expected and we explained the minor decrease in the precision by the additional steps in the data generation and reduction. We thus concluded that generally all clusters with precise temperatures in the spectra-only simulations (Sect. 4.3.1) also yielded precise temperatures with the extended and more realistic simulation procedure.
The bias in the temperatures, on the other hand, was strongly increased compared to the spectral analysis-only approach. Whereas for the low cluster masses of $M = 10^{13.6}\ \mathrm{M}_\odot$ and $M = 10^{13.9}\ \mathrm{M}_\odot$, the deviation between the two approaches presented values of $5 - 10\%$, the difference increased to up to $\sim 20\%$ and $\sim 25\%$ for the two larger cluster masses, respectively. The temperature bias now required a correction for most of the clusters within the parameter space of precise temperature estimates, which was not the case for the previous simulations. What is more, following the event file simulations, the best-fit value overestimated the model temperature, where we recorded an underestimation of the model

temperature in Sect. 4.3.2. Also other works, such as e.g. Yu et al. (2011), found an underestimation of the true ICM temperature. This systematic bias in the temperature estimates, which arose from the simulation of the event files and the extraction of the cluster spectra, asked for a further investigation of the simulation software and procedures. Several of these aspects are discussed in Sects. 5.6.3 & 5.6.5.
For the bias in the temperature uncertainties, the results by Borm et al. (2014) were mainly reproduced (comp. Sect. 4.3.3) with an average value of unity and a slightly increased scatter of ±15%. Also and similarly in both approaches, a tendency of an underestimation of the true statistical uncertainty by the `error`-command was observed as well as no general trend with neither the cluster mass nor the cluster redshift. In general, the little deterioration for the event file ansatz, which was especially observed for those clusters with the lowest number of detected photons, was expected due to the additionally performed simulation steps.
In summary, the slight decrease in the temperature precision as well as in the accuracy of the uncertainties was predicted and suggested no significant systematics to be present in the event simulation or the spectral extraction. However, the strongly increased bias in the temperature estimates required a further investigation of possible systematics in the two procedures.

5.6 Discussion

5.6.1 Understanding the Simulation Results

To explain the above described trends of the development of the relative temperature uncertainties and the biases, we summarised the guidelines for the spectral fit (comp. also Sect. 4.5.1). The fitting process was especially influenced by the spectral line emission complexes, which are dominant for ICM temperatures of $k_B T \lesssim 2.5$ keV, as well as by the exponential cut-off at large energies (comp. Fig. 2.8). The line complexes in general present the main constraining power for the different cluster characteristics.
In the above simulations, the cluster mass defined the ICM temperature through the applied scaling relations, where the temperature increased with the cluster mass for a fixed redshift (comp. Eq. 5.1). As the emission lines in the cluster spectra faded with increasing temperature, the fit results were degraded. At the same time, with increasing ICM temperatures, the exponential cut-off shifted to higher energies and thus out of the peak of the instrumental effective area, which is located at energies between (0.5−2.0) keV (comp. Fig. 2.11). These aspects explained the influence of the cluster mass on the observed temperature precisions and on the biases. However, an increased cluster mass also resulted in a raised luminosity and accordingly in a larger number of detected photons, which reduced the statistical scatter in the spectrum and thus supported the spectral fit (comp. Fig. 5.4). Following the simulation results, this improvement in the statistical scatter could not compensate for the effect of the fading emission lines and the shifting cut-off.
On the other hand, an increase in the redshifts yielded a reduction in the number of observed photon events, which decreased as $\propto 1/D_L^2$ with the luminosity distance D_L. Additionally, the energy stamp of the spectral features shifted with redshift as $\propto 1/(1+z)$.
As a whole, the computed relative temperature uncertainties as well as the biases were dependent on the complex interplay between different cluster characteristics, but especially on the cluster mass and the corresponding ICM temperature, and on the cluster redshift.

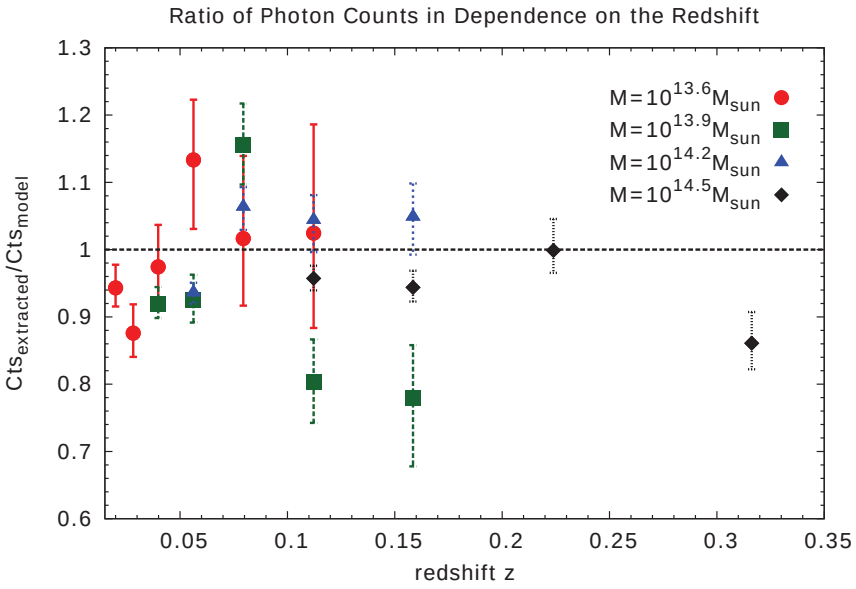

Figure 5.6: Ratio of the extracted number of cluster photon counts and the model photon numbers for all 19 distinct galaxy clusters in dependence on the redshift. The extracted number of counts is taken as the median value of the distribution of the analysis results of the (M, z)-combinations. *Credit:* Data taken from Wenzel (2014)

5.6.2 Choice of Spectral Regions

As the *eSASS* tasks for the source detection were still under investigation and their systematics were not completely quantified, yet, the source and the background regions were defined manually. This procedure also allowed us to focus only on the possible systematics in the event simulations and in the spectral extraction software. According to the observational power of the current X-ray instruments and the general definition of the cluster scaling relations (comp. Sect. 5.3.1), we described the source extent as α_{500}. In addition to the above argumentation, this choice of the cluster region was tested based on the number of included cluster photon counts.

To exclude any systematics in the total abundance of cluster photons, generated during the simulation of the event files, we simulated test clusters as single sources in the centre of the event files, while neglecting any background emission. In these cases, $\sim$ 100% of the expected model photon events were distributed in the simulated sky area. However, since the considered β-profiles for the surface brightness of the clusters showed no defined boundaries, several of the computed photon events were located outside our considered source region of α_{500}. Additionally, during the realistic simulations, the background emission had to be subtracted from the spectrum of the source region to yield only the cluster photon events. The close position of the background region to the source, which was required to allow for larger cluster catalogues to be simulated in the same survey field-of-view, resulted in few cluster photons of the order of $\sim$ 1% to be considered as background emission. Accordingly, the subtraction of the slightly overpredicted background from the source spectrum lead to a further reduction of the extracted cluster events. Despite these two aspects, for the majority of our simulated clusters, $\sim$ 90% of the expected cluster photon events were located within the defined α_{500}-region (Wenzel 2014), where this trend was observed independently of the cluster mass and of the cluster redshift (Fig. 5.6). For several (M, z)-combinations, higher numbers of the extracted photon counts were observed when compared

to the model number of photon events. A statistical scatter in the ratio between extracted and expected photon counts was expected since the generation of cluster as well as of background counts, of their energetic and their spatial distribution, was a random processes within *SIXTE*. However, averaging over 108 realisations of the same cluster observation did not compensate for this scatter, yet.
This is one of the origins for the observed increase in the uncertainties of the re-constructed cluster temperatures and is commonly encountered in the reduction of observed data. A possible small bias in the number of extracted counts, which originated from the spectral extraction software *SRCTOOL* is further investigated in the following section.

5.6.3 Bias in the Simulated Spectra?

To directly test whether the application of *SIXTE* and *SRCTOOL* resulted in systematics in the simulated cluster data, the shape of the extracted spectrum was compared to the model spectrum generated within *xspec* (comp. Figs. 5.7 & 5.8), where for this analysis several test cluster event files without any background emission were generated. Initially, the extracted spectrum showed a strong depletion of the photon events for energies below $E \approx 0.7$ keV with a complete depletion for $E \lesssim 0.3$ keV. These findings initiated a discussion on the value of the over-all energy threshold as well as on the treatment of split events for the future *eROSITA* data.
The energy threshold is defined based on the telemetry of the instrument, since the limited band width and communication time of the instrument ask for a restriction to transfer the data of only those photon events above a certain energy value. As a second influence on the event file spectra, split events need to be corrected for, which describe those detections for which the photon energy is distributed amongst different detector pixels. If these events are not considered, the spectrum is overestimated at the lower energies and underestimated at the higher energy end. They are commonly identified by their pattern and all involved pixels are flagged for this event and are neglected for the subsequent data analysis. To correct for these systematics, the occurrences of these events and their patterns need to be simulated thoroughly and accounted for in the instrumental response. Both aspects, the energy threshold as well as the treatment of the split events, may induce the observed bias in the cluster spectra.
Initially, the energy treshold value was set to $E = 0.3$ keV, which explained the observed total depletion of the extracted spectrum below these energies. In discussion with the involved software developers, this threshold was then shifted to $E = 0.1$ keV in order to reduce the bias in the spectra. The resulting extracted spectra with the adapted threshold is displayed in Fig. 5.8. Still, an underestimation of the extracted spectrum was visible for energies below $E \approx 0.4$ keV and also a further decrease in this threshold did not improve the observed bias. The software set-up with the implemented small spectral bias observed in Fig. 5.7 was then applied for the simulation and analysis of our cluster data, while the origin of this bias and its impact on the analysis results was further investigated.
Eventually, one systematic effect was discovered to originate from the conversion between the photon energy given in detector channels and in units of keV in the spectral extraction. In the observations, the energy of the detected photons is in general first listed in terms of detector channels and is later-on converted to values in units of keV. In the our applied *SRCTOOL* version, this conversion was defined based on the average energy resolution of the *eROSITA* channels. However, each of these individual channels shows slightly different resolutions, which are stored in the *response matrix file* (*RMF*)(comp. Sect. 3.1.2). Updating the *SRCTOOL* to account for the information of the RMF (version 08/2014), the bias in the spectra could almost be resolved completely (Fig. 5.8), and it was debated whether the remaining slight deviations were only a statistical artifact. Additionally, the influence of the split events treatment needs to be studied in further detail and has not been improved, yet.

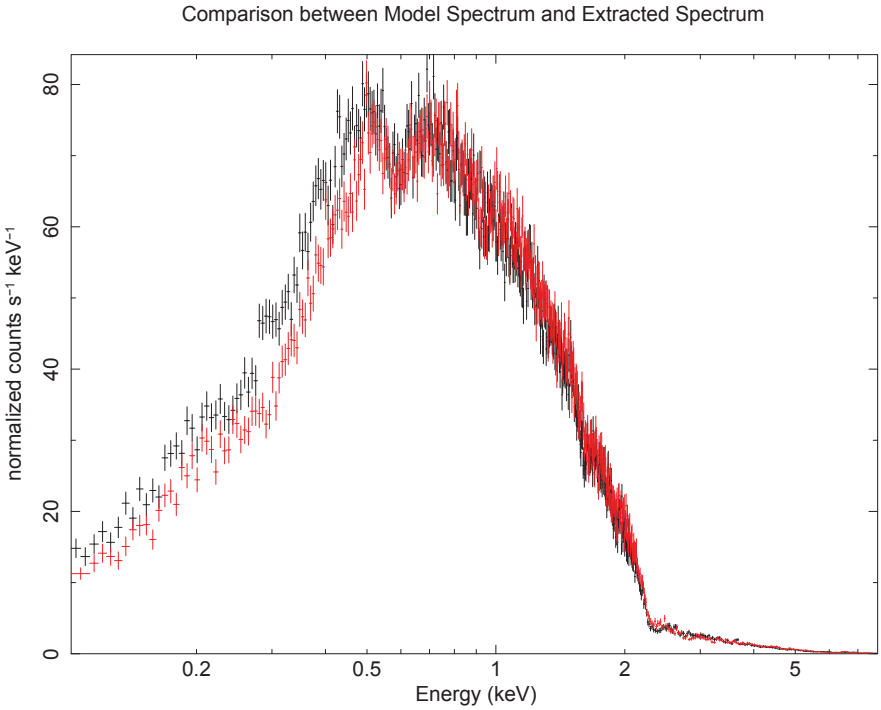

Figure 5.7: Comparison between the spectrum simulated within *xspec* in black and the corresponding extracted spectrum in red for a cluster of $M = 10^{15}$ $M_\odot$ at $z = 0.02$. The normalisation of the spectrum is artificially increased to reduce the statistical scatter in the photon counts and to allow for a clear inspection of the bias between the spectra. The extracted spectrum was generated with the *SRCTOOL* version of April 2014, which was also applied during our data reduction.

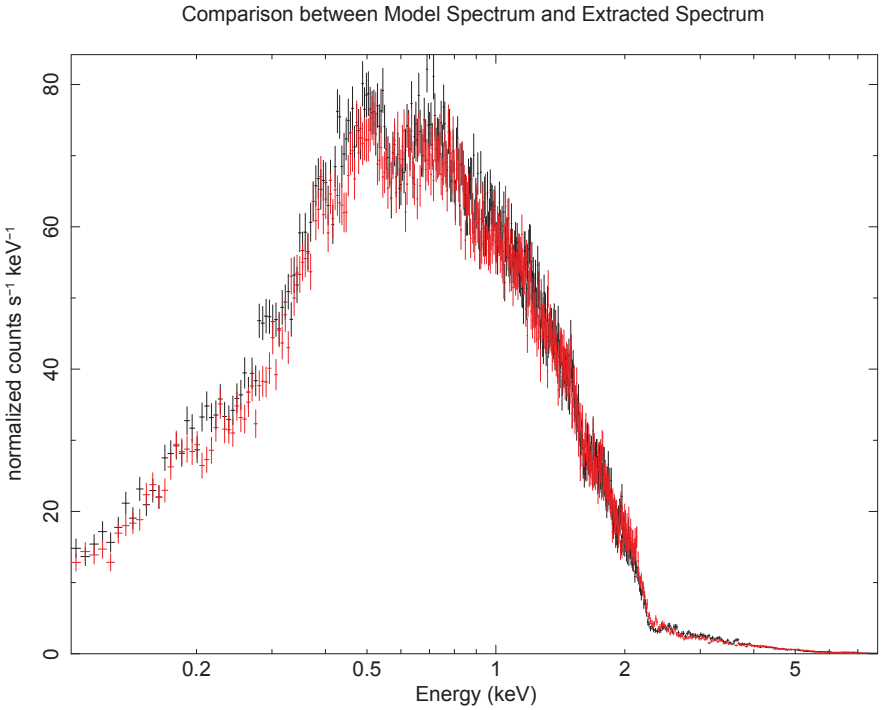

Figure 5.8: Display of the spectral bias with the same content as Fig. 5.7. However, for the spectral extraction the updated *SRCTOOL* as of August 2014 (version 09/2014) was applied and the bias could be reduced.

As our presented simulation results were based on the previous version of *SRCTOOL*, the effect of the updated task on our results was tested based on a selection of different clusters. In a first comparison, the reduced spectral bias showed only a negligible effect on our presented results and especially the bias in the estimated temperatures was not improved.

5.6.4 Catastrophic Failures

To improve the reliability of the analysis results and to approach the reduction of truly observed data, two types of catastrophic failures were defined for the spectral fit results (Borm et al. 2014, comp. also Sect. 4.2.4). The first type addressed those results for which the uncertainty region defined by the `error`-command was not set around the best-fit value. In this case, the data set was removed for the subsequent analysis steps as would be the procedure for real observed data with equivalent fit results. The second type of catastrophic failures described best-fit temperatures, which were positioned outside the $3\times1\sigma$-region in the distribution of best-fit values for the 108 repeated simulations of the same cluster. Those fit results were flagged, but still included in the analysis since these failures are not identifiable in observed data.
In the above presented results, no catastrophic failures of the first type were detected and the second type of failures occurred for only few of the 19 considered (M, z)-combinations. In those latter cases, less than 5% of the 108 realisations of the same cluster were affected by these failures (Wenzel 2014). Accordingly, the presented simulation results were only negligibly influenced by catastrophic failures. An equivalent finding was also discovered for the spectra-only simulations, where for clusters with available redshifts catastrophic failures of the first type did not arise and the second type of failures was detected only to an insignificant percentage (Sects. 4.3.1 & 4.5.3).

5.6.5 Discussing the Temperature Bias

As expressed in detail in Sect. 5.5, the ratio between the best-fit and the model ICM temperature, estimated in this extended set of simulations, was significantly increased in comparison to the spectra-only analysis (comp. Sect. 4.3.2). Several possible explanations of this bias have been investigated in the previous sections. Accordingly, we excluded the influence of catastrophic failures (Sect. 5.6.4) and of the spectral bias (Sect. 5.6.3) for generating the temperature bias. The scatter and the bias in the extracted number of cluster photon counts mainly remained within $\pm10\%$ and thus altered the normalisation of the spectrum only marginally. A small increase in the uncertainty of the best-fit values was expected due to this effect. What is more, the ratios of the numbers of extracted photons were almost randomly distributed around unity and were thus not able to account for a systematic and general overestimation of the cluster temperature.
Another possible origin for the temperature bias is the application of different instrumental responses for the simulation and the analysis of the spectra. For the steps within *SIXTE* and *SRCTOOL*, the RSP for a pointed observation was convolved with an estimated vignetting to account for a more realistic instrumental effective area. In the spectral analysis, on the other hand, we manually assigned the survey response to the spectra, where both the spectra and the response were stacked for the seven telescopes. This may have resulted in an inconsistent definition of the instrumental effective area in the different steps. A possible overestimation of the effective area during the spectral analysis would results in the assumption of reduced amplitudes of the emission lines and thus in biased-high temperature estimates.
Following these considerations, an extended, thorough inspection of the simulation set-ups within *SIXTE* as well as within *SRCTOOL* needs to be supported. Unfortunately, the steps within the two different programmes could not easily be disentangled and the simulated spectrum was only studied

after a full simulation run, which impeded the difficulty of identifying the origin of the systematics. Additionally, an additional bias, arising from the general treatment of the raw data independent of the applied analysis tools, needs to be considered and disentangled from the systematics in the software. However, new updates for both softwares have been released since the work on this project. These included e.g., the option to extract the instrumental response in addition to the spectrum when applying *SRCTOOL*, which allows to study any systematics arising from manually assigning the *eROSITA* survey RSP to the extracted spectra. Additionally, *eSASS* now includes a task to compute the exact exposure time from the event file and also *SIXTE* has been extended by further simulation options. In conclusion, a repetition of the above simulations while applying the updated software tasks presents a potential option to solve and characterise the observed bias in the temperature estimates.

5.7 Conclusion & Outlook

Within this extension to the forecasts for the determination of *eROSITA* cluster properties, we simulated event files for different galaxy clusters based on the software *SIXTE* and extracted the cluster spectra applying the *eSASS* task *SRCTOOL*. These files were thereby based on *eROSITA* survey observations with exposure times of $t_{\rm exp} = 1.6$ ks. Subsequently, we performed a spectral analysis of the extracted data, assuming the cluster redshifts to be available, and inspected the relative temperature uncertainties, the temperature bias as well as the systematics in the computed temperature uncertainties. These results were then compared to the conclusions of the spectra-only simulations by Borm et al. (2014) (chapter 4) to investigate systematic errors in the applied softwares or biases arising from the realistic treatment of the raw data, with an increased interest in the performance of the official task *SRCTOOL* for the reduction of future *eROSITA* data. The analysis of the simulated event files yielded the following main results.

- The precision of the estimated cluster temperatures was especially depending on the cluster mass and the corresponding ICM temperature, as well as on the cluster redshift. Precise temperatures are obtained for all cluster masses up to $z \approx 0.06$.
- The precision in the temperatures was slightly decreased for the clusters of interest with $\Delta T/\langle T_{\rm fit}\rangle < 10\%$ when compared to the results of the spectra-only approach in which precise temperatures were obtained for all clusters up to $z \approx 0.08$. Despite this decrease in the parameter space of high precision clusters, roughly all clusters, which showed precise temperature estimates in the previous simulation, were still included in this parameter space.
- The model cluster temperature was overestimated in the spectral fit with a temperature bias of $\lesssim 10\%$ on average and extreme values of up to $\sim 15\%$ for clusters with precise temperatures. Accordingly, this bias needs to be corrected for in the future data reduction.
- As the temperature bias was negligible for all clusters with precise temperature estimates in the spectra-only simulations and the model temperature was now overestimated in the extended approach, a systematic error in the simulation and/or analysis set-up in these second forecasts was expected.
- The results obtained for the bias in the computed uncertainty from the *xspec* `error`-command reproduced the findings in chapter 4 with only a minor increase in the bias.

The results from this extended simulation approach were expected to present slightly less precise and less accurate temperature estimates, due to the additional simulation steps and the additionally required

treatment of e.g. the raw photon events or the definition of source extraction regions. Accordingly, the minor degradation of the temperature precisions and of the accuracy of the temperature uncertainties were expected findings of this simulation set-up. However, the bias in the temperature estimates indicated a systematic error in at least one of the followed simulation and analysis steps or in the applied software. A first investigation of this problem already resulted in an improvement of both *SIXTE* and *eSASS* as well as in extensive discussions within the German *eROSITA* Collaboration. These discussions also included the general concepts for the reduction of the future *eROSITA* data as well as the adaptation of the task *SRCTOOL* to these ideas. The definition of the energy threshold or the treatment of split photon events presented e.g. two of these considered concepts. For both effects, the instrumental response needs to be adapted to compensate the observed spectral bias. However, the origin of the temperature bias has not been identified, yet. New updates of the applied software promise a more accurate and realistic treatment of the future observed data and thus a decrease of the simulated spectral as well as temperature bias. With the newly arising analysis options, included in the updated software, a repetition of the above described simulation steps and methodology is accordingly supported.
In conclusion, the presented analysis successfully indicated and quantified different systematics within the software tools *SIXTE* and *SRCTOOL* to allow for a more accurate reduction of the future *eROSITA* data as well as its interpretation. The accuracy of the re-obtained galaxy cluster temperatures asks for an extended investigation of possible systematics in the software or in the data analysis in general. However, the performed simulations applying the software versions of May 2014 already yielded promising results for the reliability of the future data analysis and thus support the instrument's cosmological potential.

CHAPTER 6

Cosmological Constraints from *eROSITA* Galaxy Clusters: testing *MCMC* Simulations and Gas Temperature Information

The project presented in this chapter investigates the cosmological constraining power of the *eROSITA* instrument and will strongly support the instrument's science goal for the study of the nature of dark energy. Several aspects of this second main project of my thesis are building up on the results of my first paper and thus on the observational data on galaxy clusters, which we expect to obtain from *eROSITA*. The content of this chapter is currently being prepared for publication by Borm et al., in prep., whereas the considerations in Sect. 6.7.2 will be included in more detail in the publication by Pillepich et al., in prep. The basic principles of several aspects in the introductory as well as in the methodology sections of this chapter (esp. Sects. 6.1, 6.2.2 & 6.4) have already been discussed especially in Sects. 2.3, 2.8 & 3.4. However, they are repeated at this point to summarise the required theoretical knowledge for the unexperienced reader.

Abstract

The up-coming X-ray telescope *eROSITA* is expected to place tight constraints on cosmology, and especially on the dark energy equation of state, by detecting and exploiting a large sample of $\sim 100,000$ clusters of galaxies.
These objects are commonly applied tracers of the large-scale structure of the Universe and studying the abundance of clusters in different observable bins reveals information on the cosmological parameters. We predict with which precision the above instrument will be able to determine these parameters when applying this approach for the complete *eROSITA* cluster sample with available redshift and luminosity information. Additionally, we investigate the improvement of the cosmological constraints in the case of accessible gas temperature information of the clusters that will realistically be available, and the impact of a lower uncertainty in the X-ray scaling relations on the cosmological credibilities.
Based on the instrumental sensitivity and the X-ray scaling relations, we derive new observable cluster population functions and the corresponding cluster mock catalogues, where we estimate a total of $98,700$ observed *eROSITA* clusters. Comparing these catalogues to our population models in *Markov-Chain Monte Carlo* (MCMC) simulations, yields the expected uncertainties on the cosmological parameters for the future observations. The simulations are considered for the different cosmological models ΛCDM, w_0CDM, wCDM, for different scaling relations and for the two observable sets (z, η)

and $(z, \mathrm{k}T_\mathrm{X})$, respectively, with the redshift z, the cluster temperature T_X, and η as the number of the cluster photon counts detected by the *eROSITA* CCDs.
Whereas the abundance of *eROSITA* clusters with precise temperature estimates is too small to allow for a significant impact on the cosmological constraints, the (z, η)-catalogue alone already yields parameter precisions which are as precise as the most recent cosmology findings by the *Planck* satellite with external priors. Combining the two data sets and accounting for a development in the precision on the scaling relations by a factor of four until the *eROSITA* data release, we obtain 68%-uncertainties of $< 1\%$ and of $\sim 1.5\%$ for σ_8 and Ω_m, respectively, in a ΛCDM- as well as in a w_0CDM-cosmology, with $\Delta w_0 \approx 2.4\%$ in the latter case. For the more general wCDM-scenario, the credibilities will be tightly constrained to $\Delta\sigma_8 = 0.009$ (1%), $\Delta\Omega_\mathrm{m} = 0.006$ (2%), $\Delta n_\mathrm{s} = 0.004$ ($< 1\%$), $\Delta w_0 = 0.077$ (8%), and $\Delta w_\mathrm{a} = 0.276$. Though the considered improvement in the uncertainties on the scaling relations show a significant impact on the constraints on e.g. Ω_m and σ_8, Δw_0 and Δw_a present only a minor influence by the scaling knowledge. A further progress in the precision on these relations, however, only allows for minor additional increases in the parameter precisions.
According to this precision in the cosmological parameters, *eROSITA* will be the first Stage IV instrument in investigating the characteristics of dark energy with a figure of merit of $\mathrm{FoM}^{2\sigma}_{w_0,w_\mathrm{a}} = 53$.

6.1 Introduction

As most massive virialised objects in the Universe, galaxy clusters have become reliable cosmological probes for mapping the large-scale structure (LSS) of matter and for studying the dark energy equation of state (e.g., Borgani & Guzzo 2001; Voit 2005; Vikhlinin et al. 2009a,b; Mantz et al. 2010a; Allen et al. 2011). To further improve the precision on the cosmological parameters by galaxy cluster studies, we require large samples of galaxy clusters as well as tight relations between the cluster observables and those cluster parameters directly linked to cosmology. The future *eROSITA* (**e**xtended **RO**entgen **S**urvey with an **I**maging **T**elescope **A**rray) telescope (Predehl et al. 2010; Merloni et al. 2012), which is scheduled for launch in early 2017, will provide such a data sample in X-rays, and will simultaneously also improve the uncertainties on the relations between the different cluster properties (Pillepich et al. 2012). According to the report of the *Dark Energy Task Force* (*DETF*), such a telescope is considered as one of the first Stage IV probes for the study of dark energy (Albrecht et al. 2006).
One commonly applied method to study cosmology with galaxy clusters is based on the distribution of these objects in dependence on their mass and redshift - on the halo mass function (e.g., Reiprich & Böhringer 2002; Voit 2005; Vikhlinin et al. 2009a,b; Mantz et al. 2010a). This function traces the evolution of structures in the Universe, which is highly dependent on the cosmological model (e.g., Press & Schechter 1974; Tinker et al. 2008). The functional form of the halo mass function itself is considered as universal with cosmology and redshift (Jenkins et al. 2001; Evrard et al. 2002; Linder & Jenkins 2003; Kuhlen et al. 2005; Tinker et al. 2008). Accordingly, counting clusters in mass and redshift bins and comparing these observations to the theoretical prediction for different cosmological models yields constraints on the cosmological parameters. However, this analysis requires the cluster redshift as well as its mass to be accessible.
Galaxy cluster redshifts are mainly obtained in optical photometric or spectroscopic observations. For the *eROSITA* cluster sample, for example, photometric redshifts will be provided e.g. by *DES* (*Dark Energy Survey*, e.g. Crocce et al. 2015), *VST ATLAS* (*VLT Survey Telescope ATLAS*, e.g. Shanks et al. 2015) and *PanSTARRS* (*Panoramic Survey Telescope & Rapid Response System*, e.g. Ebeling et al. 2013), while at the same time spectroscopic surveys are designed to focus on *eROSITA* follow-up observations, e.g. *4MOST* (*4m Multi-Object Spectroscopic Telescope for ESO*, e.g. de Jong et al. 2014)

and *SPIDERS* (*SPectroscopic IDdentification of eROSITA Sources*, e.g. Salvato 2015). We thus expect redshifts to be available for most clusters observed with this new instrument.
Cluster masses, on the other hand, are no direct observables and long exposure times are necessary for their determination. Thus, galaxy cluster scaling relations are commonly applied to estimate this property based on observables such as e.g. the cluster temperature, luminosity and redshift (e.g., Vikhlinin et al. 2009a; Pratt et al. 2009; Mantz et al. 2010a; Reichert et al. 2011; Giodini et al. 2013). The uncertainties in these scaling relations accordingly limit the precision on the computed cluster mass and thus also on the cosmological constraints (e.g., Allen et al. 2011). As this uncertainty partially results from the mass calibration, one idea is to combine observational information from different wavelengths, for example from X-ray and weak lensing data, to calibrate the X-ray hydrostatical masses (e.g. Hoekstra et al. 2013; Applegate et al. 2014; Israel et al. 2014, 2015). In fact, applying the halo mass function for cosmological studies is not limited to X-ray samples, and current *Sunyaev-Zel'dovich* (SZ) cluster surveys, performed for example by the *Atacama Cosmology Telescope* (ACT), the *South Pole Telescope* (SPT) and *Planck*, already led to an improvement in constraining the cosmological parameters (e.g. Vanderlinde et al. 2010; Planck Collaboration et al. 2013; Reichardt et al. 2013). Another idea is to determine the scaling relations simultaneously to the cosmology during the analysis (e.g., Allen et al. 2011). Low uncertainties in the scaling relations as well as a relatively low intrinsic scatter are advantageous for this method, where the latter aspect is achieved by e.g. applying the temperature-mass relation instead of the luminosity-mass relation in X-rays, with intrinsic scatters of $< 15\%$ compared to $\sim 40\%$, respectively (e.g. Vikhlinin et al. 2009a; Mantz et al. 2010a; Allen et al. 2011; Giodini et al. 2013). The approach of the simultaneous fit will be followed by the up-coming *eROSITA*-instrument, which will improve the currently available X-ray cluster samples in terms of precision, accuracy, and number of clusters and is accordingly expected to yield tight constraints on cosmology.
eROSITA is the German core instrument aboard the Russian satellite *Spektrum Roentgen Gamma* (SRG), which is scheduled for launch in early 2017 to an L2 orbit (Predehl et al. 2010; Merloni et al. 2012). Covering the X-ray sky in an energy range between $(0.1 - 10.0)$ keV, the telescope will perform eight all sky surveys in total, each lasting half a year, with subsequent three years of pointed observations. With an average effective exposure time of ~ 1.6 ks per field-of-view (FoV), *eROSITA* is expected to detect 10^5 clusters of galaxies, assuming a detection limit of 50 photons in the $(0.5 - 2.0)$ keV energy band and cluster masses above $5 \cdot 10^{13}\ \mathrm{M}_\odot/h$ (Pillepich et al. 2012). Also, this cluster sample will include all massive clusters in the entire Universe with $M > 3 \cdot 10^{14}\ \mathrm{M}_\odot/h$, and X-ray temperatures for $\sim 2,000$ clusters (Borm et al. 2014). First predictions of the constraints placed on the cosmological parameters by this cluster sample yielded an increased precision of the dark energy parameters to $\Delta w_0 \approx 0.03$ (for $w_\mathrm{a} = 0$) and $\Delta w_\mathrm{a} \approx 0.20$ (Merloni et al. 2012), assuming an evolution with redshift as $w_\mathrm{DE} = w_0 + w_\mathrm{a}/(1 + z)$ for dark energy (Chevallier & Polarski 2001; Linder 2003). Accordingly, *eROSITA* presented itself as powerful tool to determine the nature of dark energy.
The current *eROSITA* forecasts followed the approach that only the redshift and the number of observed X-ray photons, or equivalently the luminosity, will be available for the *eROSITA* clusters, and were based on the Fisher matrix approach. We now extended these predictions to *Markov-Chain Monte Carlo* (*MCMC*) simulations to allow for non-Gaussian credibility intervals of the cosmological parameters and to yield more realistic parameter degeneracies (Wolz et al. 2012; Khedekar & Majumdar 2013). Within these forecasts, the cosmological models ΛCDM, w_0CDM, assuming a constant dark energy equation of state, and wCDM for a variable dark energy equation of state were investigated, including a simultaneous fit of the scaling relations. A possible detection of primordial non-Gaussianity and the influence of additional information from angular clustering were already discussed in detail by Pillepich et al. (2012) and by Pillepich et al., in prep. Since the cosmological constraints presented in these works were strongly driven by the abundance of clusters, we focused on this observable only for our cosmo-

logical estimates. Instead, we extended the forecasts to constraints on the sum of the neutrino masses $\sum m_\nu$ (ΛCDM+ν-cosmology), and also included the knowledge of cluster temperatures, observed with the *eROSITA*-instrument (Borm et al. 2014), in our predictions for a more realistic approach.
Studying neutrino characteristics with the help of cosmological probes has been made possible only for the past years with the most recent data samples. Several investigations reported e.g. on the influence of different neutrino characteristics on the cluster abundances (comp. e.g. Ichiki & Takada 2012; Costanzi et al. 2014; Roncarelli et al. 2015) or stated upper limits on $\sum m_\nu < 0.23$ eV, by investigating the most recent data of the *Cosmic Microwave Background* (CMB) (e.g. Planck Collaboration et al. 2015c). Within the current works, cluster abundances alone did not allow for constraints on the uncertainties on the nature of neutrinos yet, due to a strong degeneracy between the standard deviation in the matter distribution σ_8 and the matter energy density Ω_m (e.g. Mantz et al. 2015; Roncarelli et al. 2015). Including the large sample of *eROSITA* clusters in this analysis, we hoped to improve on this degeneracy. The additional cluster information, on the one hand, was expected to tighten the uncertainties on the cosmological parameters (compare e.g., Mantz et al. 2010a; Clerc et al. 2012), such that we aimed at quantifying this impact.
This chapter is structured as follows: in Sect. 6.2, we introduce the theoretical models of the applied halo mass function and the scaling relations. Sect. 6.3 derives the models of the observable cluster population functions in the two cases of available photon counts and temperatures, respectively, along with the corresponding mock catalogues, whereas Sect. 6.4 describes the statistical set-up of the simulations. The following sections summarise the simulation approach of currently existing *eROSITA* forecasts (Sect. 6.5) and present our predictions for different cosmological models (Sect. 6.6). A detailed analysis of the impacts of the different simulation steps follows in Sect. 6.7 and the discussion of the results is found in Sect. 6.8. The summary and conclusion of this work are given in Sect. 6.9, and we end this chapter with an outlook of currently considered extensions to this project (Sect. 6.10).
Throughout this work, we applied a fiducial *WMAP5* (*Wilkinson Microwave Anisotropy Probe*) cosmology (Komatsu et al. 2009), which we extended to also include neutrinos (Tab. 6.1).

6.2 Theoretical Models and Simulation Strategy

6.2.1 Fiducial Cosmological Model

The details of our fiducial *WMAP5* cosmology are presented in this section and especially in Tab. 6.1. To additionally account for the influence of neutrinos on the abundance of galaxy clusters, we included $\sum m_\nu = 0.06$ eV, the neutrino mass summed over all neutrino species, and $N_\mathrm{eff} = 3.046$ for the total effective number of neutrino species to our fiducial model. This mass estimate represents the lower theoretical limit (Lesgourgues & Pastor 2012, Sect. 2.1.2), where this summed neutrino mass is equivalent to a current massive neutrino energy density of (e.g. Lesgourgues & Pastor 2006; Lesgourgues et al. 2013)

$$\Omega_\nu h^2 = \frac{\sum m_\nu}{93.14\ \mathrm{eV}} = 6.4 \cdot 10^{-4} \quad , \tag{6.1}$$

with the Hubble parameter h and $h = \mathrm{H}_0/100 \cdot [\mathrm{Mpc} \cdot \mathrm{s/km}]$. Accordingly, the current matter density was computed as $\Omega_\mathrm{m} = (\Omega_\mathrm{b} h^2 + \Omega_\mathrm{c} h^2 + \Omega_\nu h^2)/h^2$, based additionally on the energy densities of the baryons Ω_b as well as of the cold dark matter component Ω_c. In the presence of relativistic neutrinos, also the radiation energy density is influenced as

$$\Omega_\mathrm{r} = \Omega_\gamma \cdot \left(1 + \frac{7}{8} \cdot \left(\frac{4}{11}\right)^{4/3} \cdot N_\mathrm{eff,\ massless}\right) \tag{6.2}$$

with the photon energy density Ω_γ and the second summand representing the contribution of the massless neutrinos. The above equation follows from the general concepts of the thermal history of our Universe (e.g. Lesgourgues et al. 2013, Sect. 2.1.2). For the dark energy density, we defined $\Omega_{\rm DE} = \Omega_0 - \Omega_{\rm m} - \Omega_{\rm r}$ in dependence on the total energy density Ω_0, but independent of the cosmological model. In the case of a ΛCDM-model, $\Omega_{\rm DE}$ is equivalent to the cosmological constant Ω_Λ. Throughout all simulations, we assumed a spatially flat universe and thus $\Omega_0 = 1.0$, following the precise findings by e.g. Planck Collaboration et al. (2015c) with $1 - \Omega_0 = 0.0008$ with an uncertainty of only $\sim 0.4\%$. To define the dark energy equation of state as a function of time, we applied the parametrisation by Chevallier & Polarski (2001) and Linder (2003) with

$$w(a) = w_0 + w_{\rm a}(1 - a) \quad , \tag{6.3}$$

in dependence on the scale factor a, and the corresponding evolution of the dark energy

$$\Omega_{\rm DE}(a) = \Omega_{\rm DE} \cdot \exp\left[-3 \cdot \int_1^a \frac{1 + w(a')}{a'} {\rm d}a'\right] \tag{6.4}$$

$$\Omega_{\rm DE}(a) \propto \exp[-3 \cdot (w_a \cdot (1 - a) + (1 + w_0 + w_a) \cdot \ln[a])]. \tag{6.5}$$

Initially, the equation of state was fixed to $w_0 = -1$ and $w_{\rm a} = 0$ to represent a cosmological constant in accordance with the *WMAP5* results and with more recent findings by e.g. Planck Collaboration et al. (2015c). During the forecasts, we especially tested the constraining power of *eROSITA* on the equation of state of dark energy and considered amongst others a w_0CDM-model with variable w_0, but $w_{\rm a} = 0$, and a wCDM-model with variable w_0 and w_a, respectively.
Accordingly, when considering both neutrinos and variable dark energy, the scale factor dependent Hubble parameter was defined as

$$H(a) = H_0 \cdot E(a)$$

$$H(a) = H_0 \cdot \sqrt{\Omega_{\rm r} \cdot a^{-4} + (\Omega_{\rm b} + \Omega_{\rm c} + \Omega_\nu) \cdot a^{-3} + \Omega_{\rm DE}(a)}. \tag{6.6}$$

Tab. 6.1 additionally summarises the applied parameters for the scaling relation as well as aspects of the *eROSITA* survey strategy, which are both addressed in detail in the following sections.

6.2.2 The Halo Mass Function

The halo mass function, from which we inferred the expected abundances of galaxy clusters for a given cosmological model, is generally derived from the concepts of structure formation. It is thus based on the linear matter power spectrum $P(k, z)$, which describes the influence of the different perturbation scales k for the growth of structures in dependence on the redshift z. For a fixed redshift, we estimated the cosmology dependent linear power spectrum with CAMB (*Code for Anisotropies in the Microwave Background*) by Lewis et al. (2000). The influence of neutrinos as well as of the nature of dark energy on the power spectrum was included in this computation, where e.g. an increased abundance of neutrino families as well as an increased summed neutrino mass reduced the amplitude on small perturbation scales (comp. e.g. Ichiki & Takada 2012, Sect. 2.3.2). However, the following steps were based on the linear matter power spectrum of only dark matter and baryons computed at $z = 0$(Costanzi et al. 2014; Mantz et al. 2015; Roncarelli et al. 2015). The redshift evolution of this perturbation spectrum was then accounted for by the normalised solution to the differential equation of linear matter perturbations on

Table 6.1: List of applied parameter values; if not stated otherwise the values were taken from Komatsu et al. (2009) for the cosmology, from Reichert et al. (2011) for the scaling relations and from Pillepich et al. (2012) for the survey characteristics. All listed priors were simulated as a normal distribution. Additional information was taken from (a) Cooke et al. (2014), (b) Riess et al. (2011), (c) Vikhlinin et al. (2009a).

Cosmology	Fiducial Value	Prior
$\Omega_b h^2$	0.02265	$\pm 0.00046^a$
$\Omega_c h^2$	0.1143	
$\Omega_\nu h^2$	0.00064	
σ_8	0.817	
Ω_m	0.28001	
n_s	0.96	
h	0.701	$\pm 0.022^b$
Ω_b	0.046	
w_0	-1.0	
w_a	0.0	
Ω_Λ	0.71999	
Ω_r	$\sim 7 \cdot 10^{-5}$	
N_{eff}	3.046	
Scaling Relations	**Fiducial Values**	**Prior**
α_{LM}	1.923	± 0.058
β_{LM}	0.386	± 0.088
γ_{LM}	1.731	± 0.305
σ_{LM}	0.396^c	$\pm 0.039^c$
α_{TM}	0.617	± 0.049
β_{TM}	2.143	± 0.085
γ_{TM}	0.642	± 0.054
σ_{TM}	0.119^c	$\pm 0.03^c$
Survey Parameters	**Fixed Value**	
f_{sky}	0.658	
t_{exp}	1.6 ks	
response matrix	"erosita_iv_7telfov_ff.rsp"	

sub-horizon scales (comp. e.g. Linder & Jenkins 2003; Percival 2005)

$$\ddot{\delta}(t) + \frac{2\dot{a}}{a}\dot{\delta}(t) = \frac{3H_0^2\Omega_m}{2a^3}\delta(t) \quad , \tag{6.7}$$

with the density contrast $\delta(t)$ depending on time t, the scale factor a, the Hubble constant H_0, and the current mean matter density Ω_m. This homogeneous second order differential equation was coupled in scale factor and time via the relation

$$\frac{da}{dt} = \dot{a} = H(a) \cdot a \quad . \tag{6.8}$$

Rewriting the density contrast in dependence on the scale factor a and substituting the time derivatives dt by da, the coupled differential equations were simplified to a single second order differential equation.

Its normalised solution $D_+(a) = \delta(a)/\delta(1)$ is named *growth factor*. As the growth factor is thus defined by the evolution of the Hubble parameter (Eq. 6.6), it is impacted by the abundance of neutrinos as well as by the characteristics of dark energy. Based on the growth factor, we defined $P(k,z) = P(k,0) \cdot D_+^2(z)$. Smoothing the powerspectrum over the mass scale, while integrating over all perturbation scales yielded the standard deviation in the linear matter density $\sigma^2(M,z)$

$$\sigma^2(M,z) = \int_0^\infty \frac{\mathrm{d}k}{2\pi^2} k^2 \cdot P(k,z) \cdot |W(k,M)|^2 \quad . \tag{6.9}$$

For the smoothing we applied the spherical top-hat window function $W(k,M)$, which in Fourier space reads

$$W(k,M) = 3 \cdot \frac{\sin(kr) - kr \cdot \cos(kr)}{(kr)^3} \quad , \tag{6.10}$$

with a smoothing scale of $M = \frac{4}{3}\pi\bar{\rho}_{\mathrm{m},0} r^3$, with the mean matter density today $\bar{\rho}_{\mathrm{m},0} = \rho_{\mathrm{crit},0} \cdot (\Omega_\mathrm{c} + \Omega_\mathrm{b})$ and $\rho_{\mathrm{crit,z}} = 3H(z)^2/(8\pi\mathrm{G})$. Based on the matter standard deviation, the halo mass function was first derived by Press & Schechter (1974) with a general form of

$$\frac{\mathrm{d}n}{\mathrm{d}M}(M,z) = \frac{\bar{\rho}_{\mathrm{m},0}}{M} \cdot \left(\frac{\mathrm{d}\ln\sigma^{-1}(M,z)}{\mathrm{d}M} \right) \cdot f(\sigma,z) \quad , \tag{6.11}$$

to define the number density of collapsed haloes per mass bin. Note that the matter density $\bar{\rho}_{\mathrm{m},0}$ was defined by only including the dark matter as well as the baryon abundances as defined above (comp. Costanzi et al. 2014; Mantz et al. 2015; Roncarelli et al. 2015). The halo mass function shows an universal profile for different cosmological models, including variable dark energy (e.g. Jenkins et al. 2001; Evrard et al. 2002; Linder & Jenkins 2003; Kuhlen et al. 2005) and we assumed an extended universality also for the redshift evolution. For the function $f(\sigma,z)$, we applied the findings by Tinker et al. (2008)

$$f(\sigma,z) = A_\mathrm{T} \left[\left(\frac{\sigma}{b_\mathrm{T}} \right)^{-a_\mathrm{T}} + 1 \right] \cdot \exp[-c_\mathrm{T}/\sigma^2] \quad . \tag{6.12}$$

with

$$A_\mathrm{T}(z) = A_{\mathrm{T},0} \cdot (1+z)^{-0.14} \tag{6.13}$$

$$a_\mathrm{T}(z) = a_{\mathrm{T},0} \cdot (1+z)^{-0.06} \tag{6.14}$$

$$b_\mathrm{T}(z) = b_{\mathrm{T},0} \cdot (1+z)^{-\alpha_\mathrm{T}} \tag{6.15}$$

$$c_\mathrm{T}(z) = c_{\mathrm{T},0} \tag{6.16}$$

$$\ln[\alpha_\mathrm{T}(\Delta_\mathrm{m})] = -\left(\frac{0.75}{\ln[\Delta_\mathrm{m}/75]} \right)^{1.2} \quad , \tag{6.17}$$

The above parameters marked by the index "T" were estimated as a fit to collissionless cosmological structure simulations and were quantified at $z = 0$ for various halo overdensities $\Delta_{\mathrm{m,z}} = \bar{\rho}_{\mathrm{halo,z}}/\bar{\rho}_{\mathrm{m,z}}$ compared to the mean matter density $\bar{\rho}_{\mathrm{m,z}}$ (comp. Table 2 in Tinker et al. (2008)).
However, to be consistent with the general definition of cluster scaling relations, we defined halo masses based on the overdensities $\Delta_{\mathrm{crit,z}}$ compared to the critical density with

$$M_{\Delta,z} = \frac{4\pi}{3} (\Delta_{\mathrm{crit,z}} \cdot \rho_{\mathrm{crit,z}}) r_\Delta^3 \quad . \tag{6.18}$$

The conversion between the different overdensity definitions followed $\Delta_{\mathrm{crit,z}}/\Delta_{\mathrm{m,z}} = \bar{\rho}_{\mathrm{m,z}}/\rho_{\mathrm{crit,z}} = \Omega_{\mathrm{m,z}}$, where we applied a critical overdensity of $\Delta_{\mathrm{crit}} = 500$ throughout this paper, independent of redshift. This overdensity is commonly applied in X-ray scaling relations, since it represents the limit for X-ray temperature measurements with e.g. *XMM-Newton* and *Chandra* (e.g. Reiprich et al. 2013).

6.2.3 X-ray Scaling Relations

Since the reconstruction of X-ray cluster masses requires in general long exposure times, this property will be available only for a small subsample of *eROSITA* clusters. To relate direct observables, such as the X-ray luminosity or the temperature of the intra-cluster medium (ICM), to the mass, we applied the reparametrised scaling relations by Reichert et al. (2011)

$$\mathrm{k}T \quad [\mathrm{keV}] \quad = \quad \left(\frac{M}{10^{14}\ \mathrm{M}_\odot}\right)^{\alpha_{\mathrm{TM}}} \cdot \beta_{\mathrm{TM}} \cdot E(z)^{\gamma_{\mathrm{TM}}} \tag{6.19}$$

$$L_{\mathrm{X}} \quad [10^{44}\ \mathrm{erg/s}] \quad = \quad \left(\frac{M}{10^{14}\ \mathrm{M}_\odot}\right)^{\alpha_{\mathrm{LM}}} \cdot \beta_{\mathrm{LM}} \cdot E(z)^{\gamma_{\mathrm{LM}}} \quad , \tag{6.20}$$

with the mass $M \equiv M_{500}$ and the bolometric luminosity L_{X} in the energy range $(0.01, 100.)$ keV. The values of the stated parameters are summarised in Tab. 6.1 along with their corresponding priors. These scaling relations present a conservative approach for high redshift clusters and are based on a broader galaxy cluster sample with $z \lesssim 1.5$ when compared to other scaling relations (comp. e.g. Vikhlinin et al. 2009a; Pratt et al. 2009; Mantz et al. 2010a). Additionally, in a previous work we already performed the first forecasts for the precision of *eROSITA* cluster temperatures based on these scaling relations (Borm et al. 2014), and those results were applied in the following project.
We considered an intrinsic scatter in the scaling relations, which we defined by a log-normal distribution

$$P(\ln L_{\mathrm{X}}^* | M, z) = \frac{1}{\sqrt{2\pi\sigma_{\mathrm{LM}}^2}} \cdot \exp\left[-\frac{(\ln L_{\mathrm{X}}^* - \mu_{\mathrm{L}})^2}{2\sigma_{\mathrm{LM}}^2}\right] \tag{6.21}$$

for the mass-luminosity relation $M - L_{\mathrm{X}}$, where $\mu_{\mathrm{L}} = \ln L_{\mathrm{X}}(M, z)$ derived from Eq. 6.20 with no scatter in the relation. An analogous relation was applied also for the mass-temperature $M - T_{\mathrm{X}}$ relation. Since Reichert et al. (2011) were not able to quantify the intrinsic scatter in their scaling relations, we referred to the results found by Vikhlinin et al. (2009a) as commonly observed scatter values with $\sigma_{\mathrm{LM}} = 0.396$ and $\sigma_{\mathrm{TM}} = 0.119$ (comp. e.g. Mantz et al. 2010a; Allen et al. 2011).
Additionally, we implemented the scaling relations by Vikhlinin et al. (2009a) in some of our cosmological simulations to investigate the influence of the applied scaling relation on the cosmological forecasts and to compare our results to previous works, which were based on these relations (Pillepich et al. 2012, Pillepich et al., in prep.). For this second set of scaling relations, we followed the definitions

$$\begin{aligned} \ln L_{\mathrm{X}} &= [101.48 + 1.5 \cdot (\sigma_{\mathrm{LM}}^2 - 0.396^2)] \\ &+ 1.61 \cdot \ln(M/(3 \cdot 10^{14}\ \mathrm{M}_\odot)) \\ &+ 1.85 \cdot \ln E(z) - 0.39 \cdot \ln(h/0.72) \end{aligned} \tag{6.22}$$

$$\begin{aligned} \ln \mathrm{k}T &= 0.65 \cdot \ln(M/(3.02 \cdot 10^{14}\ \mathrm{M}_\odot/h)) \\ &+ 0.65 \cdot \ln E(z) + \ln(5\ \mathrm{keV}) \quad . \end{aligned} \tag{6.23}$$

The masses were still defined as M_{500}, whereas the luminosity was now computed in the $(0.5-2.0)$ keV rest frame band. For the scatter in the relations, we referred to the expressions stated above. However, as our simulations were mainly dependent on the relations by Reichert et al. (2011), the scaling relations by Vikhlinin et al. (2009a) were only applied when stated specifically.

6.3 Observable Cluster Population Functions and Mock Catalogues

Relating the cluster mass to X-ray observables via scaling relations allowed us to re-write the halo mass function into a galaxy cluster observable function and thus to apply the entire sample of the $\sim 100,000$ observed *eROSITA* galaxy clusters for cosmological studies. As observable we chose the number of cluster photons η detected by the *eROSITA* CCDs in the energy range between $(0.5-2.0)$ keV and accordingly defined the galaxy cluster photon counts function $\mathrm{d}n/\mathrm{d}\eta(\eta, z)$ (Pillepich et al. 2012), where redshifts will be available from optical follow-up observations for all clusters. At the same time, we derived a galaxy cluster temperature function $\mathrm{d}n/\mathrm{d}T(T, z)$ as an additional theoretical distribution for those clusters with expected temperature information. This second model already included the detailed instrumental specific selection of clusters with precise and accurate temperatures as determined by Borm et al. (2014).

6.3.1 Deriving the Galaxy Cluster Photon Counts Function

To convert the cluster mass M and the redshift z into the number of observed photons η, the temperature T_X and the luminosity L_X of the cluster were computed in a first step by applying the scaling relations. The parameter set $(T_\mathrm{X}, L_\mathrm{X}, z)$ defined the spectrum of the cluster unambiguously, which was modeled an absorbed apec spectrum ***phabs*apec*** (Smith et al. 2001) with the software ***xspec*** (Arnaud 1996) version 12.7.0, while assuming a constant metal abundance of $A = 0.3\ \mathrm{A}_\odot$ compared to the solar metallicity (Arnaud et al. 1992; Mushotzky & Loewenstein 1997). Convolving this spectrum with the instrumental response (RSP) yielded the observed number of photons by the instrument, such that in summary the approach read

$$(M, z) \xrightarrow{\text{scaling relations}} (T_\mathrm{X}, L_\mathrm{X}, z) \xrightarrow{\text{instr. response}} \eta \quad . \tag{6.24}$$

The approach of a constant metal abundance was preferred at this point, since a metallicity evolution with redshift could not be certainly quantified, yet (Balestra et al. 2007; Maughan et al. 2008; Baldi et al. 2012). At the same time, we set the absorbing column density to $N_\mathrm{H} = 3 \times 10^{20}$ particles/cm^2 as a commonly observed value for galactic latitudes of $b \gtrsim 20°$ (Kalberla et al. 2005). The spectral model was then convolved with the *eROSITA* RSP file for the combined resolution of all seven telescopes averaged over the entire field-of-view. Fig. 6.1 displays the dependence of the number of detected photons on the cluster temperature and redshift for a fixed luminosity. Accordingly, the photon counts remained almost constant with the temperature, when we neglect clusters with temperatures of $\lesssim 0.5$ keV, which correspond to masses of $M < 10^{13}\ \mathrm{M}_\odot/h$ and thus to objects well within the galaxy group regime. Due to the proportionality of $\eta \propto L_\mathrm{X}/D_\mathrm{L}^2$ on the luminosity distance D_L, we scaled the number of photons as $\eta = \eta_\mathrm{fid} \cdot D_\mathrm{L,fid}^2/D_\mathrm{L}^2$ to include the dependence on cosmology, with the index "fid" marking the computation in our fiducial cosmology.
Knowing the relation between the cluster mass and redshift, and the number of observed photons (Eq.

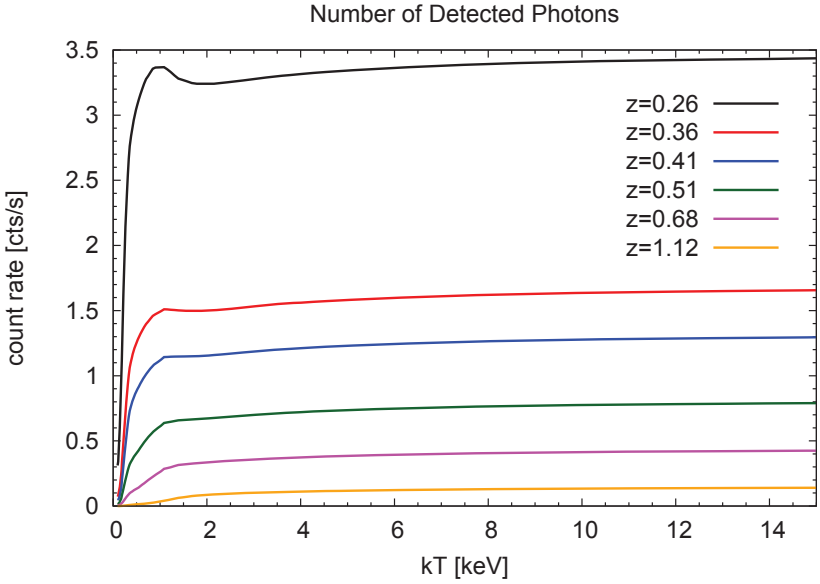

Figure 6.1: Photon count rates detected by the *eROSITA* instrument in the energy range (0.5 – 2.0) keV at different redshifts for galaxy clusters with a luminosity of $L_X = 10^{45}$ erg/s in the same rest frame energy band. The cluster emission was modeled as a *phabs*apec* spectrum and was then convolved with the *eROSITA* response for all seven telescopes within the software *xspec*.

6.24), we derived the cluster photon counts function as[13]

$$\frac{\mathrm{d}n}{\mathrm{d}\eta}(\eta^*, z) = \int \mathrm{d}\bar{M} \frac{\mathrm{d}n}{\mathrm{d}M}(\bar{M}, z) \cdot P(\eta^*|\bar{M}, z) \quad , \tag{6.25}$$

where the term $P(\eta^*|\bar{M}, z)$ represents the total scatter which might have arisen in the conversion. In the optimal, but unrealistic, case of no scatter, the above expression would simplify to

$$\frac{\mathrm{d}n}{\mathrm{d}\eta}(\eta^*, z) = \frac{\mathrm{d}n}{\mathrm{d}M}(M^*, z) \cdot \frac{\mathrm{d}M}{\mathrm{d}\eta}(M^*, \eta^*, z) \quad , \tag{6.26}$$

with the derivative $\mathrm{d}M/\mathrm{d}\eta$ inferred from the procedures in Eq. 6.24. However, since the inclusion of the scatter was inevitable for precise and reliable cosmological forecasts, we needed to consider

$$\begin{aligned} P(\eta^*|\bar{M}, z) &= P(\ln \eta^*|\bar{M}, z) \cdot \frac{1}{\eta^*} \\ &= \int \mathrm{d}\ln L_X \int \mathrm{d}\ln T_X \underbrace{P(\ln L_X, \ln T_X|\bar{M}, z)}_{\text{intrinsic scatter in scaling relations}} \\ &\cdot \underbrace{P(\ln \eta^*|\ln \eta(\ln L_X, \ln T_X, z))}_{\text{Poisson noise}} \cdot \frac{1}{\eta^*} \quad . \end{aligned} \tag{6.27}$$

[13] The general considerations for the derivation of $\mathrm{d}n/\mathrm{d}\eta(\eta^*, z)$ for *eROSITA* have first been discussed in Pillepich et al. (2012).

In general, the intrinsic scatter in the scaling relations $P(\ln L_X, \ln T_X|\bar{M}, z)$ is expressed as a bivariate log-normal distribution (comp. also Eq. 6.21) to account for a possible correlation between L_X and T_X

$$P(\mathbf{X}|\bar{M}, z) = \frac{1}{2\pi|\Sigma|^{1/2}} \cdot \exp\left[-\frac{1}{2}(\mathbf{X}-\mu)^T\Sigma^{-1}(\mathbf{X}-\mu)\right] \quad . \tag{6.28}$$

The applied vectors $\boldsymbol{X}$ and μ, and the covariance matrix Σ, which defines the correlation between the two parameters, read

$$\boldsymbol{X} = \begin{pmatrix} \ln L_X \\ \ln T_X \end{pmatrix} \text{ and } \Sigma = \begin{pmatrix} \sigma^2_{LM} & \rho_{LT}\sigma_{LM}\sigma_{TM} \\ \rho_{LT}\sigma_{LM}\sigma_{TM} & \sigma^2_{TM} \end{pmatrix} \quad , \tag{6.29}$$

with μ containing the mean values of $\ln L_X$ and $\ln T_X$, and ρ_{LT} defining the linear correlation coefficient between the two parameters. Up to now, ρ_{LT} has not been reliably quantified and different studies suggested contradictory results (Stanek et al. 2010; Kravtsov et al. 2006; Mantz et al. 2010a). Accordingly, we followed the simplified approach by Pillepich et al. (2012) with $\rho_{LT} = 0$, supported by the weak influence of the temperature on the number of observed cluster photons (comp. Fig. 6.1). Following this approach, the expression of $P(\mathbf{X}|\bar{M}, z)$ in a first step reduced to a multiplication of two one-dimensional log-normal distributions. In a second step, however, we neglected the scatter in the $M - T_X$ relation due to the mentioned weak dependence of the observable on the ICM temperatures, such that we eventually arrived at the one-dimensional integration

$$\begin{aligned} P(\eta^*|\bar{M}, z) &= \frac{1}{\eta^*} \cdot \int \mathrm{d}\ln L_X \; P(\ln L_X|\bar{M}, z) \\ &\cdot \quad P(\ln\eta^*|\ln\eta(\ln L_X, \bar{M}, z)) \quad . \end{aligned} \tag{6.30}$$

The Poisson noise was expected to show only a negligible effect on the cosmological estimates (comp. Sec. 6.8.5), such that it was defined as a Dirac delta function (Pillepich et al., in prep.)

$$P(\ln\eta^*|\ln\eta(\ln L_X, \bar{M}, z)) = \delta_D(\ln\eta^* - \ln\eta) \quad . \tag{6.31}$$

We then followed a coordinate substitution from $\ln L_X \rightarrow \ln\eta$ based on the relation $\eta \propto L_X$ and Eq. 6.27 simplified to

$$P(\eta^*|\bar{M}, z) = \frac{1}{\eta^*} \cdot \frac{1}{\sqrt{2\pi\sigma^2_{LM}}} \cdot \exp\left[-\frac{(\ln\eta^* - \mu_\eta)^2}{2\sigma^2_{LM}}\right] \quad , \tag{6.32}$$

with $\mu_\eta = \ln\eta(\bar{M}, z)$ as expected number of photons if no scatter in the scaling relations was applied. Accordingly, we finally expressed the cluster photon counts function as

$$\begin{aligned} \frac{\mathrm{d}n}{\mathrm{d}\eta}(\eta^*, z) &= \int \mathrm{d}\bar{M} \frac{\mathrm{d}n}{\mathrm{d}M}(\bar{M}, z) \cdot \frac{1}{\eta^*} \cdot \\ &\cdot \quad \frac{1}{\sqrt{2\pi\sigma^2_{LM}}} \cdot \exp\left[-\frac{(\ln\eta^* - \mu_\eta)^2}{2\sigma^2_{LM}}\right] \quad . \end{aligned} \tag{6.33}$$

Fig. 6.2 displays this function for three different redshifts. The graphs were computed for the scaling relation by Reichert et al. (2011) (solid lines) as well as by Vikhlinin et al. (2009a) (dotted lines). In general, the shape of the function reflects the evolution of the halo mass function with mass and redshift, where clusters with large numbers of observed photons represent massive clusters. A deviation of the

computed abundances of clusters between the two different scaling relations is already visible by eye and may even show ratios of up to a factor of ~ 2. Accordingly, the influence of the applied relations on the cosmological constraints needs to be quantified and discussed for their reliable interpretation (Sect. 6.7.1).

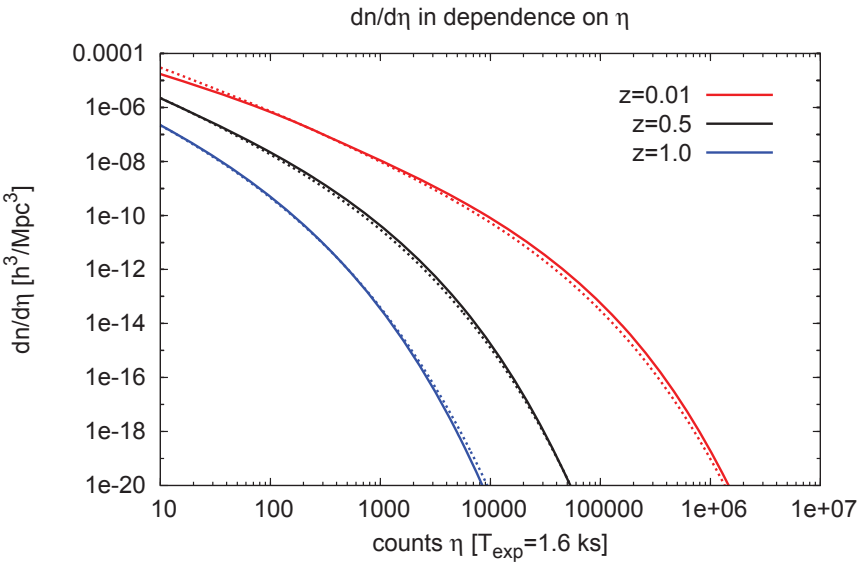

Figure 6.2: Galaxy CLuster photon counts function for the detected *eROSITA* photon events for three different redshifts when applying the scaling relations by Reichert et al. (2011) (solid lines) and by Vikhlinin et al. (2009a) (dotted lines). The functions were computed following the approach derived in Eq. 6.33.

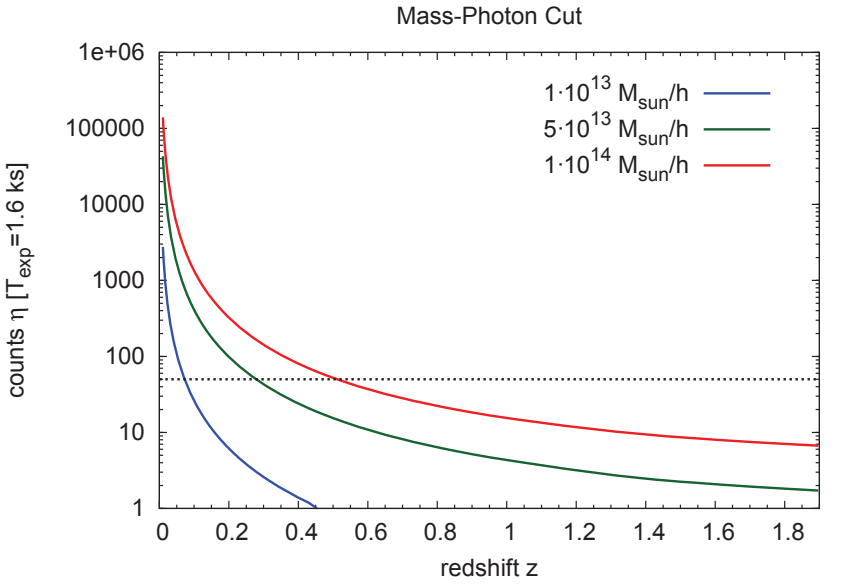

Figure 6.3: Graphical description of the photon counts cut $\eta_{\mathrm{min}} = 50$ cts (black dotted line) and the mass cut for three different cluster masses. The clusters, which pass the cuts are located in the top right, framed by the mass cut on the left and by the photon cut on the bottom.

For a more realistic treatment of the galaxy cluster photon counts function, we included a lower limit in the observed number of photon counts of $\eta_{\min} = 50$ and a lower mass cut of $M_{\text{cut}} = 5 \cdot 10^{13}\ \mathrm{M}_{\odot}/h$ in the following computations (Pillepich et al. 2012, especially Fig. 2). The photon limit was defined by the sensitivity of *eROSITA* to identify an extended source as a galaxy cluster, whereas the mass cut avoided a confusion between the characteristics of galaxy clusters and galaxy groups (e.g. Eckmiller et al. 2011). As the cluster mass was initially not known, the lower mass cut was converted into a redshift dependent photon counts cut following Eq. 6.24. This cut was computed for the fiducial *WMAP5* cosmology and remained fixed throughout the entire forecasts, which mirrors the approach for the analysis of real data. If the cut was adapted for each tested cosmology, the results would be biased to higher precision. For the applied cosmology and the scaling relations by Reichert et al. (2011), the rejection of galaxy groups dominated the defined photon limit up to redshifts of $z_{\text{cut}} = 0.28$. Above this redshift the limit was solely defined by $\eta_{\min} = 50$. Fig. 6.3 presents a graphical description of the cuts, where the parameter space of interesting clusters is located in the top right corner, framed by the mass cut on the left and by the photon cut on the bottom.

6.3.2 Including Temperature Information

The derivation of the galaxy cluster temperature function was analogous to the strategy applied in the previous section (comp. Eq. 6.25)

$$\frac{\mathrm{d}n}{\mathrm{d}T}(T^*, z) = \int \mathrm{d}\bar{M} \frac{\mathrm{d}n}{\mathrm{M}}(\bar{M}, z) \cdot P(T^*|\bar{M}, z) \cdot S(\bar{M}, z) \quad . \tag{6.34}$$

However, we included the aspect that temperature information will not be available for the entire cluster catalogue, such that we defined a multiplicative selection function $S(M, z)$ (comp. also e.g. Mantz et al. 2010a). This function defined the probability to observe a precise cluster temperature with $\Delta T/T < 10\%$ with *eROSITA* in dependence on the cluster mass and redshift. Based on the findings in our previous work (Borm et al. 2014), precise temperature estimates will be available for nearly all clusters up to $z \approx 0.08$. At higher redshifts, the majority of clusters with precise temperatures is known already from detailed X-ray observations, such as from the *eHIFLUGCS* (*extended HIgh FLUx Galaxy Cluster Sample*) (Reiprich 2012). In total, the selection function was defined to follow the shape of a step function with a detailed derivation of $S(\bar{M}, z)$ summarised in appendix D.1, where for those clusters included in *eHIFLUGCS*, the selection function read $S(\bar{M}, z) = 1$. As this derivation was based on the scaling relations by Reichert et al. (2011), we studied the function $\mathrm{d}n/\mathrm{d}T$ for these scaling relations only.

The scatter in the temperature observations $P(T^*|M, z)$ was in this case accounting for the intrinsic scatter in the $M - T_{\mathrm{X}}$ scaling relation and additionally included a statistical scatter in the temperature estimation

$$\begin{aligned} P(T^*|\bar{M}, z) \quad &= \quad \frac{1}{T^*} \int \mathrm{d} \ln T_{\mathrm{X}} \ \underbrace{P(\ln T^* | \ln T_{\mathrm{X}}, \bar{M}, z)}_{\text{statistical scatter}} \\ &\cdot \quad \underbrace{P(\ln T_{\mathrm{X}}|\bar{M}, z)}_{\text{intrinsic scatter } M - T_{\mathrm{X}}} \quad . \end{aligned} \tag{6.35}$$

Just as the scatter in the scaling relations, also the statistical scatter in the temperature estimates followed a log-normal distribution (comp. appendix D.1) with the scatter $\sigma_{\mathrm{TT}} = \Delta T/\langle T \rangle(\bar{M}, z)$ representing the computed relative temperature uncertainties for the different combinations of cluster mass and redshift. The integration over two multiplied log-normal distributions yielded again a log-normal distribution and

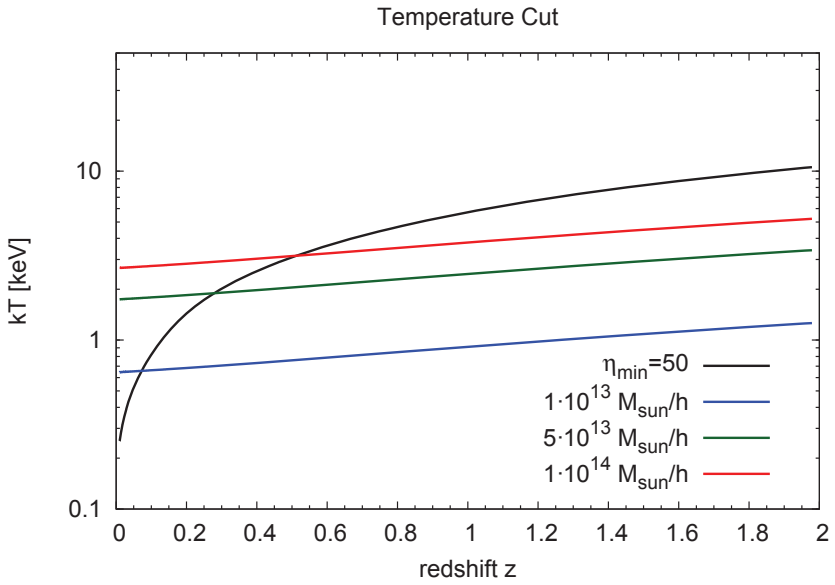

Figure 6.4: Lower temperature cut for the galaxy cluster temperature function $\mathrm{d}n/\mathrm{d}T$ described by a photon limit of $\eta_{\mathrm{min}} = 50$ and by three different mass cuts for comparison. The clusters of interest were thus limited by the mass cut at lower redshifts and by the photon cut at higher redshifts.

Eq. 6.35 simplified to

$$P(T^*|\bar{M}, z) = \frac{1}{T^*} \cdot \frac{1}{\sqrt{2\pi \cdot (\sigma^2_{\mathrm{TM}} + \sigma^2_{\mathrm{TT}})}} \cdot \exp\left[-\frac{(\ln T^* - \mu_{T_{\mathrm{X}}})^2}{2 \cdot (\sigma^2_{\mathrm{TM}} + \sigma^2_{\mathrm{TT}})}\right] \quad , \tag{6.36}$$

again with $\mu_{T_{\mathrm{X}}} = \ln T_{\mathrm{X}}(\bar{M}, z)$. We defined $\sigma_{\mathrm{TM}} = 11.9$ (Vikhlinin et al. 2009a) and obtained $\sigma_{\mathrm{TT}}(\bar{M}, z)$ by investigating the expected temperature precisions, estimated in our previous work (Borm et al. 2014). We also included our findings, that all clusters with precise temperatures also show accurate temperature values, such that no parameter bias needed to be accounted for.

Analogous to the considerations for the photon counts function, a lower detection limit was applied, where the limits on η_{min} and M_{cut} were converted into a redshift dependent temperature cut $T_{\mathrm{min}}(z)$ (Fig. 6.4). Also in this case, the temperature cut was fixed at the fiducial cosmology and a value of $z_{\mathrm{cut}} = 0.28$ was estimated, such that above these redshifts the temperature cut was in theory dominated by the minimum cluster mass. However, at these distances, the cut at low kT was in practise completely defined by the selection function $S(\bar{M}, z)$.

Fig 6.5 presents the galaxy cluster temperature function in dependence on the cluster redshift and the temperature. The dotted graphs display this function without adding instrumental characteristics for comparison reasons, such that neither the above cuts, nor the selection function or the statistical scatter in the temperature estimates were applied. The graphs show a similar shape as the halo mass and the photon counts functions with an exponential decrease towards higher temperatures, which represent the more massive clusters. When considering the above mentioned instrumental characteristics, $\mathrm{d}n/\mathrm{d}T$ additionally displays strong cut-offs toward decreasing temperatures. In principle, *eROSITA* will be able to estimate precise temperatures for all clusters up to $z \approx 0.08$, such that the cut-offs at these low redshifts were defined by the low temperature cut. At the same time, the functions display smooth shapes at these redshifts, due to a selection function of in general $S(\bar{M}, z) = 1$. On the other hand, at increas-

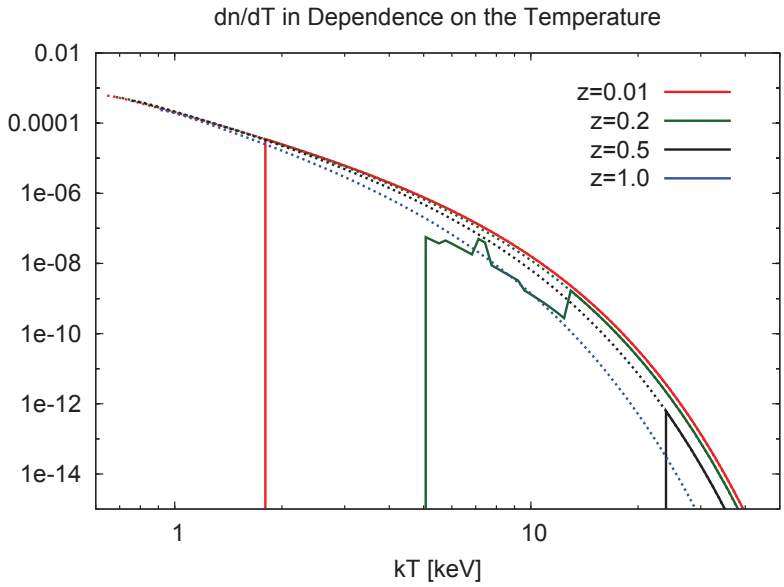

Figure 6.5: Galaxy cluster temperature function as derived in Sect. 6.3.2, plotted for four different redshifts. The dotted graphs present this function without applying any instrumental information, such that no selection function or statistical scatter in the temperature estimates was considered. The solid curves include these details as well as the computed redshift dependent temperature limit, such that the function was reduced to zero for redshifts of $z \gtrsim 0.6$.

ing redshifts the selection function started to shape these cut-offs and even reduced the galaxy cluster temperature function to zero for $z \gtrsim 0.6$. At these highest still computed redshifts of $0.5 \lesssim z \lesssim 0.6$, the observed precise teperatures were all included within *eHIFLUGCS*, such that again the selection of $S(\bar{M}, z) = 1$ yielded a smooth cluster abundance function. The wiggles observed for intermediate redshifts, for example around $z \approx 0.2$, were due to the steps defined in the selection function and mirror the rather unsmooth and inhomogeneous trend predicted in the distribution of relative temperature uncertainties with mass and redshift (comp. Fig. 4.3). However, for the case of $S(\bar{M}, z) = 1$, the function $\mathrm{d}n/\mathrm{d}T$ including the instrumental characteristics slightly exceeds the abundance function excluding theses characteristics by $\lesssim 3\%$. This small deviation is not visible in Fig. 6.5, but this behaviour was expected, as the instrumental characteristic function additionally includes the statistical scatter in the temperature estimates.

6.3.3 Mock Catalogues

Forecasting cosmology based on the abundance of clusters required the computation of their total number and thus integrations of the galaxy cluster photon counts function over the photon counts and the observed volume. The first step in this procedure was to estimate the differential abundance of clusters in dependence on the redshift

$$\frac{\mathrm{d}N}{\mathrm{d}z\,\mathrm{deg}^2}(z) = \frac{4\pi}{A} \cdot f_{\mathrm{sky}} \cdot \left[\frac{D_{\mathrm{A}}^2 \cdot c}{H(z)}\right] \cdot \int_{\eta_{\mathrm{min}}}^{\infty} \mathrm{d}\eta^* \, \frac{\mathrm{d}n}{\mathrm{d}\eta}(\eta^*, z) \quad , \tag{6.37}$$

with the observed sky fraction $f_{\mathrm{sky}} = 0.658$ (Pillepich et al. 2012), the survey area A in deg^2, the comoving angular diameter distance D_{A}, and the speed of light c. This distribution was highly dependent

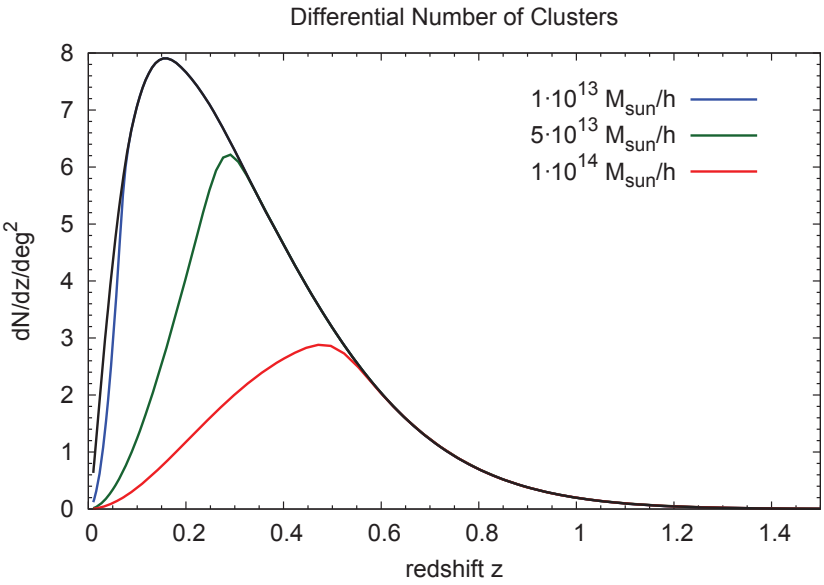

Figure 6.6: Differential number of clusters per deg^2 as a function of redshift. The black curve presents the cluster distribution of all galaxy clusters with $\eta > 50$. Different mass cut values are indicated in colour, where these cuts especially influence the distribution at the lower redshift end and thus shift the peak of the distribution.

on the applied limits for $\eta_{\rm min}$ and $M_{\rm cut}$ (Fig. 6.6), such that as expected from Fig. 6.2, the photon cut defined the shape of the distribution at higher redshifts, whereas the converted mass cut shaped the differential cluster abundance at the lower redshifts. The peak of the distribution is correspondingly located at $z_{\rm cut}$, which marks the redshift for which $\eta(M_{\rm cut}, z_{\rm cut}) = \eta_{\rm min}$. Since at low redshifts the majority of observed clusters was showing small masses, a reduced mass cut accordingly results in an increased fraction of more local clusters.
Within the next step, we described the total expected number of clusters in different observable bins and constructed two mock catalogues based on a (z, η)- and a $(z,\mathrm{k}T_{\rm X})$-grid, respectively. To compute the abundance of clusters N_j per bin, we integrated the cluster observable functions over the considered binned observable and the binned volume, represented by z

$$N_{\rm bin} = 4\pi \cdot f_{\rm sky} \cdot \int_{z_{\rm low}}^{z_{\rm up}} \mathrm{d}z \, \frac{D_{\rm A}^2(z) \cdot c}{H(z)} \int_{\eta_{\rm low}}^{\eta_{\rm up}} \mathrm{d}\eta^* \, \frac{\mathrm{d}n}{\mathrm{d}\eta}(\eta^*, z) \quad , \tag{6.38}$$

with the same parameters as in the previous equation. An equivalent computation was applied for the galaxy cluster temperature function and the abundance of clusters in the $(z,\mathrm{k}T_{\rm X})$-bins. Within these computations, we neglected the influence of halo clustering on the abundance of clusters in the individual bins, since the *eROSITA*-survey will cover the entire sky.
Figs. 6.7 & 6.8 present these expected distributions of observed galaxy clusters on the two grids with very fine binning, while accounting for all mentioned limits and selection effects. Accordingly, the cluster abundance was reduced to zero for low photon counts at low redshifts (Fig. 6.7) and at low temperatures (Fig. 6.8), respectively, due to the lower mass cut. Towards higher photon counts and equivalently towards higher temperatures, the number of clusters decreased smoothly as expected from the shape of the galaxy cluster observable functions. Additionally, the redshift put strong constraints on observing precise temperatures, such that the redshift distribution in the $(z, \mathrm{k}T_{\rm X})$-grid was significantly narrowed compared to the (z, η)-grid and showed a sharp cut-off towards increasing redshifts (Fig. 6.8).

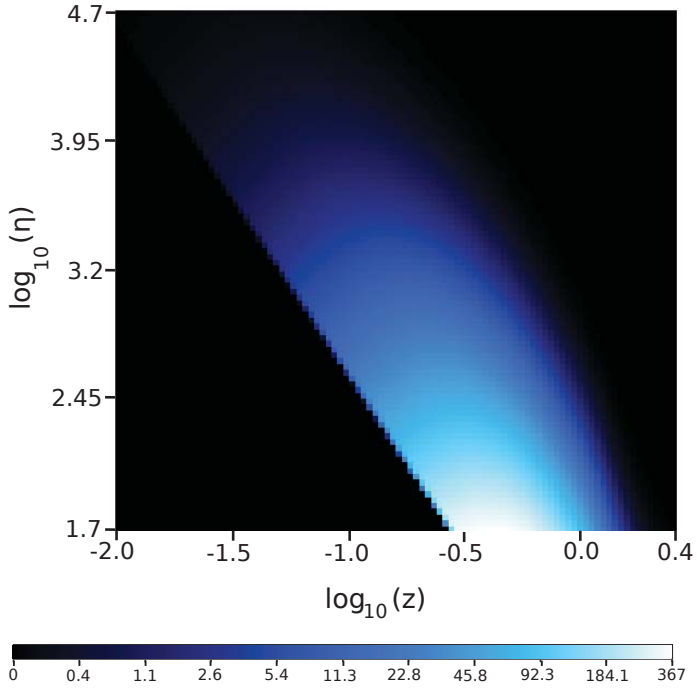

Figure 6.7: Distribution of the *eROSITA* galaxy clusters as a function of their redshift z and the number of photons η detected by the instrument. The colour of the pixels indicates the number of galaxy clusters in the different bins with the peak of the abundance being located towards the low photon counts end.

As a whole, the cluster distribution in the (z,kT_{X})-grid displayed more substructures by mirroring the shape of the selection function. These substructures consisted of *eHIFLUGCS* as clusters with the highest temperatures for a given redshift, of the *eROSITA*-clusters with $\Delta T/\langle T\rangle < 10\%$ in the centre, and clusters with an increased median relative temperature uncertainty towards the higher redshifts.
For computing the applied mock catalogues, however, we set the bin sizes according to the resolution of the individual observables with *eROSITA*. The width of the redshift bins was defined as $\Delta z \cdot (1 + z_{\mathrm{bin}})$ with $\Delta z = 0.05$ to approximate the precision of optical photometric redshift estimates. Intentionally, the applied redshift resolution was chosen to underestimate the commonly measured photometric precision of $\Delta z \approx 0.022$ (comp. e.g. Liu et al. 2015), such that the scattering of clusters between different redshift bins due to their limited redshift resolution could be neglected. Following the idea of optical follow-up observations for all *eROSITA* clusters, we defined 19 bins in redshift from $0.01 \leq z \leq 2.5$ with the last bin covering the range between $1.5 < z < 2.5$. The number of photon counts η was divided into 20 equally spaced bins in $\log_{10}$ with $50 \leq \eta \leq 50,000$. For the (z,kT_{X})-mock catalogue of clusters with precise temperatures, we kept the same binning in redshift, but reduced the number of bins to eight between $0.01 \leq z \leq 0.5$, due to the sharp drop in the selection function towards increasing redshifts. For the temperature bins, we applied a conservative resolution of $\Delta T/T = 0.15$ (comp. also Mantz et al. 2010a), which was twice the average relative uncertainty of all clusters in the precise temperature sample (estimated from the results by Borm et al. (2014)). This approach accordingly decreased the scatter of clusters between temperature bins and finally resulted in ten kT_{X}-bins between ($1.0 \leq$ k$T_{\mathrm{X}} \leq 40.0$) keV, with the last bin formally covering the range between ($15.2 \leq$ k$T_{\mathrm{X}} \leq 40.0$) keV. The upper temperature limit was chosen to consistently and in theory also include those clusters with the highest considered masses and redshifts, $M = 10^{15.7}$ M$_\odot$ and $z = 1.78$, though these were suppressed by the defined selec-

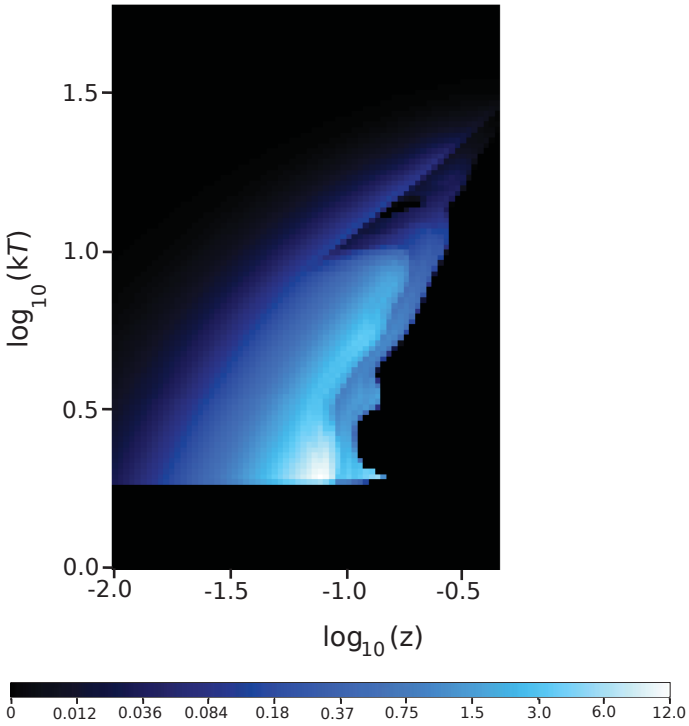

Figure 6.8: Distribution of the *eROSITA* galaxy clusters as a function of redshift z and temperature kT_X of the ICM. Again, the colour of the pixels represents the number of clusters per pixel, where the size of the redshift grid as well as the abundance of clusters was reduced due to the required instrumental selection of clusters with precise temperature estimates.

tion function and especially by the shape of the galaxy cluster temperature function (comp. Fig. 6.8). Integrating over the individual bins, we computed a total of $\sim 98,700$ galaxy clusters detected by the *eROSITA*-instrument, when following the scaling relations by Reichert et al. (2011). The all-sky surveys of this instrument, additionally allowed for a sample of $\sim 1,860$ new clusters with precise temperature information, and for a total temperature catalogue of $\sim 2,050$ clusters, including *eHIFLUGCS*.

6.4 Simulations

To forecast the constraints *eROSITA* will place on cosmology, we applied *MCMC* simulations within the package *COSMOMC* (Lewis & Bridle 2002) version 01/2015, while employing the included Metropolis sampler. Within this package we implemented our own likelihood to compare the data within our mock catalogues to the expectations for different cosmologies. Additionally, we simultaneously fitted the scaling relations by default throughout our simulations. For our main results, presented in Sect. 6.6, we investigated four distinct cosmological models for the complete *eROSITA* cluster catalogue binned as (z, η), when assuming only redshift and luminosity, or equivalently the number of photon counts, to be available. In a second set of simulations, two cosmologies were investigated for a subcatalogue of ~ 2050 clusters with *eROSITA* temperature estimates binned as (z, kT_X).

(z, η)	ΛCDM, w_0CDM, wCDM, ΛCDM+ν
(z, kT_X)	ΛCDM, wCDM

In general, each of these simulations was executed for a pessimistic as well as for an optimistic approach, differentiated by the applied priors (Sect. 6.4.3). Additionally, we combined our results for the optimistic cases with data by the *Planck* satellite to break parameter degeneracies and to further improve their precision. The following sections will describe the applied *eROSITA*-likelihood function in more detail, summarise the applied priors and variables, as well as define the strategy for the joint analysis with the *Planck* data.

6.4.1 Likelihoods

We expressed the complete likelihood $L(N|\mathcal{X},\mathcal{Y})$ to re-obtain the observed total number of clusters N, given a cosmological model $\mathcal{X}$ and a scaling relation model $\mathcal{Y}$, as a combination of the individual likelihoods to detect N_j clusters in the j different mock bins. Since the values of N_j approach zero especially towards higher observable values, these likelihoods were based on Poisson statistics

$$L(N|\mathcal{X},\mathcal{Y}) = \prod_j L(N_j|\mathcal{X},\mathcal{Y}) = \prod_j \frac{\mu_j^{Nj}}{N_j} \cdot \exp[-\mu_j]\Big|_{\mathcal{X},\mathcal{Y}} \quad , \tag{6.39}$$

with μ_j as expected number of clusters in the j-th mock bin given the cosmology $\mathcal{X}$ and the scaling relation model $\mathcal{Y}$. Following the strategy within *COSMOMC*, we implemented the negative natural logarithm of this likelihood in our code and additionally neglected all constant summands, such that the likelihood expression simplified to

$$-\ln L(N|\mathcal{X},\mathcal{Y}) = \sum_j \mu_j - N_j \cdot \ln \mu_j \quad . \tag{6.40}$$

Within our first set of forecasts, this sum was computed over the (z,η)-mock catalogue bins and we inspected the cosmological constraints given the complete *eROSITA*-sample of $\sim 98,700$ clusters. In the second simulation set-up, only the subcatalogue of ~ 2050 clusters with estimated temperatures was considered. The methodology for the joint analysis of *eROSITA* and external cosmology data is expressed in Sect. 6.4.5.

6.4.2 Variable parameters

The parameters being varied within the *MCMC* sampling followed the default set-up of *COSMOMC* and showed a close to Gaussian posterior distribution. For a ΛCDM-cosmology, our parameter set read $\mathcal{X} = \{\Omega_b h^2, \Omega_c h^2, \theta, n_s, \log A\}$[14], with θ defining the angular size of the sound horizon at the epoch of decoupling, and with $\log A \equiv \ln[10^{10} \cdot A]$ with the amplitude of the linear matter power spectrum A. In the considered extended cosmological models w_0CDM, wCDM, and ΛCDM+ν, the additional parameters w_0, $\{w_0, w_a\}$, and $\sum m_\nu$ were varied, respectively.
The scaling relations were determined simultaneously to the cosmology, where we defined two sets of scaling models $\mathcal{Y}$. In our first simulation set-up, when applying the (z,η)-mock catalogue, we defined $\mathcal{Y} = \{\alpha_{LM}, \beta_{LM}, \gamma_{LM}, \sigma_{LM}\}$ and fixed the parameters of the $M - T_X$ relation to the values in Tab. 6.1. This approach was supported by the negligible influence of the temperature on the observed number of photons (Sect. 6.3 & Fig. 6.1). Accordingly, for the forecast of a ΛCDM-cosmology, the model $(\mathcal{X},\mathcal{Y})$ consisted of nine variable parameters in total. When studying the impact of the temperature information

[14] For more info refer to the *COSMOMC*-manual: http://cosmologist.info/cosmomc/readme.html.

based on the catalogue (z, kT_X), the scaling relation model was exchanged to $\mathcal{Y} = \{\alpha_{TM}, \beta_{TM}, \gamma_{TM}, \sigma_{TM}\}$.

6.4.3 Priors

Due to the strong degeneracy between different cosmological parameters, especially between the Hubble parameter h and the index of the power spectrum n_s, which increases with increasing number of variable parameters, we applied the Gaussian priors $\Delta h = \pm 0.022$ (Riess et al. 2011) and $\Delta(\Omega_b h^2) = \pm 0.00046$ (Cooke et al. 2014). Also, we defined Gaussian priors for the parameters of the scaling relations according to their estimated uncertainties (Tab. 6.1). These uncertainties were considered as pessimistic approach since they represented the current knowledge on the scaling relations. However, we expected this information to improve by the time the final-depth *eROSITA* data will be analysed by /*sim*2020, thanks to the synergy between X-ray follow-up observations of clusters with *XMM-Newton*, *Chandra*, *Astro-H*, and *NuSTAR*. Also, *eROSITA* itself will reduce the uncertainties on the scaling relations by means of the large data catalogue of the complete survey. Accordingly, an additional optimistic scenario was adopted for the forecast, assuming four times tighter priors on the scaling relations (comp. Pillepich et al., in prep.). In the case of studying the cluster subsample with estimated *eROSITA* temperatures, the optimistic scenario was extended to also show roughly four times more clusters in the catalogue. This was achieved by reducing the expected relative temperature uncertainties in the selection function by 40%.
All remaining variable parameters followed a flat prior distribution of $\mathcal{U}(-\infty, \infty)$.

6.4.4 *Planck*-Data and Other Probes

Commonly, cosmology results from different probes are combined to break parameter degeneracies, to calibrate the best-fit cosmology values and to improve the precision of these values (comp. e.g. Vikhlinin et al. 2009b; Mantz et al. 2010a; Allen et al. 2011; Planck Collaboration et al. 2015c; Mantz et al. 2015, comp. also Sect. 2.8). Currently, the data of the *Planck* satellite in combination with other cosmological probes and data sets yield most precise estimates for various parameters, including e.g. n_s and w_0 (Planck Collaboration et al. 2015c). However, *Planck* data of the cosmic microwave background (CMB) alone, did not allow to constrain the dark energy equation of state since the influence of this energy component became relevant only much later in the evolution of the Universe. Accordingly, additional external data were required to quantify Δw_0 and Δw_a. We thus applied the data set which also included information on baryon acoustic oscillations (BAO), on the Hubble parameter, as well as on supernovae type Ia data to guarantee constraints also on the time evolution of the dark energy ("`base_w_plikHM_TT_lowTEB_BAO_H070p6_JLA`"[15]) These data were taken from the second data release of the *Planck* satellite. The applied BAO data were based especially on the newest releases of the *Sloan Digital Sky Survey* (SDSS) (e.g. Anderson et al. 2014), whereas the prior on the Hubble constant was considering the work by Efstathiou (2014) and the supernovae data were a combination of different supernovae type Ia compilations to the *Joint Light-Curve Analysis* (JLA) sample (e.g. Betoule et al. 2014). A detailed description of the applied external data sets is presented by Planck Collaboration et al. (2015c).
For the above stated combination of data, cosmological analysis results were available within the *Planck* data package for the investigated cosmologies w_0CDM and wCDM. To yield the best-fit cosmology values and their uncertainties also for a ΛCDM-model, we performed a *MCMC* analysis based on the data and on the likelihoods provided by the *Planck* data package.

[15] The *Planck* data are e.g. available from the *ESA*-webpage: http://pla.esac.esa.int/pla/#cosmology.

6.4.5 Joint likelihoods

When combining credibility regions of different cosmological probes and data sets to yield increased parameter precisions, the most accurate approach is to perform joint *MCMC* simulations. As these require a large amount of computing time and power, a first estimate of the combined credibilities can be obtained from studying the information stored in the covariance matrices C_{cov} of the individual *MCMC* chains. These square matrices are defined as

$$C_{\mathrm{cov},ij} = \begin{cases} \sigma_{\mathrm{i}}^2 & (i = j) \\ \sigma_{\mathrm{ij}} & (i \neq j) \end{cases} \tag{6.41}$$

following the computation

$$C_{\mathrm{cov},ij} = \frac{1}{N-1} \sum_{\mathrm{n=1}}^{\mathrm{N}} (X_{i,n} - \mu_i) \cdot (X_{j,n} - \mu_j) \quad . \tag{6.42}$$

In these definitions, i and j describe two distinct parameters and σ_i^2 as well as σ_j^2 their variances. Here, σ_{ij} states the correlation between the two parameters with $\sigma_{ij} = \rho_{ij}\sigma_i\sigma_j$ and the correlation coefficient ρ_{ij} (comp. also Sect. 6.3.1). N denotes the total number of data points, which is in our case equivalent to the number of chain steps, whereas $X_{i,n}$ presents the n-th data point of parameter i with the arithmetic mean μ_i. The credibilities were presumed to follow a Gaussian distribution for this approach, such that this assumption yielded the most realistic and reliable results for close to Gaussian parameter uncertainties.
The 2-dimensional credibility regions, stored in the covariance matrix, thus show elliptical shapes with the axes lengths defined as (Coe 2009)

$$a^2 = \frac{\sigma_i^2 + \sigma_j^2}{2} + \sqrt{\frac{(\sigma_i^2 - \sigma_j^2)^2}{4} + \sigma_{ij}^2} \tag{6.43}$$

$$b^2 = \frac{\sigma_i^2 + \sigma_j^2}{2} - \sqrt{\frac{(\sigma_i^2 - \sigma_j^2)^2}{4} + \sigma_{ij}^2} \quad , \tag{6.44}$$

with the angle θ between the major axis and the positive x-axis in a counter clockwise direction

$$\tan 2\theta = \frac{2\sigma_{ij}}{\sigma_i^2 - \sigma_j^2} \quad . \tag{6.45}$$

However, the true lengths of the axes depended on the confidence level of interest and the above displayed parameters a and b were multiplied by a factor $\alpha = \sqrt{\Delta\chi^2}$. For a 2-dimensional histogram, we applied $\alpha = 1.52$ ($\Delta\chi^2 = 2.3$) for the 68%-confidence level and $\alpha = 2.48$ ($\Delta\chi^2 = 6.17$) for the 95.4%-confidence level.
To combine two independent data sets, which was the case for the *eROSITA* and *Planck* data, we added the inverse of the individual covariance matrices (Coe 2009)

$$C_{\mathrm{cov,combined}}^{-1} = C_{\mathrm{cov,eROSITA}}^{-1} + C_{\mathrm{cov,Planck}}^{-1} \tag{6.46}$$

and finally inverted the resulting matrix to compute the joint ellipses. This approach required identical dimensions for the inverted covariance matrices of both data sets. For the *Planck* data, we accordingly

marginalised over all variables except for our cosmology set $\mathcal{X}$. The corresponding *Planck* covariance matrix was smaller by four dimensions when compared to the analogous *eROSITA* matrix, due to the missing scaling parameters $\mathcal{Y}$ in the *Planck* sample. These additional columns and lines were then set to zero in the inverted covariance matrix. As we introduced deviations from the accurate shapes of the parameter uncertainties when following this approach, we compared the true *MCMC* contours with the approximated ellipses to estimate the implied systematics.

6.4.6 Figure of Merit

The figure of merit (FoM) is a commonly applied parameter to quantify the performance of the studied instrument for constraining certain variables. It is inversely proportional to the covariance matrix and to the area of the credibility region, such that an increase in the FoM indicates a more suitable experiment for studying the selected parameter set. For the 2-dimensional 1σ-uncertainty refions of the parameters i, j, the FoM was computed as

$$\mathrm{FoM}_{i,j}^{1\sigma} = \left(\sigma_i \sigma_j \cdot \sqrt{1-\rho_{ij}^2}\right)^{-1} \quad , \tag{6.47}$$

based on the marginalised parameter uncertainties σ_i and σ_j and the correlations coefficient ρ_{ij} between the considered parameters. This relation followed the definition by the *DETF* (Albrecht et al. 2006, 2009; Coe 2009). The corresponding 2σ-FoM was obtained by multiplying the above expression by a factor of 0.373, which is the ratio between the area of the 1σ- and the 2σ-credibility ellipses. Over all, for the computation of the FoM, the uncertainties were again assumed to follow a Gaussian distribution.

6.5 Summary of Already Available Forecasts

First thorough and realistic investigations on cosmological constraints with *eROSITA* have been performed by Pillepich et al. (2012), from whom we adopted the strategy of applying a galaxy cluster photon counts function (comp. Sect. 6.3.1). This work focused on studying ΛCDM-cosmologies while including tests of primordial non-Gaussianity. An extension to these first forecasts, now also including predictions on the equation of state of dark energy, is currently summarised in the subsequent publication by Pillepich et al., in prep., to which we refer as P16 in the following. Also, our galaxy cluster photon counts function was calibrated in collaboration with P16 to allow for negligible deviations between our definitions of less than one percent, where e.g. for the total number of *eROSITA* clusters a difference of only $\sim 0.5\%$ was achieved (comp. Sect. 6.8.1). For the forecast simulations, P16 relied on a different statistical approach - on the *Fisher matrix formalism* - and our aim included amongst other aspects to quantify the deviations between our strategies. This comparison then enables us to test the reliability of the computed cosmological constraints and the influences of different simulation set-ups. Investigating the accuracy of the predicted parameter uncertainties, additionally allows us to suggest a preferred data reduction method for the future *eROSITA* cluster catalogue.
In the following, we thus summarise these methodology concepts, which deviate from our approach, and the general results by P16 to perform a detailed comparison between our forecasts. Tab. 6.2 presents an overview of the essential deviations between our two set-ups.

Table 6.2: Summary of the differences between the set-up to perform the forecasts in this work and those by P16.

	this work	P16
Cluster data	abundances	abundances + clustering
Strategy	*MCMC*	Fisher
Scaling Relation	Reichert et al. (2011)	Vikhlinin et al. (2009a)
Opt. Scenario	$M_{\rm cut} = 5 \cdot 10^{13}\ {\rm M}_\odot/h$	$M_{\rm cut} = 1 \cdot 10^{13}\ {\rm M}_\odot/h$
	phot. redshifts	spec. redshifts

6.5.1 Simulation Strategy

As already expressed, the derivation of the galaxy cluster photon counts function was calibrated between this work and the work by P16. However, their cosmological simulations were based on mock catalogues for abundances as well as for angular clustering of galaxy clusters, and the parameter uncertainties were obtained from the *Fisher matrix formalism*.
The angular clustering addresses the spatial distribution of objects and asks for the probability of a cluster with the characteristics (M_1, z_1) to be located at a certain distance from a second cluster (M_2, z_2). Accordingly, this probability is related to the underlying matter distribution and can be traced by the halo mass function or equivalently by our derived galaxy cluster photon counts function. These two distributions are generally correlated by the general term

$$b(k, M, z) = \sqrt{\frac{P_{\rm hh}(k, M, z)}{P(k, z)}} \quad , \tag{6.48}$$

with $P_{\rm hh}$ as the linear power spectrum of the halo density field and $b(k, M, z)$ as the bias between the two power spectra. The strength of this systematic then depends on the cluster mass and redshift, as well as on the considered clustering scale k (e.g. Mo & White 1996; Catelan et al. 1998; Smith et al. 2007). Over-all, P16 worked with the so-called angular cross-spectrum between different observable bins i, j and studied the probability to observe N_j clusters in bin j, if bin i showed N_i cluster detections.
This tomographical test is especially interesting when analysing primordial non-Gaussianity $f_{\rm NL}$ (comp. e.g. Pillepich et al. 2012). A detailed description of the derivation and application of the halo bias and the angular clustering is presented by Pillepich et al. (2012).

Another significant deviation from the statistical methodology presented in Sect. 6.4, is the performance of a Fisher matrix analysis instead of *MCMC* simulations, where the Fisher matrix element for the two parameters i, j is defined as

$$F_{ij} = \left(\frac{\partial \mathcal{L}}{\partial i\, \partial j} \right) \quad , \text{ with } \mathcal{L} = -\ln L \tag{6.49}$$

and $\mathcal{L}$ as the negative natural logarithm of the likelihood function. The Fisher matrix defines the inverse of the covariance matrix of the parameters and it accordingly contains information on the parameter uncertainties and their correlations, while assuming Gaussian likelihoods.

6.5.2 Priors

The forecasts by P16 considered the same priors as described in Sect. 6.4.3 and the simulations were also performed for a pessimistic and for an optimistic scenario. However, the optimistic case was extended to include a) four times smaller uncertainties on the scaling parameters than currently known, b) spectroscopic redshifts of $\Delta z = 0.01$, and c) a reduced mass cut of $M_{\rm cut} \geq 1{\cdot}10^{-13}\,{\rm M}_{\odot}/h$. Accordingly, this optimistic set-up resulted in an increased catalogue of $\sim 125,300$ clusters for a *WMAP5* cosmology.

6.5.3 Results

Over all, P16 presented cosmological forecasts for a ΛCDM-, a w_0CDM- and a wCDM-model, while additionally combining the results with the *Planck* data of the first release. Also in this case, the *Planck* covariance matrices for a combined analysis of the *Planck* CMB data, of BAO information, of supernovae type Ia data, and of *WMAP* polarisation maps(Planck Collaboration et al. 2014a) were considered. The complete summary of forecast results by P16 is presented in Tab. D.2 in the appendix to allow for a detailed comparison between their results and ours. Below, we state the main findings by P16 which will be most important for testing the reliability of the forecast results in general and for quantifying the influence of our deviating simulations set-ups.

- The improvement in the constraints from the pessimistic to the optimistic scenario was mainly driven by the tighter priors on the scaling parameters as well as by the increase in the cluster catalogue. The spectroscopic redshifts showed only a minor impact on the results.

- For the studied cosmological models, the angular clustering information influenced the parameter precision only minorly.

- Assuming a ΛCDM-cosmology, the optimistic approach for *eROSITA* data alone outperformed the derived constraints on σ_8 and $\Omega_{\rm m}$ for *Planck*.

- For *eROSITA* data alone, the 1σ-marginalised uncertainties were constrained to $\Delta\sigma_8 = 0.011$, $\Delta\Omega_{\rm m} = 0.008$, $\Delta w_0 = 0.091$, $\Delta w_{\rm a} = 0.36$ for the wCDM-cosmology.

- In the case of the optimistic scenario with included *Planck* data, the cosmological constraints were reduced to $\Delta\sigma_8 = 0.007$, $\Delta\Omega_{\rm m} = 0.006$, $\Delta w_0 = 0.07$, $\Delta w_{\rm a} = 0.27$.

- When including *Planck* data, the 2σ-FoM for the dark energy equation of state was estimated to a value of 55, which labels *eROSITA* as a Stage IV experiment according to the report of the *DETF* (Albrecht et al. 2006).

6.6 Final *MCMC* Results

The results of the cosmological forecasts were analysed in the following basis of $\{\sigma_8, \Omega_{\rm m}, n_{\rm s}, h, \Omega_{\rm b}\}$, which was more intuitive than the set of variable parameters $\mathcal{X}$. Depending on the studied cosmological model, the additional parameters $\{w_0, w_a, \sum m_\nu\}$ were extended to the above basis. Furthermore, the uncertainties of the variable scaling relation parameters were quantified, $\mathcal{Y}$, (comp. Sect. 6.4.2) and we generally followed the strategy expressed in Sects. 6.3 & 6.4.

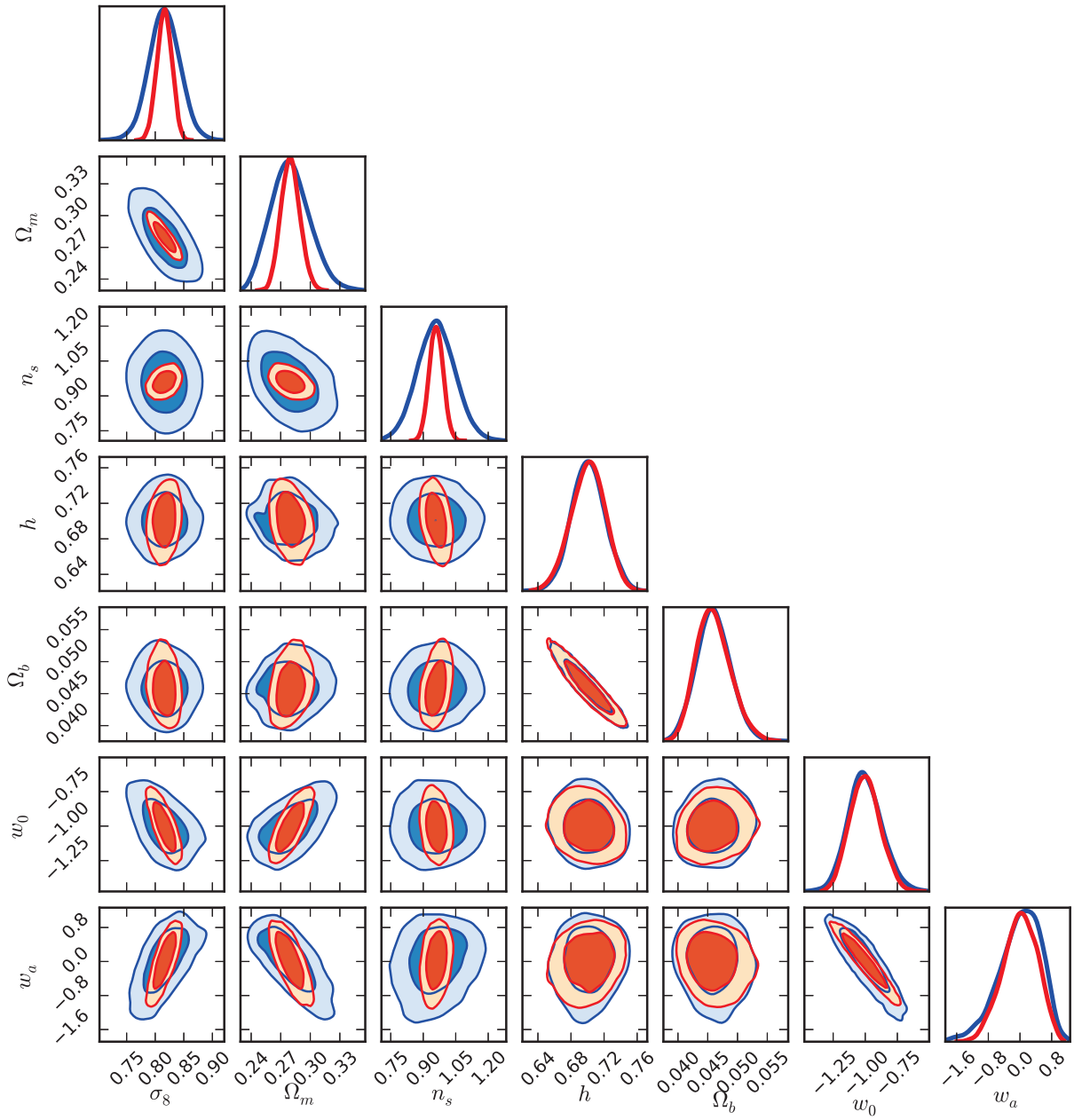

Figure 6.9: Cosmological constraints for a wCDM-cosmology for the pessimistic scenario in blue and the optimistic scenario in red. The 2-dimensional credibility regions present the 68%- as well as the 95%-uncertainties, whereas the diagonal elements display their 1-dimensional histograms normalised to the same peak value. All distributions are centred around the input cosmological values.

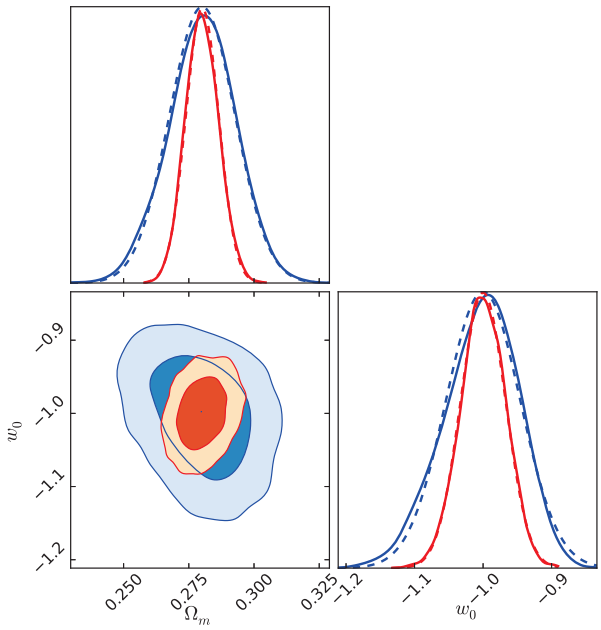

Figure 6.10: Forecasted joint credibilities for the matter density Ω_m and the normalisation of the dark energy equation of state w_0. The contour plots present the 68%- as well as the 95%-credibility regions for the pessimistic (blue) and the optimistic (red) scenario. For the 1-dimensional probability distributions, the estimate by the *MCMC* simulations is indicated by the solid curves, whereas the dashed curves present the corresponding normal distributions with the same mean and σ values.

6.6.1 Forecasts for the Complete Survey Sample (z, η)

These final results are based on the assumption of available cluster redshifts and photon counts only, such that we applied the (z, η)-mock catalogue for the four years of *eROSITA* survey observations, *eRASS:8*, where in total eight all-sky surveys will be performed. For all tested cosmological models, both the optimistic as well as the pessimistic scenarios were investigated. Tab. 6.3 presents the forecasted constraints on the cosmological as well as on the scaling parameters for the different cosmological models and simulation approaches, whereas Fig. 6.9 displays the corresponding credibility contours for a wCDM-cosmology. These 2-dimensional contours are centred around the input parameter values, while marginalising over all remaining parameters except the two presented ones. The complete triangle diagram, which also includes the contours of the scaling parameters is placed in the appendix (Fig. D.3). Of most interest in this analysis were the constraints on the parameter set $\{\sigma_8, \Omega_\mathrm{m}, n_\mathrm{s}, w_0, w_\mathrm{a}\}$ and their dependencies as completely free variables.
Expectedly, the uncertainty on the parameters increased with an extension of the variable set, especially when moving from a w_0CDM-model to a wCDM-model. Whereas Δn_s remained almost constant, $\Delta\sigma_8$ and $\Delta\Omega_\mathrm{m}$ showed an increase by $\sim 33\%$ and Δw_0 was degraded by even a factor of ~ 3.6. Accordingly, this confirmed the strong degeneracies between the parameters $\{\sigma_8, \Omega_\mathrm{m}, w_0, w_\mathrm{a}\}$ observed in Fig. 6.9.
For the cosmological parameters, the strong dependence on the knowledge of the scaling relations became visible with a significant decrease in the uncertainties for improved scaling information (comp. Fig. 6.9). The factor of this decrease differed for the individual parameters, such that for σ_8 and Ω_m the precision improved in general by a factor of ~ 2, whereas for n_s the progress was even higher with a factor of ~ 2.5. On the other hand, the parameters of the dark energy equation of state showed a weaker dependence on the scaling information. For a w_0CDM-cosmology, the constraints on w_0 improved by

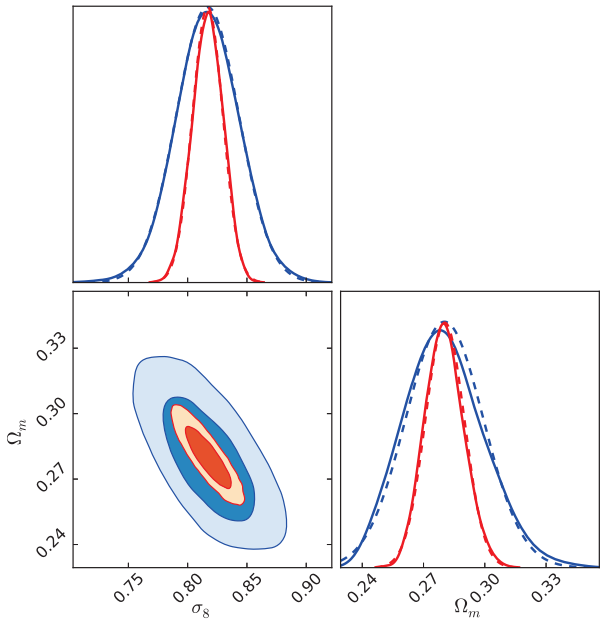

Figure 6.11: Forecasted joint credibilities for the standard deviation in the matter power spectrum σ_8 and the matter energy density Ω_m assuming a wCDM-cosmology. Again, the pessimistic as well as the optimistic scenario are presented in blue and red, respectively. The solid lines are computed based on the true parameter distribution obtained in the *MCMC* simulation, whereas the dashed lines display the estimated covariance matrices of the chains.

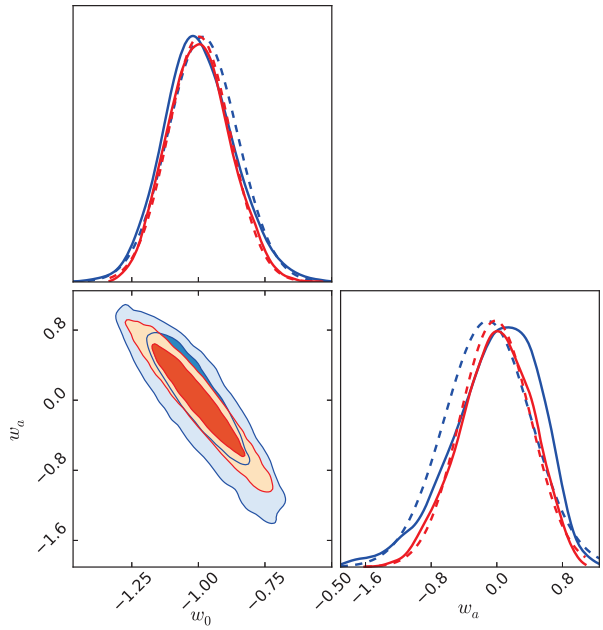

Figure 6.12: Credibility regions for the dark energy parameters w_0 and w_a. As before, we display the results for the optimistic as well as for the pessimistic scenario and additionally approximate the *MCMC* results by the corresponding covariance matrices.

only $\sim 40\%$ when moving from the pessimistic to the optimistic scenario and this development declined to only 10% for a wCDM-cosmology. A similar progress was also observed in Δw_a. These trends of the credibility regions were graphically summarised in Fig. 6.9 and emphasised upon in Figs. 6.10, 6.11 & 6.12 for different parameter combinations. When assuming even further knowledge on the scaling relations and comparing the optimistic scenario to the simulation with frozen scaling relations, the change in the cosmological constraints varied between a factor of ~ 3 to an improvement of only a couple of percent depending on the considered parameter and cosmology. This approach of fixing the scaling relations was of course idealistic, but it supported our aim of quantifying the impact of the knowledge on these relations on the cosmological constraints. The least significant improvement was recorded for the wCDM-cosmology, where the progress read only 30% for n_s and only a couple of percent for w_0 and w_a. Since we were mainly interested in studying dark energy and the wCDM-model, we concluded, that a better knowledge on the scaling relations was inevitable to obtain tight cosmological constraints as they were computed for the optimistic scenario. However, a further reduction of the uncertainties in the scaling relations resulted in only small improvements.

Fig. 6.9 also expresses the strong degeneracies between h and Ω_b, which was defined by the applied priors. However, if these priors were not considered, we would allow for a strong degeneracy especially between h and n_s with several local maxima in the likelihood. This would prevent the *MCMC* chains from converging. Defining priors on h and Ω_b thus allowed to localise the chains in the parameter space around the input cosmological values and excluded the other local maxima, depending on the width of the priors. In general, when running *MCMC* simulations for these forecasts, the applied priors did not only improve the constraints, but were required to allow for converging chains.

The priors of $\Delta h = \pm 0.022$ (Riess et al. 2011) and of $\Delta\Omega_\mathrm{b}h^2 = \pm 0.00046$ (Cooke et al. 2014), or equivalently of $\Delta\Omega_b = \pm 0.00304$, were reproduced in all considered cosmologies with a deviation of only less than 10% from the initial values. The precision on these parameters showed a statistical scatter around the prior values independent of the simulation scenario. Accordingly, the cluster data added only little information to the constraints on these parameters. As there was no trend for this deviation with cosmological model or scaling information, we neglected Δh and $\Delta\Omega_\mathrm{b}$ from our further interpretations (comp. also Fig. 6.9).

In contrast, the large sample of observed clusters allowed for a self-calibration of the scaling relations, such that the constraints on some of the scaling parameters were reduced significantly when compared to their initial prior values (comp. Fig. D.3, Tabs. 6.1 & 6.3). Whereas $\Delta\alpha_\mathrm{LM}$ reproduced the initial value for all considered simulation scenarios, the estimated uncertainties on β_LM and γ_LM reduced the prior in all set-ups by $\sim 50\%$ and by $\sim 10-65\%$, respectively. The larger deviations were commonly observed for the pessimistic approach, such that in these cases also $\Delta\sigma_\mathrm{LM}$ was improved by $\sim 20\%$. These improvements of the prior knowledge indicated that the extended *eROSITA* cluster catalogue contained additional information on the investigated parameters. On the other hand, these deviations between the priors and the computed *MCMC* uncertainties were also partially explained by the discrepancy of the *MCMC* contours from a normal distribution. Investigating Figs. 6.9 & D.3, these differences were especially visible in the shapes of the 1-dimensional, marginalised histograms for the pessimistic simulation scenarios and for the parameters h, Ω_b, β_LM, when considering parameters with prior constraints. Accordingly, the *MCMC* approach allowed for additional information on these prior values by inreasing the allowed freedom on the shape of the credibility regions.

Deviations from a normal distribution were to some extent also observed for the remaining cosmological parameters. In general, these discrepancies increased with increasing parameter uncertainties and thus with the number of free cosmological parameters as well as with the decreasing knowledge on the scaling relations. When analysing e.g. Figs. 6.10 & 6.12, we presented the *MCMC* parameter distributions as solid lines and additionally displayed the approximated Gaussian shapes, based on the

Table 6.3: *MCMC* forecasts of the cosmological and scaling relation parameters for the models ΛCDM, w_0CDM and wCDM and for both the optimistic and the pessimistic scenarios as well as for the idealistic approach of full knowledge on the scaling relations. The simulations for the *eROSITA* data alone were based on the four years of all-sky survey (*eRASS:8*) including the stated priors on h and on $\Omega_b h^2$. The *Planck* data were combined with external information on BAO, supernovae type Ia and H_0 (*Planck*+BAO+H_0+JLA), where for the combination of *eROSITA* and *Planck* data, we applied the optimistic scenario.

Data	$\Delta\sigma_8$	$\Delta\Omega_m$	Δn_s	Δh	$\Delta\Omega_b$	Δw_0	Δw_a	$\Delta\alpha_{LM}$	$\Delta\beta_{LM}$	$\Delta\gamma_{LM}$	$\Delta\sigma_{LM}$
eRASS:8+pes.	0.0187	0.0117	0.0748	0.0192	0.0027	–	–	0.0525	0.0334	0.1106	0.0283
eRASS:8+opt.	0.0082	0.0061	0.0288	0.0177	0.0024	–	–	0.0141	0.0124	0.0540	0.0095
eRASS:8+fixed	0.0027	0.0031	0.0209	0.0214	0.0029	–	–	–	–	–	–
Planck	0.0143	0.0133	0.0062	0.0096	0.0011	–	–	–	–	–	–
eRASS:8+Planck	0.0068	0.0047	0.0039	0.0036	0.0004	–	–	0.0083	0.0120	0.0454	0.0093
eRASS:8+pes.	0.0195	0.0126	0.0823	0.0208	0.0029	0.0543	–	0.0517	0.0342	0.1735	0.0279
eRASS:8+opt.	0.0087	0.0064	0.0329	0.0218	0.0030	0.0329	–	0.0143	0.0123	0.0688	0.0096
eRASS:8+fixed	0.0059	0.0048	0.0217	0.0201	0.0028	0.0255	–	–	–	–	–
Planck	0.0201	0.0093	0.0053	0.0105	0.0015	0.0476	–	–	–	–	–
eRASS:8+Planck	0.0072	0.0049	0.0042	0.0054	0.0008	0.0243	–	0.079	0.01108	0.0472	0.0094
eRASS:8+pes	0.0265	0.0190	0.0864	0.0198	0.0028	0.1308	0.5259	0.0552	0.0355	0.1980	0.0353
eRASS:8+opt.	0.0129	0.0096	0.0315	0.0200	0.0028	0.1169	0.4316	0.0141	0.0126	0.0678	0.0095
eRASS:8+fixed	0.0107	0.0078	0.0217	0.0200	0.0028	0.1136	0.4222	–	–	–	–
Planck	0.0207	0.0102	0.0057	0.0107	0.0016	0.1121	0.4467	–	–	–	–
eRASS:8+Planck	0.0085	0.0062	0.0043	0.0063	0.0009	0.0771	0.2759	0.0079	0.0114	0.0480	0.0094

covariance matrix of the chains, as dotted curves. The normalisation of the dark energy equation of state w_0 showed small indications for a non-Gaussian 1-dimensional uncertainty distribution in the w_0CDM-model for the pessimistic scenario. This deviation was enhanced in the wCDM-model. The uncertainty on the time evolution of the dark energy w_a presented the strongest non-normal shapes with a tilt of the 1-dimensional histogramm to higher values in the pessimistic approach (Fig. 6.12). And even for the optimistic scenario, slight substructures were observed in the distribution. Accordingly, the joint credibility contours of w_0 and w_a did not resemble a Gaussian ellipse, which was also observed for the joint uncertainty regions of the other parameter combinations including the dark energy characteristics (Fig. 6.9). In contrast to the dark energy parameters, however, σ_8 and Ω_m show mainly Gaussian constraints with only slight deviations for Ω_m in the pessimistic scenario (Fig. 6.11). These likelihood shapes were expected, as these two parameters are commonly best constrained by cluster experiments (comp. e.g. Reiprich & Böhringer 2002; Voit 2005; Allen et al. 2011; Mantz et al. 2015).
In summary and following the above considerations, the final constraints on the cosmological parameters for a dark energy cosmology were computed as $\Delta\sigma_8 = 0.0129$, $\Delta\Omega_m = 0.0096$, $n_s = 0.0315$, $w_0 = 0.1169$, $w_a = 0.4316$ (Tab. 6.3). This related to uncertainties of $\lesssim 3\%$ for the first three parameters and of $\sim 12\%$ for w_0. These results implied, that the *eROSITA* cluster sample **alone** was able to achieve the same precision in the dark energy characteristics as the *Planck* data, when considering all external knowledge (*Planck*+BAO+H_0+JLA). Though the estimated Δn_s was downgraded by a factor of ~ 5 when compared to the combined *Planck* results, the precision on Ω_m and σ_8 was improved by $10-60\%$ by the *eROSITA* cluster abundance. What is more, current cluster catalogues have not been sensitive for the index of the power spectrum n_s, yet, such that a tight prior was commonly applied on this parameter when applying clusters for cosmological studies (comp. e.g. Mantz et al. 2015). Though the constraints on n_s were not as precise as for other cosmological probes, the extended *eROSITA* cluster catalogue was able to break the degeneracy in this parameter (comp. also Pillepich et al. 2012).
As the main science driver for *eROSITA* is the study of dark energy, we computed the figure of merit (Sect. 6.4.6) for the joint credibility region of w_0 and w_a to test the significance of the forecasted constraints. We obtained values of $\mathrm{FoM}^{2\sigma}_{w_0,w_a} = 12$ for the pessimistic scenario and of $\mathrm{FoM}^{2\sigma}_{w_0,w_a} = 26$ for the optimistic scenario. This investigation characterised *eROSITA*'s cosmological constraining power alone as an advanced Stage III study according to the DETF (Albrecht et al. 2006). Their report requested a $\mathrm{FoM}^{2\sigma}$ of $[8, 43]$ for a Stage III dark energy mission and of $[27, 645]$ for a Stage IV mission. However, the final classification is defined for the combination of the considered probe with the *Planck* data. Accordingly, already precise estimates on the dark energy equation of state will be obtained from *eROSITA* data only, where these results will even be improved by the combination with *Planck* data (Sect. 6.6.4).

6.6.2 Investigating Neutrino Cosmologies

In addition to the cosmological scenarios described above, we investigated a ΛCDM+ν-model and the constraining power of the *eROSITA* cluster catalogue on the sum of the masses of the different neutrino species, $\sum m_\nu$. Previous works by e.g. Mantz et al. (2015) and Roncarelli et al. (2015) reported the requirement of including CMB data for the study of $\{\Delta \sum m_\nu\}$ due to the strong degeneracy between σ_8 and Ω_m for galaxy cluster experiments (comp. also Fig. 6.11). Alternatively to the CMB, additional angular clustering information was applied to constrain the sum of the neutrino masses (Sartoris et al. 2015). In analogy to these works, the uncertainty on $\{\Delta \sum m_\nu\}$ could not be quantified by the *eROSITA* cluster abundance alone. The significant extension of the currently available cluster catalogue by *eROSITA* was thus not sufficient to compensate the influence of the strong degeneracy. Instead of approaching and then exploring a defined parameter region for $\sum m_\nu$, the *MCMC* chains covered the entire allowed parameter space, independent of the defined hard boundaries. Additionally, the best-fit value increased continu-

ously with increasing step number. Accordingly, no maximum of the likelihood was determined and the burn-in process continued indefinitely. The lack of an estimated credibility region for this simulation scenario also disabled the subsequent combination of these results with *Planck* constraints in an analogous approach to the investigations in Sect. 6.6.4. Studying neutrino characteristics thus requires a joint *MCMC* simulation of both the cluster catalogue and the *Planck* data. Alternatively, the n-dimensional credibility ellipses of the cosmological parameters estimated by *Planck*, with n defining the number of variables, can be applied as priors when considering only the *eROSITA* catalogue. In this approach, not only the width of the credibility ellipses for the *Planck* data, but also the different parameter correlations are accounted for.

6.6.3 Including Temperature Information

As expressed above, cluster temperatures are commonly considered as more precise mass proxies than cluster luminosities, due to the reduced intrinsic scatter in the $M - T_\mathrm{X}$ scaling relation when compared to the $M - L_\mathrm{X}$ relation (comp. e.g. Vikhlinin et al. 2009a; Mantz et al. 2010a; Allen et al. 2011; Giodini et al. 2013). Following this consideration, we computed the cosmological constraints placed only by the *eROSITA* cluster sample with temperature estimates, (z,kT_X), and quantified its impact on the total cosmological precision.

Tab. 6.4 presents the simulation results for a ΛCDM cosmology with different simulation scenarios, depending on the knowledge on the scaling relations. As observed for the full cluster sample, the constraints on σ_8, Ω_m and n_s improved significantly by a factor of $\sim 2-3$ when moving from the pessimistic to the optimistic knowledge.

Also, the uncertainties on h and Ω_b as well as the uncertainties on the scaling parameters recovered the input priors, where in contrast to the above simulations the precision on β_TM was decreased by $\sim 50\%$. This underestimation of the prior on β_TM expresses, that the applied catalogue allowed only for weaker constraints than the current knowledge on this parameter. The shape of the uncertainty regions and 1-dimensional histograms were analogously explained by the discussion in the previous section with slight deviations from Gaussianity for Δh and $\Delta\Omega_\mathrm{b}$, and with an increasing divergence for the pessimistic approach.

As an example, the joint credibility regions for the set $\{\sigma_8, \Omega_\mathrm{m}, n_\mathrm{s}\}$ are presented in Fig. 6.13, where this simulation was based on the optimistic scenario for a ΛCDM-cosmology. The graphic compares the results of the (z,kT_X)-catalogue only in black to the constraints of the full cluster sample in red. On the one hand, the strong degeneracy between the three studied parameters was reproduced also for the cluster sub-sample. However, of more significance in this figure is the deviation between the parameter credibilities for these two approaches. When applying only the (z,kT_X)-cluster catalogue the precisions on the cosmological parameters were reduced by a factor of $\sim 3-4$ (comp. Tab. 6.3 & 6.4). Accordingly, the cluster temperature sample alone allowed for studying the uncertainties on the above cosmological parameters, but only with limited constraining power. This aspect yielded the considerations, that adding the cluster temperature sample will improve the constraints of the full sample by solely a couple of percent.

For investigating the influence of the cluster temperature information, we focused mainly on the ΛCDM-model, but tested a wCDM-cosmology and the impact on the dark energy parameters as well. In this scenario, the sub-catalogue failed to constrain Δw_a as the likelihood appeared almost constant towards the lower best-fit values and no defined credibility regions could be outlined. Thus, the optimistic (z,kT_X)-sample of $\sim 8,000$ clusters alone did not provide enough information to investigate and test more complex cosmologies than the currently accepted model.

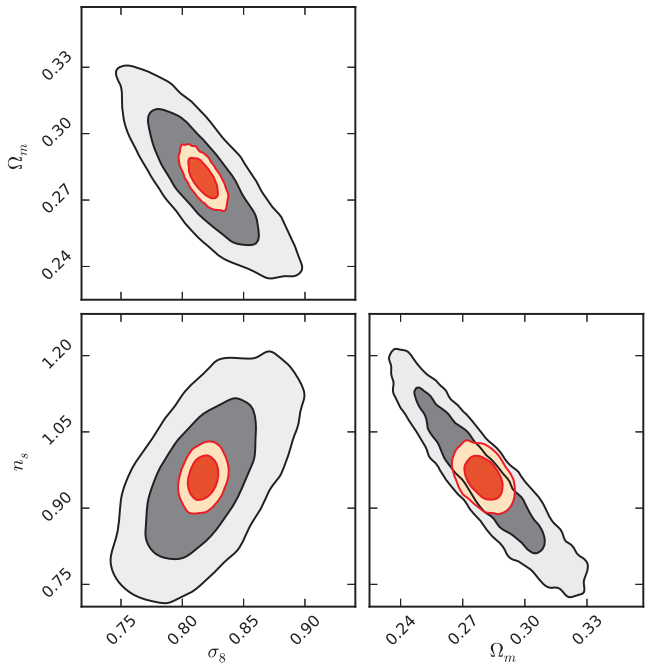

Figure 6.13: Joint credibility regions for the parameters σ_8, Ω_m and n_s of the 68%- and the 95%-uncertainty levels. The black contours represent the *MCMC* results for the temperature catalogue $(z, \mathrm{k}T_\mathrm{X})$ only, whereas the red contours show the constraints for the full (z, η)-cluster catalogue. Both approaches are displayed for the optimistic scenario. Despite the extent of the $(z,\mathrm{k}T_\mathrm{X})$-sample to $\sim 8,000$ clusters, the constraints from the cluster temperatures were still not comparable to the results for the full cluster catalogue without temperatures.

These results were reasoned by the following arguments. Though the intrinsic scatter in the $M - T_\mathrm{X}$ relation undercut that of the $M - L_\mathrm{X}$ relation by a factor of $\gtrsim 3$ (comp. e.g. Vikhlinin et al. 2009a; Mantz et al. 2010a; Allen et al. 2011; Giodini et al. 2013), the percentaged uncertainties on the remaining scaling parameters and thus also the defined priors were comparable for both scaling relations. In general, these uncertainties remained below $\sim 10\%$ with an increase up to $\sim 20\%$ for γ_LM (comp. e.g. Maughan 2007; Pratt et al. 2009; Vikhlinin et al. 2009a; Mantz et al. 2015; Giles et al. 2015). Accordingly, the main influence on the cosmology results could be addressed to the reduced number of clusters in the $(z,\mathrm{k}T_\mathrm{X})$-sample when compared to the full (z, η)-catalogue. This sub-catalogue of clusters with temperature estimates did only contain a factor of ~ 12 less clusters in the optimistic case, which thus limited the statistical constraining power of the sample. At the same time, clusters at redshifts above $z \approx 0.16$ (comp. Figs. 6.8 & 4.3) were not included, due to the selection function of the instrument (Sect. 6.3.2). In total, more than half of the redshift bins were neglected, where the information in the bins at higher redshifts are most sensitive to cosmology. Additionally, the reduced intrinsic scatter in the $M - T_\mathrm{X}$ relation lowered the number of observed clusters even further as less clusters were scattered up above the defined temperature cuts.
What is more, when comparing the $M - L_\mathrm{X}$ and the $M - T_\mathrm{X}$ relation, the smaller intrinsic scatter in the latter relations should in principle allow for the determination of smaller statistical uncertainties on the scaling parameters from a given observed catalogue. As discussed above, this is not observed, however, such that there is still room for improvement in the cluster observations to reduce these uncertainties and to establish the gas temperatures as more precise cosmological estimate than the luminosity.

Table 6.4: Forecasts for the 1σ-uncertainties when applying the cluster temperature catalogue only, eRASS:8 k$T_{\rm X}$. Additionally, we summarised the constraints for the optimistic approach with a frozen redshift evolution in the scaling relation as well as for a completely fixed $M - T_{\rm X}$ relation.

Data	$\Delta\sigma_8$	$\Delta\Omega_m$	Δn_s	Δh	$\Delta\Omega_b$	$\Delta\alpha_{TM}$	$\Delta\beta_{TM}$	$\Delta\gamma_{TM}$	$\Delta\sigma_{TM}$
eRASS:8 k$T_{\rm X}$+pes.	0.0917	0.0417	0.1949	0.0204	0.0029	0.0446	0.1251	0.0636	0.0280
eRASS:8 k$T_{\rm X}$+opt.	0.0325	0.0209	0.1047	0.0207	0.0029	0.0121	0.0338	0.0166	0.0075
eRASS:8 k$T_{\rm X}$+opt. frozen γ_{TM}	0.0308	0.0203	0.1013	0.0200	0.0028	0.0120	0.0333	–	0.0075
eRASS:8 k$T_{\rm X}$+opt. frozen	0.0285	0.0194	0.0909	0.0203	0.0028	–	–	–	–

Table 6.5: Cosmological parameter constraints when applying the scaling relations by Vikhlinin et al. (2009a) for different cosmological models. The scaling relations remained fixed during all simulations, except for the last run in which the $M - L_{\rm X}$ parameters were fit simultaneously for a pessimistic scenario. The black results were obtained in our *MCMC* simulations, whereas the grey values were taken from the Fisher analysis by A. Pillepich, which we discussed in private communication. Both simulation approaches followed an identical set-up apart from the deviation between the *MCMC* and the Fisher formalism.

Data	$\Delta\sigma_8$	$\Delta\Omega_m$	Δn_s	Δh	$\Delta\Omega_b$	Δw_0	Δw_a	$\Delta\alpha_{LM}$	$\Delta\beta_{LM}$	$\Delta\gamma_{LM}$	$\Delta\sigma_{LM}$
eRASS:8	0.0031	0.0030	0.0252	0.0180	0.0026	–	–	–	–	–	–
eRASS:8 (Fisher)	0.0031	0.0030	0.0292	0.0234	0.0032	–	–	–	–	–	–
eRASS:8	0.0082	0.0057	0.0307	0.0204	0.0029	0.0293	–	–	–	–	–
eRASS:8 (Fisher)	0.0086	0.0059	0.0333	0.0236	0.0033	0.0310	–	–	–	–	–
eRASS:8	0.0136	0.0083	0.0281	0.0182	0.0026	0.1324	0.4542	–	–	–	–
eRASS:8 (Fisher)	0.0152	0.0093	0.0358	0.0237	0.0033	0.1451	0.4892	–	–	–	–
eRASS:8+pes.	0.0231	0.0169	0.0668	0.0205	0.0028	–	–	0.0493	0.0809	0.1453	0.0329

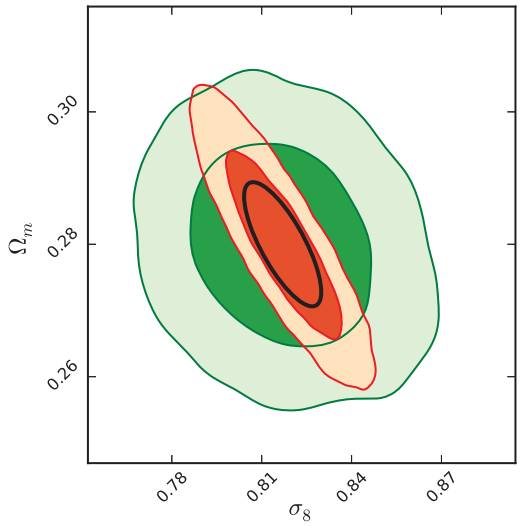

Figure 6.14: Marginalised uncertainty regions for the *Planck*+BAO+H_0+JLA data in green and for *eRASS:8*, assuming an optimistic scenario, in red for the deviation in the matter perturbations σ_8 and the mean matter energy density Ω_m, and a wCDM-cosmology. When assuming a normal distribution of these uncertainties, the black ellipse represents the joint 68%-credibility contour for both data sets. The *Planck* data have been shifted to yield a *WMAP5* cosmology.

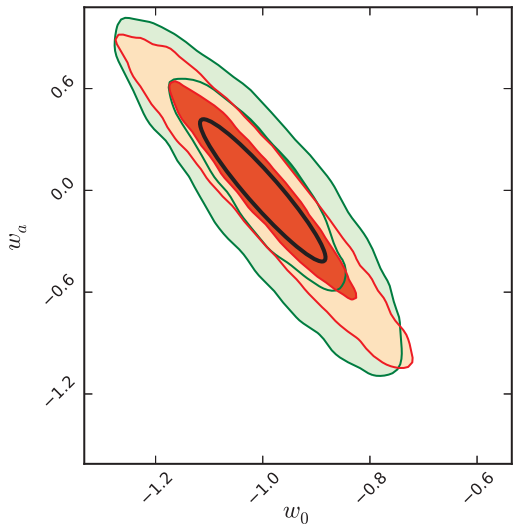

Figure 6.15: Marginalised uncertainty regions for the *Planck*+BAO+H_0+JLA data in green and for *eRASS:8*, assuming an optimistic scenario, in red for the parameters of the dark energy equation of state. When assuming a normal distribution for these uncertainties, the black ellipse represents the joint 68%-credibility contour for both data sets. Again, the *Planck* data have been shifted to yield a *WMAP5* cosmology.

6.6.4 Including *Planck*-Data and Other Probes

For an estimate on how the inclusion of the *Planck*+BAO+H_0+JLA data improves the *eROSITA*-only cosmological constraints, we approximated the *MCMC* constraints of both data sets by their Gaussian covariance matrixes. These were then inverted and summed (Sect. 6.4.5), while applying the results of the full (z, η)-cluster set and of the optimistic scenario. This strategy of summing the inverse of the covariance matrices was allowed due to the independence of the two data sets. At the same time, this approach focused on the shapes of the credibility ellipses and not on their location in the parameter space, such that the problematic of the not fully consistent cosmology constraints between the *Planck* and the *WMAP* data was avoided (comp. e.g. Komatsu et al. 2009; Hinshaw et al. 2013; Planck Collaboration et al. 2015c). However, when assuming Gaussian uncertainties, we introduced a bias since e.g. the dark energy equation of state parameters and also the priors Δh and $\Delta\Omega_b$ suggested a non-normal distribution of the likelihoods for the *eROSITA* data. For the latter two parameters, the deviation from Gaussianity was computed to $\lesssim 10\%$. The shape of the 1-dimensional histograms in Fig. 6.9 suggested discrepancies from a normal distribution of the same order for the remaining parameters, especially when considering the optimistic scenario. Analogously, the *Planck* data were investigated and showed a comparable trend and deviations from Gaussianity (comp. Fig. D.4).
The uncertainties on the cosmological parameters for applying a joint analysis of the *eRASS:8* and the *Planck*+BAO+H_0+JLA data are presented in Tab. 6.3. The strongest improvement is observed in Δn_s, Δh and $\Delta\Omega_b$ for all studied cosmological models with deviations of $\sim 70 - 80\%$ when compared to the *eROSITA*-only results. Since clusters alone allow for only weak constraints on these three variables

and external priors were required on at least two of them (comp. e.g. Pillepich et al. 2012; Mantz et al. 2015), this trend was expected. On the other hand, the standard deviation in the matter perturbations σ_8, in the mean matter energy density Ω_m, and in the dark energy parameters w_0 and w_a presented the highest precisions for our cluster analysis, such that the combination of the data sets yielded only a smaller progress of $\sim 20 - 35\%$ in their uncertainties (Figs. 6.14 & 6.15). For a wCDM-cosmology, $\Delta\Omega_m$, Δw_0 and Δw_a became comparable between the two individual analyses, in which case the expected improvement by a factor of $\sqrt{2}$, or equivalently by $\sim 40\%$, was obtained for the joint analysis. In summary, we estimated precisions of $\Delta\sigma_8 = 0.0085(4\%)$, $\Delta\Omega_\mathrm{m} = 0.0062(2\%)$, $\Delta w_0 = 0.0771(8\%)$, and $\Delta w_\mathrm{a} = 0.2759$ for the combination of the two data sets. Though the *Planck* data did not contain any information on the parameters of the scaling relations, the joint analysis allowed for improvements in their precisions of up to $\sim 40\%$ depending on their degeneracy with the cosmological parameters (comp. Fig. D.3). Accordingly, for stronger degeneracies a more significant decrease of the uncertainties was obaerved, which was the case for α_LM and γ_LM. Over all, the best improvements could be obtained for the wCDM cosmology as most complex investigated model. In this case, the combination of the in total four different probes and two additional priors in our two data sets - clusters, CMB temperatures, BAO, supernovae type Ia, and additional priors on the Hubble constant and the baryon density - were best applied to break degeneracies and to benefit from the individual constraining characteristics of each probe.
For this joint analysis, we repeated the computation of the figure of merit and achieved a result of $\mathrm{FoM}^{2\sigma}_{w_0 w_\mathrm{a}} = 53$. Accordingly, *eROSITA* is classified as the first Stage IV mission for the study of dark energy (comp. Sect. 6.6.1).
As already expressed, this Gaussian approach for the uncertainty regions introduced a bias in the joint credibility results. Assuming the uncertainties to be biased low by $\sim 10\%$ each, the systematic error in the joint uncertainties would increase to $\sim 0.1 \cdot \sqrt{2} \approx 14\%$. Including this consideration also in the figure of merit estimate, the results reduced to $\mathrm{FoM}^{2\sigma}_{w_0 w_\mathrm{a}} \approx 46.5$, which did not degrade the classification of the instrument. Although this deviation still allowed for a reliable estimate of the joint credibilities, the non-normal distributions for the dark energy parameters asked for a combined *MCMC*-simulation of the two data sets. The obstacles and necessary considerations for this approach are presented in the outlook of this project, where we also discuss different approaches to work with the deviating best-fit cosmologies from the *Planck* and the *WMAP* data (Sect. 6.10).

6.7 Influences on the Forecast Results

As the simulation set-up included a variety of different assumptions, we tested their influences on the cosmological forecasts. For this study, we varied our own simulation strategy in several aspects and at the same time performed a detailed comparison to the results by P16.

6.7.1 The Applied Scaling Relations

Galaxy cluster scaling relations obtained from different studies deviate especially in the computed scaling parameters, which we named as α, β, γ, and σ in the previous sections (comp. Eqs. 6.19 & 6.20). Accordingly, also the priors on these parameters vary from work to work and especially the shape of the cluster abundance function and thus the number of expected galaxy clusters observed by *eROSITA*. Since the previous cosmology forecasts for this instrument were based on the scaling relations by Vikhlinin et al. (2009a) (Pillepich et al. 2012, comp. also Sect. 6.5), we performed *MCMC* simulations also for this relation for various cosmologies and compared the computed parameter constraints to our results for the scaling relations by Reichert et al. (2011).

The total number of expected *eROSITA* clusters was reduced to 89, 300 when applying the scaling relations by Vikhlinin et al. (2009a) for the same set-up as expressed in Sects. 6.3 & 6.4. While this cluster abundance reproduced the estimates by P16 to more than 99%, it simultaneously displayed $\sim 10\%$ less clusters than in the above described mock catalogue. This deviation was explained by the difference in the distribution of the observed clusters for both scaling relations as expressed by Borm et al. (2014). Both distributions peaked around cluster masses of $M \approx 10^{14}$ $M_\odot$ and redshifts of $z \approx 0.3$, while the distribution for the scaling by Reichert et al. (2011) showed a broader maximum.
To quantify the influence of the two different cluster samples on the cosmological constraints, we performed forecasts applying the Vikhlinin et al. (2009a) scaling relations for the three cosmologies ΛCDM, w_0CDM, and wCDM, while initially fixing the scaling parameters during the fit (Tab. 6.5) to focus on the cosmological constraints. Similar to the forecast results for the scaling relations by Reichert et al. (2011) (comp. Tab. 6.3), also for this set-up the constraints decreased significantly as additional variable parameters were introduced. Whereas Δn_s remained almost constant, the strong degeneracy between the parameters $\{\sigma_8, \Omega_\mathrm{m}, w_0, w_\mathrm{a}\}$ was reproduced with an increase of a factor of even ~ 4.5 in Δw_0 when moving to a wCDM cosmology. These comparable degeneracies were also visible in the comparison of the 2-dimensional credibility regions (Fig. D.5) with very similar shapes for all parameter combinations. As before, also for these simulations the constraints on h as well as on Ω_b generally represented the defined priors on h and $\Omega_\mathrm{b}h^2$ for all considered cosmological models with deviations of on average $\sim 12\%$.
Not considering the computed uncertainties on h and Ω_b, the strongest deviations between the two scaling relation approaches were found for the constraints on n_s and σ_8 with a slightly higher deviation in Δn_s. For the cosmologies ΛCDM and w_aCDM, the divergence in these two parameter uncertainties was of the order of $\lesssim 20\%$, where the approach including the scaling relation by Vikhlinin et al. (2009a) generally resulted in weaker constraints. The deviation even increased up to $\sim 30\%$ for the w_0CDM-cosmology. The remaining uncertainties $\Delta\Omega_\mathrm{m}$, Δw_0, and Δw_a were very comparable and altered by less than $\lesssim 15\%$ between the two set-ups for all cosmologies. Accordingly, the different distributions of clusters and the thus increased abundance for the scaling relations by Reichert et al. (2011) yielded a higher precision on the parameters n_s and σ_8, whereas the constraints on Ω_m as well as on the dark energy characteristics were only less impacted.
To extent the above comparison, we performed one additional simulation based on the scaling relations by Vikhlinin et al. (2009a) for a ΛCDM-cosmology with variable scaling parameters (Tab. 6.5), for which we applied the following parameter values and Gaussian priors

$$\begin{aligned} \alpha_\mathrm{LM} &= 1.61 \pm 0.14 \\ \beta_\mathrm{LM} &= 101.483 \pm 0.085 \\ \gamma_\mathrm{LM} &= 1.85 \pm 0.42 \\ \sigma_\mathrm{LM} &= 0.396 \pm 0.039 \quad . \end{aligned}$$

This was equivalent to assuming a pessimistic approach and thus the current knowledge on the scaling parameters. These priors were of the same percentage for both scaling relations apart from the uncertainty on β_LM, which showed a significant reduction for the relation by Vikhlinin et al. (2009a).
As in Sect. 6.6.1, we again observed a strong dependence of the cosmological constraints on the knowledge on the scaling relations (comp. Tab. 6.5). For the variables σ_8, Ω_m, and n_s, the increase in the uncertainties was of a factor of $\sim 2.5 - 7.3$, which is of the same order of magnitude as the analogous comparison for the simulations applying the relations by Reichert et al. (2011). The priors on h, on Ω_b and on the scaling parameters were again reproduced, with an improvement of 65% in the uncertainties

on $\alpha_{\rm LM}$ and $\gamma_{\rm LM}$. As in the above comparison, deviations in the parameter uncertainties were observed between the two scaling relation approaches with a difference of 20% in $\Delta\sigma_8$ as well as in $\Delta\Omega_{\rm m}$, and of 11% in $\Delta n_{\rm s}$. Except for $\Delta n_{\rm s}$, the precisions computed in this section underestimated those obtained for the relations by Reichert et al. (2011).
In summary, the applied scaling relations mainly impacted the computed mock catalogue of cluster observations and thus influenced the cosmological constraints accordingly. The general trends in the parameter degeneracies, in the dependencies on the number of variable parameters and in the reproduction of the priors were comparable for both scaling relations. Though the computed precisions were similar for several parameters as e.g. for w_0 and for $w_{\rm a}$, a divergence of $\sim 30\%$ or more may be observed for other variables, depending on the considered cosmology and scaling knowledge. Following this train of thoughts, for cosmological studies it is essential to calibrate the scaling relations to yield the correct total number of clusters. The cluster catalogue from the *eROSITA* all-sky observations, which includes clusters down to fluxes of $\sim 3\cdot10^{-14}$ erg/s (Merloni et al. 2012; Pillepich et al. 2012), will allow for these investigations in detail at least for the $M - L_{\rm X}$ relation (Sect. 6.6.1 & Tab. 6.3), which shows a stronger impact on the expected number of observed clusters (comp. Sect. 6.3.1). Thus, the *eROSITA*-instrument will not only obtain tight cosmological constraints due to the observed broad cluster sample, but it will also allow for even further improvements by calibrating the scaling relations.

6.7.2 Fisher Formalism vs. *MCMC* Simulations

As previous cosmology forecasts for *eROSITA* were performed based on the Fisher formalism, we quantified the improvement in the accuracy of those results when applying *MCMC* simulations. For this investigation, we compared our constraints for the scaling relations by Vikhlinin et al. (2009a) to those presented by P16 in a constructive discussion with the authors.
Excluding any biases between the two works in programming the galaxy cluster photon counts function, the computed total number of clusters agreed very well with a deviation of only $\sim 0.5\%$. To emphasise on the cosmological forecasts only, the scaling relations remained fixed during these fits and we investigated the results for the cosmological models ΛCDM, w_0CDM, and wCDM (Tab. 6.5). The interpretation of the Fisher forecasts were prepared by P16, such that we focused on the comparison of the two statistical approaches.
The strongest divergences were observed for the uncertainties in the parameters $n_{\rm s}$, h, and $\Omega_{\rm b}$, with the Hubble constant as the most influenced parameter (Fig. D.6). At the same time, these were the parameters which could be constrained the least by galaxy clusters as cosmological probes. Studying the results for the different cosmological models from top to bottom, the precisions for these three parameters indicated deviations of $< 23\%$, $< 14\%$, and $< 23\%$, respectively, between the two statistical scenarios, where the *MCMC* analysis yielded tighter constraints in general. On the other hand, the credibilities of σ_8, of $\Omega_{\rm m}$, as well as of the parameters of the dark energy equation of state, which are of most interest to us, were very well approximated by the Fisher formalism with deviations of only $\lesssim 10\%$ (comp. Fig. 6.16). Also, the same parameter degeneracies were obtained within the two approaches.
The discrepancy in the uncertainty values arose since the Fisher approach reproduced the priors on h and $\Omega_{\rm b}$, whereas the *MCMC* forecast tightened the constraints on these parameters (comp. Sect. 6.6.1). As the Hubble parameter and the index of the power spectrum are strongly degenerate, the deviation from Gaussianity in Δh was transferred to $\Delta n_{\rm s}$. Accordingly, the *MCMC* forecasts were improved compared to the results of the Fisher formalism since the first scenario allowed for non-normal credibility regions.
In conclusion, the Fisher approach proved itself as reliable method for a first estimate of the cosmological constraints, which also included the dark energy parameters. On the other hand, the allowance of non-Gaussian uncertainty distributions was the main cause for the difference between the two ap-

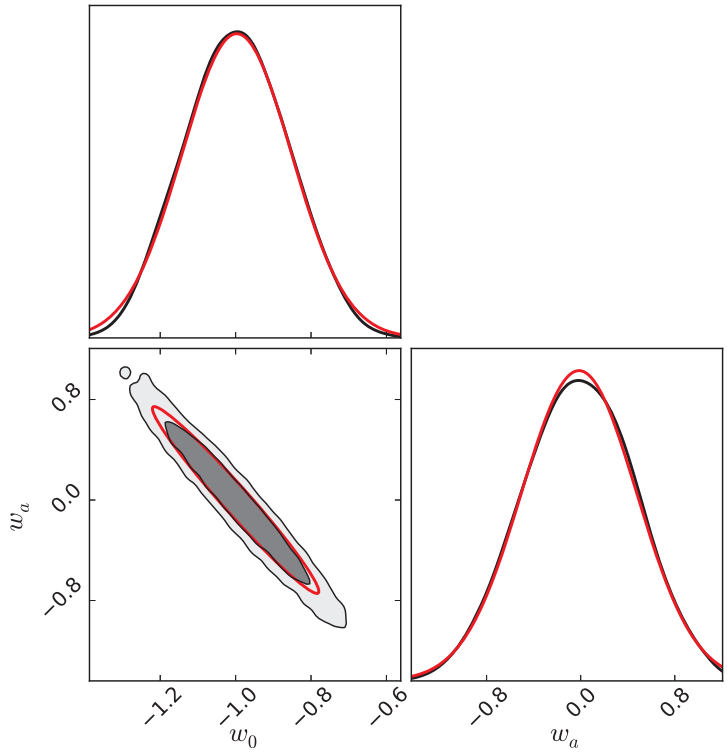

Figure 6.16: Comparison of the joint credibility forecasts on w_0 and w_a, applying the scaling relations by Vikhlinin et al. (2009a). The black regions display the *MCMC* results for the 68%- and the 95%-uncertainty levels, whereas the red contours represent the results of the Fisher formalism for the 68%-credibilities only.

proaches, especially for those parameters $\{n_s, h, \Omega_b\}$ with only little constraining power by galaxy clusters. However, for more complex and more realistic simulation scenarios with variable scaling relations, deviations from Gaussianity became visible also for the dark energy parameters (comp. Fig. 6.12). Accordingly, these findings supported the *MCMC* simulation strategy in general and a subsequent comparison between the two statistical approaches and their impact on the dark energy constraints is presented in the following section.

6.7.3 Comparison to Previous Work

This section emphasises on the comparison between our work and that of P16 to investigate the impact of our deviating simulation set-ups on the final results, while accounting for the information obtained in the previous two sections.
In general, we observed similar trends in both works for the dependence on the knowledge on the scaling relations or on the inclusion of additional variables. However, our simulation scenario yielded a stronger dependence on the priors of the scaling parameters with a factor of ~ 2 compared to a factor of $1.3 - 2$ for the work by P16 between the uncertainties in the pessimistic and the optimistic scenario. At the same time, the precision on σ_8 and Ω_m decreased similarly in both approaches when including a variable dark energy equation of state, whereas Δw_0 increased more significantly for our simulation strategy by a factor of ~ 3.5 in comparison to a factor of ~ 2.6 for P16.
When investigating the absolute values of the constraints, we additionally considered the comparison of the results between the scaling relations by Vikhlinin et al. (2009a) and Reichert et al. (2011) (Sect.

6.7.1), which resulted in similar constraints on Ω_m, w_0 and w_a, but in improved constraints by up to $\sim 30\%$ for σ_8 and the latter scaling relation (Sect. 6.7.1). Despite this degradation in the precision for the relations by Vikhlinin et al. (2009a), P16 now yielded more precise estimates for σ_8 by up to $\sim 30\%$ in the pessimistic scenarios. We accordingly interpreted this improvement as the result of the included clustering information. The assumed Gaussianity in the Fisher formalism was not expected to account for this effect as the parameter σ_8 displayed a close to normal distribution in our *MCMC* simulations (Fig. 6.9). For the optimistic scenarios on the other hand, the constraints were very well comparable, such that the stronger dependence on the scaling information for the relations by Reichert et al. (2011) compensated not only for the additional clustering information, but also for the reduced mass cut and the thus increased cluster sample by $\sim 25\%$ by P16. What is more, this cluster sample was only extended to lower mass clusters, which are mainly observed at the local redshifts. As the cosmological constraints, except for the dark energy characteristics, are most sensitive to the massive clusters at the highest redshifts, this enhanced catalogue allowed only for a limited improvement in $\{\sigma_8, \Omega_\mathrm{m}, n_\mathrm{s}\}$ in addition to the better statistics.
Especially significant was the increased precision for all cosmological parameters in the optimistic scenario of a wCDM cosmology for the Fisher formalism. As an example, the deviations in Δw_0 and Δw_a were of the order of $\sim 22\%$ and of $\sim 17\%$, respectively, between the two approaches. Since these uncertainties did not deviate for the optimistic cases when assuming more simple cosmological models, this effect could not be explained by the deviating cluster catalogues or the additional clustering information. Instead, we discussed these results based on a discrepancy of the credibility regions from Gaussianity, which increased with the complexity of the cosmology as well as with the number of variable parameters (Sect. 6.6.1).
In summary, the main information from this comparison is the stronger dependence on the scaling priors for the relations by Reichert et al. (2011) as well as especially the overestimation of the precisions by the Fisher formalism for complex cosmological models. This latter argument supported the reliability of our *MCMC* results to forecast the observational cosmological potential of the *eROSITA* instrument. Apart from these aspects, the computed forecasts were in very good agreement between the two approaches, which was also reflected by the computed values of the $\mathrm{FoM}^{2\sigma}$ of 55 by P16 and of 53 for our work.

6.8 Discussion

6.8.1 Reliability of the Cosmological Results

To investigate the credibility of our above stated forecast results, we compared the best-fit values of the variable parameters with their input values as a first test. These two sets of values were in very good agreement with deviations of only $\lesssim 1\%$, such that we excluded the existence of any possible parameter bias in our simulations. Additionally, the convergence criterion for the chains was defined to show a difference in the over-all mean fit values as well as in their 1σ-uncertainties of less than 1% when comparing the chains every $\sim 10,000$ steps. Accordingly, we could ensure the robustness of our computed parameter uncertainties.
As a more thorough reliability test, we examined our predicted parameter uncertainties in contrast to the *eROSITA*-forecasts by P16. Based on the conclusions on Sect. 6.7.3 we concluded our forecasts and those by P16 to be in very good agreement with each other when considering the different simulation set-ups. The observed deviations in the results are likely explained by these described differences in the approaches.
Especially the shape of the $w_0 - w_\mathrm{a}$ credibility region and how well it can be approximated by the Fisher

formalism has been investigated by several works and for several cosmological probes and data sets. As an example, Wolz et al. (2012) and Khedekar & Majumdar (2013) found strong deviations between the Fisher and the *MCMC* approach for the study of dark energy, where the first formalism in general underestimated the uncertainties. According to Khedekar & Majumdar (2013), this difference was expected to be of the order of a factor of $\gtrsim 4$ for the *eROSITA* cluster sample and the computed *MCMC* credibilities diverged strongly from Gaussianity. However, for our *MCMC* simulations only small deviations from a normal distribution were observed in the $w_0 - w_a$ contours, which we estimated to a factor of the order of ~ 1.2 when we compared our results to those by P16. Khedekar & Majumdar (2013) applied a different simulation set-up that resulted in completely different cosmological constraints, which accordingly explain the differences in the comparisons between *MCMC* and Fisher results. Though they applied only a flux cut as instrumental characteristic and thus increased their sample to $\sim 120,000$ clusters, their computed *MCMC*-uncertainties for a wCDM model were less precise by a factor of up to ~ 8 compared to our results. On the other hand, the Fisher formalism by Khedekar & Majumdar (2013) yielded tighter constraints on w_a by a factor of ~ 2.2 when compared to P16. Accordingly, a particularly strong deviation between their two simulation methods was computed. Apparently, our developed cosmological simulations strategy and the applied increased information on the instrumental response resolved the strong deviation between the *MCMC* and the Fisher approach.
Recent work by Mantz et al. (2015) also presented a $w_0 - w_a$ credibility region for cluster observations, which was similarly shaped to Fig. 6.12. Their analysis was based on a sample of only ~ 100 clusters, but it included gas mass estimates and also weak lensing masses for some of the clusters. Though their constraints on the dark energy parameters were a factor of ~ 2 above our computed uncertainties, Mantz et al. (2015) also obtained close to Gaussian credibility regions, which thus supported our findings.

6.8.2 Discussing the Dark Energy Constraints

To evaluate our computed constraints for the nature of dark energy, we analysed them in comparison to the results of other current and planned cosmology studies of different cosmological probes (Tab. 6.6).

- *Planck:* Following the newest data release of the *Planck* satellite, we computed uncertainties of $\Delta w_0 = 0.11$ and of $\Delta w_a = 0.45$ when considering *Planck*+BAO+H_0+JLA data. A further improvement of $\Delta w_0 = ^{+0.075}_{-0.080}$ could only be achieved if additional weak lensing information was applied (Planck Collaboration et al. 2015c).

- *Dark Energy Survey (DES):* This optical and near-infrared survey was started in 2011 over a time period of 5 years to cover $5,000$ deg^2 in the southern hemisphere, while observing from Cerro Tololo in the Chilean Alps (The Dark Energy Survey Collaboration 2005). It is expected to include observations of $\sim 4,000$ supernovae type Ia, ~ 300 Million galaxies and redshifts for $\sim 100,000$ clusters of galaxies. According to the *DETF*, *DES* is ranked as a Stage III dark energy project (Albrecht et al. 2006). This constraining power will e.g. be obtained in the cosmological study of supernovae type Ia (Bernstein et al. 2012) and especially in the investigation of galaxy clustering and shear measurements (comp. e.g. Giannantonio et al. 2012). When combining the expected *DES* dark energy constraints with the information of *Planck*, uncertainties of $\Delta w_0 = 0.09$ and $\Delta w_a = 0.35$ were expected (Giannantonio et al. 2012).

- *Euclid:* The *Euclid*-satellite is scheduled for launch in 2020 to an L2 orbit to perform a survey of $10,000$ deg^2 in the optical and in the near-infrared (Laureijs 2009). It will map ~ 60 Million galaxies out to $z \approx 2$ to especially reconstruct the LSS and its evolution, while being classified as Stage IV mission for the study of dark energy (Albrecht et al. 2006). In combination with the

Table 6.6: Comparison of the constraints on the nature of dark energy for various data sets. For the constraints from *eROSITA*, the optimistic cases for the knowledge on the scaling parameters were considered as well as the data of *Planck*+BAO+H_0+JLA.

Data	Δw_0	Δw_a	Reference
*e*RASS:8	0.117	0.432	this work
*e*RASS:8+Planck	0.077	0.276	this work
*e*RASS:8+Planck	0.071	0.27	Pillepich et al. in prep.
DES+Planck	0.090	0.35	Giannantonio et al. (2012)
Euclid+Planck	0.035	0.15	Giannantonio et al. (2012)
Euclid+Planck	0.017	0.07	Sartoris et al. (2015)

cosmological constraints from the *Planck* data, the *Euclid* instrument is expected to even tighten the *eROSITA* constraints on the nature of dark energy by a factor of $\sim 2-3.5$ (Giannantonio et al. 2012; Sartoris et al. 2015, comp. also Tab. 6.6). The different predictions in the two works are due to deviating simulation set-ups and different applied cosmological probes, where Giannantonio et al. (2012) studied the clustering of galaxies, including also weak lensing information. Sartoris et al. (2015) applied galaxy clusters as probes, while assuming a perfect knowledge on the scaling relations. However, the start of this mission is scheduled well after the launch of *eROSITA*.

- *BAO:* Current cosmology studies based on BAOs, such as e.g. *BOSS* (*Baryon Oscillation Spectroscopic Survey*), are not yet competitive with the above results and yield uncertainties on w_0 around $\sim$ 14% (comp.e.g. Anderson et al. 2014; Kazin et al. 2014). Future BAO surveys, such as e.g. *4MOST* (de Jong et al. 2014) or *eBOSS* (*extended Baryon Oscillation Spectroscopic Survey* Zhao et al. 2015), will extend the current data sample. While forecasts on the cosmological impact by *4MOST* have not been published, yet, *eBOSS* is expected to achieve a figure of merit of 24.9 for the dark energy parameters in combination with *Planck* and H_0 data. Only when applying additional information from the *Lyα-forest*, this results can be improved to a value of 73.7 and thus to tighter constraints than are expected for *eROSITA*. *eBOSS* is scheduled to start observing in late 2016, comparable to the time schedule of *eROSITA*.

- *Redshift space distortion (RSD):* Studies by means of RSD are commonly considering catalogues of galaxy surveys, such as e.g. *DES*,*eBOSS* or data from the *Euclid* observations. If RSD data were available for a *DES*-like sky area, the nature of dark energy could be identified with precisions of $\Delta w_0 \approx 0.03$ and $\Delta w_a = 0.07$, when simultaneously also applying the angular clustering of galaxies (Gaztañaga et al. 2012). However, this analysis requires deep spectroscopic observations of the considered sky area, which have not been planned, yet.

Accordingly, especially the studies listed in Tab. 6.6 define the unique features of *eROSITA* for investigating the nature of dark energy. With $\mathrm{FoM}^{2\sigma} = 53$, the instrument fulfills the requirements of a Stage IV experiment and improves on the constraints from the current *DES* and *BOSS* surveys. The up-coming *Euclid* instrument will allow for even higher cosmological precisions. However, the launch of *Euclid* is

scheduled for $\sim$ 3 years after the launch of *eROSITA*, such that the latter represents the first Stage IV instrument for the study of dark energy.

6.8.3 Discussing Possible Information from the Temperatures

Following the results for the inclusion of the temperature information (Sect. 6.6.3), even for the optimistic scenario this additional data did not yield an impact on the final cosmological constraints. Accordingly, we investigated the required knowledge on the scaling relations for the optimistic (z,k$T_{\rm X}$)-catalogue of $\sim 8,000$ clusters in order to significantly improve the over-all cosmology results. We thus first considered a reduced basis of scaling parameters $\mathcal{Y}$ by $\gamma_{\rm TM}$ for the predictions and froze the redshift evolution of the $M - T_{\rm X}$ relation to $\gamma_{\rm TM} = -1.04$. This approach was motivated by the study of other scaling relations, which commonly assume self-similarity of $\gamma_{\rm TM} = -1$ for the redshift evolution in this relation (comp. e.g. Maughan 2007; Pratt et al. 2009; Vikhlinin et al. 2009a; Mantz et al. 2015; Giles et al. 2015). Additionally, we assumed a perfect knowledge on the $M - T_{\rm X}$ parameters to quantify the maximum constraining power of the optimistic cluster set with precise temperatures. During these simulations, we first considered the influence on the cosmology when applying the only the sub-sample of clusters with temperature measurements.
When approaching self-similarity in the redshift evolution of the $M - T_{\rm X}$ relation and freezing $\gamma_{\rm TM}$, the precision on these parameters improved only negligibly by a couple of percent (Tab. 6.4). Accordingly, though these cosmological parameters are in general strongly influenced by the priors on the scaling parameters, the redshift evolution yielded only a minor influence on their determinations. Furthermore, also a perfect knowledge on the scaling relation resulted in an increased parameter precision of only $\sim 10\%$.
Accordingly, even the latter, most optimistic scenario was not able to reproduce the constraints placed by the full *eROSITA* cluster catalogue with a deviation of a factor of ~ 3.4 (comp. Tab. 6.3). Thus, only an improvement in the knowledge on the scaling relations does not suffice for the temperature sample to impact the cosmological constraints significantly. As already expressed in Sect. 6.6.3, the cosmological study from the smaller sample of clusters with precise temperatures is strongly limited by its statistics as well as by the reduced covered redshift range, rather than by a less efficient mock catalogue based on the $M - T_{\rm X}$ relation.
Following another train of thoughts, we investigated the impact of only the $M - T_{\rm X}$ relation on the mock catalogue to test new concepts of how the temperature information improves the cosmological constraints. Just as the $M - L_{\rm X}$ relation, also this relation was applied during the conversion of the halo mass function into the galaxy cluster photon counts function. Up to now, however, the intrinsic scatter in the $M - T_{\rm X}$ relation, $\sigma_{\rm TM}$ was neglected for this derivation, due to the small impact of the temperature on the observed number of photons (comp. Sect. 6.3.1). Following this argumentation, the temperature scaling parameters remained frozen during our *MCMC* simulations (comp. also Pillepich et al. 2012). To now quantify the influence of this scaling relation on the cluster catalogue and the cosmology in general, we fixed the relation to be constant with mass and redshift with different well-defined temperature values of k$T_{\rm X}$ = 1 keV, 2keV and 5keV. Based on this simplified approach, the total number of expected *eROSITA* clusters showed deviations of around $\pm 17\%$. These findings supported the necessity of a correct calibration of the scaling relations since according to the considerations in Sect. 6.7.1, such a scatter in the total number of clusters may even result in deviation of on average $\sim 20\%$ in the parameter uncertainties. Though, applying only the sub-sample of clusters with precise temperature estimates was not able to yield tight constraints on the $M - T_{\rm X}$ scaling parameters, the idea was now to obtain information from the full cluster catalogue including the temperature information. According to the above considerations, a simultaneous fit of both scaling relations may yield tight constraints on the scal-

ing parameters, especially if temperatures are available for a cluster sub-sample. Within this extended, detailed simulation approach, the observed cluster temperatures may thus allow for an improvement in the cosmological constraints.

6.8.4 Defining the Temperature Selection Function

To derive the galaxy cluster temperature function for the *eROSITA* all-sky surveys, we defined a selection function $S(\bar{M}, z)$ (Appendix D.1) based on the mass and the redshift of the cluster and neglected any possible dependence on the applied cosmology or scaling relation. As both cosmology and scaling parameters were varied during our *MCMC* sampling, we investigated the influence of these variations on our selection function. To do so, we first needed to understand the dependences of the catalogue of clusters with precise temperatures on the different cluster properties.
The expected relative temperature uncertainties were estimated on a cluster mass-redshift grid. However, since these predictions were based on a spectral analysis, the results do not simply depend on the cluster mass, but rather on the corresponding temperature T_X and luminosity L_X, which defined the cluster spectrum. This correspondence was given by the scaling relations by Reichert et al. (2011) and their applied ΛCDM-cosmology of $\Omega_\mathrm{m} = 0.3$, $\Omega_\Lambda = 0.7$, and $h = 0.7$. As the cosmology enters in the $E(z)$-terms of the scaling relations, it altered this correspondence between the different cluster properties, such that the same mass related to a different temperature and thus a different temperature precision. For our redshift range of interest with mainly $z \lesssim 0.16$, the deviation in T_X and L_X was of the order of $\lesssim 1\%$ and therefore negligible, even for an unrealistic sampling of $\Delta\Omega_\mathrm{m} = \pm 0.2$. On the other hand, the cosmology also influenced the number of observed photons as $\eta \propto L_\mathrm{X}/D_\mathrm{L}^2$ with a quadratic dependence on the luminosity distance D_L. With a realistic variation in the cosmology within our *MCMC* sampling, especially in the Hubble parameter of e.g. $\Delta h \approx \pm 0.05$, we needed to expect a deviation in the measured number of photons of $\sim 10\%$. As observed in our previous work (Borm et al. 2014), however, the parameter space of clusters with precise temperatures seemed to be rather dependent on the cluster redshift and temperature itself than on η. Accordingly, we concluded that our defined selection function $S(\bar{M}, z)$ was constant under the variation of cosmological parameter values within our *MCMC* sampling.
To inspect the influence of varying scaling relations on the parameter space of clusters with precise temperatures, we considered the scatter in the scaling parameters during the *MCMC* simulations. For the pessimistic approach, these parameters scattered within a region of roughly twice the size of the prior and yielded a maximum deviation in the temperature of $\sim 15\%$. These altered correlations between cluster mass and temperature lead to a shift of the parameter space of precise temperature clusters of up to half a pixel in mass. However, this was only for the pessimistic approach and for the expected improved priors on the scaling relations by a factor of four, the deviations in the temperature became negligible around a couple of percent. Additionally, our definition of the selection function as a step function already allowed for a more robust handling of the dependences of the temperature estimates on the cluster mass and redshift. In conclusion, both variations in the cosmological as well as in the scaling parameter values only lead to negligible changes in our defined selection function, such that the *eROSITA* cluster temperature function was a reliable expression throughout our simulations.
In a final test, we compared the expected number of *eROSITA* clusters with precise temperatures from the galaxy cluster temperature function with the results from Borm et al. (2014). Within our previous work we computed this sample to include $\sim 1,700$ clusters, excluding *eHIFLUGCS*, where this result was based on the transfer function by Eisenstein & Hu (1998) and applied only a simply selection of $S(\bar{M}, z) \in \{0, 1\}$. Our new estimation of $\sim 1,860$ newly determined precise temperatures with *eROSITA* reproduced this result to a reliable level despite the different transfer function and the improved selection.

6.8.5 Including Poisson Noise in the Mock Data

In general, Poisson noise in the number of detected photon counts from the clusters (comp. Eq. 6.27) as well as in the number of detected clusters in the different observation bins was expected. For the previous *eROSITA* cosmology forecasts by Pillepich et al. (2012), the noise in the photon counts was included in the definition of the galaxy cluster photon counts function to allow for a detailed analysis. However, reducing this Poisson noise to a Dirac delta function as expressed in Sect. 6.3.1 altered the total number of detected clusters only negligibly by less than a couple of percent. In discussion with the authors of P16, this approach of the reduced noise level was thus applied to simultaneously improve the required simulation time for the *MCMC* analysis.
To quantify the impact of Poisson noise in the abundance of clusters in the individual (z, η)-bins, we generated a mock catalogue including this noise and quantified the cosmology forecasts for different cosmological models and simulation set-ups. Those simulations were based on fixed scaling relations to focus on the influence on the cosmological constraints, and were performed for both the scaling relations by Reichert et al. (2011) as well as by Vikhlinin et al. (2009a). The strongest effect of the Poisson scatter on the cluster counts was observed in the deviation of the best-fit values from the input values, which scattered within the 68%-credibility regions for the idealistic case of fixed scaling relations. The strength of this bias depended on the considered parameters as well as on the realisation of the Poisson noise. In the realistic simulation scenario with a simultaneous fit of the scaling relation, the credibility regions increase, however, such that this additional uncertainty is very unlikely to contribute to the final cosmological constraints. Additionally, the parameter uncertainties, on the other hand, were almost independent of the scatter in the cluster counts and agreed by more than 98% percent for different Poisson noise realisations and when compared to the scenario with no noise. Since our project emphasised on the precision of the parameter forecasts, also the Poisson noise in the cluster counts was neglected.

6.8.6 Influence of Baryons on the Halo Mass Function

Over the last years, several studies investigated the impact of cluster gas physics on the halo mass function and thus on the number of expected galaxy clusters and on the cosmological estimates (e.g. Stanek et al. 2009; Cui et al. 2012; Balaguera-Antolinez & Porciani 2013). Recent simulations by Bocquet et al. (2015) now estimated the systematic error on the computed cosmological parameters values when neglecting the influence of baryons on the halo mass function also for the *eROSITA* instrument. In this case, the shift in the best-fit value of the matter density Ω_m was computed as -0.01 when accounting for the baryons in a ΛCDM model. However, the credibilities on the cosmological parameters were reproduced also with the altered halo mass function, such that we could neglect the effect of baryons on this function for our forecasts. As the deviation in the best-fit estimate surpassed our expected uncertainty by $\sim 60\%$, the accounting of baryonic effects on the shape of the halo mass function will be essential for the future data analysis of the *eROSITA* instrument.

6.9 Summary & Conclusion

Within this project, we presented forecasts on the cosmological parameters for the upcoming *eROSITA* instrument, while investigating the different models ΛCDM, w_0CDM, w_aCDM, and ΛCDM+ν. These results were obtained based on the derivation of a galaxy cluster photon counts function to describe the abundance of galaxy clusters observed by *eROSITA*, as well as on the performance of *MCMC* simulations.
Applying the scaling relations by Reichert et al. (2011), we predicted *eROSITA* to observe a total of $\sim 98,700$ galaxy clusters, where precise temperature measurements where expected for a subsample of $\sim 2,050$ clusters. When accounting for a development in the knowledge on the scaling relations until the surveys are completed, the full cluster catalogue allowed for cosmological constraints for the 68%-credibilities of $< 1\%$ and of $\sim 1.5\%$ for σ_8 and Ω_m, respectively, in a ΛCDM- as well as in a w_0CDM-cosmology, with $\Delta w_0 = 2.4\%$ in the latter case. In the more complex wCDM-scenario, the cosmological parameters will be estimated to a high precision of $\Delta\sigma_8 = 0.013$ (1.6%), $\Delta\Omega_m = 0.01$ (3.4%), $\Delta n_s = 0.032$ (3.3%), $\Delta w_0 = 0.117$ (11%), and $\Delta w_a = 0.432$. These results are slightly more precise than the recent results from the *Planck* satellite, including external priors on BAOs, on the Hubble parameter and on supernovae type I data. When combining both data sets, the precision on the dark energy parameters could be improved to $\Delta w_0 = 0.077$ (7.7%) and $\Delta w_a = 0.276$. According to the latter results, we computed a figure of merit of $\mathrm{FoM}^{2\sigma} = 53$ for the dark energy characteristics, which classified *eROSITA* as first Stage IV instrument. Further results are summarised as follows.

- Significant degeneracies were observed between the parameters of the set $\{\sigma_8, \Omega_m, w_0, w_a\}$, similar to previous cluster cosmology experiments.
- A strong dependence of the parameter credibilities on the knowledge on the scaling relations was computed with an improvement by a factor of ~ 2 when moving from the pessimistic to the optimistic scenario, where the dark energy parameters displayed the least influence. However, when decreasing the priors on the scaling parameters even further, this cosmological improvement starts to flatten and especially the constraints on the dark energy parameters remain constant.
- The size of the full *eROSITA* catalogue contained additional information especially on the scaling relation parameters β_{LM} and γ_{LM} with improvements beyond the prior information by up to 65%. Accordingly, these data allowed for a more precise calibration of the $M - L_X$ relation.
- Even the smaller subsample of clusters with precise temperature estimates yielded constraints on the parameters $\{\sigma_8, \Omega_m, n_s\}$, though its constraining power was strongly limited by the size of the sample even for the optimistic scenario. Accordingly, these information improved the computed credibilities from the total cluster sample only negligibly.
- The *eROSITA* cluster catalogue alone did not allow for the study of neutrino characteristics. For this case a joint *MCMC* simulation of our data sample and the information from e.g. the *Planck* results are suggested.

In addition to forecasting the cosmological constraints placed by the *eROSITA* instrument, we investigated the influence of the different simulation steps and assumption on the results. Accordingly, several simulations were repeated based on the scaling relation by Vikhlinin et al. (2009a) to quantify the influence of the applied relation. The comparison of the results for the two scaling relations showed a strong dependence on the considered cosmological model. Whereas the constraints on the dark energy parameters remained comparable, deviations for $\Delta\sigma_8$ and for $\Delta\Omega_m$ by 20% were observed when assuming

the current knowledge of the scaling relations. However, deviations in the uncertainties may increase up to $\sim$ 30%, where on average the application of the relations by Reichert et al. (2011) resulted in tighter credibility values. Accordingly, precision cosmology is strongly dependent on the accuracy of the scaling relations. However, from the simulation results above, we expect *eROSITA* to not only allow for tight cosmological constraints, but also for an improved calibration of the scaling relations and thus for a more accurate accounting of the total number of clusters.
As another essential study, we quantified the reliability of a Fisher formalism approach when compared to the more detailed *MCMC* simulations. For the less complex cosmological models and especially when simplifying the set-up to a perfect knowledge on the scaling relations, both statistical approaches yielded very similar constraints for the parameters $\{\sigma_8, \Omega_\mathrm{m}, w_0, w_\mathrm{a}\}$ with deviations by $\lesssim 10\%$. When considering the parameter set $\{n_\mathrm{s}, h, \Omega_\mathrm{b}\}$, which is less decisively defined by galaxy clusters, the *MCMC* methodology introduced additional information, which improved the uncertainties on these parameters by up to $\sim 23\%$. On the other hand, when moving to more complex cosmological models with a realistic treatment of the knowledge on the scaling relations, we partially observed strong deviations from Gaussianity in the computed *MCMC* credibility regions. This discrepancy was especially significant for the dark energy parameters w_0 and w_a, such that the Fisher approach overestimated the precision on these parameters by $\sim 22\%$ and by $\sim 17\%$, respectively. Accordingly, the Fisher formalism proved as a reliable statistical tool for the simulations with frozen scaling relations. For the more realistic simulation set-ups as well as for the more complex cosmologies, however, the *MCMC* approach needs to be applied.

In conclusion, we summarise that *eROSITA* will be a very powerful instrument for cosmological studies, especially for the investigation of the nature of dark energy. The computed figure of merit with $\mathrm{FoM}^{2\sigma} = 53$, when including the information from the *Planck* mission, classified the instrument as first Stage IV mission for the determination of dark energy, according to the considerations of the *DETF*. In addition to the dark energy constraints, the large catalogue of *eROSITA* galaxy clusters will allow for unprecedented precision especially on the parameters σ_8 and Ω_m as well as for high parameter precisions.

6.10 Outlook

One further study that we consider is to further quantify the bias in the cosmological constraints, that may arise from applying inaccurate scaling relations in the data analysis, and to test the self-calibration potential of these relations by their simultaneous fit during the *MCMC* simulations. For the first investigation, the mock catalogue is computed applying e.g. the scaling relations by Vikhlinin et al. (2009a), while during the *MCMC* analysis we assume the functions by e.g. Reichert et al. (2011), including the corresponding priors. To consider the self-calibration, an idea is to implement the same scaling relations in the mock catalogue as well as in the analysis, but to change the normalisation of the relations by e.g. $\pm 10\%$ for the simulation of the catalogue. Following this approach, we can test whether the simultaneous fit of the scaling relations in the *MCMC* run allows for a compensation of the bias introduced by the off-set in the considered scaling relations.

As already expressed in Sect. 6.6.4, to explore the full cosmological significance of the *eROSITA* cluster catalogue, a joint *MCMC* analysis of this cluster sample with the *Planck* data was suggested. However, while investigating this project, several obstacles and different possible approaches had to be addressed. As a first scenario, we downloaded the *Planck* likelihoods and their parameter files, and implemented

them in *CosmoMC* as suggested by the readme,[16] of this software to allow for a joint simulation of the data sets. Following this approach, it was necessary to first quantify the deviation between our default *WMAP5* and the *Planck* cosmology. Assuming a ΛCDM-cosmology, we derived the following model within *CosmoMC* from the *Planck*+BAO+H_0+JLA data and the corresponding likelihoods with the results from the *WMAP5* data stated in the brackets for comparison

$$\begin{aligned} \sigma_8 &= 0.8296 \pm 0.0143 \quad (0.8170 \pm 0.026) \\ \Omega_\mathrm{m} &= 0.3152 \pm 0.0133 \quad (0.2800 \pm 0.0058) \\ n_\mathrm{s} &= 0.9655 \pm 0.0062 \quad (0.9600 \pm 0.013) \\ h &= 0.6730 \pm 0.0096 \quad (0.7010 \pm 0.013) \\ \Omega_\mathrm{b} &= 0.0491 \pm 0.0011 \quad (0.0460 \pm 0.0015) \quad . \end{aligned}$$

Accordingly, the individual credibility regions for the *Planck* data set and for our defined *eROSITA* mock catalogue were shifted from one another while still being consistent within the 68%-credibility level. This deviation suggested the following two approaches: to either apply the cluster mock catalogue based on the *WMAP5*-cosmology or to adapt the catalogue to the findings by *Planck*. For the first case, the joint simulations would thus suggestedly result in systematically increased credibility regions when compared to the uncertainties of the individual analysis of each data set. However, this approach represents a realistic scenario in the reduction of observed data. If we decided to recompute the mock catalogue based on the *Planck* cosmology, on the other hand, most important would be the increase in σ_8 by $\sim 2\%$ and in Ω_m by $\sim 11\%$, which also surpasses the typically found values by cluster studies (comp. e.g. Mantz et al. 2015). Therefore, applying this cosmology without adapting the scaling relations would lead to an overprediction of the number of clusters observed by *eROSITA*, where we computed this sample to include a total of $\sim 122,900$ clusters. This development to $\sim 20\%$ more clusters originated from the influence of these increased values of σ_8 and Ω_m on the power spectrum and was only insignificantly impacted by the changing $E(z)$-factor in the scaling relations. Accordingly, this larger sample of clusters would by default allow for tighter cosmological constraints due to improved statistics. Additionally, the distribution of the clusters would be altered as an increased matter density suggested a reduced number of clusters at higher redshifts (comp. e.g. Voit 2005, Sect. 2.8). To dissolve this bias, we decreased the considered sky fraction to $f_\mathrm{sky} = 0.528$ to yield the same number of clusters as for the *WMAP*5 cosmology, while neglecting the deviation in the distribution of the cluster abundances. For both concepts of not altering and of re-defining the mock catalogue, we launched joint *MCMC* forecasts for the *eROSITA* and the *Planck* data within *CosmoMC*. However, due to the evaluation of several likelihoods and data samples in these simulations, the chains were running very slowly and we estimated the necessary time for convergence to several months.

We thus considered an alternative scenario which was based on the so-called *importance sampling*. The main concept of this strategy was to define the chains of the *MCMC* analysis of the first data set as basis to compute the likelihoods of the second data set. In this sense, this second likelihood was evaluated at the chain steps of the first data catalogue. Depending on the computed likelihood values, weights were assigned to the individual steps of these second chains, such that eventually the credibility regions were defined analogously to the analysis of a full *MCMC* simulation.

As this latter approach required the development of an additional script as well as its testing to perform the importance sampling, this project is still on-going, where these results will be published in Borm et al. in prep. together with the general findings of the cosological *MCMC* forecasts for *eROSITA* presented

[16] Information on how the *Planck* likelihoods are integrated into *CosmoMC* as well as their download link could be found on the webpage: *http://cosmologist.info/cosmomc/readme.html*.

in the previous sections. However, based on our findings in Sect. 6.6.4, deviations of only $\sim 10-15\%$ from Gaussianity were observed for the computed *MCMC* results. Accordingly, we expected the uncertainties to slightly increase for the joint *MCMC* analysis, but to still reproduce precisions around $\Delta w_0 \approx 0.08$ and $\Delta w_\mathrm{a} \approx 0.28$. In summary, the results stated in Tab. 6.3 can thus be considered as very reliable and representative for the constraining power of the *eROSITA* instrument.

CHAPTER 7

Final Conclusions and Outlook

The main science driver of the future *eROSITA* X-ray instrument is the investigation of the dark energy equation of state, one of the most challenging questions of modern astrophysics. The characteristics of dark energy are e.g. accessible via the observations of galaxy clusters and their distributions. The projects of this thesis were structured to forecast the potential of the *eROSITA* instrument for the study of galaxy clusters as well as of their cosmological implications. Accordingly, we emphasised first on estimating the reliability of the cluster properties, which are expected to be observed by *eROSITA*. Based on this obtained knowledge on the future cluster catalogue, we then inferred the constraints, which the instrument will be able to place on the different cosmological parameters. Accordingly, the work presented in this thesis, states a detailed as well as realistic scheme for studying precision cosmology, while starting from the instrumental characteristics and the initially observed galaxy cluster raw data to applying complex cosmological models and statistical methods to obtain the credibilities of the cosmological parameters.
The following sections summarise the results achieved in these projects as well as the conclusions of their interpretations. The final sections allow for an outlook of currently on-going work, of suggestions for future studies as well as of how this work is essential for the analysis and interpretation of the future *eROSITA* data.

7.1 Summary of the Projects and the Results

In our first project, we estimated how well *eROSITA* will be able to observe different cluster properties, while focussing on the ICM temperature and on the redshift. This study was based on the simulation of cluster spectra and accounted for the instrumental response as well as for the planned survey exposure maps. The computed results indicated that *eROSITA* will allow for precise temperature measurements for clusters as distant as $z \lesssim 0.16$, when applying the average effective survey exposure time and assuming cluster redshifts to be accessible. For distances up to $z \approx 0.08$ precise temperatures will even be estimated for all cluster masses. Precise redshifts will be available up to distances of $z \lesssim 0.45$, where for the local clusters these precisions are comparable to optical photometric estimates. However, for clusters with the highest as well as with the lowest considered masses, the ICM temperature and the redshift were degenerate properties, which resulted in catastrophic failures during the spectral fit. These failures limited especially the deep exposure observations and will thus need to be considered in the subsequent pointed observation phase of the instrument. Additionally, for those clusters with precise measurements, no systematics in the accuracy of the parameter values or in the error computation needed to be corrected for when assuming an average exposure time. For the remaining clusters, correction functions for the parameter bias as well as for the bias on the uncertainties were defined. Convolving the above

results with the halo mass function, we estimated *eROSITA* to obtain precise temperatures for $\sim 1,700$ new clusters. This will increase the current cluster catalogue with precise temperature information by a factor of $5 - 10$ depending on the referred-to sample.
Whereas these computations assumed cluster spectra to be available directly, in a realistic observation and analysis procedure several pre-analysis steps need to be applied first to the raw data. These include e.g. coordinate transformations, event selections, the detection of the objects as well as their spectral extraction. These steps as well as the realistic data treatment itself might cause an additional bias, which impacts the final spectral fit results and thus the interpretation of the data. Following these considerations, we extended the first project to investigate these pre-analysis strategies, while applying the software packages *SIXTE* for the simulation of *eROSITA* event files and *SRCTOOL* for their analysis.
Based on these studies, we allowed for the improvement of several aspects in both tools. For the relative parameter uncertainties, small increases were retrieved as expected, due to the additional analysis steps. Thus, the determination of precise temperatures was now limited to redshifts of up to $z \lesssim 0.09$, where up to distances of $z \approx 0.06$ clusters of all considered masses were included in the parameter space of precise properties. Despite small reductions, all clusters, which showed precise property estimates in the previous simulations, were thus on average still included in the parameter space of clusters with precise temperatures. Despite these agreements, the model temperature value was overestimated by on average $\approx 10\%$ for those cluster, which suggested a systematic error in the simulation and/or in the analysis set-up of the two applied tools. Though this bias could not be solved yet, these results supported the improvement of both software packages and the present advancements of these tools promise a reduction of these systematics (Sect. 7.2).

Considering this knowledge on the expected observations of galaxy clusters with the *eROSITA* instrument, we forecasted the constraints these clusters will place on the cosmological parameters. For these simulations, we derived the halo photon counts function based on galaxy cluster scaling relations, where this cluster abundance function was defined by the number of detected photon counts as direct cluster observable. This function then defined a mockcatalogue for the expected cluster observations and the statistical analysis of this catalogue was performed by a *MCMC* approach.
For the scaling relations by Reichert et al. (2011), this abundance function yielded a total of $\sim 98,700$ observed galaxy clusters. Only probing the cluster abundances and assuming a progress in the knowledge on the scaling relations until the *eROSITA* surveys are completed, this large catalogue alone allowed for cosmological constraints of $< 1\%$ and of $\sim 1.5\%$ on σ_8 and on Ω_m, respectively, in a ΛCDM- and a w_0CDM-cosmology. In the latter scenario, the normalisation of the dark energy equation of state was predicted with a precision of $\Delta w_0 = 2.4\%$. For the more complex wCDM-cosmology our computed *eROSITA* constraints alone were comparable to the *Planck* results with external priors. Accordingly, we computed credibilities of $\Delta\sigma_8 = 0.013(1.6\%)$, $\Delta\Omega_\mathrm{m} = 0.01(3.4\%)$, $\Delta n_\mathrm{s} = 0.032(3.3\%)$, $\Delta w_0 = 0.117(12\%)$, and $\Delta w_\mathrm{a} = 0.432$ from the *eROSITA* cluster abundances alone. When combining both data sets, the dark energy equation of state was constrained to $\Delta w_0 = 0.077(8\%)$ and $\Delta w_\mathrm{a} = 0.276$. At the same time, a figure of merit of $\mathrm{FoM}^{2\sigma}_{w_0,w_\mathrm{a}} = 53$ was retrieved, which classified the instrument as first Stage IV probe for the study of dark energy. Especially the investigation of these two parameters supported the application of *MCMC* simulations as a reliable analysis strategy since their credibility regions showed deviations from a Gaussian distribution.
In addition, we were able to quantify the dependence of the credibilities on the knowledge on the applied scaling relations, where the dark energy constraints showed the least influence and are not expected to improve for a further increased precision in the scaling parameters. However, the *eROSITA* cluster sample will at the same time tighten the constraints on the $M - L_\mathrm{X}$ relation, especially on the parameters β_LM and γ_LM. The inclusion of the cluster temperature information, on the other hand, did not directly

improve the above stated results, due to the limited size of the cluster sample with precise ICM temperatures. However, for a more complex and extended forecast scenario, these temperature information will be beneficial. Instead, impacts on the cosmological constraints were caused e.g. by the applied scaling relations, which strongly defined the total number of observed clusters. Deviations of on average $\sim 20\%$ in the parameter credibilities needed to be considered.

Finally, the main conclusions of the above explained projects are summarised as follows.

- *eROSITA* will be able to observe precise and accurate temperatures for clusters up to distances of $z \lesssim 0.16$, which relates to $\sim 1,700$ new clusters with precise temperatures.
- Accounting for the additional analysis of the raw data yielded only a small decrease in the expected temperature precisions. However, the arising strong bias in the accuracy of this property asked for a further investigation of the individual data reduction steps and for an improvement of the applied tools.
- Considering the large *eROSITA* cluster catalogue only, allowed for forecasted precisions on the cosmological parameters, which were comparable to the information obtained from the *Planck* data with external priors. The combination of both data sets retrieved a figure of merit of $\mathrm{FoM}^{2\sigma}_{w_0,w_\mathrm{a}} = 53$, which classified *eROSITA* as the first Stage IV instrument for the study of dark energy.

Accordingly, the *eROSITA* instrument presented itself as powerful tool to study galaxy cluster characteristics, on the one hand, with an increase in the sample of clusters with precise temperatures by a factor of $5 - 10$. In total, the all-sky survey of this instrument will extend the number of known X-ray clusters by a factor of the order of ~ 50. On the other hand, *eROSITA* will allow for cosmological studies with unprecedented precision, especially on the parameters σ_8, Ω_m, w_0 and w_a.

7.2 Significance of this Work

This work does not only present forecasts for the observational potential of the *eROSITA* instrument, but it also allows for a robust and reliable preparation of the analysis strategy of the future data. For example, the inspection of the pre-analysis software already initiated improvements of the two packages *SIXTE* and *SRCTOOL*, and helped to identify and to quantify systematics in the applied software procedures and in the realistic treatment of the raw data. Additionally, the arising discussions on this topic in the collaboration supported structuring reliable and detailed concepts for the future data reduction.
Similarly, the simulation of the expected precisions on the cluster properties yielded suggestions for a robust analysis of the spectra. However most importantly, we were able to quantify the systematics in the estimated best-fit parameter values as well as in the computed parameter uncertainties. The accordingly defined bias correction functions will thus allow for the consideration of these biases in the future data reduction to support an accurate interpretation of the results.
Though the most interesting conclusion from the cosmological forecast was the approved classification of *eROSITA* as a Stage IV instrument, we also established a new cluster abundance function and recorded diverse advices as well as lessons-learned for the future data reduction. For example, the importance of an accurate and reliable calibration of the applied scaling relations was emphasised. Also, the developed scripts for these simulations can build the basis for the software of the future cosmological data evaluations.
In summary, the projects presented in this thesis support the development of a reliable, accurate and robust strategy for the analysis of the future *eROSITA* data.

7.3 On-Going Work and Outlook

At this point, we summarised the different outlooks, which we already presented in the previous chapters. Currently, there are continuous investigations on two of these projects - on the study of the systematics in the pre-analysis tools and in the treatment of the raw data, as well as on the cosmological forecasts.
The current identifications of possible systematics in the pre-analysis software, already presented a continuation to the project of cluster temperature predictions. An advancement of the applied tools now allows for additional and more flexible applications and specifications in the data reduction. This update thus suggests a re-simulation of the expected ICM temperature precisions and accuracies, while promising a more realistic treatment of the observed raw data. One aim is to identify the origin of the strong bias in the temperature estimates and solve it, but at the same time, these tests allow for an improvement of the entire analysis methodology and for an adaptation of the individual tools to one another. Accordingly, during the current development of *eSASS*, frequent tests of its packages are required. For the final *eSASS* release, it will be essential to identify and to quantify its systematics, to understand their origin and to provide the corresponding correction functions. Only if these aspects are covered, an accurate reduction and interpretation of the *eROSITA* data is supported.
For the cosmological forecasts, on the other hand, we currently investigate the joint credibility constraints from the *eROSITA* and the *Planck* data. Whereas the results stated above were based on approximating the individual *MCMC* uncertainty regions as Gaussians, we now follow a joint *MCMC* analysis for the eRASS:8+*Planck* data sample. Accounting for the different arising problematics, three distinct simulation approaches are followed. Though, the reported cosmological constraints were already robust estimates, they presented deviations from Gaussianity, especially for the dark energy parameters. Accordingly, these newly combined *MCMC* results will then allow for more accurate and reliable credibility regions, which is of interest especially for w_0 and w_a. However, since only minor deviations from a normal distribution were observed, the newly computed figure of merit will still classify *eROSITA* as a Stage IV instrument for the study of dark energy.
In addition to approving the reliability of the cosmological conclusions, the combination of the cluster information with the *Planck* data will also allow for the test of more complex cosmological models, including e.g. neutrino characteristics. Apart from considering the constraints from *Planck*, possible extensions to this study include e.g. the additional application of information from spatial clustering, or the quantification of the credibilities of primordial non-Gaussianity and even of modified gravity. Furthermore, we defined the idea of introducing the uncertainties on the $M - T_X$ relation in the simulations, in which case the available temperature estimates will be beneficial. In a further step, it is also interesting to quantify the impact of available information on cluster masses, e.g. from weak lensing observations, on the cosmological constraints.

According to the ideas and concepts expressed above, the scientific preparation of the *eROSITA* instrument in the fields of galaxy cluster science and cosmology still shows room for a variety of investigations. Especially of interest is the ambition to improve these applied forecasting strategies and to convert them into tools for the future data analysis. These improvements may e.g. include the reduction in the systematics of the pre-analysis steps as well as a scheme for parallelising the *MCMC* simulations. Though, the final calibration of the analysis procedures requires observed data, already at the moment it is essential to provide a reliable and effective strategy for the analysis as well as for the interpretation of the data. Following this scheme, we significantly support the exploration of the nature of dark energy.

APPENDIX A

Details for Applying the Software Tools *SIXTE* and *SRCTOOL*

This chapter explains in detail how event files are first simulated with the software *SIXTE* (Schmid, C. 2008; Schmid 2012) and subsequently analysed by the package *eSASS*, especially by the tool *SRCTOOL*. For both applications the software versions as of May 2014 are considered.

A.1 Considering the Instrumental Resolution for the Events Simulation

To account for the correct spatial resolution of the *eROSITA* instrument during the simulation of event files, a few considerations are necessary beforehand. The future observational data will be stored in event files of the size 1.02×1.02 deg^2 for pointed observations and of a FoV of 3.6×3.6 deg^2 for the survey mode. Since the geometry of the *eROSITA* telescopes together with the installed CCDs yields a spatial resolution of 9.6 arcsec, or equivalently 0.002667°, per CCD-pixel, a survey event file will thus be cover by an area of 1345×1345 pixels.

A.2 Simulating Event Files with *SIXTE*

For the event simulator *SIXTE*, we describe the procedures for simulating the events of a point source as well as of an extended source and elaborate both cases for a pointed as well as for a survey mode observation. However, for all approaches the first step is to define the *SIMPUT*-file (*SIMulation inPUT*), which includes the catalogue of sources to be simulated and their characteristics. This file follows the commonly applied *FITS*-format and contains columns for the source coordinates, for its flux, for its mission independent spectrum, and for its surface brightness distribution (Schmid et al. 2013).

Step 1: How to create the *SIMPUT*-files
The simulation of a *SIMPUT*-file for a well defined source is managed by the executable `simputfile`.

```
simputfile RA DEC XSPECFile="model.xcm" Emin Emax Simput="outputfile.simput"
```

The parameters (`RA,Dec`) and (`Emin,Emax`) describe the source position and the energy range, in which the source flux is computed, respectively. The file "model.xcm" contains the spectral model of the source in the syntax read by *xspec*. For example, for a galaxy cluster this is the command `phabs*apec`,

followed by the values of the model parameters. The simulated *SIMPUT*-file presents the source characteristics in the second *FITS*-extension with the flux being computed from the provided spectral model in the given energy range. The spectrum is attached in the third extension of the file, while the first extension remains empty. However, the executable `simputfile` does not generate a surface brightness profile, which needs to be provided either by an image from observations or by an independent simulation step. If no link to an image is defined in the second extension, the object is assumed to be point-like.

Step 2: How to simulate source images
For the simulation of brightness profiles as *FITS*-images, we apply the software *dis45x*, which is commonly implemented in the analysis of *Suzaku* data of galaxy clusters. Two files need to be defined for running this programme: a ".mod"file, which contains the header keywords for the created image, and a ".com"-file, which defines the spatial resolution of the image and the shape of the simulated surface brightness. In both files, we fix the spatial resolution to the characteristics of the *eROSITA*-telescopes (comp. Sect. A.1) and define the parameters

```
CRPIX1 =       672.5
```

and equivalently `CRPIX2` in the ".mod"-file. These parameters present the half-extent of the image in pixels, where the value stated above covers the FoV for an *eROSITA* survey observation. We applied the survey FoV for convenience and to ensure that due to the large covered area no essential information on the surface brightness profile is cut. However, the size of the simulated source image can be chosen arbitrarily and does not define the size of the final event file.
In the ".com"-file, several parameters need to be specified, where for this example we simulate the surface brightness of a galaxy cluster as a β-profile:

`OUTFILE`	name of the output file, where the name of the ".mod"-file needs to have the same prefix
`PIXEL2DEG`	coverage of one detector pixel given in degrees
`NX`	pixel size of the simulated image; equivalent to "NY"
`CX`	x-coordinate of the centre of the image in pixels; equivalent to "CY"
`RC.ARCMIN`	core radius of the source in arcmin
`RC.PIXEL`	core radius of the source in pixels
`BETA`	value of the β-parameter
`NORM`	normalisation of the β-profile.

Again, we apply the resolution of the *eROSITA* telescopes as well as the survey FoV for the image size (comp. Sect. A.1). The normalisation of the profile can be set to an arbitrary value as in the simulation of the event file it is later-on defined by the source flux. Modeling the profile is then run by the command

```
./dis45x
DIS45X> @make-prefix.com
```

Step 3: How to attach the image to the *SIMPUT*-file
To link a created or an observed image to the source information stored in the *SIMPUT*-file, the *HEASARC FTOOLS*[17] are applied for the manipulation of *FITS*-files. The name of the image file simply needs to be stored in the "IMAGE"-column of the *SIMPUT*-file.

```
fpartab "image.fits[IMAGE,0]" source.simput[1] 'IMAGE' 1
```

The same image can be linked to several sources. For sources with a different core radius but the same β-profile, the image can be rescaled by the "IMGSCAL"-column in the *SIMPUT*-file. This keyword is defined as

`IMGSCAL`= angular extend of the image / angular extend of the source

Step 4: How to create source catalogues
The *SIMPUT*-file, created by the `simputfile`-command, contains per default only one source. To simulate several objects within the same event file, it is convenient to define a source catalogue in one single *SIMPUT*-file. Accordingly, we stack files of single sources by applying the *FTOOLS*. Since multiple extensions of *FITS*-files cannot be stacked simultaneously, we first stack the different extensions into separate files with the command `fmerge` and in a second step append the stacked extensions into one *SIMPUT*-file by means of the command `fappend`.

Step 5: How to simulate event files
Having defined the catalogue of our objects of interest, we proceed in simulating the event file, which is especially depending on the instrumental characteristics. In addition to this information also the centre of the simulated event file (`RA,Dec`) and the exposure time in seconds need to be provided for this step. Depending on the observation mode, different simulation approaches are followed. For modelling a pointed observation, one runs

```
erosim Mode=none Simput=outputfile.simput Background=yes RA Dec Exposure
MJDREF=51544
```

where the command `erosim` calls all required characteristics of the *eROSITA*-instrument. However, also the simulation of event files of other X-ray instruments is implemented within *SIXTE* and is initialised by just applying a different command at this point. The parameter "`MJDREF`" defines the reference coordinate system and needs to be set to the above stated value, whereas the keyword "`Background`" expresses whether an instrumental specific particle background is convolved with the source events. To also add a X-ray background to the events, this emission needs to be defined as a source with a flat surface brightness profile either in the *SIMPUT*-catalogue or in a second *SIMPUT*-file. In the latter case, the key "`SIMPUT2=bkg.simput`" needs to be extended to the simulation command. Eventually, the procedure above yields seven event files as "events_*i*.fits" with $i \in [1, 7]$, one for each of the *eROSITA* telescopes. These files list the detected photons from the simulated sky region, including amongst others the information on the photon energy, on the coordinates of its origin, as well as on its time stamp. To ensure that the total number of observed photons as well as their distributions are randomly assigned with a statistical scatter between the event files for the different telescopes as well as between subse-

[17] A catalogue as well as a description of the different *FTOOLS* can be found at *https://heasarc.gsfc.nasa.gov/lheasoft/ftools/futils.html*.

quent simulation runs, the additional parameter `seed=1` can be added to the command line above. For pointed *eROSITA* observations, the simulated FoV always covers an area of 1.02×1.02 deg^2.
For the simulation of an observation in survey mode, the exposure time of the considered FoV needs to be computed from a so-called attitude-file, which defines the pointing directions of the telescopes at the different times during the all-sky survey. Running the command `ero_vis` on the attitude-file, the time intervals of interest are extracted and stored in a ".gti"-file.

```
ero_vis Attitude=attitude.fits Simput=outputfile.simput GTIFile=sim.gti RA Dec
TSTART=0.0 Exposure=1.26e8 dt=1.0 visibility_range=3.6
```

The coordinates (`RA,Dec`) define the centre of the considered FoV and the keyword "`visibility_rage`" describes the size of the FoV in degrees. The exposure time is set to the total of four years to account for all observations of the region of interest. Applying the obtained ".gti"-file, the simulation of an *eROSITA* survey event file is run as

```
erosim Mode=survey Simput=outputfile.simput Background=yes RA Dec
Exposure=1.26e8 Attitude=attitude.fits GTIFile=sim.gti MJDREF=51544
```

Different than for the pointed mode, the survey observations are not limited to a well-defined FoV, but in principle cover the entire sky.
For both survey strategies, the resulting events are best inspected with the programme *fv*, while investigating the additionally created "pattern_*i*.fits" files. Defining a histogramme over (`RA,Dec`) yields an image of the spatial distribution of photon detections and visualises the simulated sources. However, the coordinates stated in the event and pattern files are defined in detector pixels only, such that for the analysis of these files a transformation into sky coordinates is required.

Step 6: How to convert the event files into sky coordinates
The conversion is managed by another *SIXTE*-command, `ero_calevents`, which is applied onto the pattern-file, while stating the centre coordinates of the observation and a projection type. For the latter, we consider the projection "`SIN`" for consistency with the later-on used analysis software *eSASS*. Before the coordinate transformation, an additional key, which describes the possible rotation of the CCD, needs to be included in the header of the pattern-files.

```
fparkey fitsfile=pattern.fits[1] keyword='CCDROTA' value='0.'  add=yes

ero_calevents PatternList=pattern.fits eroEventList=events_SIN.fits CCDNr=1
RefRA RefDec RA Dec Projection=SIN
```

The coordinates (`RA,Dec`) represent the centre of the observed FoV in the converted sky coordinates, whereas the pair (`RefRA,RefDec`) states the initial centre of the simulated region. Both coordinate pairs should naively be equal. During the above transformation, a second set of coordinates (`X,Y`) is added, which describes the spatial distribution of the photons in pixels with (0,0) defining the centre of the FoV. Each of the pixels shows a resolution of $1.38 \cdot 10^{-5}$ deg, such that for a survey observation the FoV is covered by a total of $260,870 \times 260,870$ pixels.
After this coordinate conversion, we proceed to the analysis of the event files.

A.3 Analysing Event Files with *eSASS*

Applying the simulation steps above for the *eROSITA* instrument yields a total of seven event files. Merging these into one single file simplifies the following analysis steps and represent a joint observation of all seven telescopes. The procedure for merging the files is equivalent to the considerations explained in step 4. Before spectra are extracted from the sources in the event file by means of the tool *SRCTOOL*, we select the photon events of interest.

Step 7: How to select the events of interest
The first selection step is based on the location of the observed photons. Since for an event file in pointed mode the FoV is already limited to an area of 1.02×1.02 deg^2, no further spatial selection is necessary. For a survey simulation, however, the FoV needs to be cut to a 3.6×3.6 deg^2 sky frame. This selection is managed by the coordinates (`X,Y`) as these are showing a finer binning than the sky coordinates (`RA,Dec`), with $1.38 \cdot 10^{-5}$ deg compared to $2.7 \cdot 10^{-3}$ deg, respectively. We again apply the *FTOOLS* for this procedure.

```
fselect events_SIN.fits events_selected.fits "X >= -130435 && X <= 130435"
```

Repeating the above step also for the `Y`-coordinate yields the asked for survey FoV. Additionally, for both observation modes, we select the pattern type of the photon events, which is also stored in the event file, to `PAT_TYP < 12`. This filtering rejects all patterns, which are likely to result only from a statistical clustering of photons. Further selections might e.g. include the energy range of the photon events.

Step 8: How to extract the source spectra
For the extraction of the source spectra, the *SRCTOOL*, which was developed by T. Dwelly and is implemented within the *eSASS* software kit, is applied. Three further manipulations of the event files are required first, though. The name of the "GTI"-extension needs to be changed according to

```
fparkey fitsfile=events_selected.fits[2] keyword='EXTNAME' value='STDGTI'
```

Also, the value of the two keys "DATE-OBS" and "DATE-END" in the file header are altered to the value given for the "DATE" key applying `fparkey`.
For the spectral extraction, the source coordinates, the source region as well as the background region need to be provided. These are either defined manually, as in our approach with e.g. R_{500} for the source extent, or obtained by means of a source detection algorithm. The *SRCTOOL* is then run with the following parameters.

`evtfiles`	input file
`outstem`	output file
`todo`	"SPEC"
`srccoord`	file containing the coordinates of the sources
`insts`	1
`refarfs`	erosita_iv_1telonaxis_ff_convert.arf
`ebounds`	erosita_iv_1telonaxis_ff_convert.rmf
`vigndesc`	sim1_tvignet_100302v01.fits
`extpars`	”

`psfdesc`	erosita.psf.fits
`xgrid`	1.0
`tstep`	1.0
`srcreg`	file defining the source region
`backreg`	file defining the background region
`badpix`	BADPIX.txt

A more detailed explanation of the different parameters is presented in the *eROSITA*-wiki[18].
Following the set of the above stated steps, we finally generate one spectral file for each source region and one for each additional background-only region as they are observed for the total of seven *eROSITA* telescopes. To continue with the spectral analysis in *xspec*, the value of the exposure time and the name of the instrumental response file need to be added manually to the header of the spectral file. In our case, no tool was available yet to compute the exact exposure time of the simulated sky region, and we define the position of the region such, that it is observed with the effective exposure time of $t_{\rm exp} = 1.6$ ks based on the exposure maps by J. Robrade (comp. Fig. 2.12). For the instrumental response, we apply the survey resolution, averaged over all seven telescopes, "erosita_iv_7telfov_ff.rsp". The final analysis steps to re-obtain the source characteristics are analogous to the approach described in Sects. 4.2.3 & 4.2.4.

[18] https://wiki.mpe.mpg.de/eRosita/TaskDescriptions?action=AttachFile&do=view&target=srctool_doc.html

APPENDIX B

Brief Manual for Running *COSMOMC*

The following sections briefly summarise, how the *COSMOMC* software package is structured in general as well as how additional likelihood modules and data are added. The described features are valid and have been tested for the software versions of 02/2015 and 06/2015, and applying the *Intel Fortran Compiler*, *ifort15*. We would like to note to the reader, that only those applications required for our simulations are discussed. More general information on the software and its installation are expressed in the *COSMOMC* readme[19] by A. Lewis.

B.1 General Outline of *COSMOMC*

COSMOMC contains the likelihoods as well as the data samples for a variety of different cosmological probes, including e.g. supernovae type Ia, BAO, and also the CMB. These different information are organised in the folders "./source/" together with the modules, which perform the *MCMC* simulation, and "./data/", respectively. Running the *MCMC* simulations is managed by ".ini"-files, which contain all the required information on the characteristics of the simulations, such as e.g. the number of variable parameters, the convergence criterium, which sampling method to use and which likelihoods to compute. Per default, there exists one main, driver ".ini"-file, called "params.ini", in the *COSMOMC* home directory and many sub-files, which are launched by this driver and are located generally in the "/batch1/"-directory. The main file e.g. includes the information on the names and the output directory of the created files and defines the action to be executed. For performing a *MCMC* simulation based on the Metropolis-Hastings algorithm, one needs to set

```
root_dir=
file_root=
action=0
sampling_method=1
```

while the first two parameters define the output directory as well as the name of the resulting chains, respectively. This driver also calls additional ".ini"-files, such as e.g. "./batch1/likelihood_batch1.ini", which defines the likelihoods to be applied during the simulation, or "./batch1/params_CMB_defaults.ini". The latter file describes which parameters to vary during the fit, their priors as well as the values of the frozen parameters. By default, the variables are defined e.g. as

[19] The *COSMOMC* readme is available at *http://cosmologist.info/cosmomc/readme.html*

```
param[name]= centre, min, max, starting width, proposed width
```

with an applied flat prior between the minimum and maximum boundary of the parameter value and an estimate for the width of its proposal density. However, the option exists to update the latter property during the simulation based on the distribution of the chain steps.
In addition to these definitions, an additional parameter file ".paramnames" needs to be available for each simulation. It lists all parameters, which are stated in the ".ini"-file, with their names and their LaTeX notations, as e.g.

```
omegabh2      \Omega_b h^2      #physical baryon density.
```

These parameter files are stored in the "./paramnames/"-directory and are referenced by the likelihood codes (Sect. B.2). For those likelihoods already contained within *COSMOMC*, these files have been defined and do not need to be edited.
Having adapted the performance of the simulations to your requests, you can launch one single chain with the command

```
./cosmomc params.ini
```

To run several chains at the same time, an additional tool is required to manage the communication between the individual chains, for example to update the proposal width or to test for convergence. This parallelisation is commonly achieved by applying the software *MPI* (*Message Passing Interface*)[20], where both this software and *COSMOMC* need to be built by the same compiler. After this set-up, the *MCMC* simulations can be launched as

```
mpirun -np #chains ./cosmomc params.ini
```

with `#chains` representing the number of chains. Each chain is then run on a separate core.

B.2 Writing Your Own Likelihood Module

The descriptions in the previous section focused on applying likelihoods, which are already available within *COSMOMC*. To run your own likelihood function on an already defined data set or on your own data, you need to develop a module, which computes the negative logarithmic likelihood, $-\log[P(x|\Theta)]$, and which shows a certain set-up, such that it can be integrated into the *COSMOMC* infrastructure. Calculating the likelihood is left to the reader as it depends strongly on the considered model and data set. However, to implement this likelihood into the software, the module needs to mirror the following structure. As we constructed this module to compute the cosmological constraints based on the number of observed galaxy clusters, we call the example "clustercounts" and the corresponding file "clustercounts.f90", while writing the entire code in *Fortran*.

[20] This tool is e.g. freely available at *http://www.open-mpi.org/software/ompi/v1.10/*.

```
module clustercounts

!Defining the required COSMOMC modules
use settings
use CosmologyTypes
use CosmoTheory
use likelihood
use MatrixUtils
use Calculator_Cosmology
use Likelihood_Cosmology
use iniObjects
implicit none
private


type, extends(TCosmoCalcLikelihood) ::  ClusterCountsLikelihood
     !define all constants, e.g.
     real(mcp) ::  Msun,Mpc,AU
     ...
     contains
          procedure ::  Loglikelihood
          procedure ::  Loglike => ClusterCounts_LnLike
end type ClusterCountsLikelihood

public ClusterCountsLikelihood, ClusterCountsLikelihood_Add

contains


subroutine ClusterCountsLikelihood_Add(Likelist, Ini)
     class(TLikelihoodList) ::  Likelist
     class(TSettingIni), intent(in) ::  Ini
     class(ClusterCountsLikelihood), pointer ::  this

     if (.not.  Ini%Read_Logical('use_clustercounts',.false.))  return
     allocate(this)

     !define all constants and load data, e.g.
     this%Mpc=3.085678d22
     ...

     call this%loadParamNames(trim(DataDir)//'../paramnames/
     params_clusters.paramnames')
     call LikeList%Add(this)
end subroutine ClusterCountsLikelihood_Add
```

```
function ClusterCounts_LnLike(this,CMB,Theory,DataParams) results (Loglike)
     class(ClusterCountsLikelihood) ::  this
     class(CMBParams) ::  CMB
     class(TCosmoTheoryPredictions), target ::  Theory

     real(mpc) ::  DataParams(:)
     real(mpc) ::  LogLike

     LogLike = this%LogLikelihood(CMB,Theory)
end function ClusterCounts_LnLike


function LogLikelihood(this,CMB,Theory)
     implicit none
     class(ClusterCountsLikelihood) ::  this
     class(CMBParams) ::  CMB
     class(TCosmoTheoryPredictions), target ::  Theory

     !Here goes your likelihood code in Fortran

     LogLikelihood = ...

end function LogLikelihood

end module clustercounts
```

B.3 Implementing Your Own Module into *COSMOMC*

Having developed your own likelihood code following the above structure, the default *COSMOMC* modules need to be manipulated at several spots to integrate the new likelihood function. In a first step, the new code and the additional data sets need to be copied to the directories "./source/" and "./data/", respectively. In addition to the likelihood module, two more files need to be created, "./batch1/params_clustercounts.ini" and "./paramnames/params_clusters.paramnames". These contain the boundaries of the additional variables, required in the new likelihood, as well as their definitions in analogy to the CMB parameter example presented above.
To attach the new likelihood to the procedures within *COSMOMC*, we edit the file "./source/DataLikelihoods.f90" by the following lines.

```
use clustercounts

call ClusterCountsLikelihood_Add(DataLikelihoods,Ini)
```

This file lists all available likelihood functions within the package and checks the input from the ".ini"-files, which likelihood functions to consider. Additionally, the new function needs to be defined within the Makefile with several comments.

```
#can go anywhere at the top
CLUSTERCOUNTS ?=
ifneq ($(CLUSTERCOUNTS),)
CLUSTERCOUNTSO = clustercounts.o
CLUSTERCOUNTSF = clustercounts.f90
endif

#add to the end of the DATAMODULES
$(OUTPUT_DIR)/clustercounts.o

#somewhere after OBJFILES
ifneq ($(CLUSTERCOUNTS),)
LINKFLAGS += -lgsl -lgslcblas
LINKFLAGS += -L$(CLUSTERCOUNTS)
endif
```

Within a last step, the keywords for the new likelihood function need to be included into one of the ".ini"-files, e.g. into "params.ini". This way, we can treat the new likelihood as an equivalent to the others and specify whether to apply this new function. To do so, we add the lines.

```
use_clustercounts = T
INCLUDE(batch1/clustercounts.ini)
```

Recompiling the entire software package then allows for applyiing the tools within *COSMOMC* on your own likelihood function and data.

B.4 Some Further Notes

Even after implementing your own likelihood function into *COSMOMC*, adding details to your code or to the performance of the *MCMC* simulations may become tedious and involve detailed knowledge of the over-all infrastructure of the software package. The following paragraphs summarise our personal requirements and how to implement them.

Gaussian Priors: By default the variables of the *MCMC* simulation are confined by flat priors, which are defined within the ".ini"-files as expressed in Sect. B.1. For Gaussian priors, the additional information

```
prior[name]= center, width
```

is required. Gaussian priors on these variables are allowed by default within *COSMOMC*. However, more complex information, such as e.g. multivariate Gaussians, are currently not supported. First ideas on how to develop add-ons for these kind of priors were expressed by A. Mantz (*https://sites.google.com/site/adambmantz/work/cosmomc_priors*).

Prior on H_0: As H_0 is only insufficiently constrained by the abundance of galaxy clusters, we defined a Gaussian prior on this parameter (Sect. 6.4.3). Since H_0 or h were no initial variables and were computed based on the variable θ, the size of the sound horizon at the recombination epoch, the approach above could not be applied. Instead, the prior knowledge on the Hubble constant was included as an additional likelihood function. This function was already available in the package, such that the corresponding"HST.ini-file" had to be attached to one of the ".ini"-files applied to manage our simulations.

```
use_HST = T
INCLUDE(./batch1/HST.ini)
```

Additionally, the considered file "HST.ini" had to be edited according to the mean value for H_0 and the requested uncertainty. For the prior by Riess et al. (2011), this resulted in the definitions

```
Hubble_zeff = 0.0001
Hubble_angconversion = 30.0028
Hubble_H0 = 70.1
Hubble_H0_err = 2.2
```

where the first to keywords defined the redshift at which the mean value of the Hubble constant is measured, and the angular conversion, which is equivalent to

$$H_0 = \frac{\text{angconversion}}{D_\text{A}(z_\text{eff})} \quad . \tag{B.1}$$

The last two keys stated the measured value of the Hubble constant and its 1σ-uncertainty. Similar editions for z_eff and the angular conversion also needed to be included within the file "./source/HST.f90". Following these steps, the applied constraints on H_0 resemble a Gaussian prior knowledge on this parameter.

Implementing *CAMB*: One significant aspect in our simulations was the application of *CAMB* for the computation of the linear matter power spectrum. The tool itself was already implemented within *COSMOMC*, but we had to call the module within our likelihood function. Accordingly, the following commands had to be added to our own likelihood module to compute the power spectrum at the redshift $z = 0$.

```
!Within the subroutine add the following commands, with "numdatasets" stating the
total number of data sets to be loaded for the likelihood computation
do j = 1, numdatasets, 1
     this%LikelihoodType = 'ClusterCounts'
     this%needs_powerspectra = .true.
     this%needs_exact_z = .false.
     this%num_z = 1
     this%max_z = 0.d0
     this%needs_nonlinear_pk = .false.
     this%kmax = 50.d0
     this%num_mpk_kbands_use = 1000
```

```
     if (j.eq.1) then
          ...  !Load data files, one for each j
     end if
end do



!Add to both functions right after defining the applied classes
type(TCosmoTheoryPK), pointer ::  PK



!In the Likelihood function add
PK => Theory%MPK
allocate (mpk_lin(this%num_mpk_kbands_use)) !Vector containing the P(k) values
allocate (kbands(this%num_mpk_kbands_use)) !Vector containing the k values

do i = 1, this%num_mpk_kbands_use, 1
     kbands(i) = !Define the vector at which wavenumbers to compute the power
     spectrum
     mpk_lin(i) = PK%PowerAt(kbands(i),0._mpc) !Compute P(k) at the given k and
     at redshift z = 0
end do
```

APPENDIX C

Appendix for the Determination of Galaxy Cluster Temperatures

C.1 Parameter Bias

Within this section we state the estimated correction functions for the parameter bias and describe for which mass and redshift ranges these corrections apply (Tabs. C.1 – C.3). Because the parameter biases are independent of the cluster mass for the simulations with unknown redshift, the correction function covers the entire simulated redshift space $-2 \leqslant \log(z) \leqslant 0.25$ in these cases. The functions are expressed by equation 4.9 with the variables A and B and present an approximated estimate for the bias correction.

Table C.1: Mass and redshift ranges for the application of the individual correction functions of the parameter bias in case of known cluster redshift.

group	mass range in $\log(M/\mathrm{M}\odot)$	redshift range in $\log(z)$	
		t_{exp} = 1.6 ks	t_{exp} = 20 ks
1	13 – 13.4.5	(-2) – (-1.35)	(-2) – (-0.8)
2	13.45 – 14.05	(-1.7) – (-0.8)	(-1.7) – (-0.2)
3	14.05 – 14.65	(-1.1) – (-0.2)	(-1.1) – 0.25
4	14.65 – 15.25	(-0.65) – 0.25	(-0.65) – 0.25
5	15.25 – 15.7	(-0.2) – 0.25	(-0.2) – 0.25

Table C.2: Parameters of the correction function for the simulation with known redshift.

group	t_{exp} = 1.6 ks		t_{exp} = 20 ks	
	A	B	A	B
1	50.0	5.25	2.53	4.34
2	-0.05	2.47	-0.22	3.25
3	-0.45	3.85	-0.41	2.51
4	-0.17	2.02	-0.22	2.43
5	-0.03	2.56	-0.05	1.07

Table C.3: Parameters of the correction functions for the biases in the temperature and the redshift when the cluster redshift itself is unavailable. For these simulations these biases are independent of the cluster mass.

parameter	$t_{\rm exp}$ = 1.6 ks		$t_{\rm exp}$ = 20 ks	
	A	B	A	B
temperature	-0.46	2.29	-0.32	2.53
redshift	-0.28	2.91	-0.37	3.54

C.2 Comparison between Different Scaling Relations

In addition to the comparison of the number of clusters for the scaling relations given by Reichert et al. (2011) and Vikhlinin et al. (2009a), we performed a thorough analysis of the distribution of galaxy clusters with mass and redshift for these two relations. For both relations a cosmology of $\Omega_{\rm m} = 0.3$, $\Omega_\Lambda = 0,7$, $h = 0.7$ and $\sigma_8 = 0.795$ was assumed. The distribution are presented for three different minimum numbers of detected photons $\eta_{\rm min} = 50, 500$ and 1500 (Figs. C.1 & C.2). Even though sources with as few as 50 photon counts were assumed to be identified as galaxy clusters, a larger number of counts improves the precision and the accuracy of the reduced cluster properties. The simulation of these distributions follows the same setup as described in Sect. 4.4.

With an increasing value for $\eta_{\rm min}$, the total number of detected clusters declines significantly because the distribution of clusters becomes shallower and the low- and intermediate-mass clusters are no longer detected at the high redshifts. According to this, the total number of detected clusters decreases from 113,400 for $\eta_{\rm min} = 50$ to 11,000 for $\eta_{\rm min} = 500$ and to 3,000 for $\eta_{\rm min} = 1500$. At the same time, the maximum of the distribution shifts to lower redshift values $z < 0.3$. In comparison, both scaling relations yield the same position of the maximum of the distribution where the distribution based on the scaling relation by Reichert et al. (2011) displays a broader peak. This development results in a total number of clusters that is 15 – 20% higher than the value for the study of the scaling relation by Vikhlinin et al. (2009a) with a total number of cluster of 103,700 for $\eta_{\rm min} = 50$, 8,900 for $\eta_{\rm min} = 500$ and 2,300 for $\eta_{\rm min} = 1500$.

This analysis emphasises the strong dependence of the distribution of clusters and of the total number of detected clusters on the applied scaling relations and the defined minimum number of photons $\eta_{\rm min}$.

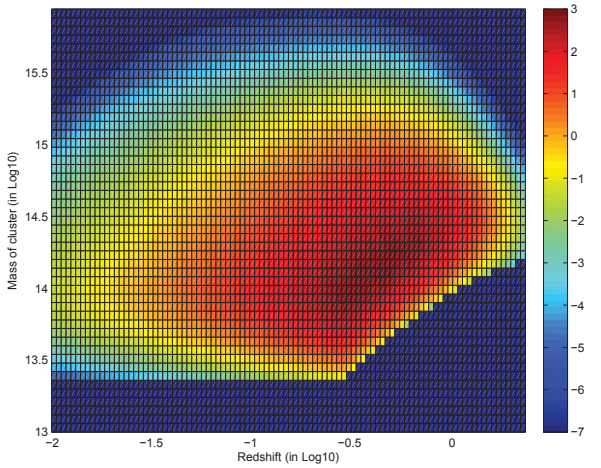

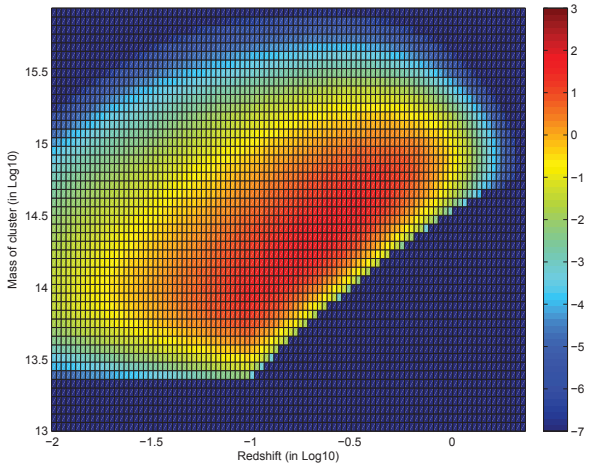

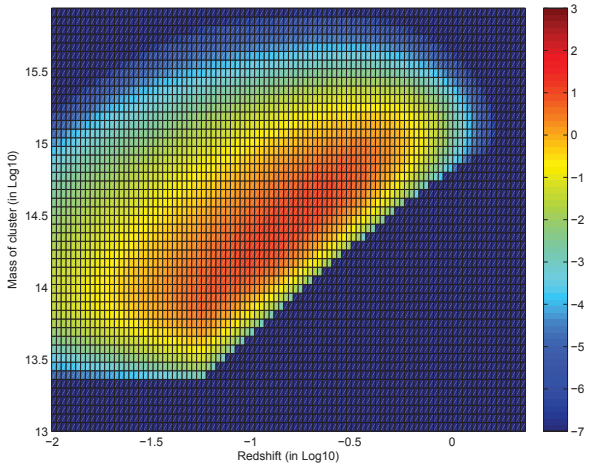

Figure C.1: Distribution of galaxy clusters with mass and redshift for three different photon detection minimums $\eta_{\text{min}} = 50$, 500 and 1500 from top to bottom for the scaling relation by Reichert et al. (2011). All plots are generated for a lower mass cut of $M = 5{\times}10^{13}/h_{100}\,\text{M}_{\odot}$ with $h_{100} = 0.7$. The colour indicates the number of detected clusters in the individual bins in units of $\log_{10}$, where the cluster mass is considered in units of $\log(M/\text{M}_{\odot})$. The total number of detected clusters reads from top to bottom $N_{\text{cluster}} = 113,400$; 11,000; and 3,000.

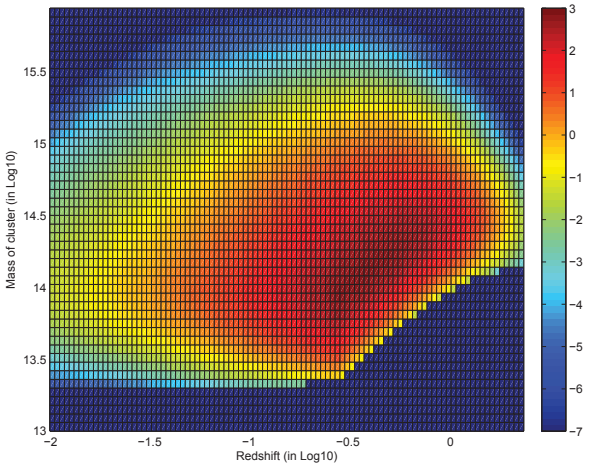

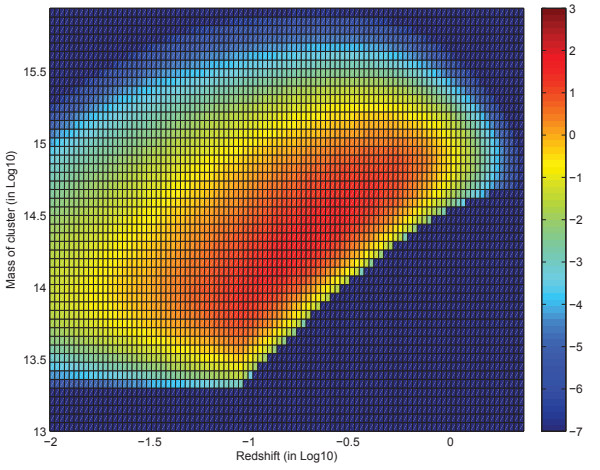

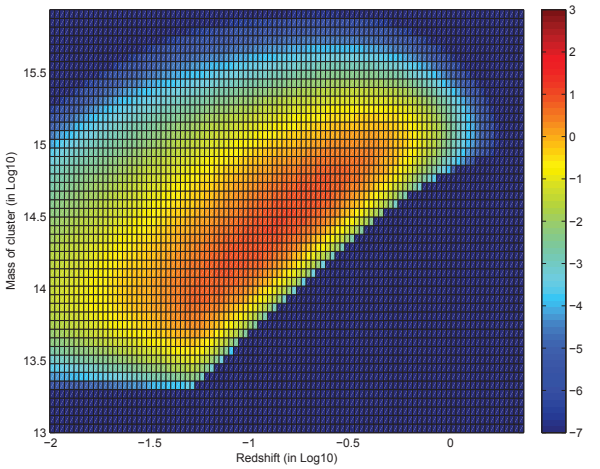

Figure C.2: Distribution of galaxy clusters with mass and redshift for three different photon detection minimums $\eta_{\text{min}} = 50$, 500 and 1500, when applying the scaling relations by (Vikhlinin et al. 2009a). All plots are generated for a lower mass cut of $M = 5\times10^{13}/h_{100}\,\text{M}_{\odot}$ with $h_{100} = 0.70$, where the labeling is equivalent to Fig. C.1. The total number of detected clusters reads from top to bottom $N_{\text{cluster}} = 103,700$; 8,900; and 2,300.

APPENDIX D

Appendix for the Cosmological Forecasts

D.1 Details on the Halo Temperature Function

To define a realistic halo temperature function, we needed to include information on the subsample of *eROSITA* clusters for which temperatures will be available and to account for the statistical uncertainties in the temperature measurements. These aspects were realised by a multiplicative selection function $S(\bar{M}, z)$ and by defining a probability distribution of best-fit temperature values $P(\ln T^* | \ln T, \bar{M}, z)$, respectively. These functions were based on our previous findings (Borm et al. 2014) and included the information, that no parameter bias needed to be considered for clusters with precise temperature estimates.

We defined a cluster temperature to be available, if its relative uncertainty $\Delta T/T \lesssim 10\%$, such that this uncertainty was below the scatter in the $M - T_X$ relation. Fig. D.1 presents the estimates for the median precision of the *eROSITA* cluster temperatures in dependence on the cluster mass and redshift. This simulation was based on the same planned observation strategy with an average exposure time of $t_{exp} = 1.6$ ks and available redshifts for all clusters. The upper left corner defines *eHIFLUGCS* (*extended HIgh FLUx Galaxy Cluster Sample*) (Reiprich 2012) and thus all clusters with a flux of $F > 9 \times 10^{-12}$ erg/s/cm^2 in the energy range of $(0.1 - 2.4)$ keV. For these clusters, temperatures will already be accessible with high precision due to *Chandra* or *XMM-Newton* observations and we defined $S(\bar{M}, z)_{\mathrm{eHIFLUGCS}} = 1$. On the other hand, clusters in the lower right corner show $\eta < 100$ and were thus not expected to show precise temperature measurement and were subject to the simulation limits within *xspec*, such that we concluded $S(\bar{M}, z)_{\eta<100} = 0$.

For the simulated results within the dashed white contour lines, we had 300 repeated fits for each mass-redshift combination and we inspected the distribution of the fit results of each individual pixel to define the selection function. However, even for clusters with a median $\Delta T/\langle T \rangle > 10\%$, some of the fit results showed an individual $\Delta T/T$ below this limit. An opposite consideration was valid for clusters with a median $\Delta T/\langle T \rangle < 10\%$. Accordingly, we defined $S(\bar{M}, z)$ as a step function (Tab. D.1) to incorporate this smooth transition in the relative temperature uncertainties. The different combinations of cluster mass and redshift were divided into steps according to the average probability to obtain a precise temperature estimate, which then defined the value of the selection function. We intentionally added a step function at this point instead of an interpolation, since the grid of the temperature forecast was rather broad and we were thus missing the required statistics to define a more detailed allocation between $\Delta T/\langle T \rangle$ and $S(\bar{M}, z)$, such that a step function allowed for the most robust estimate of the selection.

After defining the selection function, we inspected the statistical scatter in the best-fit temperature values in the different mass-redshift pixels (Fig. D.2). Both the width of the distribution of best-fit values as well as its shape were strongly dependent on the median relative temperature uncertainty and thus on

$(\bar{M}, z)$. For precise temperature estimates of the order of $\Delta T/\langle T\rangle \lesssim 0.05$, a normal and a log-normal distribution yielded an equally accurate fit, where for lower precisions the log-normal distribution described the best-fit values more properly. Accordingly, we defined the scatter in the temperature estimates as

$$P(\ln T^*|\ln T_{\rm X}, \bar{M}, z) = \frac{1}{\sqrt{2\pi\sigma^2_{TT}(\bar{M}, z)}} \cdot \exp\left[-\frac{(\ln T^* - \ln T_{\rm X})^2}{2\sigma^2_{\rm TT}(\bar{M}, z)}\right] \quad , \tag{D.1}$$

with $\sigma_{\rm TT} = \langle \Delta T/T\rangle(\bar{M}, z)$.

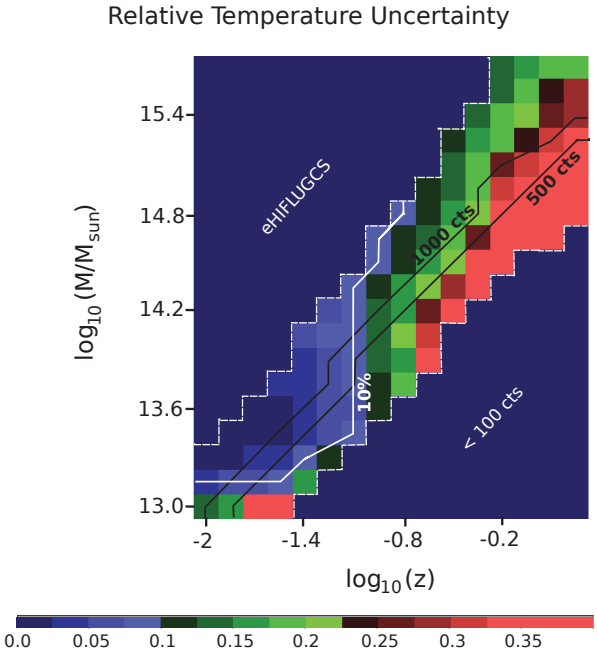

Figure D.1: Expected relative temperature uncertainties for the *eROSITA* galaxy clusters in dependence on the cluster mass and redshift. The colour of the pixels depicts the median relative temperature uncertainty, where the dark-blue regions outside the white dashed contours are excluded from the simulations. Solid white and black contours are included to emphasise on the levels of relative uncertainties and photon counts, respectively. *Credit: Borm et al. (2014)*

Table D.1: Selection function $S(\bar{M}, z)$ of clusters with available temperature information

$\Delta T/\langle T\rangle$	$S(\bar{M}, z)$
< 0.07	1.0
< 0.09	0.94
< 0.10	0.73
< 0.11	0.42
< 0.13	0.12
≤ 0.14	0.08
> 0.14	0.0

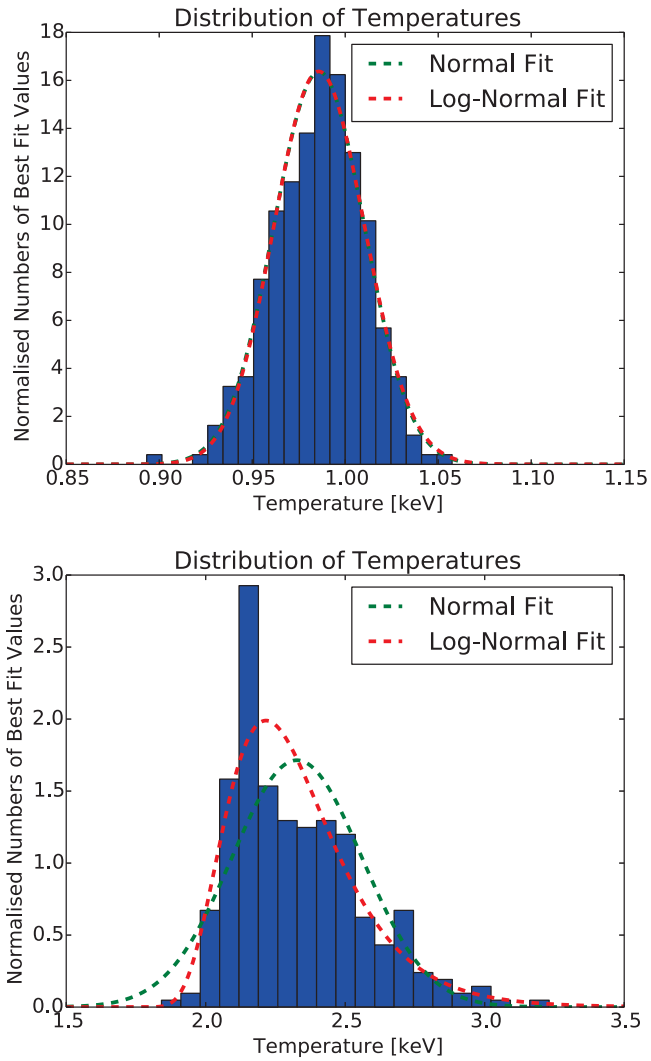

Figure D.2: Distribution of best-fit temperatures for two different cluster mass-redshift combinations with relative uncertainties of $\Delta T/\langle T\rangle = 0.025$ (top) and $\Delta T/\langle T\rangle = 0.094$ (bottom), respectively. Presented are a normal as well as a log-normal fit to these distributions, where the log-normal fit reproduces the data more accurately, especially in the case of the higher relative uncertainty.

D.2 Additional Data

At this point, we summarise additional data, which is required to follow the detailed comparisons between different forecast set-ups and scenarios.

Table D.2: Forecasts of the cosmological constraints by P16, considering four years of all-sky observations, eRASS:8, and the inclusion of the first year *Planck*-data (*Planck*+BAO+H_0+polarisation+supernovae type Ia) (Planck Collaboration et al. 2014a). The *eROSITA*-observations always include the described priors on the Hubble parameter and the baryon density (comp. Sect. 6.5.2), where the simulations were based on the information of cluster abundances and angular clustering. Different cosmological models of a ΛCDM universe, of a cosmology with a constant, w_0CDM, and with an evolving, wCDM, dark energy equation of state were tested.

Data	Scenario	Model	$\Delta\sigma_8$	$\Delta\Omega_m$	Δw_0	Δw_a
eRASS:8	Pessimistic	ΛCDM	0.014	0.012	–	–
eRASS:8	Optimistic	ΛCDM	0.009	0.007	–	–
eRASS:8+*Planck*	Pessimistic	ΛCDM	0.008	0.007	–	–
eRASS:8+*Planck*	Optimistic	ΛCDM	0.006	0.004	–	–
eRASS:8	Pessimistic	w_0CDM	0.014	0.012	0.053	–
eRASS:8	Optimistic	w_0CDM	0.009	0.007	0.034	–
eRASS:8+*Planck*	Pessimistic	w_0CDM	0.009	0.007	0.033	–
eRASS:8+*Planck*	Optimistic	w_0CDM	0.007	0.005	0.026	–
eRASS:8	Pessimistic	w_aCDM	0.019	0.017	0.139	0.48
eRASS:8	Optimistic	w_aCDM	0.011	0.008	0.091	0.36
eRASS:8+*Planck*	Pessimistic	w_aCDM	0.010.	0.008	0.093	0.31
eRASS:8+*Planck*	Optimistic	w_aCDM	0.007	0.006	0.071	0.27

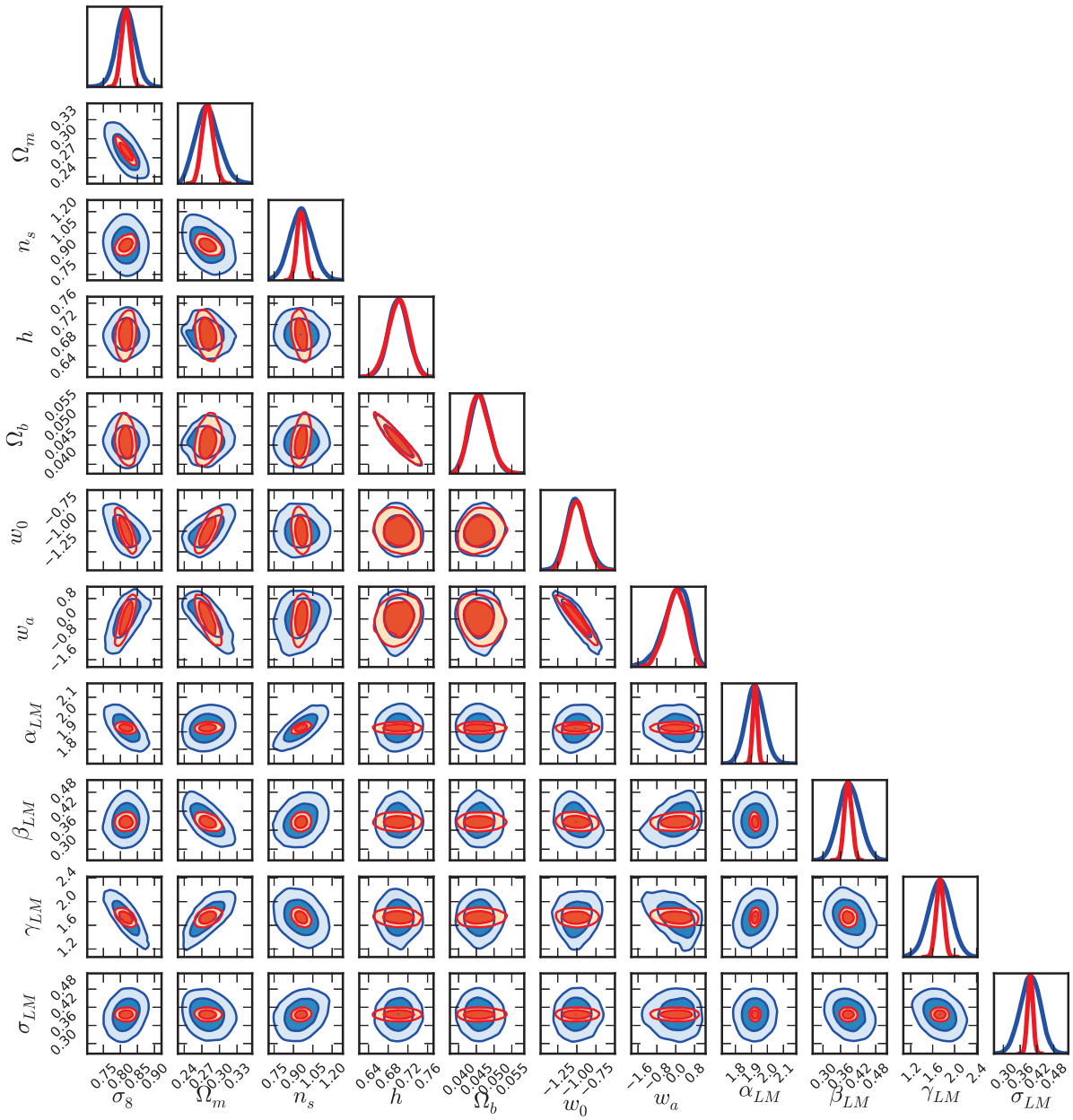

Figure D.3: Expected constraints on the cosmological as well as on the scaling parameters for a *w*CDM-cosmology when applying the *eRASS:8* catalogue containing the redshifts and photon counts of all observed *eROSITA* clusters. We present the results for the pessimistic (blue) and for the optimistic (red) simulation scenarios with the contour plots displaying the 68%- and the 95%-credibility regions. The 1-dimensional histograms show the 68% distributions only.

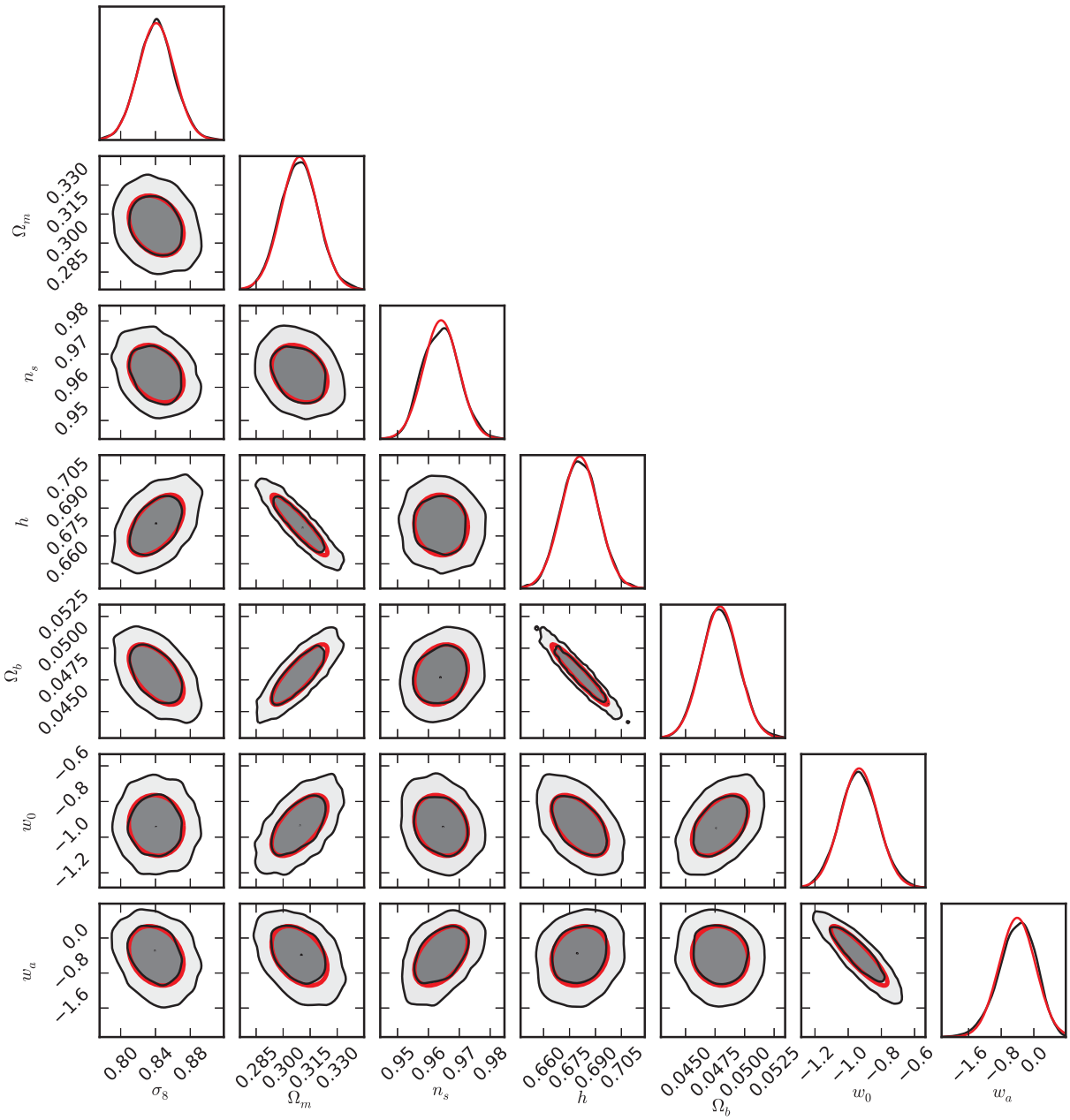

Figure D.4: Credibility region of the *Planck*-data analysis in black with superimposed Gaussian uncertainty ellipses in red. The 2-dimensional as well as the 1-dimensional histograms display Gaussian-like distributions with only small deviations for especially n_s and w_a, which we estimate to by of the order of $\lesssim 10\%$ based on the comparison between the prior values and the computed uncertainties Δh and $\Delta\Omega_b$ in the *eROSITA* forecasts (Sect. 6.6.1 & Fig. 6.9).

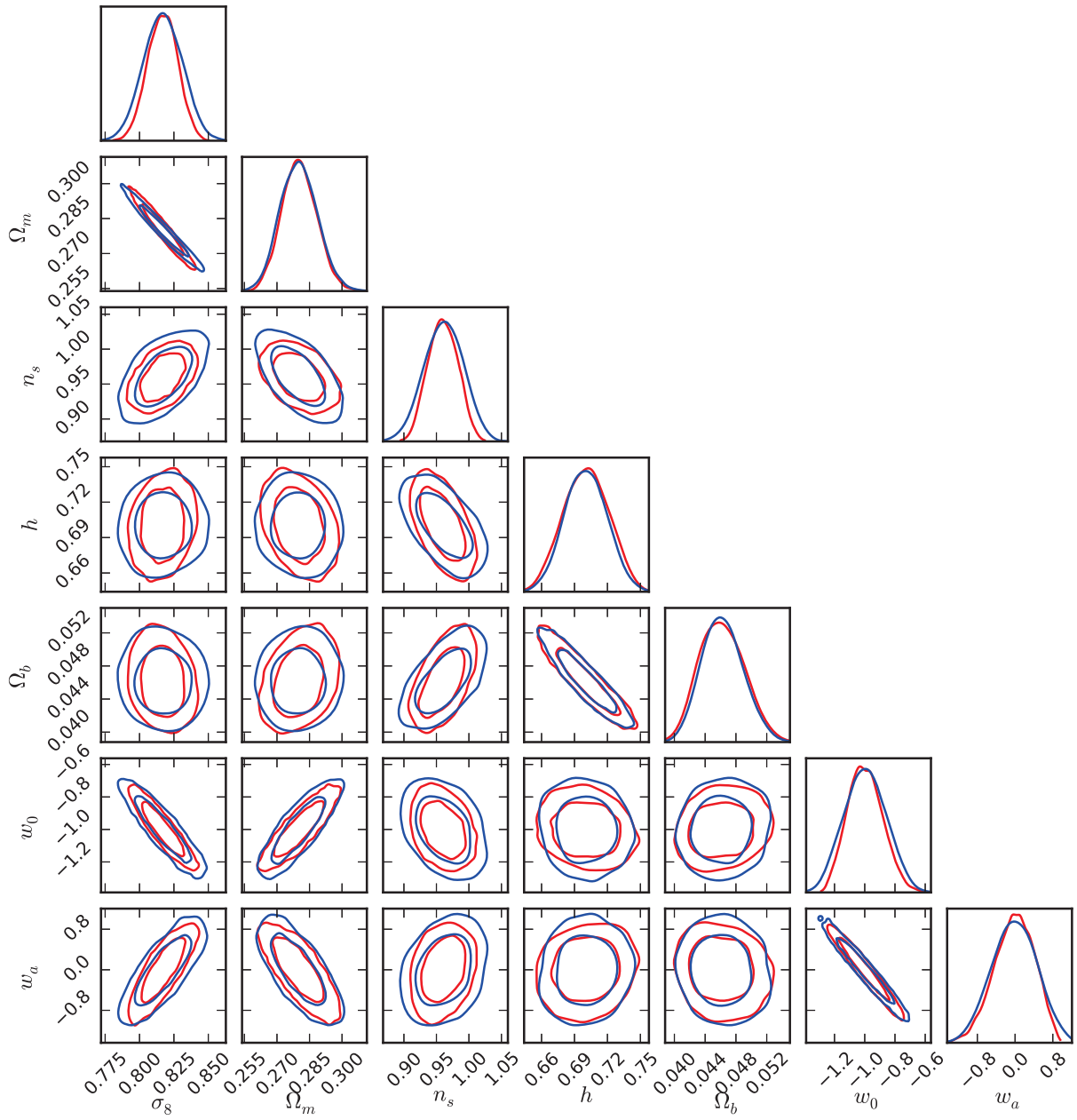

Figure D.5: Credibility regions for the *MCMC* forecasts of a *w*CDM-cosmology with fixed scaling parameters. The comparison is shown between the simulation approach for the scaling relations by Reichert et al. (2011) (red contours) and by Vikhlinin et al. (2009a) (blue contours), while presenting the 68%- as well as the 95%-credibility intervals.

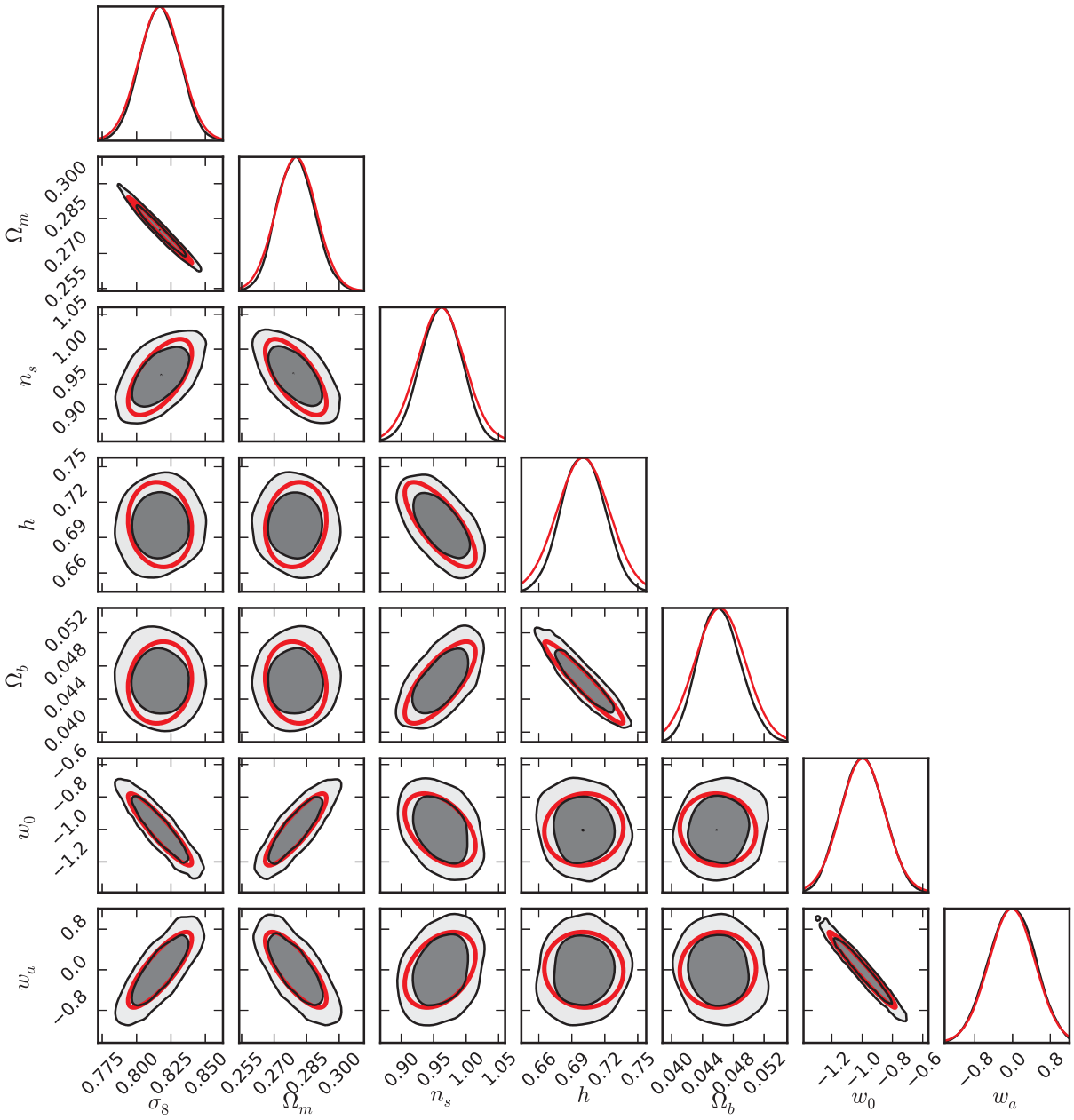

Figure D.6: Comparison between the results of the *MCMC* and the Fisher formalism. Presented are the joint credibility regions for a *w*CDM cosmological model, applying the scaling relations by Vikhlinin et al. (2009a). The black contours show the results of the *MCMC* approach, whereas the red ellipses and normal distributions display the Fisher forecasts.

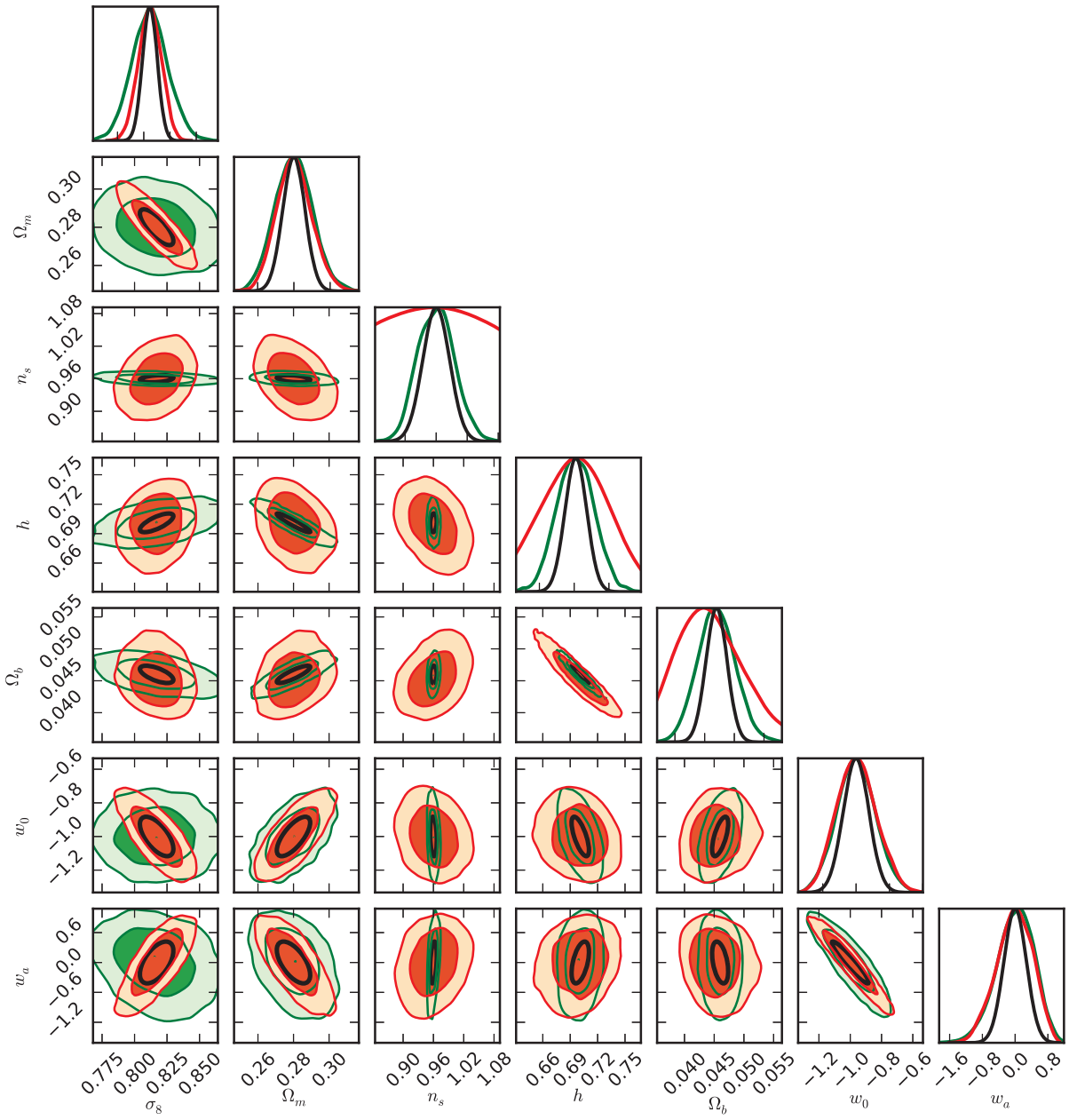

Figure D.7: Comparison between the 68%- and the 95%-constraints from the full *eROSITA* cluster catalogue in an optimistic scenario (red) and the results from *Planck*+BAO+H_0+JLA (green) for a wCDM cosmology. The *Planck* data have been shifted to the best-fit *WMAP5* cosmology to match the mean values of the *eROSITA* constraints. The black ellipses indicate the computed joint 68%-credibilities of the two data sets, while approximating Gaussianity for the *MCMC* contours.

Bibliography

Ackermann, M., Ajello, M., Albert, A., et al. 2014, ApJ, 787, 18

Acquaviva, V., Bartolo, N., Matarrese, S., & Riotto, A. 2003, Nuclear Physics B, 667, 119

Akamatsu, H., Hoshino, A., Ishisaki, Y., et al. 2011, PASJ, 63, 1019

Albrecht, A., Amendola, L., Bernstein, G., et al. 2009, ArXiv e-prints

Albrecht, A., Bernstein, G., Cahn, R., et al. 2006, ArXiv Astrophysics e-prints

Allen, S. W., Evrard, A. E., & Mantz, A. B. 2011, ARA&A, 49, 409

Allen, S. W., Schmidt, R. W., & Fabian, A. C. 2001, MNRAS, 328, L37

Anders, E. & Grevesse, N. 1989, Geochim. Cosmochim. Acta, 53, 197

Anders, M., Trezzi, D., Menegazzo, R., et al. 2014, Physical Review Letters, 113, 042501

Anderson, L., Aubourg, É., Bailey, S., et al. 2014, MNRAS, 441, 24

Anderson, L., Aubourg, E., Bailey, S., et al. 2012, MNRAS, 427, 3435

Applegate, D. E., Mantz, A., Allen, S. W., et al. 2015, ArXiv e-prints

Applegate, D. E., von der Linden, A., Kelly, P. L., et al. 2014, MNRAS, 439, 48

Arnaud, K., Dorman, B., & Gordon, C. 2011, xspec - An X-ray pectral fitting package, HEASARC

Arnaud, K. A. 1996, in Astronomical Society of the Pacific Conference Series, Vol. 101, Astronomical Data Analysis Software and Systems V, ed. G. H. Jacoby & J. Barnes, 17

Arnaud, M., Rothenflug, R., Boulade, O., Vigroux, L., & Vangioni-Flam, E. 1992, A&A, 254, 49

Asplund, M., Grevesse, N., Sauval, A. J., & Scott, P. 2009, ARA&A, 47, 481

Balaguera-Antolinez, A. & Porciani, C. 2013, JCAP, 4, 22

Baldi, A., Ettori, S., Molendi, S., et al. 2012, A&A, 537, A142

Balestra, I., Tozzi, P., Ettori, S., et al. 2007, A&A, 462, 429

Bardeen, J. M., Bond, J. R., Kaiser, N., & Szalay, A. S. 1986, ApJ, 304, 15

Baumann, D. 2009, ArXiv e-prints

Bergström, L. 2000, Reports on Progress in Physics, 63, 793

Bernstein, J. P., Kessler, R., Kuhlmann, S., et al. 2012, ApJ, 753, 152

Bertone, G., Hooper, D., & Silk, J. 2005, Phys. Rep., 405, 279

Betoule, M., Kessler, R., Guy, J., et al. 2014, A&A, 568, A22

Beutler, F., Saito, S., Seo, H.-J., et al. 2014, MNRAS, 443, 1065

BICEP2 Collaboration, Ade, P. A. R., Aikin, R. W., et al. 2014, Physical Review Letters, 112, 241101

BICEP2 Collaboration, Keck Collaboration, SPIDER Collaboration, et al. 2015, ApJ, 812, 176

Bocquet, S., Saro, A., Dolag, K., & Mohr, J. J. 2015, ArXiv e-prints

Böhringer, H. & Chon, G. 2015, A&A, 574, L8

Borgani, S. & Guzzo, L. 2001, Nature, 409, 39

Borgani, S. & Kravtsov, A. 2011, Advanced Science Letters, 4, 204

Borm, K., Reiprich, T. H., Mohammed, I., & Lovisari, L. 2014, A&A, 567, A65

Bradač, M., Allen, S. W., Treu, T., et al. 2008, ApJ, 687, 959

Burles, S., Nollett, K. M., Truran, J. W., & Turner, M. S. 1999, Physical Review Letters, 82, 4176

Burles, S. & Tytler, D. 1998, ApJ, 507, 732

Carroll, S. M., Press, W. H., & Turner, E. L. 1992, ARA&A, 30, 499

Cash, W. 1979, ApJ, 228, 939

Catelan, P., Lucchin, F., Matarrese, S., & Porciani, C. 1998, MNRAS, 297, 692

Cavaliere, A. & Fusco-Femiano, R. 1976, A&A, 49, 137

Cen, R. & Fang, T. 2006, ApJ, 650, 573

Chevallier, M. & Polarski, D. 2001, International Journal of Modern Physics D, 10, 213

Clerc, N., Pierre, M., Pacaud, F., & Sadibekova, T. 2012, MNRAS, 423, 3545

Coe, D. 2009, ArXiv e-prints

Colless, M., Dalton, G., Maddox, S., et al. 2001, MNRAS, 328, 1039

Cooke, R. J., Pettini, M., Jorgenson, R. A., Murphy, M. T., & Steidel, C. C. 2014, ApJ, 781, 31

Costanzi, M., Sartoris, B., Viel, M., & Borgani, S. 2014, JCAP, 10, 81

Crocce, M., Carretero, J., Bauer, A. H., et al. 2015, ArXiv e-prints

Cui, W., Borgani, S., Dolag, K., Murante, G., & Tornatore, L. 2012, MNRAS, 423, 2279

Danforth, C. W. & Shull, J. M. 2005, in Bulletin of the American Astronomical Society, Vol. 37, American Astronomical Society Meeting Abstracts, 120.10

de Jong, R. S., Barden, S., Bellido-Tirado, O., et al. 2014, in Society of Photo-Optical Instrumentation Engineers (SPIE) Conference Series, Vol. 9147, Society of Photo-Optical Instrumentation Engineers (SPIE) Conference Series, 0

Dodelson, S. 2003, Modern cosmology

Ebeling, H., Edge, A. C., Burgett, W. S., et al. 2013, MNRAS, 432, 62

Eckmiller, H. J., Hudson, D. S., & Reiprich, T. H. 2011, A&A, 535, A105

Efstathiou, G. 2014, MNRAS, 440, 1138

Eisenstein, D. J. & Hu, W. 1998, ApJ, 496, 605

Eisenstein, D. J., Zehavi, I., Hogg, D. W., et al. 2005, ApJ, 633, 560

Evrard, A. E., MacFarland, T. J., Couchman, H. M. P., et al. 2002, ApJ, 573, 7

Fields, B. D. 2011, Annual Review of Nuclear and Particle Science, 61, 47

Fixsen, D. J. 2009, ApJ, 707, 916

Friedmann, A. 1922, Zeitschrift für Physik, 10, 377

Fukugita, M. 2003, The Mass Assembly History of Field Galaxies, Subaru Proposal

Fukugita, M., Hogan, C. J., & Peebles, P. J. E. 1998, ApJ, 503, 518

Gaztañaga, E., Eriksen, M., Crocce, M., et al. 2012, MNRAS, 422, 2904

Giannantonio, T., Porciani, C., Carron, J., Amara, A., & Pillepich, A. 2012, MNRAS, 422, 2854

Giles, P. A., Maughan, B. J., Dahle, H., et al. 2015, ArXiv e-prints

Giodini, S., Lovisari, L., Pointecouteau, E., et al. 2013, Space Sci. Rev., 177, 247

Hamilton, A. J. S. 1998, in Astrophysics and Space Science Library, Vol. 231, The Evolving Universe, ed. D. Hamilton, 185

Harrison, F. A., Craig, W. W., Christensen, F. E., et al. 2013, ApJ, 770, 103

Hawkins, E., Maddox, S., Cole, S., et al. 2003, MNRAS, 346, 78

Henriksen, M. J. & Mushotzky, R. F. 1986, ApJ, 302, 287

Hinshaw, G., Larson, D., Komatsu, E., et al. 2013, ApJS, 208, 19

Hoekstra, H., Bartelmann, M., Dahle, H., et al. 2013, Space Sci. Rev., 177, 75

Hu, W. & Dodelson, S. 2002, ARA&A, 40, 171

Hudson, D. S., Mittal, R., Reiprich, T. H., et al. 2010, A&A, 513, A37

Humphrey, P. J., Liu, W., & Buote, D. A. 2009, ApJ, 693, 822

Ichiki, K. & Takada, M. 2012, Phys. Rev. D, 85, 063521

Israel, H., Reiprich, T. H., Erben, T., et al. 2014, A&A, 564, A129

Israel, H., Schellenberger, G., Nevalainen, J., Massey, R., & Reiprich, T. H. 2015, MNRAS, 448, 814

Jenkins, A., Frenk, C. S., White, S. D. M., et al. 2001, MNRAS, 321, 372

Kaiser, N. 1986, MNRAS, 222, 323

Kalberla, P. M. W., Burton, W. B., Hartmann, D., et al. 2005, A&A, 440, 775

Kazin, E. A., Koda, J., Blake, C., et al. 2014, MNRAS, 441, 3524

Khedekar, S. & Majumdar, S. 2013, JCAP, 2, 30

King, I. 1962, AJ, 67, 471

Kitayama, T., Bautz, M., Markevitch, M., et al. 2014, ArXiv e-prints

Kolb, E. W. & Turner, M. S. 1990, The early universe.

Komatsu, E., Dunkley, J., Nolta, M. R., et al. 2009, ApJS, 180, 330

Komatsu, E., Smith, K. M., Dunkley, J., et al. 2011, ApJS, 192, 18

Kravtsov, A. V., Vikhlinin, A., & Nagai, D. 2006, ApJ, 650, 128

Krumpe, M., Lamer, G., Corral, A., et al. 2008, A&A, 483, 415

Kuhlen, M., Strigari, L. E., Zentner, A. R., Bullock, J. S., & Primack, J. R. 2005, MNRAS, 357, 387

Laureijs, R. 2009, ArXiv e-prints

Leccardi, A. & Molendi, S. 2007, A&A, 472, 21

Lesgourgues, J., Mangano, G., Miele, G., & Pastor, S. 2013, Neutrino Cosmology

Lesgourgues, J. & Pastor, S. 2006, Phys. Rep., 429, 307

Lesgourgues, J. & Pastor, S. 2012, ArXiv e-prints

Lewis, A. & Bridle, S. 2002, Phys. Rev. D, 66, 103511

Lewis, A., Challinor, A., & Lasenby, A. 2000, ApJ, 538, 473

Linder, E. V. 2003, Physical Review Letters, 90, 091301

Linder, E. V. & Jenkins, A. 2003, MNRAS, 346, 573

Liu, J., Hennig, C., Desai, S., et al. 2015, MNRAS, 449, 3370

Lloyd-Davies, E. J., Romer, A. K., Mehrtens, N., et al. 2011, MNRAS, 418, 14

Lovisari, L., Schindler, S., & Kapferer, W. 2011, A&A, 528, A60

Lumb, D. H., Warwick, R. S., Page, M., & De Luca, A. 2002, A&A, 389, 93

Mahdavi, A., Hoekstra, H., Babul, A., et al. 2013, ApJ, 767, 116

Mahdavi, A., Hoekstra, H., Babul, A., & Henry, J. P. 2008, MNRAS, 384, 1567

Maldacena, J. 2003, Journal of High Energy Physics, 5, 13

Mantz, A., Allen, S. W., Ebeling, H., Rapetti, D., & Drlica-Wagner, A. 2010a, MNRAS, 406, 1773

Mantz, A., Allen, S. W., Rapetti, D., & Ebeling, H. 2010b, MNRAS, 406, 1759

Mantz, A. B., von der Linden, A., Allen, S. W., et al. 2015, MNRAS, 446, 2205

Markevitch, M., Bautz, M. W., Biller, B., et al. 2003, ApJ, 583, 70

Markevitch, M., Randall, S., Clowe, D., Gonzalez, A., & Bradac, M. 2006, in COSPAR Meeting, Vol. 36, 36th COSPAR Scientific Assembly, 2655

Maughan, B. J. 2007, ApJ, 668, 772

Maughan, B. J., Jones, C., Forman, W., & Van Speybroeck, L. 2008, ApJS, 174, 117

Maurin, D., Combet, C., Nezri, E., & Pointecouteau, E. 2012, A&A, 547, A16

Meneghetti, M., Rasia, E., Merten, J., et al. 2010, A&A, 514, A93

Merloni, A., Predehl, P., & Becker, W. 2012, eROSITA Science Book

Mittal, R., O'Dea, C. P., Ferland, G., et al. 2011, MNRAS, 418, 2386

Mo, H. J. & White, S. D. M. 1996, MNRAS, 282, 347

Mushotzky, R. F. & Loewenstein, M. 1997, ApJ, 481, L63

Muzzin, A., Wilson, G., Yee, H. K. C., et al. 2009, ApJ, 698, 1934

Nagai, D., Vikhlinin, A., & Kravtsov, A. V. 2007, ApJ, 655, 98

Nandra, K., Barret, D., Barcons, X., et al. 2013, ArXiv e-prints

Newman, A. B., Treu, T., Ellis, R. S., & Sand, D. J. 2011, ApJ, 728, L39

O'Hara, T. B., Mohr, J. J., & Bialek, J. J., e. a. 2006, ApJ, 639, 64

Ota, N., Nagai, D., & Lau, E. T. 2015, ArXiv e-prints

Peacock, J. A. 1999, Cosmological Physics

Percival, W. J. 2005, A&A, 443, 819

Perlmutter, S., Aldering, G., Boyle, B. J., e. a., & Supernova Cosmology Project. 1998, in 19th Texas Symposium on Relativistic Astrophysics and Cosmology, ed. J. Paul, T. Montmerle, & E. Aubourg

Piffaretti, R., Arnaud, M., Pratt, G. W., Pointecouteau, E., & Melin, J.-B. 2011, A&A, 534, A109

Pillepich, A., Porciani, C., & Reiprich, T. H. 2012, MNRAS, 422, 44

Planck Collaboration, Ade, P. A. R., Aghanim, N., et al. 2013, ArXiv 1303.5080

Planck Collaboration, Ade, P. A. R., Aghanim, N., et al. 2014a, A&A, 571, A16

Planck Collaboration, Ade, P. A. R., Aghanim, N., et al. 2014b, A&A, 571, A24

Planck Collaboration, Ade, P. A. R., Aghanim, N., et al. 2015a, ArXiv e-prints

Planck Collaboration, Ade, P. A. R., Aghanim, N., et al. 2015b, ArXiv e-prints

Planck Collaboration, Ade, P. A. R., Aghanim, N., et al. 2015c, ArXiv e-prints

Planck Collaboration, Aghanim, N., Arnaud, M., et al. 2012, ArXiv e-prints

Planck Collaboration, Aghanim, N., Arnaud, M., et al. 2011, A&A, 536, A9

Pratt, G. W., Croston, J. H., Arnaud, M., & Böhringer, H. 2009, A&A, 498, 361

Predehl, P., Andritschke, R., Böhringer, H., et al. 2010, in Society of Photo-Optical Instrumentation Engineers (SPIE) Conference Series, Vol. 7732, Society of Photo-Optical Instrumentation Engineers (SPIE) Conference Series

Press, W. H. & Schechter, P. 1974, ApJ, 187, 425

Press, W. H., Teukolsky, S. A., Vetterling, W. T., & Flannery, B. P. 2007, Numerical Rescipes, 3rd edn. (Cambridge University Press)

Prokhorov, D. A. & Churazov, E. M. 2014, A&A, 567, A93

Randall, S. W., Markevitch, M., Clowe, D., Gonzalez, A. H., & Bradač, M. 2008, ApJ, 679, 1173

Reichardt, C. L., Stalder, B., Bleem, L. E., et al. 2013, ApJ, 763, 127

Reichert, A., Böhringer, H., & Fassbender, R., e. a. 2011, A&A, 535

Reiprich, T. 2012, Completing eHIFLUGCS: the Ultimate Precise and Accurate Local Baseline, Chandra Proposal

Reiprich, T. H. 1998, Master's thesis, Diploma Thesis, Ludwig-Maximilians-Universität München, (1998)

Reiprich, T. H., Basu, K., Ettori, S., et al. 2013, Space Sci. Rev., 177, 195

Reiprich, T. H. & Böhringer, H. 2002, ApJ, 567, 716

Riess, A. G., Filippenko, A. V., & Challis, P., e. a. 1998, AJ, 116, 1009

Riess, A. G., Macri, L., Casertano, S., et al. 2011, ApJ, 730, 119

Roncarelli, M., Carbone, C., & Moscardini, L. 2015, MNRAS, 447, 1761

Rosati, P., Borgani, S., & Norman, C. 2002, ARA&A, 40, 539

Salvato, M. 2015, IAU General Assembly, 22, 42709

Sarazin, C. L. 1986, Reviews of Modern Physics, 58, 1

Sartoris, B., Biviano, A., Fedeli, C., et al. 2015, ArXiv e-prints

Savage, B. D., Lehner, N., & Narayanan, A. 2011, ApJ, 743, 180

Schmid, C. 2012, PhD thesis, Dr. Remeis-Sternwarte Bamberg, http://www.sternwarte.uni-erlangen.de/Arbeiten/2012-07_Schmid.pdf

Schmid, C., Smith, R., & J., W. 2013, SIMPUT - A File Format for SIMulation InPUT, http://hea-www.harvard.edu/heasarc/formats/simput-1.1.0.pdf

Schmid, C. 2008, diploma thesis, Dr. Remeis-Sternwarte Bamberg, http://www.sternwarte.uni-erlangen.de/~schmid/download/schmid_erosita.pdf

Schneider, P. 2015, Extragalactic Astronomy and Cosmology: An Introduction

Shanks, T., Metcalfe, N., Chehade, B., et al. 2015, MNRAS, 451, 4238

Smith, R. E., Scoccimarro, R., & Sheth, R. K. 2007, Phys. Rev. D, 75, 063512

Smith, R. K., Brickhouse, N. S., Liedahl, D. A., & Raymond, J. C. 2001, ApJ, 556, L91

Spitzer, L. 1956, Physics of Fully Ionized Gases

Springel, V., White, S. D. M., & Jenkins, A., e. a. 2005, Nature, 435, 629

Stanek, R., Rasia, E., Evrard, A. E., Pearce, F., & Gazzola, L. 2010, ApJ, 715, 1508

Stanek, R., Rudd, D., & Evrard, A. E. 2009, MNRAS, 394, L11

Stocke, J. T., Keeney, B. A., Danforth, C. W., et al. 2013, ApJ, 763, 148

Sunyaev, R. A. & Zeldovich, Y. B. 1970, Comments on Astrophysics and Space Physics, 2, 66

Sunyaev, R. A. & Zeldovich, Y. B. 1972, Comments on Astrophysics and Space Physics, 4, 173

Takahashi, T., Mitsuda, K., Kelley, R., et al. 2014, ArXiv e-prints

Tejos, N., Prochaska, J. X., Crighton, N. H. M., et al. 2015, ArXiv e-prints

Tenzer, C., Warth, G., Kendziorra, E., & Santangelo, A. 2010, Proceedings of the SPIE, 7742

The Dark Energy Survey Collaboration. 2005, ArXiv Astrophysics e-prints

Tinker, J., Kravtsov, A. V., Klypin, A., et al. 2008, ApJ, 688, 709

Trümper, J. 1985, Bulletin d'Information du Centre de Donnees Stellaires, 28, 81

Vanderlinde, K., Crawford, T. M., de Haan, T., et al. 2010, ApJ, 722, 1180

Vikhlinin, A., Burenin, R. A., & Ebeling, H., e. a. 2009a, ApJ, 692, 1033

Vikhlinin, A., Kravtsov, A. V., Burenin, R. A., et al. 2009b, ApJ, 692, 1060

Vikhlinin, A., Markevitch, M., Murray, S. S., et al. 2005, ApJ, 628, 655

Voges, W., Aschenbach, B., Boller, T., et al. 1999, A&A, 349, 389

Voit, G. M. 2005, Reviews of Modern Physics, 77, 207

Wenzel, A. 2014, Bachelor thesis, Universität Bonn

Werk, J. K., Prochaska, J. X., Tumlinson, J., et al. 2014, ApJ, 792, 8

Werner, N., Durret, F., Ohashi, T., Schindler, S., & Wiersma, R. P. C. 2008, Space Sci. Rev., 134, 337

Wilson, G., Muzzin, A., Yee, H. K. C., et al. 2009, ApJ, 698, 1943

Wolter, H. 1952a, Annalen der Physik, 445, 94

Wolter, H. 1952b, Annalen der Physik, 445, 286

Wolz, L., Kilbinger, M., Weller, J., & Giannantonio, T. 2012, JCAP, 9, 9

Yu, H., Tozzi, P., & Borgani, S., e. a. 2011, A&A, 529, A65

Zhang, Y.-Y., Finoguenov, A., Böhringer, H., et al. 2004, A&A, 413, 49

Zhao, G.-B., Wang, Y., Ross, A. J., et al. 2015, ArXiv e-prints

Zwicky, F. 1933, Helvetica Physica Acta, 6, 110

Acknowledgements

Along the busy but also exciting road of working on this PhD thesis, I was guided and supported by many people, to whom I want to dedicate a share in this thesis.
I would like to express my deepest gratitude to my supervisors, Thomas. H. Reiprich, for his professional as well as methodical assistance and encouragement, which started already during the work on my master thesis, and Cristiano Porciani, for the professional guidance especially in all theoretical aspects as well as for his general support and guidance. Thanks to both of them, I developed a strong interest in the research field of cosmology, learned to work independently and thoroughly as well as to always scrutinise results and data. Also, I was offered the opportunity to work on the scientific preparation of the future *eROSITA* instrument, to be introduced into the corresponding collaboration and to contribute to this high-potential mission.
Additionally, I would like to give a warm thanks to Lorenzo Lovisari, not only for his expertise on galaxy clusters and the support for the first project of my thesis, but also for creating a welcoming and friendly working atmosphere.
I greatly appreciate my financial sponsorship and interdisciplinary continuing education by the *Deutsche Telekom Stiftung* during three full years of my PhD work. Thanks to their stipend and the associated annual travel allowances, I was able to focus on my research without needing to apply for further fundings, and to attend many attractive and advanced international conferences, schools, and seminars. Additionally, their assistance measures allowed me to amplify and to expand my knowledge on various different soft skills. Of great importance to me, was also and especially their mentoring scheme and my associated support by Dr. Rolf Densing from the *Deutsches Zentrum für Luft- und Raumfahrt*. He offered many insights and contacts into this institution and I was invited to many internal events.
Besides the *Deutsche Telekom Stiftung*, I also want to thank the *Bonn Cologne Graduate School*, the *Max-Planck Research School* as well as the *TransRegio 33: "The Dark Universe"* for their methodical as well as financial support.
I also want to express a special thanks to my entire research group: Lorenzo, Gerrit, Miriam, Alberto, Bharad, Yuying, Sophia and Aarti for their experience and help in different science aspects as well as for their friendly camaraderie and the fun times at conferences and meeting, especially including the skiing lessons. The same is true also for my (former) office mates: Jennifer, Alex and Dori for the pleasant and easy atmosphere in the office, for your sympathy and for the padding on the back during the busy months of working on the thesis.
I want to address especially much appreciation also to my other colleagues and good friends: Denise, Verena, Nadya, Daniel, Lars, Shahram, Tobias and Fabian for the merry lunch and coffee breaks, for the diverse support in all matters, from python programming to a shoulder to lean and depend on, and for dragging me into the public outreach. Thanks also for the joint time outside the institute, for the movie nights and concert trips, for the sport appointments and the cheers along my marathon race track.
Save the best for last, I want to give great recognition to my family, to my parents, Andreas and Regina, to my brother, Jannik, and especially to my boyfriend, René, as all of them accompanied my journey to complete my PhD starting from the very beginning. Thanks for believing in me, for always supporting my decisions and lending a helping hand, and for telling me to never give up.